polymers

MDPI

Article

Thermoplastic Recycling of WEEE Carcasses with the Incorporation of Talc, Fly Ash, and Elastomers for Composites with Electromagnetic Interference Shielding Characteristics for Electric Car Components

Mihaela Aradoaei [1], Alina Ruxandra Caramitu [2,*], Magdalena Valentina Lungu [2], Andrei George Ursan [1], Romeo Cristian Ciobanu [1,*], Magdalena Aflori [3] and Adrian Parfeni [1]

[1] Department of Electrical Measurements and Materials, Gheorghe Asachi Technical University, 700050 Iasi, Romania; mihaela.aradoaie@gmail.com (M.A.); andrei_urs@yahoo.com (A.G.U.); adrian.parfeni@student.tuiasi.ro (A.P.)
[2] National Institute for Research and Development in Electrical Engineering ICPE—CA, Splaiul Unirii 313, 030138 Bucharest, Romania; magdalena.lungu@icpe-ca.ro
[3] Petru Poni Institute of Macromolecular Chemistry, 41A Aleea Gr. Ghica Voda, 700487 Iasi, Romania; maflori@icmpp.ro
* Correspondence: alina.caramitu@icpe-ca.ro (A.R.C.); romeo-cristian.ciobanu@academic.tuiasi.ro (R.C.C.); Tel.: +40-747116044 (A.R.C.); +40-751164501 (R.C.C.)

Abstract

In this research, thermoplastic waste (polyethylene and propylene) from waste electrical and electronic equipment (WEEE) was used to manufacture polymer composite materials that included talc, fly ash, and elastomers, with tailored electromagnetic interference shielding properties, for the potential use for electric car components. A distribution of inorganic components within the polymer structures without particle clustering were observed, illustrating an effective melt compounding process. The gradual replacement of talc with fly ash lowered both the fluidity index and the softening temperature values. The increase in fly ash content resulted in higher values of both permittivity and dielectric loss factor. The novelty was related to a significant increase in both dielectric characteristics at increased quantities of fly ash at higher temperatures, an aspect more relevant at higher frequencies where they approached a steady value. The permittivity values surpassed five, and the dielectric loss factor values exceeded 0.04, fulfilling the requirements for their application in electrical equipment. The recipes containing 10% fly ash may guarantee an electromagnetic shielding effectiveness of at least 99% within the frequency domain of 0.1–4 GHz. Composites with greater amounts of fly ash can conduct heat more efficiently, leading to improved diffusivity and thermal conductivity values, with significant thermal conductivity values surpassing 0.2 W/(m*K). Finally, it was concluded that the composites with 10% talc, 10% fly ash, and elastomer using recycled high-density polyethylene might be the best choice for electric vehicle parts, in line with all required standards for these uses.

Keywords: recycled thermoplastics; WEEE; fly ash; talc; electromagnetic interference shielding; electric car components

check for updates

Academic Editor: Jianhui Qiu

Received: 11 August 2025
Revised: 28 August 2025
Accepted: 1 September 2025
Published: 2 September 2025

Citation: Aradoaei, M.; Caramitu, A.R.; Lungu, M.V.; Ursan, A.G.; Ciobanu, R.C.; Aflori, M.; Parfeni, A. Thermoplastic Recycling of WEEE Carcasses with the Incorporation of Talc, Fly Ash, and Elastomers for Composites with Electromagnetic Interference Shielding Characteristics for Electric Car Components. *Polymers* **2025**, *17*, 2394. https://doi.org/10.3390/polym17172394

1. Introduction

The European Commission and the Climate Technology Centre and Network (CTCN) report that in the European Union, waste electrical and electronic equipment (WEEE) is increasing each year by 3–5%. Although it seems relatively low, the yearly growth rate indicates that WEEE production is anticipated to double in around 15–20 years, emphasizing the critical demand for efficient management strategies [1]. Improving the collection, treatment, and recycling of WEEE at the end of its life can improve sustainable production, increase resource efficiency, and contribute to the circular economy.

Recovering the components of WEEE is still difficult due to the variety of materials involved [2]. Thermoplastic waste generated from WEEE poses challenges as well as interesting opportunities for recycling [3]. These come mostly from the carcasses of electronic devices and imply distinct regulations for management and disposal because of the existence of harmful substances and possible environmental and health hazards. The recycling technology requires appropriate gathering, disassembly, and material segregation, aiming to reduce environmental effects and enhance resource recovery [4].

In mixed WEEE, 15 distinct varieties of engineering plastics can usually be identified, e.g., as polyethylene (LDPE/HDPE), polypropylene (PP), acrylonitrile–butadiene–styrene (ABS), polyurethane (PU), polyamide (PA), but when referring to selective recycling of carcasses, most predominant are polyethylene (LDPE/HDPE), polypropylene (PP), and acrylonitrile–butadiene–styrene (ABS) [3,4]. In addition, some additives (both organic and inorganic) are already incorporated into plastics to confer specialized features, such as the following: color, impact resistance, flammability, weathering resistance, etc. Such additives may include inorganic oxides (e.g., TiO_2, ZnO, Cr_2O_3, Fe_2O_3), flame retardants, stabilizers, and/or plasticizers, according to the applied thermoplastic technology [2]. The implementation of the Restriction of Certain Hazardous Substances (RoHS), according to the Directive 2002/95/EC [5], has constrained the presence of these hazardous substances. However, the WEEE that is currently being processed still contains these additives, affecting the further processing [6,7]. It is considered that innovative research on recycling processes can provide important insights to ensure eco-design measures and to determine the effectiveness of any technological measures aiming to increase the recyclability of products at the design stage [8–11].

As previously demonstrated in the literature, thermoplastics modified with talc (hydrated magnesium silicate) and conductive additives (especially metallic or carbon) may find applications in various fields, with talc mainly used for improved mechanical properties and conductive fillers for tailoring the electrical conductivity. Thermoplastics filled with talc are used in automotive parts due to their improved rigidity, dimensional stability, and surface finish. Conductive thermoplastics are crucial in electronics for electrostatic dissipation, electromagnetic interference (EMI) shielding, etc.

Studies upon polyethylene composites with talc [12–15], or polypropylene composites with talc [16–19] demonstrated an increase in physical and mechanical properties, making talc an effective additive intended for large temperature applications, with reduced shrinkage by promoting uniform formation and enhancing cooling efficiency. On the other hand, talc offers a cost-effective alternative to other fillers and additives commonly used in thermoplastics. By replacing heavier fillers or reinforcing agents with talc, it lowers material density while preserving mechanical strength, stiffness, and heat resistance and assuring a lower thermal expansion. Some combinations of talc and other mineral additives, such as alumina [20,21] or calcium carbonate [22], within thermoplastic composites may enhance their performance. Recent studies have also taken into account the combination of talc and elastomers within thermoplastic composites [23–25], in order to improve their characteristics such as flexibility, durability, and resistance to impact. Elastomers generally act as compatibilizers, enhancing the interaction between different phases in the composites and contributing to overall material performance, especially in terms of chemical, water, and UV radiation resistance. In this context, talc/elastomer-filled thermoplastics may be successfully used in automotive applications, where maintaining performance and durability between −50 °C and +90 °C is currently required [26].

Previous studies also analyzed the use of fly ash, a by-product of coal combustion, as an additive in thermoplastic composites in principle as a reinforcing and flame-retardant filler used alone [27–32], or in combination with other inorganic additives [33–37], or in combination with elastomers [38]. The main purpose was the enhancing of thermo-mechanical features of composites, mainly for building applications [39], but with the potential of use for automotive applications too [40]. The main gain considered for using fly ash as an additive was related only to sustainability issues and its low cost, and the main reason to test it was to substitute other fillers which are more costly. But no research addressed its potential as an additive in thermoplastic composites for offering shielding against electromagnetic interference due to its composition, including a significant content of Fe/Cr/Ni oxides. The use of fly ash for materials with tailored electromagnetic shielding performance was mentioned in the literature, but exclusively in relation with building materials, either based on cement/geopolymers [41,42] or other types of complex panels [43,44].

Electronic equipment enclosures, also referred to as cases, must fulfill various criteria to guarantee the safety, performance, and durability of the devices they contain, especially when used in the automotive industry. These specifications include protection against physical damage, environmental factors, water and dust resistance, and electromagnetic interference, alongside factors related to optimal dimensions, weight, and installation process. The requirements are even stricter when addressing electric car components, where more sensitive electronics are involved. The case materials technology needs electromagnetic compatibility issues to guarantee that equipment operates correctly without generating or being influenced by electromagnetic interference (restricted electromagnetic emissions and immunity to interference), in this way avoiding operational failures and disruption to other equipment [45]. Consequently, the optimal choice of materials for electric car components must offer a balance of mechanical strength, electrical insulation, thermal management, and resistance to environmental factors like moisture, chemicals, and electromagnetic interference [46].

No study known up to date has tackled the use of fly ash as a component in composites with electromagnetic interference shielding characteristics for automotive applications, especially for electric car components. On the other hand, the use of recycled thermoplastic matrices from WEEE for specialized composites with tailored electrical properties for electronic equipment enclosures was not addressed in the literature.

In our work, we aimed to utilize thermoplastic waste (polyethylene and propylene) from WEEE by creating polymer composite materials with hybrid fillers. The innovation of the study is related to the development and testing of thermoplastic composite materials based on talc, fly ash, and elastomers in order to be potentially used for automotive applications, especially for electric car components, i.e., electronic equipment enclosures with tailored electromagnetic interference shielding characteristics.

2. Materials and Methods

2.1. Materials

The polymer composite materials were prepared using the following raw materials:

- HDPE, LDPE, and PP recycled from WEEE waste (denoted as HDPEDE, LDPEDE, and PPDE, respectively), technologically obtained by ALL GREEN SRL, Iași, Romania, with the methodology and characteristics being described in [44]. Before use, the recycled polymer matrices were regranulated into pellets with a size of approximately 2 mm.
- Industrial talc (Ta) (Imerys S.A., Paris, France), up to 20% (wt%),

- Thermal power plant ash of Romanian origin (FA), with particles average size under 20 µm and a D50 of 9.1 µm, up to 10% (wt%).
- A 10% (wt%) elastomer type: ethylene-methyl acrylate-glycidyl methacrylate terpolymer, Lotader AX 8840 (SK Functional Polymer S.A.S., Courbevoie, Île-de-France, France).
- Up to 3% (wt%) compatibilizing and coupling agents in all developed composites, including PEGMA 400 (Polysciences, Warrington, PA, USA), an Ethylene Acrylic Acid Copolymer, and Tegomer E 525 (Evonik Operations GmbH, Essen, Germany).

2.2. Equipment and Methods

2.2.1. Obtaining the Composite Materials

The raw materials, in powdered form, were mixed together for 15 min in a TURBULA T2F cylindrical mixer (Artisan Technology Group, Champaign, IL, USA), with a rotation speed of 40 rpm. The obtained mixtures were subsequently placed into the feed hopper of a Dr. Boy 35A injection machine (Dr. Boy GmbH & Co. KG, Neustadt-Fernthal, Germany), where they underwent an injection molding process, with key operating parameters detailed in [26,44]. The temperatures in the screw zones of the machine were kept between 150 and 190 °C, and the applied pressure varied from 116 to 120 kN, to create disk-shaped and parallelepiped samples with a thickness of 2 ± 0.1 mm, according to the needed sample types for the specific tests, as shown in Figure 1.

Figure 1. Disk-shaped and parallelepiped samples.

In the second stage, the obtained mixtures were submitted to an extrusion process for obtaining larger plates with a thickness of 2 ± 0.1 mm, to be embedded within a specialized frame for thermal shielding and electromagnetic compatibility tests, as seen in Figure 2. The equipment used was a laboratory twin-screw extruder, MD 30 (Bausano, Torino, Italy).

Figure 2. Extruded plate sample.

2.2.2. Characterization Methods

(i) Electron scanning microscopy SEM was performed with a field emission and focused ion beam scanning electron microscope (SEM), model Quanta FEG 250, with STEM and EDX detectors (Thermo Fisher Scientific Inc., Waltham, MA, USA).

(ii) Elemental chemical analysis by X-ray fluorescence spectrometry (XRF) was performed on the Bruker XRF analyzer S8 TIGER X-ray fluorescence spectrometer (Germany).

(iii) A Netzsch STA PC 409 thermal analyzer (Erich NETZSCH B.V. & Co. Holding KG, Selbwas, Germany) was used for thermogravimetric analysis. The heating program was 35–1200 °C, with a heating speed of 10 °C/min.

(iv) Physical characterization presumed the following procedures:

- Melt flow rate and melt density were determined according to [47] with a Lab BP-8164-B Melt Flow Index Tester (Dongguan Baopin Precision Instrument Co., Ltd., Dongguan City, Guangdong Province, China).
- Ash content of samples was determined using an LVT calcination oven (Nabertherm GmbH, Lilienthal, Germany) and a UF 55 forced convection oven (Memmert GmbH + Co. KG., Schwabach, Germany). The samples were first dried in the oven to remove moisture, then burned in the oven, and the tests were carried out according to [48].
- The VICAT soaking temperature test was carried out according to [49].

(v) The density of materials was determined using a XS204 hydrostatic balance (Mettler-Toledo, Greifensee, Switzerland), according to [50], as an average of 5 specimens per material.

(vi) Shore hardness measurements were taken with a common Microdurometer Vickers FM700 (Future-Tech Corp, Tokyo, Japan), as the mean of 5 measurements, [51].

(vii) The equipment for determining the mechanical features was a specialized PC-controlled universal tensile testing machine (Qiantong, China), with a nominal force of min 20 kN, allowing measurement of tensile strength and elongation, as indicated in [52,53]. Charpy impact strength was tested according to [54] on an Izod/Charpy impact tester (Qualitest, London, UK).

(viii) The dielectric properties were carried out using a broadband dielectric spectrometer (Novocontrol GMBH, Montabaur, Germany) encompassing an alpha frequency response analyzer and a quattro temperature controller, with tailored measurement cells, in the frequency band of 10 Hz–10 GHz.

(ix) The resistivity tests were carried out using a Keithley 6517B/E electrometer (Tektronix/Keithley, Cleveland, OH, USA), in accordance with the procedure described in [55].

The dielectric strength test was performed according to the method outlined in [56], with an applied voltage rate of 2 kV/s.

(x) Electromagnetic compatibility tests were carried out by applying the coaxial transmission line method and measuring the reflection in free space, with coaxial transmission devices, anechoic chamber, and Schwartzbeck antennas (Schönau, Germany). The main equipment used was a signal generator SMCV100B RF (Rohde & Schwarz, Munich, Germany) in the frequency band of 1 kHz–4 GHz, and a signal analyzer FPC1500-Desktop Spectrum Analyser (Rohde & Schwarz, Munich, Germany), in the frequency band of 1 kHz–4 GHz, according to IEEE 299-2006 [57].

(xi) The degree of swelling (water and solvent absorption) was determined by measuring the variation in the mass of the samples at predefined immersion intervals, utilizing the XS204 Analytical Balance (Mettler-Toledo, Greifensee, Switzerland), according to ISO 62:2008 [58], after 168 h of immersion.

(xii) Laser flash analyzer equipment, model LFA457 (NETZSCH-Gerätebau GmbH, Selb, Germany), was used to determine the thermal shielding parameters: 5 determinations were made for each sample.

(xiii) Martens thermal stability is achieved by exposure to progressive temperatures up to 150 °C in a UF 55 forced convection oven (Memmert GmbH + Co. KG., Schwabach, Germany), using samples with standard dimensions (length 120 mm, section 10 × 20 mm^2), according to [59] and associated with a Vicat test [60].

3. Description and Characterization of the Studied Materials

3.1. Composition and Labeling of the Studied Materials

The composition and identification of the analyzed materials are shown in Table 1 (M1–M3 with LDPEDE matrix, M4–M6 with HDPEDE matrix, and M7–M9 with PPDE matrix). The melting intervals for the obtained composites (M1–M9) are presented in Table 2.

Table 1. Composition and labeling of the studied materials.

Samples Labeling	Matrix	Component Concentration	
		Ta (wt.%)	FA (wt.%)
M1	LDPEDE	20	0
M2		15	5
M3		10	10
M4	HDPEDE	20	0
M5		15	5
M6		10	10
M7	PPDE	20	0
M8		15	5
M9		10	10

Table 2. Melting intervals for the obtained composites.

Melting Interval (°C)				
M1	**M2**	**M3**	**M4**	**M5**
115–130	115–135	120–135	130–150	135–155
M6	**M7**	**M8**	**M9**	
135–155	155–170	160–170	160–175	

3.2. Characterization of the Studied Materials

3.2.1. SEM Analysis

The micrographs obtained for the raw materials are presented in Figure 3.

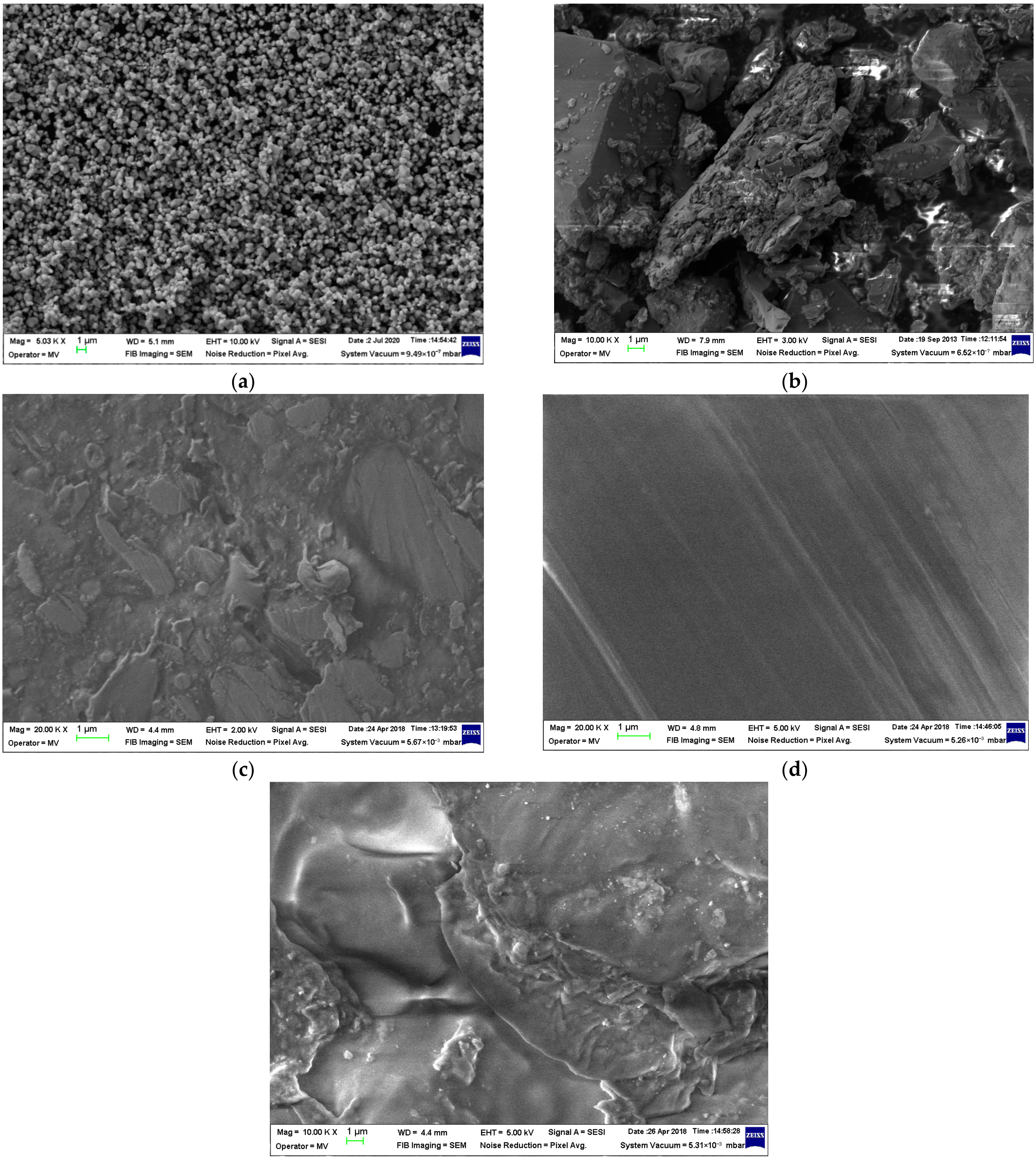

(**a**) (**b**) (**c**) (**d**) (**e**)

Figure 3. Micrographs for (**a**) talc powder, (**b**) fly ash, (**c**) LDPEDE, (**d**) HDPEDE, and (**e**) PPDE.

Based on the obtained SEM image, Figure 3a, the talc powder was observed to be relatively uniform in dimension, with an average close to 1 µm. In regard to fly ash, Figure 3b, one can notice a mixture and conglomerate of particles of irregular shapes which may turn friable into smaller dimensional powders during the mixing process.

In regard to the matrix structure, the recycled LDPE and PP seem to mix microstructures with irregular forms, Figure 3c,e, compared to HDPEDE, Figure 3d, which seems to maintain a more uniform structure, similar to the initial virgin polymer form.

In regard to the composites structures, they are observable in Figure 4. In all circumstances, it is obvious that the partial substitution of talc with fly ash is hardly noticeable as the particles distributed among the polymer structures are in quite similar dimensions, meaning that the fly ash was chopped and dispersed into micro-particles comparable in dimension to talc, all being mixed and subjected to a relatively uniform dispersion. When comparing the structures of initial matrices, Figure 3c–e, with the composites containing elastomer, a more uniform and consistent form of matrices was obtained, especially in the case of LDPEDE and PP, as seen in Figure 4a,b and Figure 4e,f, respectively. On the other hand, no significant alteration was noticed in the case of HDPEDE when comparing Figure 3d with Figure 4c,d. In all, that means that the addition of the elastomer enhanced the quality of recycled polyolefins as matrices during the thermoplastic process.

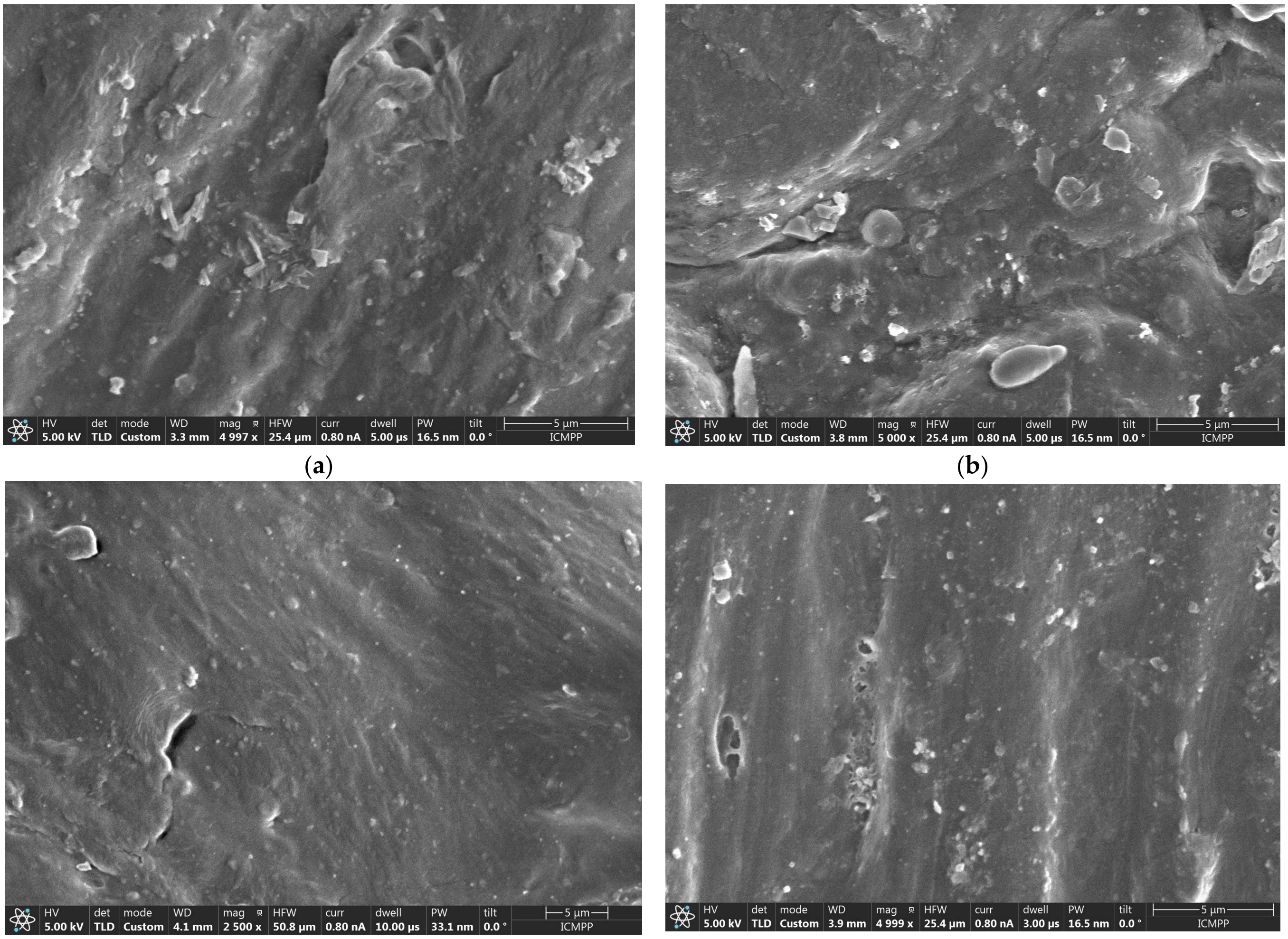

(**a**) (**b**)

(**c**) (**d**)

Figure 4. *Cont.*

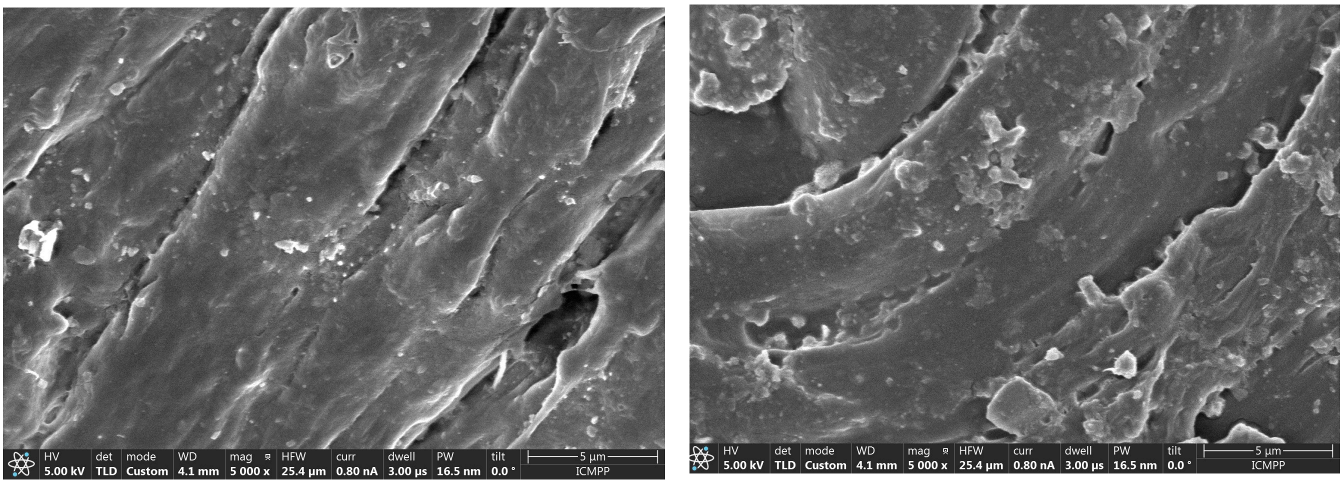

(**e**) (**f**)

Figure 4. Micrographs for (**a**) M1, (**b**) M3, (**c**) M4, (**d**) M6, (**e**) M7, and (**f**) M9.

This relatively uniform dispersion with the aid of the elastomer and with no agglomeration of inorganic particles suggests an effective mixing during melt compounding, which may contribute to the overall structural integrity of such composites which are obviously superior to those lacking elastomer [14,18,23–25,44].

3.2.2. XRF Analysis of the Fly Ash

The XRF pattern of the fly ash is presented in Figure 5, and the quantitative analysis in Table 3.

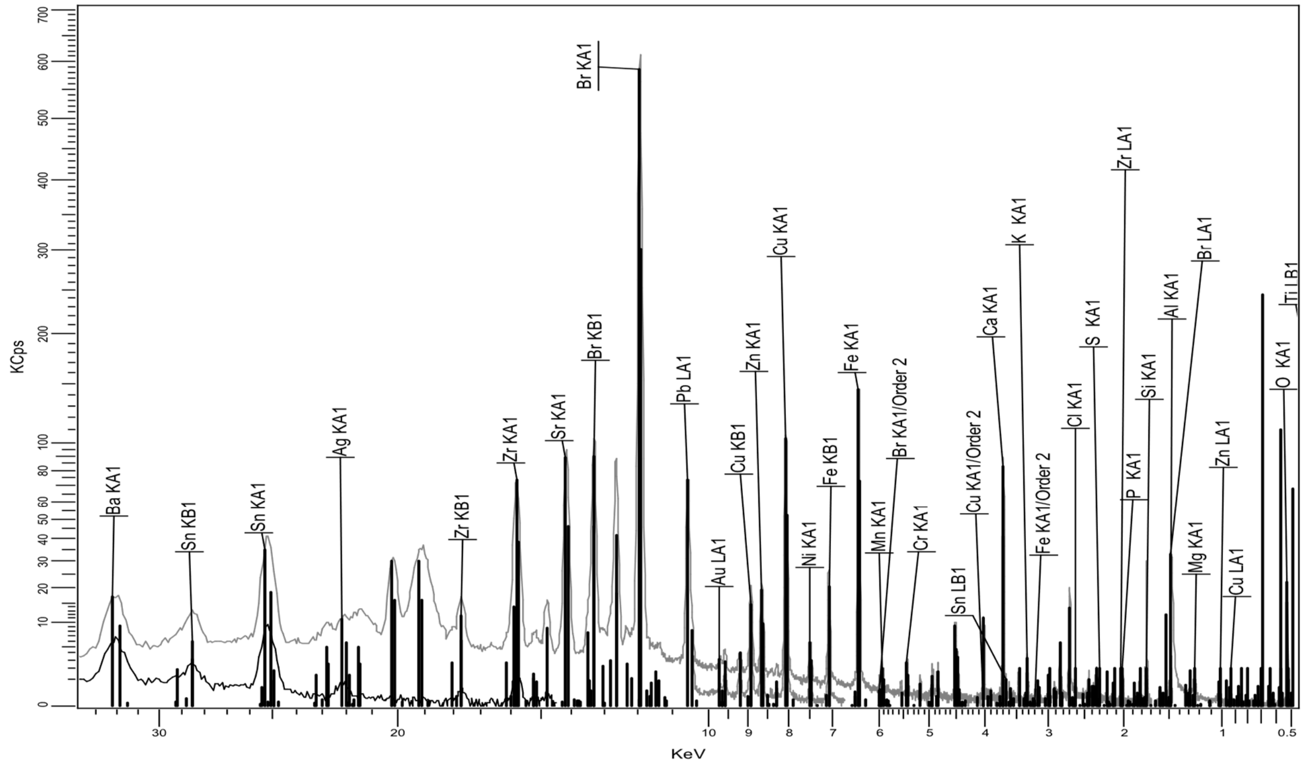

Figure 5. XRF pattern of the fly ash.

Table 3. XRF analysis of fly ash.

Formula	Z	Concentration	Line	Net Int.	Stat. Error	Analyzed Layer
SiO_2	14	32.53%	Si KA1-HR-Tr	29.94	1.03%	4.4 µm
CaO	20	21.19%	Ca KA1-HR-Tr	90.50	0.595%	19.3 µm
Al_2O_3	13	10.15%	Al KA1-HR-Tr	10.44	1.77%	4.0 µm
Fe_2O_3	26	8.13%	Fe KA1-HR-Tr	145.3	0.471%	48 µm
Br	35	7.35%	Br KA1-HR-Tr	595.6	0.233%	195 µm
CuO	29	3.82%	Cu KA1-HR-Tr	33.97	0.974%	74 µm
PbO	82	2.73%	Pb LB1-HR-Tr	82.75	0.653%	228 µm
TiO_2	22	2.45%	Ti KA1-HR-Tr	10.02	1.80%	20.7 µm
SnO_2	50	2.38%	Sn KA1-HR-Tr	34.54	1.13%	0.95 mm
BaO	56	2.13%	Ba LA1-HR-Tr	3.999	2.88%	20.3 µm
P_2O_5	15	1.26%	P KA1-HR-Tr	1.570	4.65%	4.6 µm
SrO	38	1.08%	Sr KA1-HR-Tr	90.00	0.626%	215 µm
MgO	12	0.95%	Mg KA1-HR-Tr	0.7436	8.03%	2.66 µm
K_2O	19	0.81%	K KA1-HR-Tr	3.766	2.97%	14.9 µm
SO_3	16	0.75%	S KA1-HR-Tr	1.781	4.43%	6.3 µm
ZrO_2	40	0.66%	Zr KA1-HR-Tr	69.03	0.729%	278 µm
Cl	17	0.54%	Cl KA1-HR-Tr	1.985	4.26%	8.2 µm
ZnO	30	0.36%	Zn KA1-HR-Tr	19.26	1.40%	90 µm
Cr_2O_3	24	0.28%	Cr KA1-HR-Tr	2.624	3.89%	31 µm
MnO	25	0.10%	Mn KA1-HR-Tr	1.587	5.61%	39 µm

It is obvious that the fly ash includes a large variety of metallic oxides, some of them compatible with talc and enhancing the effect of talc in regard mainly to the mechanical properties, as observed also in [20–22], and others offering potential ferritic properties of such powders. This is to be innovatively demonstrated further when analyzing the behavior of composites at higher frequencies.

3.2.3. XRF Spectrum for Recycled Matrices

An important issue is related to the analysis of the composition of recycled polyolefin matrices from WEEE. This is because they are expected to contain additional substances, some of them introduced for technological purposes while others arose due to contamination effects. The XRF spectrum results are presented in Figures 6–8, and the analytical analyses are in Tables 4–6.

Table 4. XRF analysis of LDPEDE.

Formula	Z	Concentration	Line 1	Net Int.	Stat. Error	LLD	Analyzed Layer
C (organic)	6	98.4%	Matrix				
TiO_2	22	0.67%	Ti KA1-HR-Tr	43.19	0.866%	16.2 PPM	206 µm
CaO	20	0.62%	Ca KA1-HR-Tr	30.93	1.02%	13.8 PPM	124 µm
Cl	17	0.10%	Cl KA1-HR-Tr	4.007	2.94%	19.3 PPM	45 µm
SiO_2	14	0.09%	Si KA1-HR-Tr	0.7221	6.66%		13.4 µm
P_2O_5	15	0.05%	P KA1-HR-Tr	0.6496	7.52%	29.8 PPM	20.5 µm
ZnO	30	0.01%	Zn KA1-HR-Tr	16.54	1.82%	4.3 PPM	1.32 mm
Fe_2O_3	26	0.01%	Fe KA1-HR-Tr	4.522	3.47%	7.7 PPM	0.53 mm

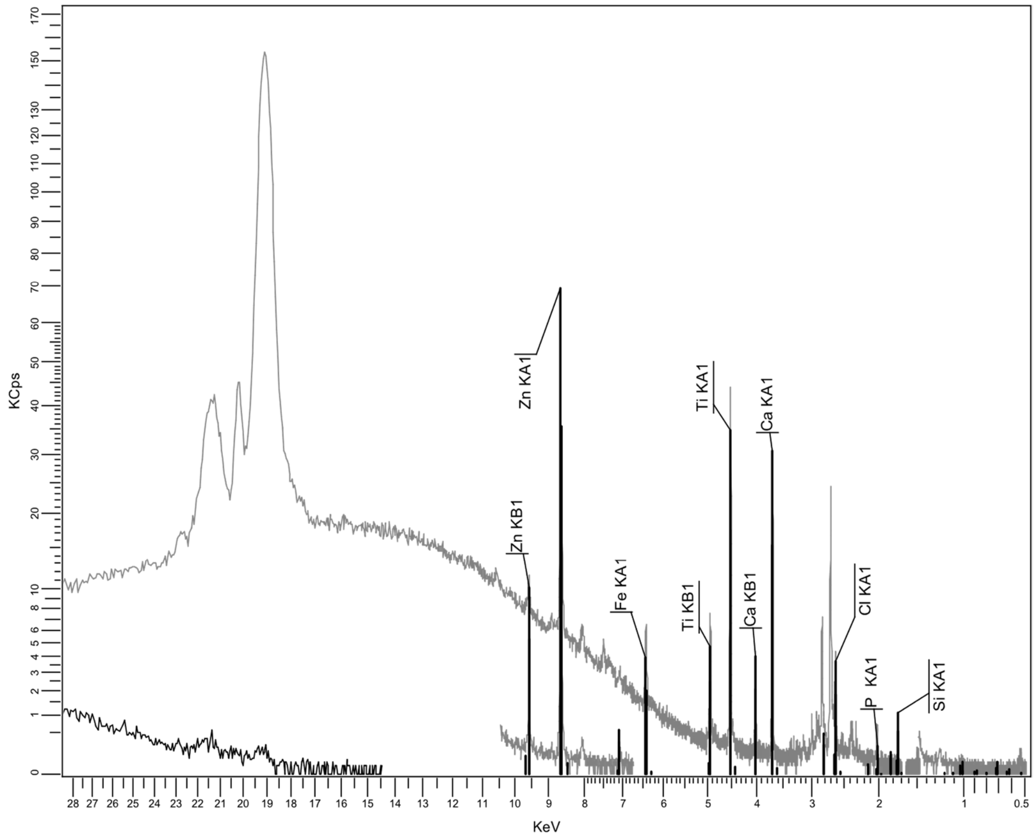

Figure 6. XRF spectrum for LDPEDE.

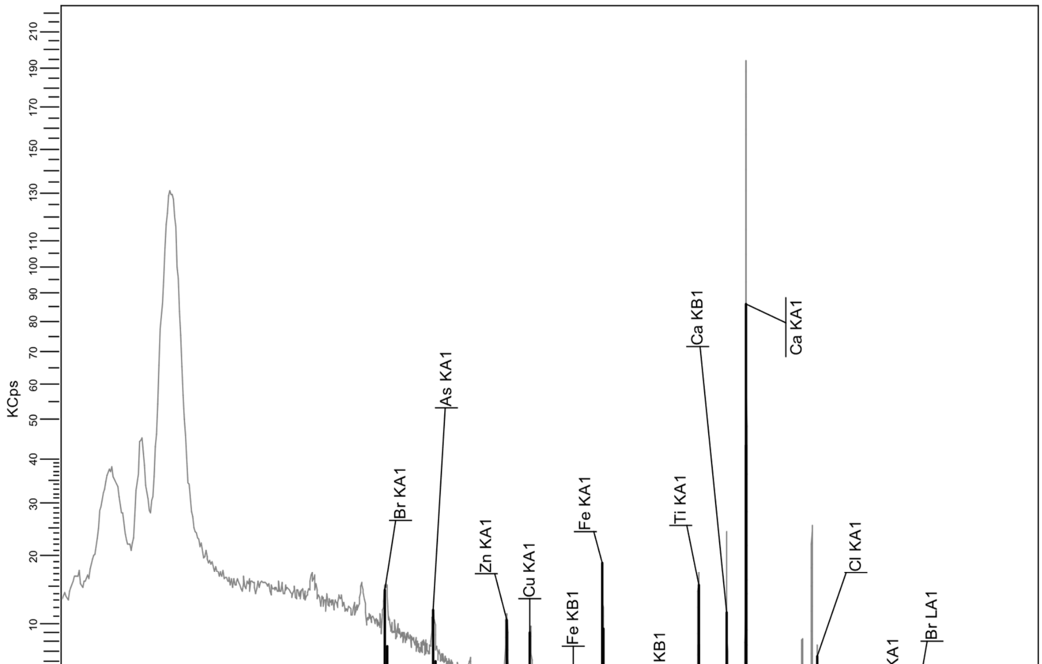

Figure 7. XRF spectrum for HDPEDE.

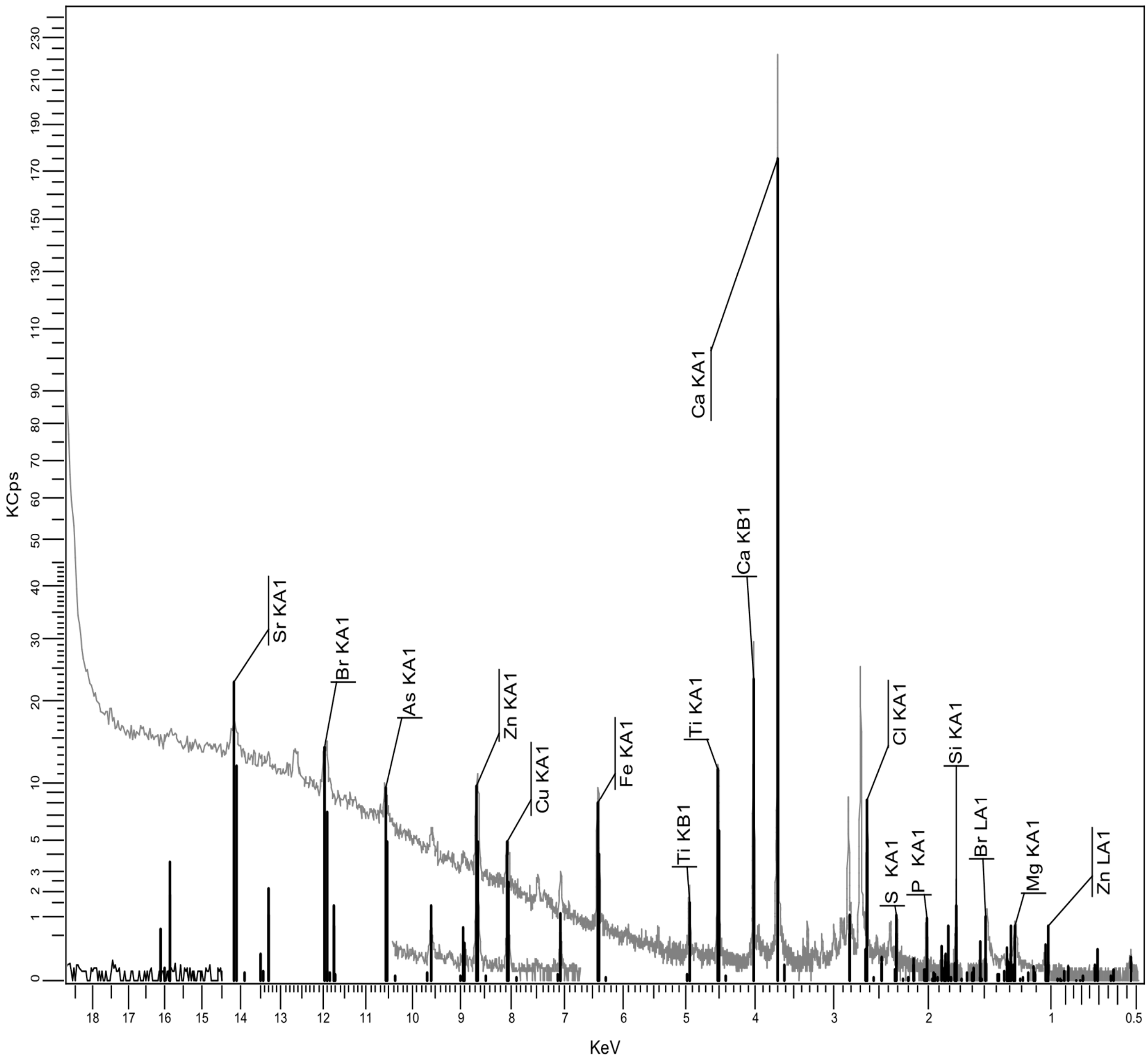

Figure 8. XRF spectrum for PPDE.

Table 5. XRF analysis of HDPEDE.

Formula	Z	Concentration	Line 1	Net Int.	Stat. Error	LLD	Analyzed Layer
C (organic)	6	93.7%	Matrix				
CaO	20	4.84%	Ca KA1-HR-Tr	192.8	0.408%	20.5 PPM	114 μm
TiO_2	22	0.46%	Ti KA1-HR-Tr	16.66	1.40%	23.5 PPM	117 μm
SiO_2	14	0.31%	Si KA1-HR-Tr	2.346	3.77%	51.1 PPM	12.9 μm
Cl	17	0.21%	Cl KA1-HR-Tr	7.331	2.15%	23.3 PPM	42 μm
MgO	12	0.09%	Mg KA1-HR-Tr	0.5441	8.51%	70.5 PPM	5.1 μm
Fe_2O_3	26	0.07%	Fe KA1-HR-Tr	12.70	1.69%	10.2 PPM	0.30 mm
CuO	29	0.02%	Cu KA1-HR-Tr	1.533	4.71%	4.4 PPM	0.58 mm
ZnO	30	0.01%	Zn KA1-HR-Tr	7.896	2.74%	6.0 PPM	0.71 mm
Br	35	48 PPM	Br KA1-HR-Tr	5.695	4.99%	5.1 PPM	1.82 mm

Table 6. XRF analysis of PPDE.

Formula	Z	Concentration	Line 1	Net Int.	Stat. Error	LLD	Analyzed Layer
C (organic)	6	92.2%	Matrix				
CaO	20	5.90%	Ca KA1-HR-Tr	221.0	0.381%	21.5 PPM	110 µm
TiO_2	22	0.37%	Ti KA1-HR-Tr	12.02	1.65%	24.3 PPM	106 µm
SiO_2	14	0.36%	Si KA1-HR-Tr	2.649	3.48%		12.7 µm
Cl	17	0.23%	Cl KA1-HR-Tr	7.558	2.11%	22.7 PPM	41 µm
MgO	12	0.11%	Mg KA1-HR-Tr	0.6985	7.30%	67.7 PPM	5.1 µm
P_2O_5	15	0.08%	P KA1-HR-Tr	0.8862	6.33%	33.8 PPM	19.1 µm
Fe_2O_3	26	0.06%	Fe KA1-HR-Tr	8.673	2.10%	11.2 PPM	275 µm
SO_3	16	0.05%	S KA1-HR-Tr	0.9963	6.24%	27.4 PPM	28.3 µm
ZnO	30	0.01%	Zn KA1-HR-Tr	7.457	2.80%	6.4 PPM	0.64 mm
CuO	29	93 PPM	Cu KA1-HR-Tr	0.7932	6.73%	4.9 PPM	0.52 mm
Br	35	45 PPM	Br KA1-HR-Tr	4.833	5.70%	5.6 PPM	1.65 mm
SrO	38	28 PPM	Sr KA1-HR-Tr	4.145	7.55%	4.9 PPM	2.74 mm

It seems that PPDE, Table 6, presents the largest variety of additional residual compounds, but the content of most of them may be negligible. On the other hand, the most significant ingredients are, in all cases, CaO, TiO_2, and SiO_2, which are particles fully compatible with talc, as mentioned before when discussing the effect of fly ash composition. Finally, the presence of Fe_2O_3 in all recycled matrices is beneficial from the electromagnetic point of view. No relevant heavy metal as type or percentage was identified. Consequently, the compositions of recycled matrices and of fly ash offer a good background for obtaining specialized composites for electric car components.

Particular focus should be given to the potential presence of flame retardants within recycled polymer matrices, especially in the case of brominated flame retardants. One can notice the Br occurrence only in relation to HDPEDE and PPDE, with an extremely low concentration. That is because the research took into account only the carcasses, which constitute the most relevant source of recyclable polyolefins, where the flame retardants are not generally used in large quantities. It is obvious that through improper recycling methods like open burning, flame retardants, being persistent and bioaccumulative chemicals, could be released into air, contaminating the environment. However this is not present in our case, which uses controlled thermo-mechanical processing. It is clear that, as demonstrated in the literature, the use of recycled thermoplastics containing flame retardants for similar thermoplastic technologies brings two major advantages: the diminishing of the new addition of flame retardants to meet the technical requirements of the application, and, on the other side, the indirect control of the pre-existing flame retardants which are reincorporated in new components [44] without being eliminated into the environment.

3.2.4. Thermogravimetric Analysis of Recycled Thermoplastic Matrices

The thermogravimetric analysis of recycled thermoplastic matrices is presented in Figures 9–11.

For all recycled matrices, the thermal behavior consisted of a melting process and an oxidation–thermo-oxidation process. The data are presented in Table 7. A vitreous transition in the case of PPDE was not identified.

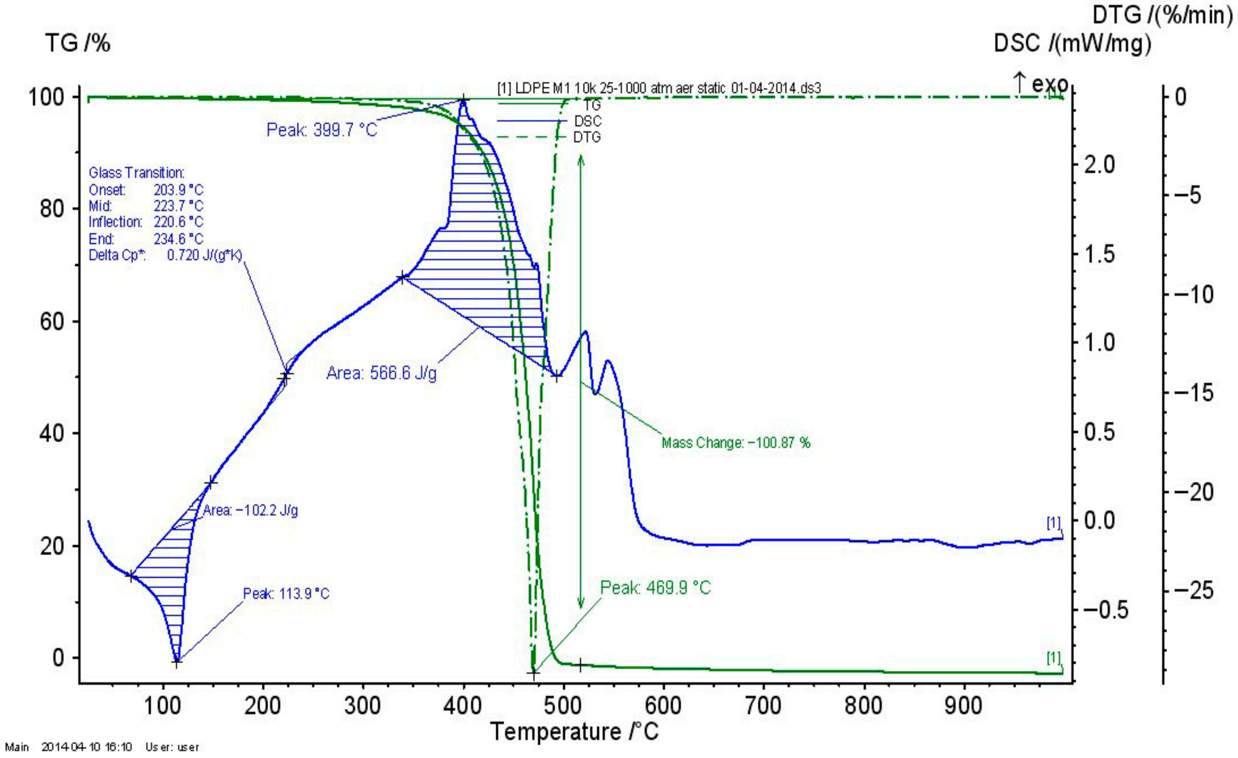

Figure 9. TG_DSC curves for LDPEDE.

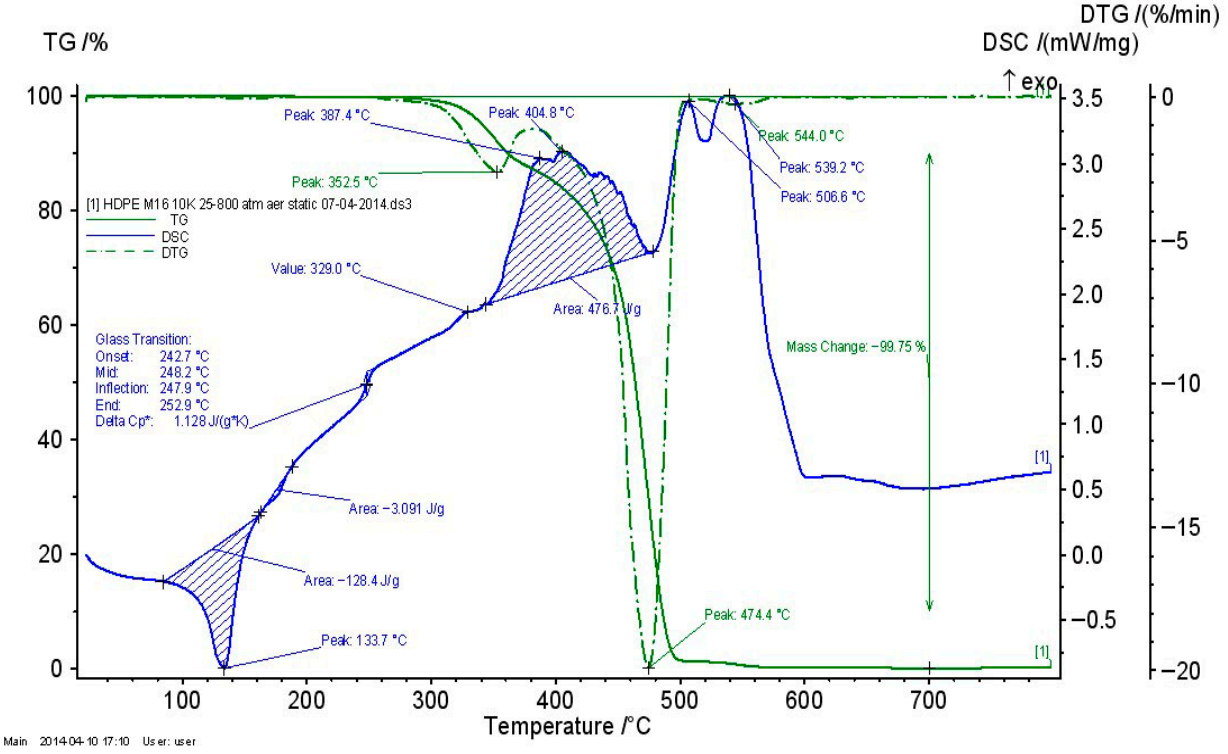

Figure 10. TG_DSC curves for HDPEDE.

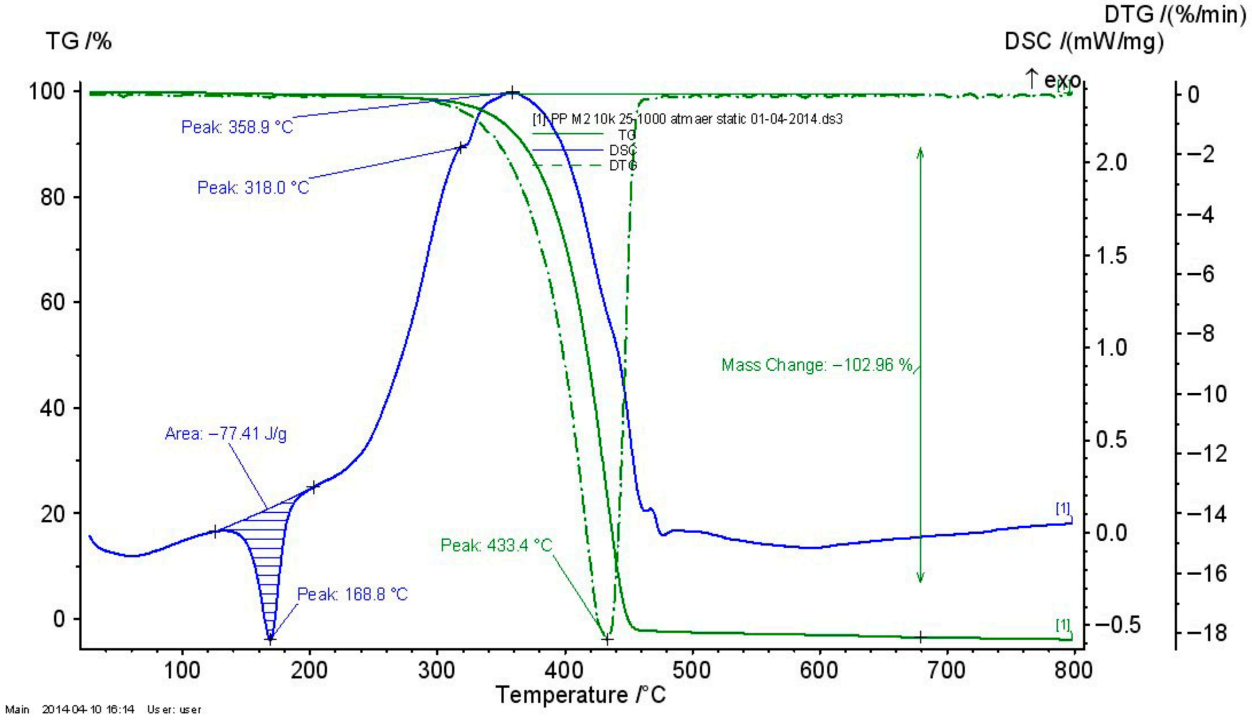

Figure 11. TG_DSC curves for PPDE.

Table 7. Experimental results regarding the vitreous transitions for recycled matrices.

Sample	**Melting**	**Vitreous Transitions**		
	Specific Heat [J/g]	**Specific Heat Capacity [J/g*K]**	**Initial Temperature [°C]**	**Final Temperature [°C]**
LDPEDE	102	0.72	203.9	234.6
HDPEDE	128.4	1.128	242.7	252.9
PPDE	77.41	-	-	-

3.2.5. Physical Analysis

The analysis of physical parameters, Table 8, reveals that even if theoretically the percent of inorganic ingredients in composites stands at 20% (wt%), the gradual replacement of talc with fly ash at 5%, and finally at 10%, diminishes the fluidity index and softening temperature values. An explanation may be related to the homolog diminishing of both bulk and melt density values due to the lower density of fly ash compared to talc powder. This assertion is partially supported by the change in ash content following combustion [48], which also decreased with the progressive substitution of talc with fly ash. In this case, the reduction is not as significant as anticipated since the combustion of talc generates magnesium oxide (MgO) and silicon dioxide (SiO_2), along with water vapor, which are eliminated. As a result, fly ash remains unchanged under combustion, while talc decomposes and loses mass at high temperatures; nevertheless, the mass reduction associated with talc cannot compensate the density difference when referring to the leftover materials in ash. The conclusions apply to all the polymer matrices involved, although the effective values and decreasing intensities varied.

Table 8. Physical analysis, error < 1% [48–50].

		Samples								
Characteristic	**Unit**	**M1**	**M2**	**M3**	**M4**	**M5**	**M6**	**M7**	**M8**	**M9**
Fluidity index	g/10 min	0.95	0.92	0.90	0.63	0.62	0.60	1.123	1.089	1.067
Melt density	kg/m^3	781	776	769	754	749	744	841	839	832
Bulk density	g/cm^3	0.919	0.915	0.911	0.928	0.923	0.919	0.931	0.926	0.922
Ash content	%	21.38	21.13	21.08	21.01	20.79	20.52	20.62	20.43	20.25
Softening temperature VICAT	°C	118	117	113	137	136	133	143	142	140

3.2.6. Electrical, Dielectric, and Electromagnetic Compatibility Tests

In Figure 12, test equipment for breaking strength, dielectric spectroscopy and, respectively, electromagnetic shielding are briefly presented. The most important features of the analyzed composites when referring to their potential applications for electric car components are related to dielectric analysis (dielectric permittivity and dielectric loss factor).

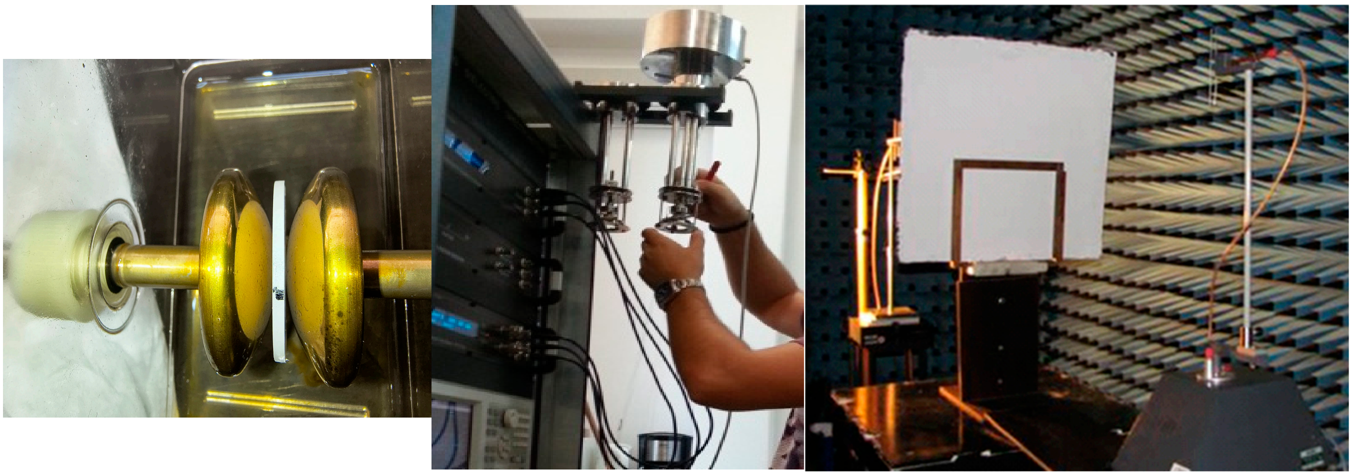

(**a**) (**b**) (**c**)

Figure 12. Experimental equipment: (**a**) breaking strength cell; (**b**) broadband dielectric spectroscopy equipment; and (**c**) coaxial transmission line in anechoic chamber.

In Figures 13–15, dielectric permittivity at different temperatures is presented for M1-M9 samples. The temperature was selected to range between 25 °C and 120 °C, because the use of such equipment is for the interior of the vehicle, on one side, and on the other side, after all, and the thermoplastic material must correspond to the class E (120 °C) of insulation (temperature) with a maximum temperature rise till the hot spot margin of 120 °C and a recommended ambient temperature of 40 °C [61].

In all instances, it is obvious that the increase in fly ash content leads to increased values of permittivity. In regard to the variation in permittivity with temperature, for all contents of fly ash and for all matrices the values increased with the increase in temperature. It should be noted that it is a common phenomenon for the permittivity to gradually decrease as the frequency increases. The novelty is related to the fact that the decrease is lowered for a higher content of fly ash, as seen in Figures 13c,14c, and 15c, and more divergent at higher frequencies. The case is even exceptional for PPDE, Figure 15c, where until 45 °C the characteristic is practically constant versus frequency, with a higher value of permittivity exceeding five.

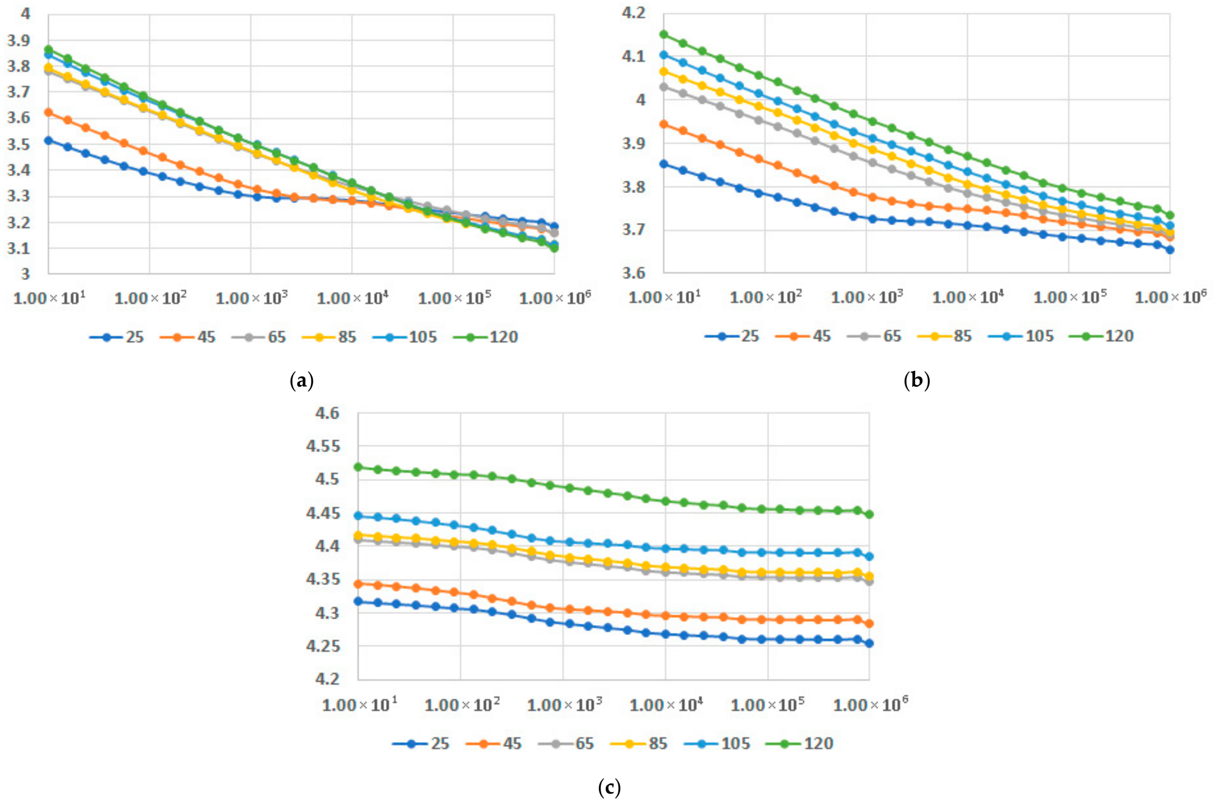

(**a**) (**b**)

(**c**)

Figure 13. Dielectric permittivity vs. frequency [Hz] at different temperatures [°C] for (**a**) M1, (**b**) M2, and (**c**) M3.

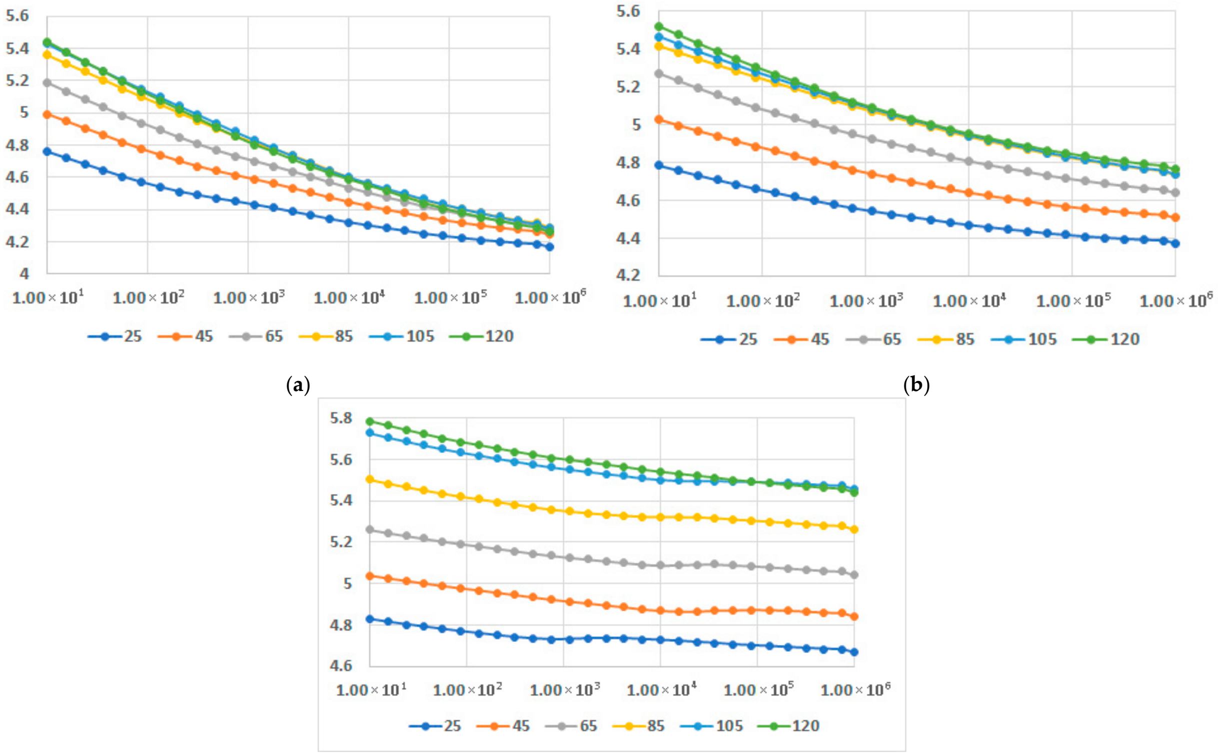

(**a**) (**b**)

(**c**)

Figure 14. Dielectric permittivity vs. frequency [Hz] at different temperatures [°C] for (**a**) M4, (**b**) M5, and (**c**) M6.

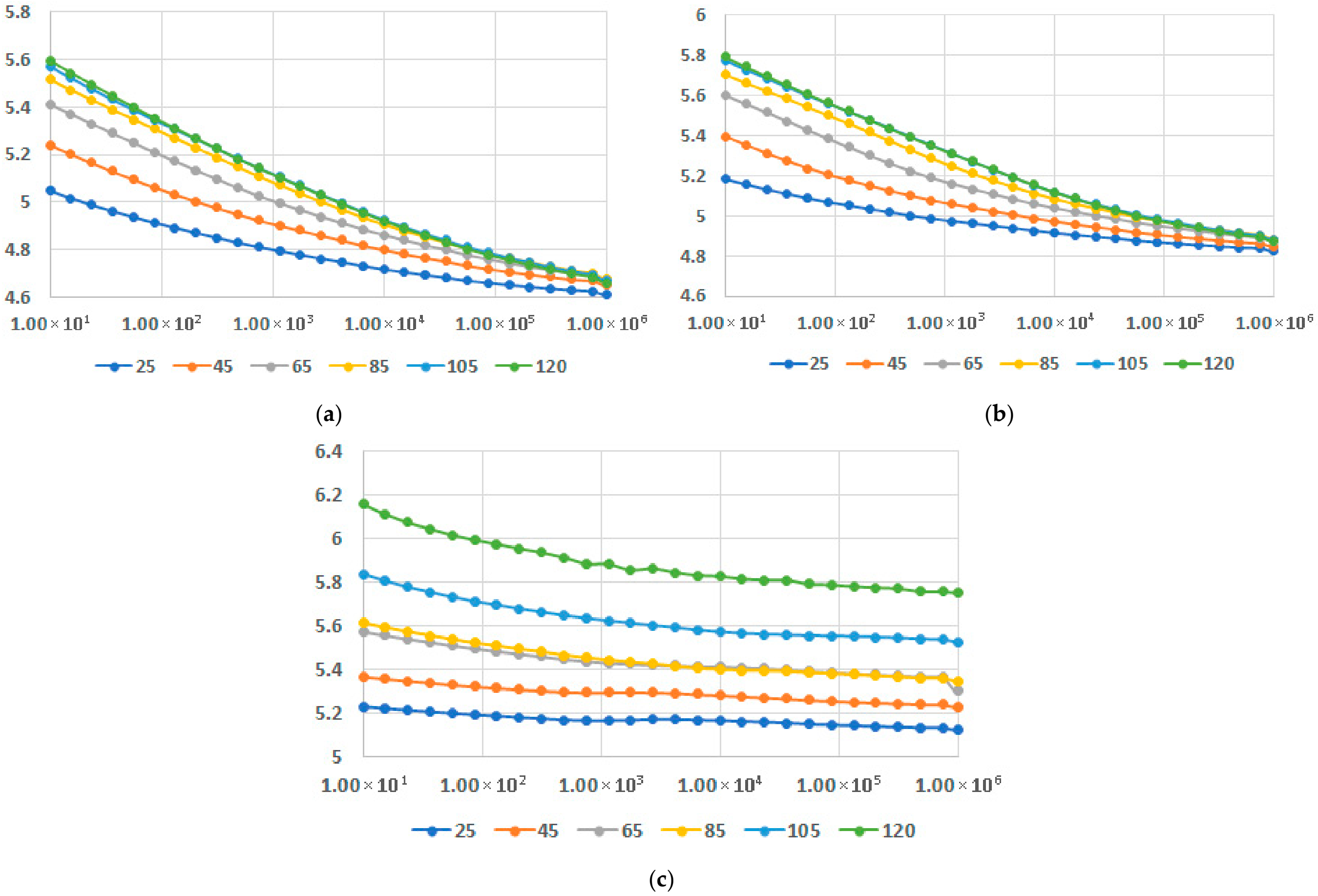

Figure 15. Dielectric permittivity vs. frequency [Hz] at different temperatures [°C] for (**a**) M7, (**b**) M8, and (**c**) M9.

In Figures 16–18, dielectric loss factor at different temperatures is presented for M1-M9 samples. In all instances the interfacial polarization can be identified at lower frequencies followed by the dipolar polarization at frequencies around 10^4–10^5 Hz, depending on the recipe, where a maximum of the characteristics may be identified. When the temperatures rise, the maximum is translated progressively towards lower frequencies. The effect is more relevant for LDPEDE, e.g., Figure 16 c when compared to PPDE, Figure 18c. In all cases, the values of the dielectric loss factor increase with the content of fly ash and with the increase in temperature for all matrices. On the other hand, also for this characteristic, the novelty is related to the fact that the decrease is lowered for a higher content of fly ash, as seen in Figures 16c and 17c, and Figure 18c, and more divergent at higher frequencies. The exceptional case is for LDPEDE, Figure 16c, where until 45 °C the characteristic is practically constant versus frequency. But the highest value of dielectric loss at higher frequencies is reached by HDPEDE composites, Figure 17c, with values exceeding 0.04.

Figure 19 presents the comparison of dielectric permittivity and dielectric loss factor for the highest fly ash content, for the matrices involved, at 45 °C—the most common temperature of service for the derived components based on such composites. In all cases, the permittivity is practically invariant with the frequency. The highest value is reached by M9, which is of about 5.3, followed by M6, which is of about 4.9. In the case of dielectric loss factor, a slight variation with the frequency can be noticed for M3 and M6, but it is more significant in the case of M9. The most reliable characteristic is considered M6 in this instance, with values exceeding 0.045.

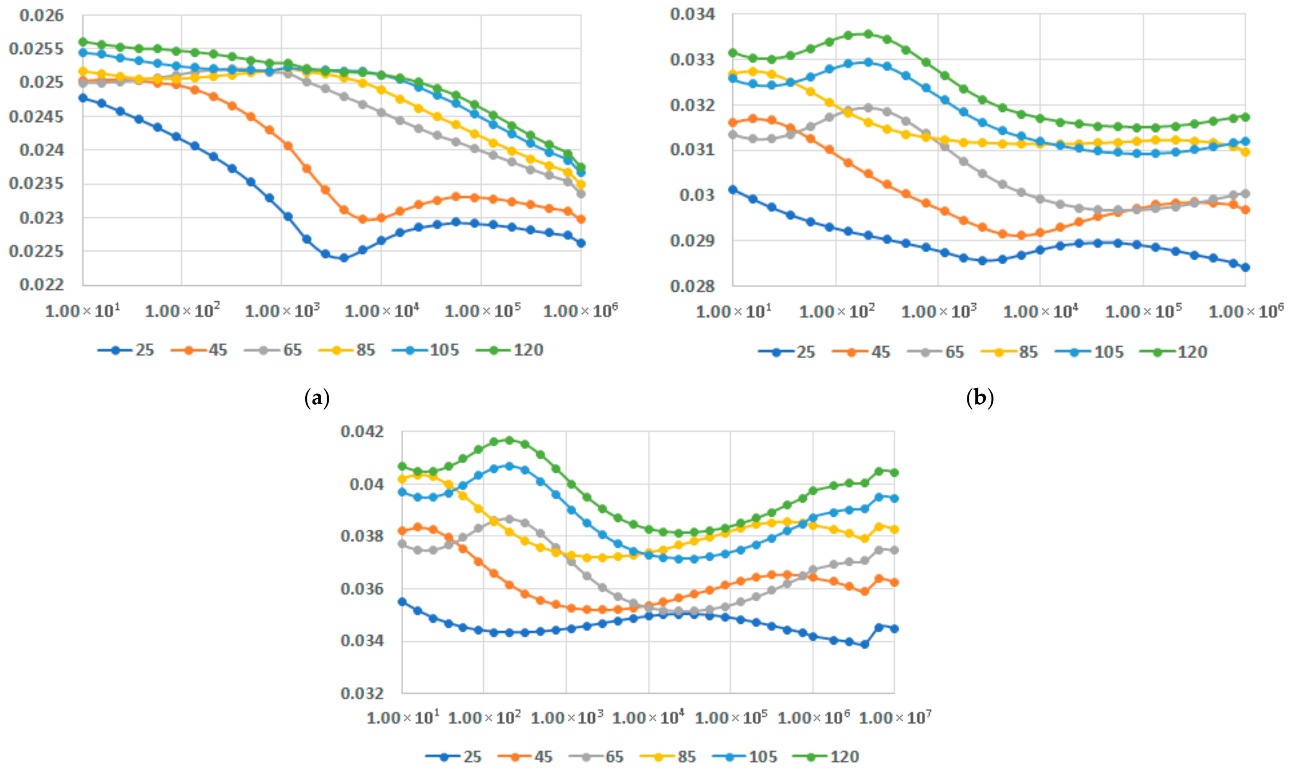

(**a**) (**b**)

(**c**)

Figure 16. Dielectric loss factor vs. frequency [Hz] at different temperatures [°C] for (**a**) M1, (**b**) M2, and (**c**) M3.

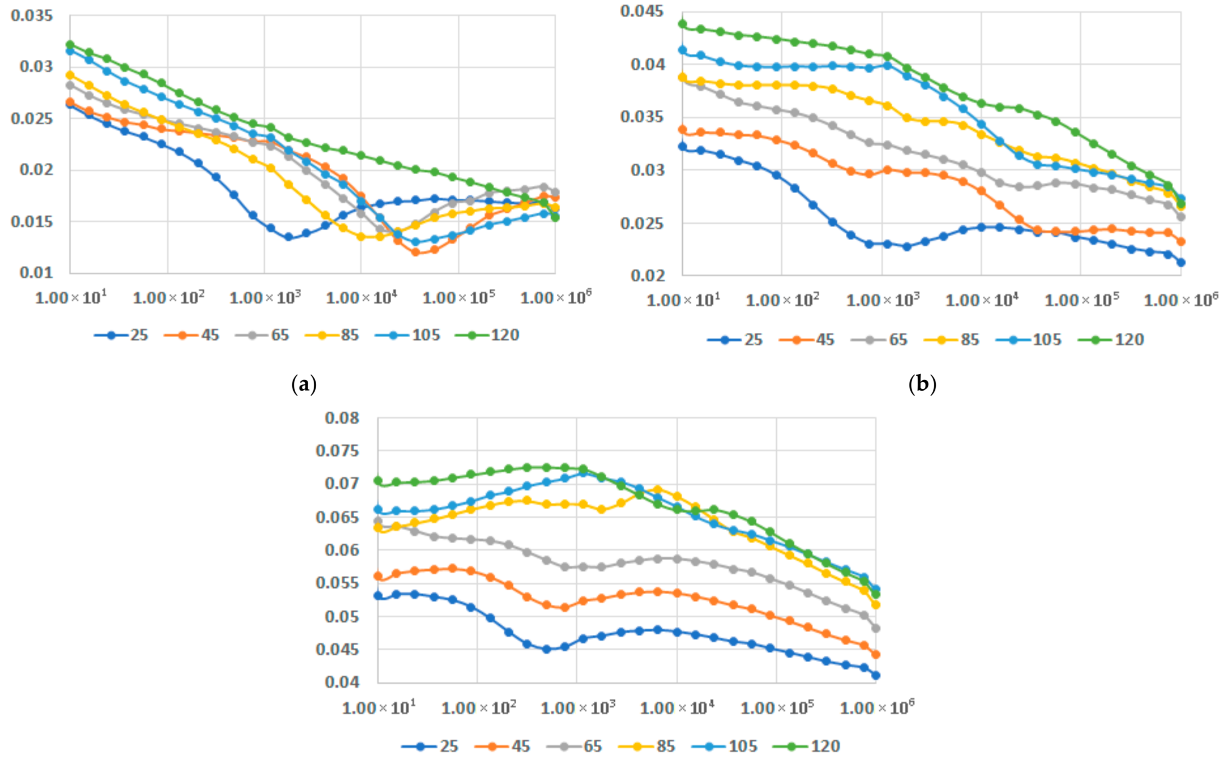

(**a**) (**b**)

(**c**)

Figure 17. Dielectric loss factor vs. frequency [Hz] at different temperatures [°C] for (**a**) M4, (**b**) M5, and (**c**) M6.

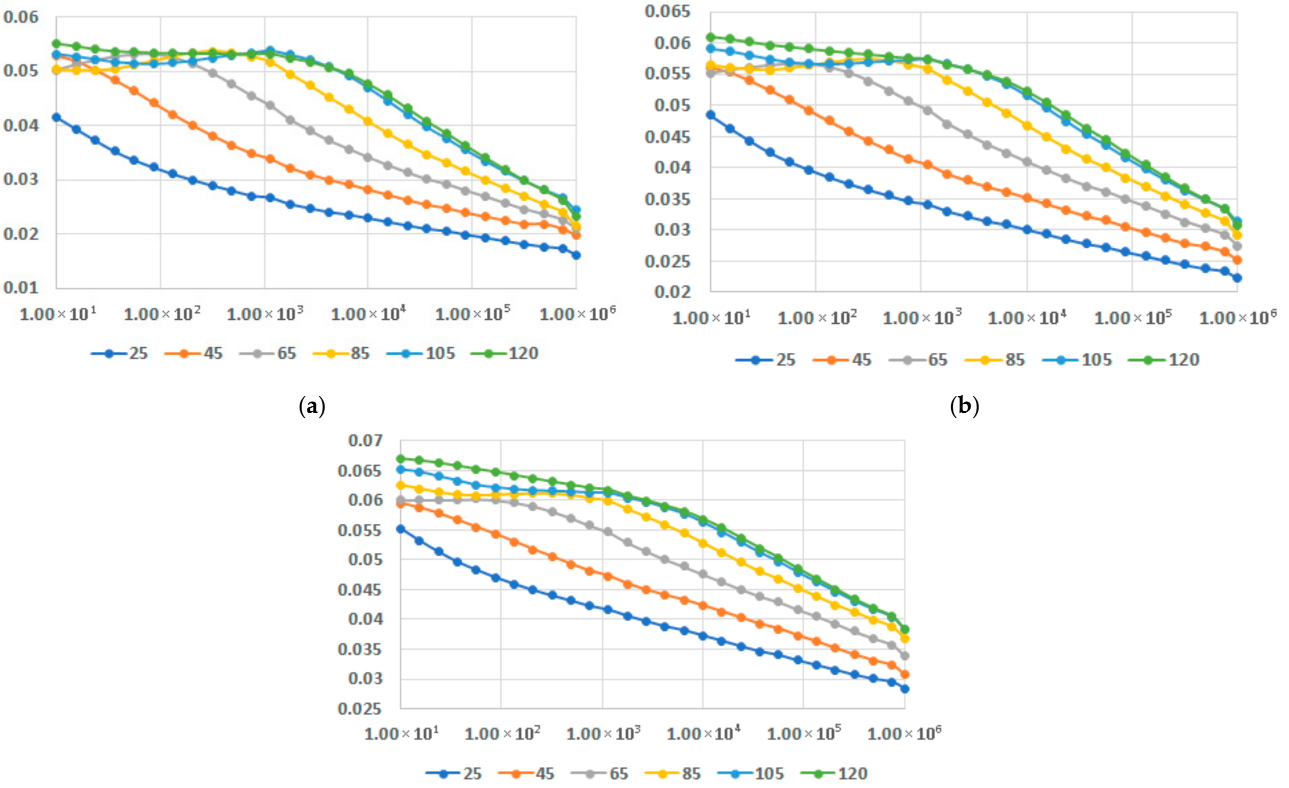

(**a**) (**b**)

(**c**)

Figure 18. Dielectric loss factor vs. frequency [Hz] at different temperatures [°C] for (**a**) M7, (**b**) M8, and (**c**) M9.

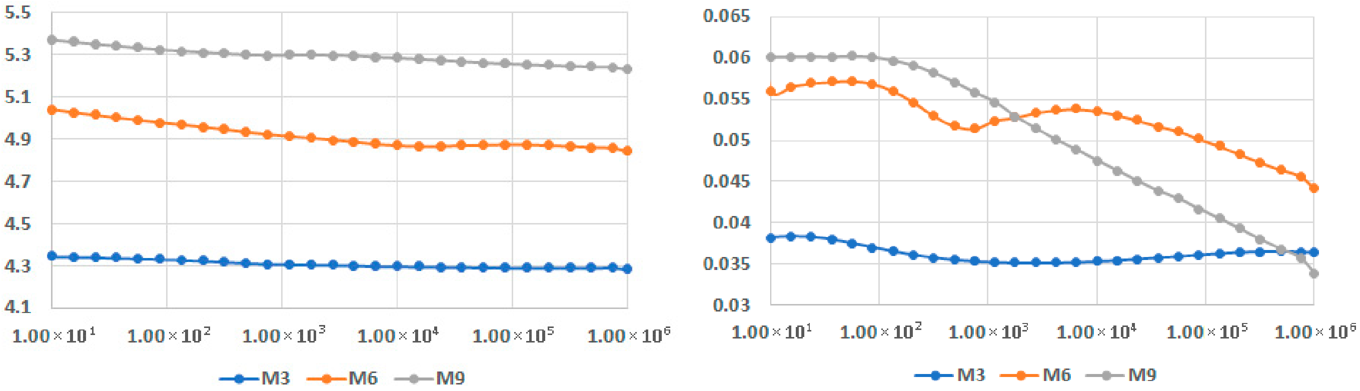

(**a**) (**b**)

Figure 19. Dielectric permittivity (**a**) and dielectric loss factor (**b**) vs. frequency [Hz] for the highest fly ash content.

Finally, the comparison of dielectric permittivity and dielectric loss factor for variable fly ash content, for the matrices involved, at 45 °C, is presented in Figures 20 and 21. It is confirmed that the characteristics substantially increase with the addition of fly ash. On the other hand, at the highest content of fly ash both dielectric permittivity and dielectric loss factor tend to become constant versus frequency, with only one exception: dielectric loss factor for PPDE, as shown in Figure 21c. According to this comparison, the recommended recipe might be M6, with the highest values of characteristics at higher frequencies.

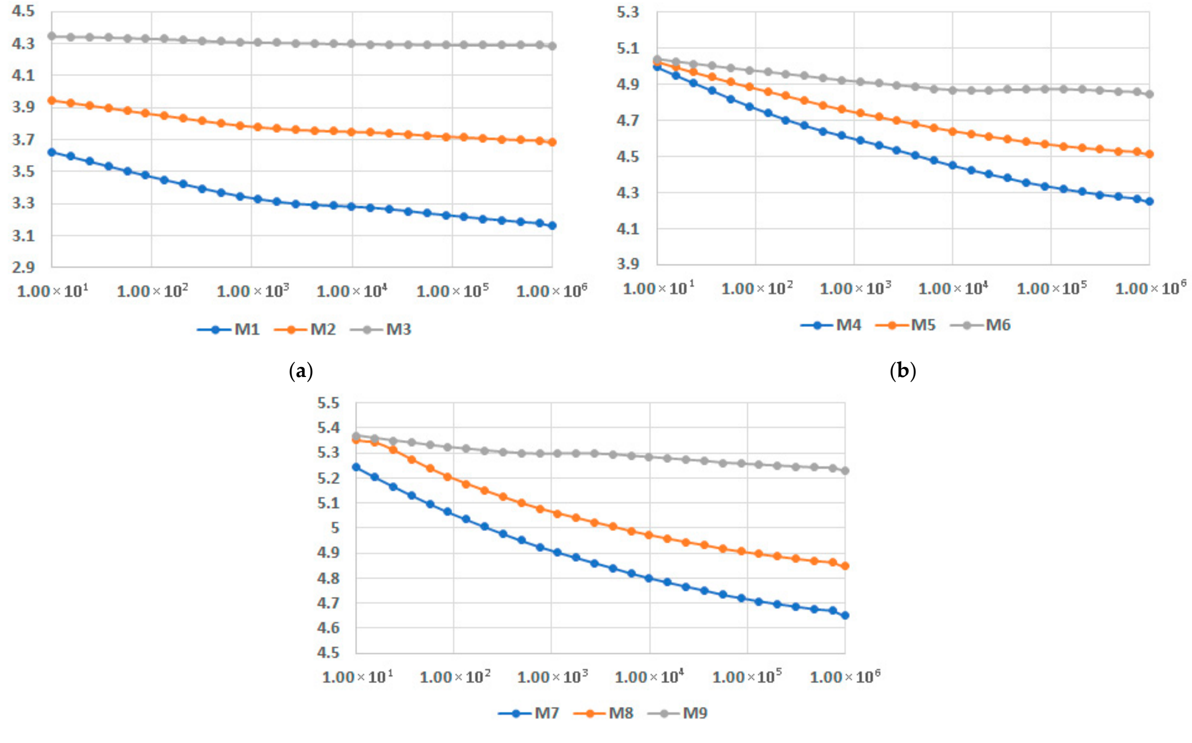

(**a**) (**b**)

(**c**)

Figure 20. Dielectric permittivity vs. frequency [Hz] for different fly ash content: (**a**) LDPEDE, (**b**) HDPEDE, and (**c**) PPDE.

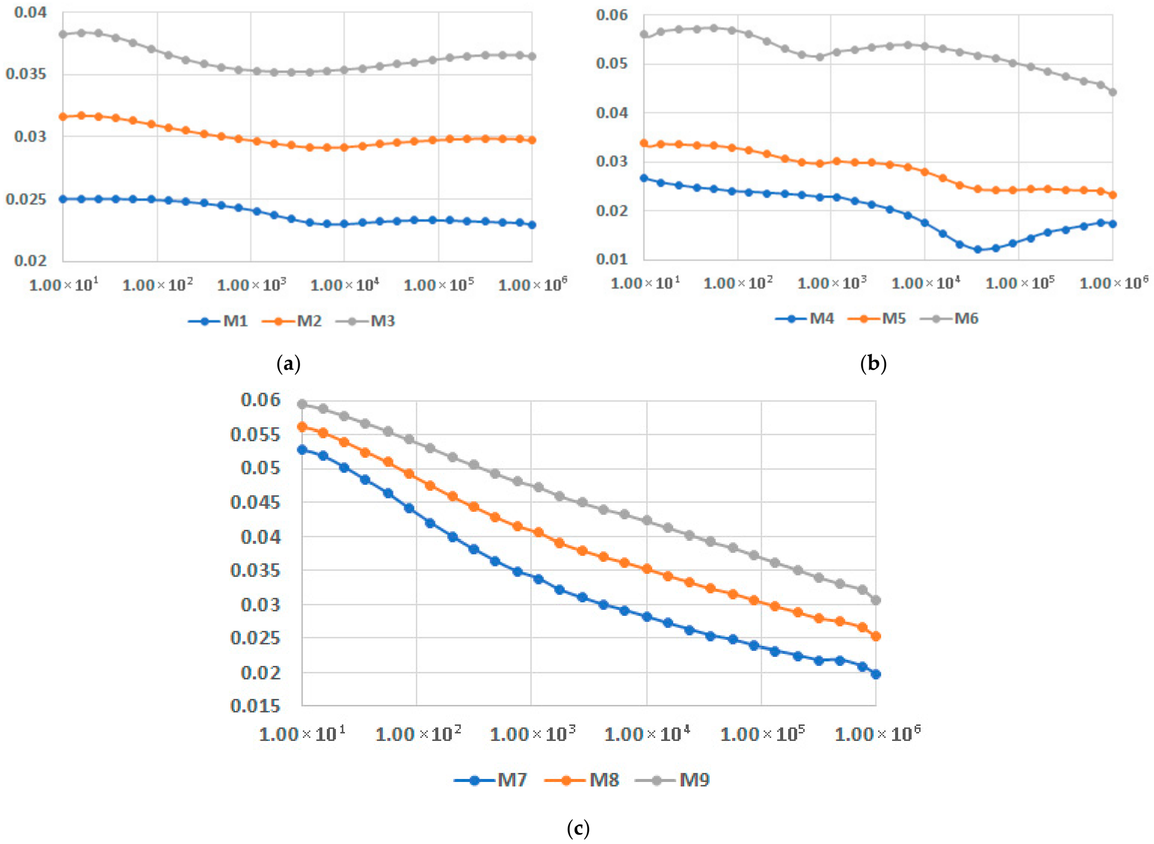

(**a**) (**b**)

(**c**)

Figure 21. Dielectric loss factor vs. frequency [Hz] for different fly ash content: (**a**) LDPEDE, (**b**) HDPEDE, and (**c**) PPDE.

Table 9 presents the electrical and electromagnetic features of composites.

Table 9. Electrical and electromagnetic features, error < 1% [55–57].

Characteristic	Unit	Samples								
		M1	**M2**	**M3**	**M4**	**M5**	**M6**	**M7**	**M8**	**M9**
Dielectric strength	kV/mm	53.5	52.8	52.5	54.8	54.5	54.1	54.4	53.7	52.9
Surface resistivity	Ω	1.4×10^9	5.7×10^8	3.3×10^8	3.5×10^9	2.6×10^9	1.3×10^9	4.1×10^9	2.8×10^9	1.9×10^9
Volume resistivity	Ω cm	2.1×10^9	7.8×10^8	5.2×10^8	5.4×10^9	3.5×10^9	2.6×10^9	4.8×10^9	3.8×10^9	2.3×10^9
Attenuation 0.1 GHz	-dB	13.62	21.61	24.27	13.55	22.40	25.36	13.65	22.14	24.98
Attenuation 4 GHz	-dB	18.75	25.04	28.44	18.64	26.85	32.67	18.52	25.96	31.12

In regard to the electrical features of composites, it was expected that the dielectric strength and resistivity would decrease with increased fly ash content due to the composition of fly ash, including semiconductive particles instead of talc which is an insulator. This observation is valid for all polymeric matrices. It is important to highlight that, when comparing the M3, M6 and M9 recipes, M6 continues to exhibit the highest values for dielectric strength and resistivity, a characteristic that supports the preliminary results regarding the dielectric features. Conversely, the significant reduction in surface and volume resistivity (even up to 10 times in the case of LDPEDE matrix) through the addition of fly ash may provide added characteristics associated with electric charge dissipation, a crucial requirement for electronic equipment in the automotive sector.

The research can be expanded by examining the impact of talc and fly ash, along with elastomer, in comparison to similar materials containing inorganic additives, as shown in [44], utilizing the same recycled polymer matrices. Even if the values of dielectric permittivity and loss factor are similar, due to the presence in both cases of 10% inorganic additive with similar features (in our case fly ash, and semiconducting powder in [44]) the shape of the characteristics are superior in our case, as presented in Figures 19 and 21a,b, respectively, for both dielectric permittivity and dielectric loss factor as they tend to become constant versus frequency. This peculiar occurrence is a result of talc and elastomer presence, which join various forms of polarization with fly ash, balancing the general polarization effects across the frequency spectrum.

The effectiveness of electromagnetic interference shielding is presented in Table 9 as attenuation at two frequencies, specific for the usage of electronic equipment with IoT support. The attenuation depends on several factors, including the shielding material, its thickness, the signal frequency, and the shape of the enclosure. Taking into account the achieved data, M3, M6, and M9 may ensure a shielding performance of at least 99% (an attenuation of over -20 dB) at 2 mm thickness for the frequency interval of 0.1–4 GHz, a value which might be increased by an adequate design of the enclosures. The highest attenuation at both 0.1 and 4 GHz was achieved by M6 too.

3.2.7. Thermal Shielding Evaluation

An important feature of electronic enclosures is related to their capacity to disperse the heat generated during the usage of electrical/electronic equipment. For this reason, the thermal shielding performance must be evaluated, as seen in Table 10. The polyethylene and polypropylene matrices are known as good thermal insulators, with a thermal conductivity of about 0.2 W/(m*K). On the other hand, talc itself is a good thermal insulator, possessing a thermal conductivity of about 0.15 W/(m*K). Therefore, the composites made solely of talc (M1, M4, M7) were expected to exhibit a thermal conductivity that is less than that of the corresponding polymer matrices. But due to the composition of fly ash, containing metal oxides with higher thermal conductivity, and to the composites structures, the composites with a higher percentage of fly ash can better transfer the heat and consequently their diffusivity and thermal conductivity values are higher. This observation is valid for all polymeric matrices, but it seems that the composites with PPDE (e.g., M9) exhibited higher values compared to HDPEDE (e.g., M6). Nevertheless, values of thermal conductivity of over 0.25 W/(m*K) are considered reasonable for electric car components, and practically there are samples at the highest content of fly ash in line with this requirement.

Table 10. Thermal shielding performance, error < 1%.

Characteristic	Unit	Samples								
		M1	**M2**	**M3**	**M4**	**M5**	**M6**	**M7**	**M8**	**M9**
Diffusivity	mm^2/s	0.198	0.224	0.229	0.199	0.222	0.248	0.224	0.236	0.269
Thermal conductivity	W/(m*K)	0.179	0.193	0.217	0.181	0.189	0.227	0.207	0.223	0.251
Specific heat capacity	J/g/K	2.547	2.319	2.272	2.726	2.545	2.334	2.397	2.246	2.029

3.2.8. Mechanical Properties

In contrast to traditional polymers, the mechanical characteristics of polymer composites can be customized by selecting the most adequate ingredient materials, their concentrations, along with the processing conditions used. The strength and stiffness of the fillers, which generally act synergistically with the polymer matrices, may significantly improve these properties. For this reason, talc was among the selected options concerning inorganic additives together with the fly ash, which could enhance the overall mechanical features. The results of the mechanical properties are briefly presented in Table 11. At a first view, according to expectations the addition of fly ash slightly diminished the values of the Shore hardness, elongation, and mechanical resistance in all circumstances related to the polymer matrix used. The elongation is higher in the case of LDPEDE, also due to the combined effect provided by the elastomer to the structure of the respective polymer. This is an aspect not met by the other polymers, which are more rigid, a factor already perceived when the Shore hardness was examined. In all, both M6 and M9 recipes present reasonable values for mechanical properties, but the shock resistance value of M6 is clearly superior, a factor required for automotive applications. This finally recommends M6 as the best recipe from the mechanical point of view.

Table 11. Mechanical properties, error < 1% [52,54].

Characteristic	Unit	Samples								
		M1	**M2**	**M3**	**M4**	**M5**	**M6**	**M7**	**M8**	**M9**
Shore hardness Shore D	^{0}Sh D	46	44	40	61	60	56	68	67	62
Shock resistance CHARPY	KJ/m^2	-	-	-	22.6	22.4	22.1	8.6	8.4	8.2
Mechanical resistance	MPa	13.92	13.55	13.25	16.88	16.27	16.11	19.46	18.84	18.45
Flow resistance	MPa	2.62	1.84	1.37	6.25	6.14	5.84	7.05	6.84	6.38
Elongation	%	188	159	132	27	24	18	22	19	16
Young's Modulus	GPa	0.25	0.19	0.14	0.58	0.57	0.56	0.62	0.59	0.57

The values achieved for the mechanical properties are in line with the technical requirements for basic electronic enclosures. The study can be enlarged by analyzing the effect of talc and fly ash, and, respectively, elastomer and comparing them with homolog materials with inorganic additives, as presented in [44], using the same recycled polymer matrices. In our case, the elongation presents higher values (up to 100 times), especially when comparing homolog materials with HDPEDE and PPDE matrices, in spite of the higher percentage of talc due to the addition of elastomer. In regard to the mechanical resistance, the respective values are at least 10% higher due to the presence of talc as an additive for all polymer matrices involved, and the influence of the elastomer is negligible. Finally, the flow resistance values are about 10% lower in our case when comparing to the materials described in [44] due to the presence of a higher amount of inorganic fillers.

3.2.9. Analysis of the Degree of Water and Solvent Absorption

One of the weathering and chemical resistance tests for automotive applications involves the amount of water and solvent (toluene) absorbed by the composite materials. The experimental results are presented in Table 12. With a 95% confidence level, the degree of swelling was calculated as the average of five measurements performed on five different samples, removing out-of-range values. It is already known that composites with inorganic powders absorb a higher amount of water and solvent (toluene) compared to the homolog polymer matrix only [26,44,62]. But this study expanded the experiments when fly ash was used as an ingredient. It is obvious that the absorption properties depend both on composite structure—given by the structure of the polymer matrix used—and on the type and concentration of the inorganic additive. In our case, LDPEDE determines a more porous structure, compared to HDPEDE and PP, which are denser. This aspect partially explains the much higher values of absorbed amounts of water and solvent (toluene) in the case of LDPEDE matrix. On the other hand, due to its composition fly ash presents metallic oxides with a higher affinity to water when partially substituting talc, which is less receptive; hence one can notice a significant difference between the values of, e.g., M3 vs. M1, M6 vs. M4, or M9 vs. M7. In regard to the solvent absorption, the differences are not so high when comparing recipes with different ash content, because in this case only the polymer structure and formula matter. But the absorption of solvent is clearly more significant when compared with the absorption of water, an aspect fully explainable when dealing with organic substances. In all, both M6 and M9 recipes present reasonable values for the amount of water and solvent (toluene) absorbed.

Table 12. Water and solvent absorption data, error < 1% [58].

		Samples								
Characteristic	**Unit**	**M1**	**M2**	**M3**	**M4**	**M5**	**M6**	**M7**	**M8**	**M9**
Water	%	0.25	0.38	0.96	0.18	0.36	0.67	0.16	0.31	0.62
Solvent	%	2.13	2.20	2.28	1.86	2.04	2.17	1.83	2.01	2.16

3.2.10. Martens Thermal Stability

The thermal stability data are presented in Table 13.

Table 13. Thermal stability data, error < 0.1% [60].

		Samples								
Characteristic	**Unit**	**M1**	**M2**	**M3**	**M4**	**M5**	**M6**	**M7**	**M8**	**M9**
Thermal stability	°C	94	92	90	96	94	92	95	93	91

The conclusions of the Martens thermal stability test are:

- Martens thermal stability [°C]: 90–110.
- Flammability class without flame retardant: V-2.
- Permanent service temperature [°C]: <80.
- Short-term high temperature resistance [°C]: 170–200.

These data are fully compatible with the best usage for electric car components and under the conditions imposed by the insulation class (temperature).

Taking into account all results presented above, we can appreciate that the recipe with 10% talc, 10% fly ash, and elastomer embedded within HDPEDE matrix fulfills all requirements for the use for electric car components, representing the best choice for such applications, eventually followed by the same composition embedded in PPDE.

The technical results are comparable with the features of homologous composites for electronic enclosures with a low percentage of conductive fillers, as presented in [63–65], but in those cases the composites are more complex, more expensive, and harder to recycle. In our situation, the benefits consist of a simpler technology, the utilization of recycled materials, being eco-friendly, and a very low cost of materials. Beyond being lightweight and offering good resistance to impact, chemicals, corrosion, and a pre-defined electromagnetic shielding, the actual problem related to plastic enclosures for automotive applications consists of the need to be recyclable in the context of the circular economy [66].

A preliminary view upon the recyclability of the materials developed by this research may be found according to the assumptions in [43] and by a cradle-to-gate analysis. The advantage of the materials developed by the presented research is that they are self-recyclable by the same thermoplastic technology, i.e., they can be used directly as raw material for similar components with a minimal addition of ingredients, especially specific agents for polymer regeneration and also compatibilizing and coupling agents, in order to achieve the optimal products.

4. Conclusions

In this study, thermoplastic waste (polyethylene and propylene) from WEEE was used for producing polymer composite materials incorporating talc, fly ash, and elastomers intended for electric car components with customized electromagnetic interference shielding features. The compositions were balanced from 20% talc to 10% talc and 10% fly ash, with all recipes including 10% elastomer. The analysis upon the fly ash revealed a wide range of metallic oxides, some of which are compatible with talc and improve talc's positive impact upon mechanical properties, while others provide potential ferritic characteristics needed for an efficient electromagnetic interference shielding.

A relatively uniform dispersion of inorganic ingredients without particle agglomeration was noticed, facilitated by the elastomer, indicating an efficient mixing during melt compounding.

Although the percentage of inorganic components in composites remains 20%, the progressive substitution of talc with fly ash reduces the fluidity index and softening temperature values. A possible explanation when also considering the reduction in both bulk and melt density values may be based on the lower density of fly ash in comparison to talc powder.

The increase in fly ash content leads to increased values of both permittivity and dielectric loss factor. Concerning the change in permittivity and dielectric loss with temperature, the values substantially increased with increasing temperature for all fly ash contents and all polymer matrices. The novelty pertains to the observation that at higher amounts of fly ash, more divergent characteristics occurred for both characteristics at higher frequencies, tending to a constant value. Very relevant values were reached for the permittivity, exceeding five, and for dielectric loss factor, exceeding 0.04, a prerequisite for their use for electrical equipment purposes.

The dielectric strength and resistivity values slightly decreased with increased fly ash content, but the respective values remained functional.

The recipes with 10% fly ash may assure an electromagnetic shielding efficiency of no less than 99% (an attenuation exceeding -20 dB) at a thickness of 2 mm for the frequency range of 0.1–4 GHz, values that could be enhanced through a more professional design of the enclosures.

Composites containing a higher content of fly ash can transfer heat more effectively, resulting in increased values for diffusivity and thermal conductivity, with very relevant values being reached for the thermal conductivity as they exceed 0.2 W/(m*K), in line with the requirements for electric vehicle parts applications.

The analysis of mechanical characteristics, of degree of water and solvent absorption, and of thermal stability confirmed that the composites with high values of fly ash present functional values in line with the applications for automotive industry.

Considering all the results mentioned above, we can estimate that the recipes containing 10% talc, 10% fly ash, and elastomer compounded within HDPEDE, followed by PPDE, may represent the optimal selection for electric car components as they meet all necessary criteria for such applications.

Author Contributions: Conceptualization, A.R.C. and R.C.C.; methodology, R.C.C., A.R.C., and M.A. (Mihaela Aradoaei); software, A.P.; validation, R.C.C., M.A. (Mihaela Aradoaei), M.A. (Magdalena Aflori), and A.R.C.; formal analysis, A.R.C. and R.C.C.; investigation, A.R.C., M.V.L., A.P., A.G.U., R.C.C., M.A. (Mihaela Aradoaei) and M.A. (Magdalena Aflori); resources, A.R.C., M.A. (Mihaela Aradoaei), and R.C.C.; data curation, A.R.C., M.A. (Mihaela Aradoaei), M.A. (Magdalena Aflori), and R.C.C.; writing—original draft preparation, A.R.C. and R.C.C.; writing—review and editing, R.C.C.; visualization, R.C.C. and A.R.C.; supervision, R.C.C. All authors have read and agreed to the published version of the manuscript.

Funding: This research received no external funding.

Institutional Review Board Statement: Not applicable.

Data Availability Statement: The data are included within the paper.

Conflicts of Interest: The authors declare no conflicts of interest.

References

1. European Union. Directive 2002/96/EC of the European Parliament and of the Council of 27 January 2003 on waste electrical and electronic equipment (WEEE). *Off. J. Eur. Union* **2003**, *L37*, 24–38.
2. Goosey, E.; Goosey, M. The materials of waste electrical and electronic equipment—Book chapter. In *Waste Electrical and Electronic Equipment (WEEE) Handbook*; Woodhead Publishing: Cambridge, UK, 2019; pp. 231–262.
3. Martinho, G.; Pires, A.; Saraiva, L.; Ribeiro, R. Composition of plastics from waste electrical and electronic equipment (WEEE) by direct sampling. *Waste Manag.* **2012**, *32*, 1213–1217. [CrossRef] [PubMed]
4. Cardamone, G.; Ardolino, F.; Arena, U. About the environmental sustainability of the European management of WEEE plastics. *Waste Manag.* **2021**, *126*, 119–132. [CrossRef]
5. European Union. Directive 2002/95/EC of the European Parliament and of the Council of 27 January 2003 on the restriction of the use of certain hazardous substances in electrical and electronic equipment. *Off. J. Eur. Union* **2003**, *L37*, 19–23.
6. Chaine, C.; Hursthouse, A.S.; McLean, B.; McLellan, I.; McMahon, B.; McNulty, J.; Miller, J.; Viza, E. Recycling Plastics from WEEE: A Review of the Environmental and Human Health Challenges Associated with Brominated Flame Retardants. *Int. J. Environ. Res. Public Health* **2022**, *19*, 766. [CrossRef]
7. Lahtela, V.; Hamod, H.; Kärki, T. Assessment of critical factors in waste electrical and electronic equipment (WEEE) plastics on the recyclability: A case study in Finland. *Sci. Total Environ.* **2022**, *830*, 155627. [CrossRef]
8. Haba, B.; Djellali, S.; Abdelouahed, Y.; Boudjelida, S.; Faleschini, F.; Carraro, M. Transforming Plastic Waste into Value: A Review of Management Strategies and Innovative Applications in Sustainable Construction. *Polymers* **2025**, *17*, 881. [CrossRef]
9. Jagadeesh, P.; Rangappa, S.M.; Siengchin, S.; Puttegowda, M.; Thiagamani, S.M.K.; Rajeshkumar, G.; Kumar, M.H.; Oladijo, O.P.; Fiore, V.; Cuadrado, M.M.M. Sustainable recycling technologies for thermoplastic polymers and their composites: A review of the state of the art. *Polym. Compos.* **2022**, *43*, 9. [CrossRef]
10. Balu, R.; Dutta, N.K.; Roy Choudhury, N. Plastic Waste Upcycling: A Sustainable Solution for Waste Management, Product Development, and Circular Economy. *Polymers* **2022**, *14*, 4788. [CrossRef]
11. Fenwick, C.; Mayers, K.; Lee, J.; Murphy, R. Recycling plastics from e-waste: Implications for effective eco-design. *J. Ind. Ecol.* **2023**, *27*, 5. [CrossRef]
12. Karrad, S.; Lopez Cuesta, J.-M.; Crespy, A. Influence of a fine talc on the properties of composites with high density polyethylene and polyethylene/polystyrene blends. *J. Mater. Sci.* **1998**, *33*, 453–461. [CrossRef]
13. Adib Kalantar Mehrjerdi, A.K.; Åkesson, D.; Skrifvars, M. Influence of talc fillers on bimodal polyethylene composites for ground heat exchangers. *J. Appl. Polym. Sci.* **2020**, *137*, 49290. [CrossRef]

14. Mehrjerdi, A.; Bashir, T.; Skrifvars, M. Melt rheology and extrudate swell properties of talc filled polyethylene compounds. *Heliyon* **2020**, *6*, e04060. [CrossRef]
15. Tsioptsias, C.; Leontiadis, K.; Ntampou, X.; Tsivintzelis, I. Modification of Talc and Mechanical Properties of Polypropylene-Modified Talc Composite Drawn Fibers. *J. Compos. Sci.* **2024**, *8*, 91. [CrossRef]
16. Castillo, L.A.; Barbosa, S.E. Influence of Processing and Particle Morphology on Final Properties of Polypropylene/Talc Nanocomposites. *Polym. Compos.* **2020**, *41*, 3170–3183. [CrossRef]
17. Malyuta, D.; Matteson, K.; Ryan, C.; Berry, M.; Bajwa, D. An investigation into the tensile properties of recycled high-density polyethylene (rHDPE) blended with talc filler. *Results Mater.* **2023**, *17*, 100377. [CrossRef]
18. Vyncke, G.; Fiorio, R.; Cardon, L.; Ragaert, K. The effect of polyethylene on the properties of talc-filled recycled polypropylene. *Plast. Rubber Compos.* **2020**, *51*, 118–125. [CrossRef]
19. Racca, L.M.; Pacheco, E.B.A.V.; Bertolino, L.C.; Campos, C.X.D.S.; Andrade, M.C.D.; de Sousa, A.M.F.; Silva, A.L.N.D. Composites Based on Polypropylene and Talc: Processing Procedure and Prediction Behavior by Using Mathematical Models. *Adv. Condens. Matter Phys.* **2018**, *2018*, 6037804. [CrossRef]
20. Benabid, F.Z.; Said Salem, M.E.C.M.; Mallem, O.K.; Zouai, F. Investigation of the influence of mineral fillers on the structural and mechanical characteristics of polyethylene high-density (PEHD) composites reinforced with alumina and talc. *Res. Eng. Struct. Mater.* **2024**, *10*, 1399–1408. [CrossRef]
21. Anderson, C.; et al. Synergistic Effects of Alumina and Talc Fillers in High-Density Polyethylene: A Comprehensive Study. *Compos. Sci.* **2020**, *28*, 201–215.
22. Leong, Y.W.; Mohd, Z.A.; Ishak, A. Mechanical and thermal properties of talc and calcium carbonate filled polypropylene hybrid composites. *J. Appl. Polym. Sci.* **2004**, *91*, 3327–3336. [CrossRef]
23. De Oliveira, C.I.R.; Rocha, M.C.G.; De Assis, J.T.; Da Silva, A.L.N. Morphological, Mechanical, and Thermal Properties of PP/SEBS/Talc Composites. *J. Thermoplast. Compos. Mater.* **2022**, *35*, 281–299. [CrossRef]
24. Wu, J.; Chen, C.; Wu, Y.; Wu, G.; Kuo, M.; Tsai, Y. Mechanical properties, morphology, and crystallization behavior of polypropylene/elastomer/talc composites. *Polym. Compos.* **2015**, *36*, 69–77. [CrossRef]
25. Denaca, M.; Samit, I.; Musila, V. Polypropylene/talc/SEBS (SEBS-g-MA) composites. Part 1. Structure. *Composites* **2005**, *36*, 1094–1101. [CrossRef]
26. Caramitu, A.R.; Lungu, M.V.; Ciobanu, R.C.; Ion, I.; Pătroi, D.; Sbârcea, B.G.; Marinescu, V.E.; Constantinescu, D. Biodegradable Polymer Composites Based on Polypropylene and Hybrid Fillers for Applications in the Automotive Industry. *Processes* **2025**, *13*, 1078. [CrossRef]
27. Wong, F.R.; Maszahar, N.S.; Ahmad, N.; Shahrum, M.A.M.; Zamri, S.F.M.; Yong, S.K. Effects of Fly Ash on Thermal and Mechanical Properties of Various Fly Ash-Recycled Thermoplastic Composite. *Malays. J. Chem.* **2024**, *26*, 125–136. [CrossRef]
28. Dagar, A.; Narula, A.K. Fabrication of thermoplastic composites using fly-ash a coal and hollow glass beads to study their mechanical, thermal, rheological, morphological and flame retradency properties. *Russ. J. Appl. Chem.* **2017**, *90*, 1494–1503. [CrossRef]
29. Sakai, Y.; Ogiwara, N.; Uchida, S.; Nakagawa, S.; Yoshie, N. Mechanistic characterization of polyethylene by incorporating fly ash. *Compos. Part B Eng.* **2024**, *287*, 111864. [CrossRef]
30. Yadav, J.; Ramkumar, P.; Parwani, A.K. Fly Ash-Linear Low Density Polyethylene Composites for Rotational Molding: Morphological and Thermal Analysis. *J. Mater. Eng Perform* **2024**, *34*, 18039–18049. [CrossRef]
31. Porabka, A.; Jurkowski, K.; Laska, J. Fly ash used as a reinforcing and flame-retardant filler in low-density polyethylene. *Polimery* **2015**, *60*, 4. [CrossRef]
32. Alghamdi, M. Performance for Fly Ash Reinforced HDPE Composites over the Ageing of Material Components. *Polymers* **2022**, *14*, 2913. [CrossRef]
33. Chinh, N.T.; Mai, T.T.; Trang, N.T.T.; Giang, N.V.; Trung, T.H.; Huong, N.T.T.; Hoang, T. Tensile, electrical properties and morphology of polyethylene/modified fly ash composites using ultraflow. *Vietnam. J. Chem. Int. Ed.* **2016**, *54*, 776–780. [CrossRef]
34. Kaleni, A.; Magagula, S.I.; Motloung, M.T.; Mochane, M.J.; Mokhena, T.C. Preparation and characterization of coal fly ash reinforced polymer composites: An overview. *Express Polymer Letters* **2022**, *16*, 735–759. [CrossRef]
35. Alghamdi, M. Effect of Filler Particle Size on the Recyclability of Fly Ash Filled HDPE Composites. *Polymers* **2021**, *13*, 2836. [CrossRef]
36. Caban, R.; Gnatowski, A. Analysis of the Impact of Waste Fly Ash on Changes in the Structure and Thermal Properties of the Produced Recycled Materials Based on Polyethylene. *Materials* **2024**, *17*, 3453. [CrossRef] [PubMed]
37. Meena, R.; Hashmi, A.W.; Ahmad, S.; Iqbal, F.; Soni, H.; Meena, A.; Al-Kahtani, A.A.; Pandit, B.; Kamyab, H.; Payal, H.; et al. Influence of fly ash on thermo-mechanical and mechanical behavior of injection molded polypropylene matrix composites. *Chemosphere* **2023**, *343*, 140225. [CrossRef]

38. Ez-Zahraoui, S.; Sabir, S.; Berchane, S.; Bouhfid, R.; El Kacem Qaiss, A.; Aouragh Hassani, F.; El Achaby, M. Toughening effect of thermoplastic polyurethane elastomer on the properties of fly ash-reinforced polypropylene-based composites. *Polym. Compos.* **2023**, *44*, 1534–1545. [CrossRef]
39. Nasir, N.H.M.; Usman, F.; Woen, E.L.; Ansari, M.N.M.; Sofyan, M. Effect of fly ash on mechanical properties and microstructural behaviour of injected moulded recycled polypropylene composites. *Constr. Build. Mater.* **2024**, *447*, 138130. [CrossRef]
40. Ajorloo, M.; Ghodrat, M.; Kang, W.H. Incorporation of Recycled Polypropylene and Fly Ash in Polypropylene-Based Composites for Automotive Applications. *J. Polym. Environ.* **2021**, *29*, 1298–1309. [CrossRef]
41. Cao, J.; Chung, D. Use of fly ash as an admixture for electromagnetic interference shielding. *Cem. Concr. Res.* **2004**, *34*, 1889–1892. [CrossRef]
42. Ciobanu, R.C.; Schreiner, C.; Caramitu, A.R.; Ion, I. Sustainable Geopolymer Structural Insulation Panels Obtained with the Addition of Power Plant Ash and Furnace Slag with Potential Uses in the Fabrication of Specialized Structures. *Sustainability* **2024**, *16*, 2323. [CrossRef]
43. La Rosa, A.D.; Grammatikos, S.A.; Ursan, G.A.; Aradoaei, S.; Summerscales, J.; Ciobanu, R.C.; Schreiner, C.M. Recovery of electronic wastes as fillers for electromagnetic shielding in building components: An LCA study. *J. Clean. Prod.* **2021**, *280*, 124593. [CrossRef]
44. Aradoaei, M.; Ciobanu, R.C.; Schreiner, C.; Ursan, A.G.; Hitruc, E.G.; Aflori, M. Thermoplastic Electromagnetic Shielding Materials from the Integral Recycling of Waste from Electronic Equipment. *Polymers* **2023**, *15*, 3859. [CrossRef]
45. EC Electromagnetic Compatibility (EMC) Directive. Available online: https://single-market-economy.ec.europa.eu/sectors/electrical-and-electronic-engineering-industries-eei/electromagnetic-compatibility-emc-directive_en (accessed on 7 July 2025).
46. Available online: https://www.dxtseals.com/articles/how-to-choose-the-right-plastic-material-for-electronic-product-housings (accessed on 7 July 2025).
47. *ISO 1133-1:2022*; Plastics—Determination of the Melt Mass-Flow Rate (MFR) and Melt Volume-Flow Rate (MVR) of Thermoplastics Part 1: Standard Method. International Organization for Standardization: Geneva, Switzerland, 2022.
48. *ISO 3451-1:2019*; Plastics—Determination of Ash Part 1: General Methods. International Organization for Standardization: Geneva, Switzerland, 2019.
49. *ISO 306:2022*; Plastics—Thermoplastic Materials—Determination of Vicat Softening Temperature (VST). International Organization for Standardization: Geneva, Switzerland, 2022.
50. *ISO 1183-2:2019*; Plastics—Methods for Determining the Density of Non-Cellular Plastics. Part 2: Density Gradient Column Method. International Organization for Standardization: Geneva, Switzerland, 2019.
51. *ISO 868:2003*; Plastics and Ebonite. Determination of Indentation Hardness by Means of a Durometer (Shore Hardness). International Organization for Standardization: Geneva, Switzerland, 2003.
52. *ISO 527-1:2019*; Plastics—Determination of Tensile Properties. Part 1: General Principles. International Organization for Standardization: Geneva, Switzerland, 2019.
53. *ISO 527-3:2018*; Plastics—Determination of Tensile Properties Part 3: Test Conditions for Films and Sheets. International Organization for Standardization: Geneva, Switzerland, 2018.
54. *ISO 179-2:2020*; Plastics—Determination of Charpy Impact Properties Part 2: Instrumented Impact Test. International Organization for Standardization: Geneva, Switzerland, 2020.
55. *IEC 62631-3-1:2023 RLV*; Dielectric and Resistive Properties of Solid Insulating Materials—Part 3-1: Determination of Resistive Properties (DC Methods)—Volume Resistance and Volume Resistivity—General Method. International Electrotechnical Commission: Geneva, Switzerland, 2023.
56. *IEC 60243-1:2013*; Electric Strength of Insulating Materials—Test Methods—Part 1: Tests at Power Frequencies. International Electrotechnical Commission: Geneva, Switzerland, 2013.
57. *IEEE 299-2006*; IEEE Standard Method for Measuring the Effectiveness of Electromagnetic Shielding Enclosures. IEEE Standards Association: Piscataway, NJ, USA, 2006. Available online: https://standards.ieee.org/ieee/299/3090/ (accessed on 7 July 2025).
58. *ISO 62:2008*; Plastics—Determination of water absorption. International Organization for Standardization: Geneva, Switzerland, 2008. Available online: https://www.iso.org/standard/41672.html (accessed on 7 July 2025).
59. *ISO 14577-1:2015*; Instrumented indentation test for hardness and materials parameters, Part 1: Test method. International Organization for Standardization: Geneva, Switzerland, 2015. Available online: https://www.iso.org/standard/56626.html (accessed on 7 July 2025).
60. *ASTM C191-21*; Standard Test Methods for Time of Setting of Hydraulic Cement by Vicat Needle. ASTM International: West Conshohocken, PA, USA, 2008. Available online: https://store.astm.org/c0191-21.html (accessed on 7 July 2025).
61. *IEC 60034-1:2022*; Insulation Class and Temperature Rise. International Electrotechnical Commission: Geneva, Switzerland, 2022. Available online: https://cdn.standards.iteh.ai/samples/103428/616faa0eff3b4c7c8ccf217b2f80fb6f/IEC-60034-1-2022.pdf (accessed on 7 July 2025).

62. Głogowska, K.; Pączkowski, P.; Gawdzik, B. Assessment Study on the Solvent Resistance of Low-Density Polyethylene with Pumpkin Seed Hulls. *Materials* **2022**, *16*, 138. [CrossRef]
63. Li, D.; Dong, C.; Zhang, A.P.; Lin, H.L.; Peng, B.Y.; Ni, K.Y.; Yang, K.C.; Bian, J.; Chen, D.Q. Polymer-based composites for electromagnetic interference shielding: Principles, fabrication, and applications. *Compos. Part A Appl. Sci. Manuf.* **2025**, *194*, 108927. [CrossRef]
64. Wang, Y.; Zhao, W.; Tan, L.; Li, Y.; Qin, L.; Li, S. Review of Polymer-Based Composites for Electromagnetic Shielding Application. *Molecules* **2023**, *28*, 5628. [CrossRef] [PubMed]
65. Zecchi, S.; Cristoforo, G.; Bartoli, M.; Tagliaferro, A.; Torsello, D.; Rosso, C.; Boccaccio, M.; Acerra, F. A Comprehensive Review of Electromagnetic Interference Shielding Composite Materials. *Micromachines* **2024**, *15*, 187. [CrossRef] [PubMed]
66. Directive on End-of-Life Vehicles 2000/53/EC. Available online: https://eur-lex.europa.eu/legal-content/EN/TXT/?uri=CELEX%3A02000L0053-20230330 (accessed on 7 July 2025).

polymers

MDPI

Article

Silicone Composites with Electrically Oriented Boron Nitride Platelets and Carbon Microfibers for Thermal Management of Electronics

Romeo Cristian Ciobanu [1,*], Magdalena Aflori [2], Cristina Mihaela Scheiner [1], Mihaela Aradoaei [1] and Dorel Buncianu [3]

[1] Department of Electrical Measurements and Materials, Gheorghe Asachi Technical University, 700050 Iasi, Romania; cschrein@tuiasi.ro (C.M.S.); mihaela.aradoaei@academic.tuiasi.ro (M.A.)
[2] Petru Poni Institute of Macromolecular Chemistry, 41 A Gr. Ghica Voda Alley, 700487 Iasi, Romania; maflori@icmpp.ro
[3] Faculty of Mechanics, University Politehnica of Timisoara, Piata Victoriei 2, 300006 Timisoara, Romania; dorel.buncianu@upt.ro
* Correspondence: r.c.ciobanu@tuiasi.ro

Abstract: This study investigated silicone composites with distributed boron nitride platelets and carbon microfibers that are oriented electrically. The process involved homogenizing and dispersing nano/microparticles in the liquid polymer, aligning the particles with DC and AC electric fields, and curing the composite with IR radiation to trap particles within chains. This innovative concept utilized two fields to align particles, improving the even distribution of carbon microfibers among BN in the chains. Based on SEM images, the chains are uniformly distributed on the surface of the sample, fully formed and mature, but their architecture critically depends on composition. The physical and electrical characteristics of composites were extensively studied with regard to the composition and orientation of particles. The higher the concentration of BN platelets, the greater the enhancement of dielectric permittivity, but the effect decreases gradually after reaching a concentration of 15%. The impact of incorporating carbon microfibers into the dielectric permittivity of composites is clearly beneficial, especially when the BN content surpasses 12%. Thermal conductivity showed a significant improvement in all samples with aligned particles, regardless of their composition. For homogeneous materials, the thermal conductivity is significantly enhanced by the inclusion of carbon microfibers, particularly when the boron nitride content exceeds 12%. The biggest increase happened when carbon microfibers were added at a rate of 2%, while the BN content surpassed 15.5%. The thermal conductivity of composites is greatly improved by adding carbon microfibers when oriented particles are present, even at BN content over 12%. When the BN content surpasses 15.5%, the effect diminishes as the fibers within chains are only partly vertically oriented, with BN platelets prioritizing vertical alignment. The outcomes of this study showed improved results for composites with BN platelets and carbon microfibers compared to prior findings in the literature, all while utilizing a more straightforward approach for processing the polymer matrix and aligning particles. In contrast to current technologies, utilizing homologous materials with uniformly dispersed particles, the presented technology reduces ingredient consumption by 5–10 times due to the arrangement in chains, which enhances heat transfer efficiency in the desired direction. The present technology can be used in a variety of industrial settings, accommodating different ingredients and film thicknesses, and can be customized for various applications in electronics thermal management.

Academic Editors: Denis Mihaela Panaitescu and Yang Yu

Received: 25 November 2024
Revised: 5 January 2025
Accepted: 14 January 2025
Published: 15 January 2025

Citation: Ciobanu, R.C.; Aflori, M.; Scheiner, C.M.; Aradoaei, M.; Buncianu, D. Silicone Composites with Electrically Oriented Boron Nitride Platelets and Carbon Microfibers for Thermal Management of Electronics. *Polymers* **2025**, *17*, 204. https://doi.org/10.3390/polym17020204

Keywords: silicone composites; distributed boron nitride platelets; carbon microfibers; electrical characteristics; thermal conductivity; electronics thermal management

1. Introduction

Thermal management involves controlling heat in a system to guarantee ideal and secure operation through the utilization of conduction, convection, and radiation techniques to remove or spread out extra heat. Effective thermal regulation is crucial for a range of devices and systems like electronic devices, vehicles, power plants, imaging systems, and high-performance computing systems. Failure to properly manage heat in these devices can result in excessive heat, leading to reduced performance, a shorter lifespan, and potential damage to components. Implementing effective thermal management techniques like heat sinks, fans, liquid cooling systems, and thermal interface materials enables devices and systems to operate safely, reach peak performance, and prolong their lifespan. Deciding on the best thermal management solution depends on the particular needs of the application and achieving a balance between performance, cost, and complexity. Failure to meet these criteria may result in legal consequences, fines, or even life-threatening consequences. Poor temperature control leads to increased energy consumption, which has a negative impact on the efficiency, longevity, and environmental footprint of the device. Developing products with predefined thermal management can decrease energy consumption and lead to a more environmentally friendly device, [1,2]. Incorporating thermal control early in the design process avoids costly redesigns or repairs, [3,4]. Device reliability is guaranteed by using a variety of Thermal Interface Materials (TIMs) made of substances such as greases, fillers, adhesives, thermal conducting films, etc. They are applied through methods like potting, encapsulation, gap fillers, coatings, etc. TIMs made of metal, carbon, and polymers have the potential to achieve high thermal conductivity and show promise for cooling high-power electronics.

Thin conformal coatings in electronic devices provide initial protection for small components to avoid overheating, to be followed by degradation and oxidation. Basically, there are four main types of polymeric materials used as TIMs for the needs of electrical and electronic parts, each with unique qualities, [5]. Acrylic resins provide easy heat control and serve as a protective shield from moisture. They have high elasticity and provide good electrical insulation, convenience, and cost-efficiency, but they lack durability in tough conditions and against harsh substances. Epoxy resins (ERs) provide little thermal insulation and are mainly used to protect against moisture, abrasives (thanks to their hard surface), and chemicals. As a result, they are mainly used for potting in order to provide sturdy physical shielding. Urethane resins (URs), or polyurethane resins, provide sufficient thermal protection for a variety of applications. They are easy to use and provide excellent moisture and fuel vapor protection, along with better chemical resistance than acrylics, though they require a longer curing time. Because of their high chemical resistance, these substances may be difficult to dissolve for reworking or repairing purposes, as the necessary solvents could potentially damage the underlying components. Finally, silicone resins (SRs) are recognized for their flexibility and capability to produce tailored formulations for TIMs, whether for large objects (such as batteries) or tiny devices (such as smartphones). Their wide temperature resistance range sets them apart from the majority of urethanes, reaching up to 600 °C in certain formulations. They also offer a robust defense against chemicals, protecting against contact with outside substances. From a processing perspective, they are user-friendly (especially in highly precise manual or automated spraying), quick to cure, and rapid at ambient temperature. Hence, silicones are becoming more popular for safeguarding delicate electronics like sensors, actuators, and other components due to their exceptional wetting abilities, reducing air pockets and flaws. Silicone structural adhesives offer simple processing and deliver trustworthy, durable bonds as well as thermal shielding. Typical specifically formulated silicone elastomers are mixed with particular fillers in a composite, and common conductive fillers include metals such as silver and aluminum, carbon-based materials like carbon nanotubes and graphene, and ceramics like alumina and boron nitride (BN). Unlike metals or carbon-based materials, ceramic fillers usually possess exceptional electrical insulation properties in addition to high thermal conductivity, qualities that make them perfect for application as thermally conductive fillers in TIMs [6]. Hence, the shape and type of fillers used in thermal functional composites play a crucial role in enhancing thermal performance, indicating that the careful selection of materials is essential.

Hexagonal BN, similar to graphene, is a ceramic filler possessing a 2D structure and displaying impressive thermal conductivity and electrical insulation properties. Researchers have recently been continuously concerned with exploring the potential of BN for high-performance thermal management [7–10]. Different thermally conductive polymer composites using hexagonal boron nitride were generally examined [11,12], but also particularized by utilizing various polymeric bases such as silicone [13,14], polyurethane [15,16], polyimide [17,18], polyamide, polypropylene [19], poly(methyl methacrylate) [20], poly(ether ether ketone) [21], epoxy [22,23], polyetheretherketone [24], and poly(p-phenylene benzobisoxazole) [25]. An initial approach to improving the thermal conductivity of BN-containing materials involved combining BN with carbon nanostructures, such as graphene [26], carbon nanotubes [27], carbon nanotubes, and aluminum oxide [28], or creating hybrid structures like boron nitride-coated carbon fibers or equivalents [29–33]. Other hybrid structures utilizing BN were also examined, as discussed in [34–36]. Although such hybrid composites, as presented above, offer unique technical advantages, they also have significant technological limitations.

Among all forms of presentation, BN in platelet form exhibits a higher D/t ratio, displaying significant anisotropy, with thermal conductivity strongly influenced by the orientation of the platelet. Its in-plane thermal conductivity can approximately reach 300–600 W $m^{-1}K^{-1}$, and through-plane only reaches about 30 W m^{-1} K^{-1}. Therefore, the orientation of the BN platelets was anticipated to have a significant impact on the thermal conductivity of the BN-filled composites. However, research on the influence of orientation has only been thoroughly examined in recent times and continues to be a significant subject for scientists [37]. In a schematic manner, in Figure 1, the orientation process of composites containing BN platelets is presented.

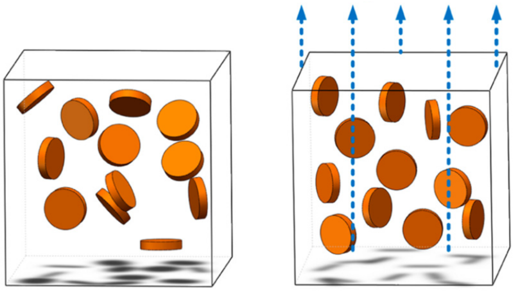

Figure 1. Orientation process of composites containing BN platelets.

Various research studies have experimented with incorporating BN particles into composites using different methods of particle orientation, such as thermal–mechanical techniques, like the orientation stacking–cutting method [38], the multi-folding and multi-laminating process [39,40], and fused deposition modeling [41]. Additionally, some studies have explored chemical–mechanical processes of particle orientation, like template-assisted chemical conversion [42] or the microfluidic spinning process with template-assisted chemical vapor deposition conversion [43]. Recently, there have been additional studies focusing on BN particle alignment through the application of magnetic fields, as seen in references [44,45]. While these procedures do reasonably enhance the thermal conductivity of BN composite structures with oriented particles, they are not easily implemented on an industrial level.

Finally, certain authors are examining how the chemical functionalization of BN particles using coupling agents can improve dispersibility, polymer chain affinity, and composite homogeneity when combined with various polymeric matrices, as discussed in references [46–50]. The thermal conductivity of composites typically increases by approximately 5%, and occasionally slightly more, with the addition of coupling agents. A minimum of 2% additive is necessary for a BN particle content above 10%, and structures with BN particles exceeding 25% are not advisable from technological and economic perspectives.

Based on the scientific data presented above, in the current research, the authors created BN platelet-containing silicone composites by adding carbon microfibers, incorporated at a specific percentage to improve the thermal conductivity of the composite. The composites also contained a specified percentage of silane coupling agent. The authors creatively employed DC and AC electric fields to align BN particles and carbon microfibers, based on a technique for orienting particles as described, e.g., in [51]. The new idea involved using two fields for orienting particles: a higher voltage stationary field to align the particles in chains and a lower voltage alternating field at a specific frequency to help move the particles in the polymer and facilitate the orientation, a decisive factor that enhances the uniform spread of carbon microfibers among BN in the created chains. No previous records exist of a technology using electric fields to vertically align boron nitride platelets and carbon fibers to enhance directional heat properties for heat management purposes. On the other hand, no prior research has examined the impact of simultaneously applying DC and AC electric fields to create anisotropies in composites, particularly by creating uniformly dispersed vertically aligned chains.

2. Materials and Methods

2.1. Materials

Pourable, room-temperature-cured, silicone rubber with 2 components (RTV-2) ELASTOSIL® RT 620 A/B type was sourced from Wacker Chemical Corporation, Ann Arbor, MI, USA.

High-purity standard boron nitride platelets SP12 type, with a tight particle size distribution (D50 = 12 µm), were obtained from Saint-Gobain Boron Nitride, Amherst, MA, USA. In-plane thermal conductivity was 300 W $m^{-1}K^{-1}$; through-plane plane thermal conductivity was 30 W $m^{-1}K^{-1}$; and heat capacity was 0.77 J g^{-1} K^{-1} (producer datasheet).

Carbon microfibers Carbiso™ MCF type, with a fiber length < 200 µm and a diameter < 10 µm were sourced from Easy Composites Ltd., Stoke-on-Trent, UK. Thermal conductivity was 350–400 W $m^{-1}K^{-1}$ and heat capacity was 1.11 J g^{-1} K^{-1} (datasheet).

A silane-coupling agent used to form a durable bond between organic and inorganic materials, KH550 type, was sourced from Dongguan Hongrui Chemical Co. Ltd., Dongguan City, China. To simplify the technological process, the silane coupling agent was added to the composite formula while mixing the inorganic and organic materials.

Table 1 shows the details of the technological recipes, including the percentage of filler concentration indicated in weight (wt%).

Table 1. Recipe description.

No.	Recipe	Structure
R1	12% BN platelet; 2% KH550	Uniform
R2		Oriented
R3	10% BN platelet; 2% carbon microfibers; 2% KH550	Uniform
R4		Oriented
R5	12.5% BN platelet; 1% carbon microfibers; 2% KH550	Uniform
R6		Oriented
R7	15.5% BN platelet; 2.5% KH550	Uniform
R8		Oriented
R9	15% BN platelet; 0.5% carbon microfibers; 2.5% KH550	Uniform
R10		Oriented
R11	20% BN platelet; 2.5% KH550	Uniform
R12		Oriented

2.2. Technological Equipment and Methods

Composite films, according to the recipes in Table 1, were produced by using a modified ATC-71LC LAB TAPE CASTING SYSTEM (HED International Inc., Ringoes, NJ, USA), as shown in Figure 2. The electrical exposure of composites was made by using a programmable signal, generated by a pulsating high-voltage source-type amplifier HA51U (Hivolt.de GmbH & Co. KG, Hamburg, Germany), and the programming was performed using the Arduino kit, an open-source microcontroller development board, [52], by use of a computer with an operating system compatible with the Arduino Uno board.

The technological process included the following main stages:

(1) Homogenization and dispersion of nano/microparticles in the liquid polymer:

- Dosage of the components of the composite material.
- Homogenization of the composition, carried out as ultrasonic dispersion in 5 mixing cycles with a total time of approximately 5 min.

(2) Launching of the composite film:

- Loading the dispersion zone and adjusting the flow nozzle, depending on the desired thickness of the film.
- Drawing the composition on a circulating PET support.

(3) Orienting the particles under an electric field:

- Aligning the particles in the electric field, according to a programmable signal scheme; the electrical exposure was performed in our case at 1000 Vcc + 750 Vac/2.5 kHz for approximately 8 s, at an equivalent electric field intensity of approximately 18 kV/m.

The film moves between two adjustable rectangular electrodes; the space between the electrodes can range from 5 mm to 2 cm, based on the matrix and the particle content, and is also aligned with the electrical exposure to ensure the ideal intensity of the DC electric field, which firmly maintains the stability of the vertically aligned chains.

(4) Composite final curing to block particles within chains, by use of IR radiation:

- In our case, the curing with IR radiation was performed with a 3 kW heater, for approximately 4 s; the curing temperature is automatically controlled and adjusted.

- Unwinding the film and pulling it onto the reel; the film speed is automatically controlled, and it was approximately 0.05 m/s in the presented case, to guarantee the efficient alignment and curing of particles within the previously stated time frames.

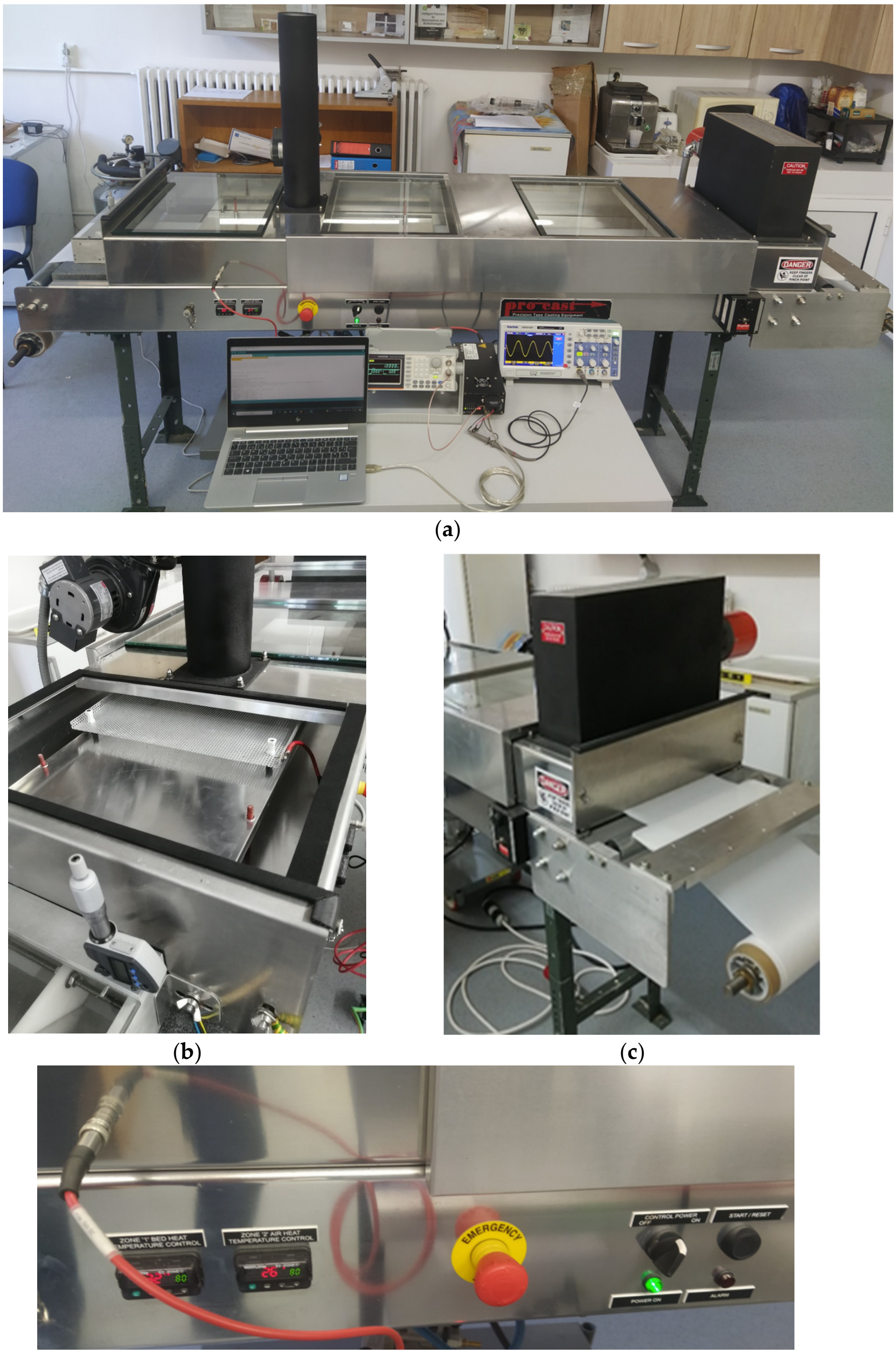

(**a**)

(**b**) (**c**)

(**d**)

Figure 2. Laboratory tape caster equipment: (**a**) setup assembly; (**b**) adjustable electrodes area; (**c**) IR curing area; (**d**) curing temperature control panel.

Because carbon microfibers are up to 200 µm in length, the research was conducted on composites that were 1 mm thick to ensure that the fibers were adequately dispersed and integrated. The final samples were cut from a film that was 40 cm wide, depending on the analysis needed for each sample.

It is important to point out that the technological settings mentioned above align with the recipes listed in Table 1 for a film with a maximum thickness of 1 mm.

In terms of technology, the voltage values and frequency are determined by the type and concentration of fillers. These parameters need to be determined through experimentation before successfully launching a material with properly aligned chains of particles. Also, the duration of exposure to electric fields and IR radiation necessary for curing is significantly influenced by the thickness of the film. According to the technical capabilities of the equipment, the thickness of the film can be adjusted to a greater extent, e.g., from 50 µm to 2 mm, sizes commonly utilized for the thermal management of electronic devices [6], and covering various thermal management applications in the electronics field.

2.3. Testing Equipment and Methods

Optical scanning microscopy SEM and energy-dispersive X-ray spectroscopy (EDX) were performed with a field emission and focused ion beam scanning electron microscope (SEM) model Tescan Lyra III XMU (Libušina tř. 21 623 00, Brno-Kohoutovice, Czech Republic). Structural characterization was carried out by X-ray diffraction (XRD) using CuKα radiation with the Ni filter Bruker AXS D8 Advance with CuKα radiation (λ = 0.154 nm). Diffraction patterns were recorded at room temperature in Bragg–Brentano geometry at an angle 2θ of 20° to 65° at a rate of 0.6°/min (2θ)/min.

Laser Flash Analyzer equipment, model LFA457, from NETZSCH-Gerätebau GmbH, Selb, Germany, was used to determine the thermal conductivity; 5 determinations were made for each sample at the same temperature of 25 °C.

The dielectric features were determined by broadband dielectric spectroscopy with a Solartron 1260 A dielectric spectrometer (Solartron Analytical, Farnborough, UK). The measurements were conducted with an AC voltage amplitude of 3 V over a frequency range of 1–10 kHz, using a measuring electrode with a diameter of 30 mm.

Tensile tests were carried out at room temperature (22 °C), using a universal testing machine (Instron, Norwood, MA, USA), at a speed of 30 mm/min. Three replicates were used for each sample to obtain the averaged values and standard deviation. Tensile strength values were directly determined from the stress–strain curves.

3. Results and Discussion

3.1. SEM Analysis

The analysis using SEM is important for evaluating the composition structure and effectiveness of the orientation method with the tailored electric field. Figure 3 shows the composition and size of BN platelets before being processed for compounding, as well as their integration into composites, specifically for the R1 sample. Figures 4 and 5 present the comparison between uniform dispersion and chain formation, specifically for R1 and R2 samples. For R2, the BN particles are seen moving closer together and forming a vertical chain in a gradual process. The key point is that the orientation in chains occurs along the length of the platelet, potentially enhancing thermal conductivity.

Figures 6–10 display the arrangement of composites containing varying levels of carbon microfibers, at magnifications of 70 and 500, which are deemed the most straightforward for visualizing the distribution of particles in composites. The significance of the analysis is in showcasing how the chains are evenly spread across the sample's surface, fully developed, and mature.

By comparing Figures 6 and 7, it is evident that there is a formation of chains with a higher particle concentration on the material surface in Figure 7 and fewer horizontal carbon microfibers. The higher level of carbon microfibers (2%) and lower BN content

(10%) make the carbon microfiber orientation more challenging in this scenario, with some carbon microfibers not being attached to the chains and remaining horizontal.

The outcomes appear alike for both R5 and R6, as shown in Figures 8 and 9 compared to Figures 6 and 7, but here, the carbon microfibers' orientation is more facile due to their lower content (1%) at a comparable BN content (here 12.5%). However, it can be noted that there are still areas where the carbon microfibers are not completely absorbed in the chains, with some remaining partially attached horizontally to the surface of the material. When Figures 7 and 9 are compared at 70 magnification, it is clear that there are fewer chains in the composite with fewer carbon microfibers.

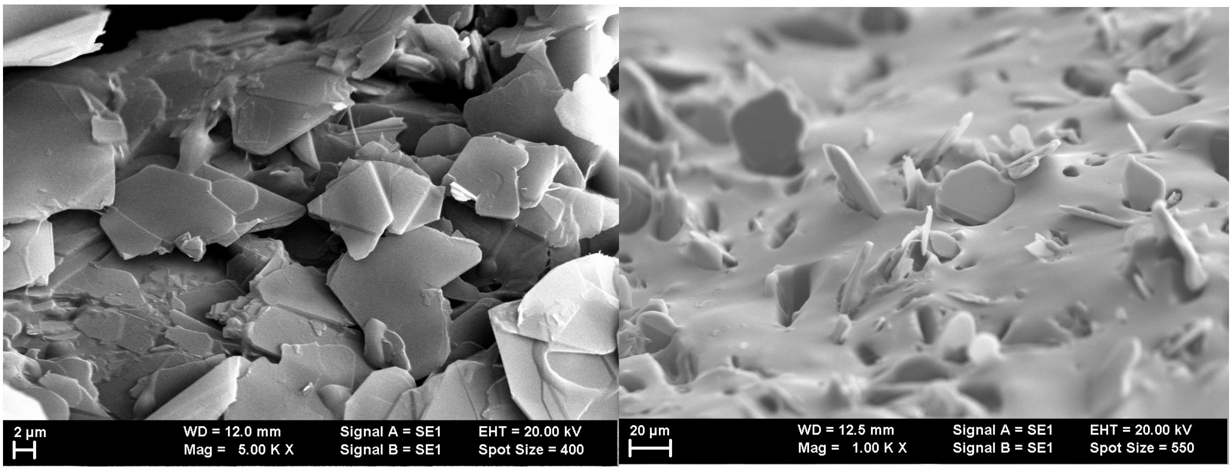

Figure 3. BN platelets before and after integration into composites with uniformly distributed particles.

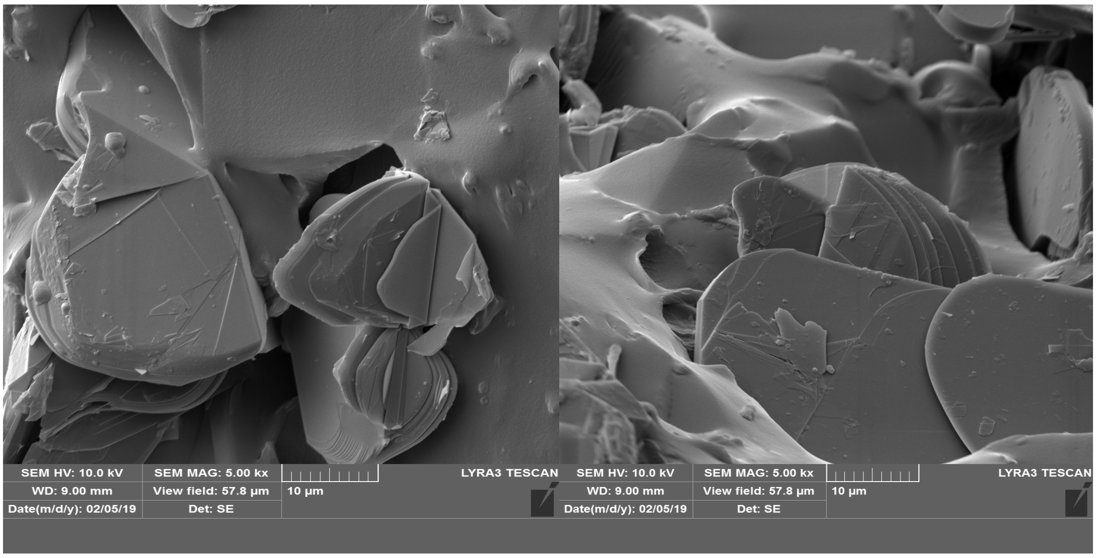

Figure 4. Internal structure of composite R1, with 12% BN platelet (uniformly distributed particles).

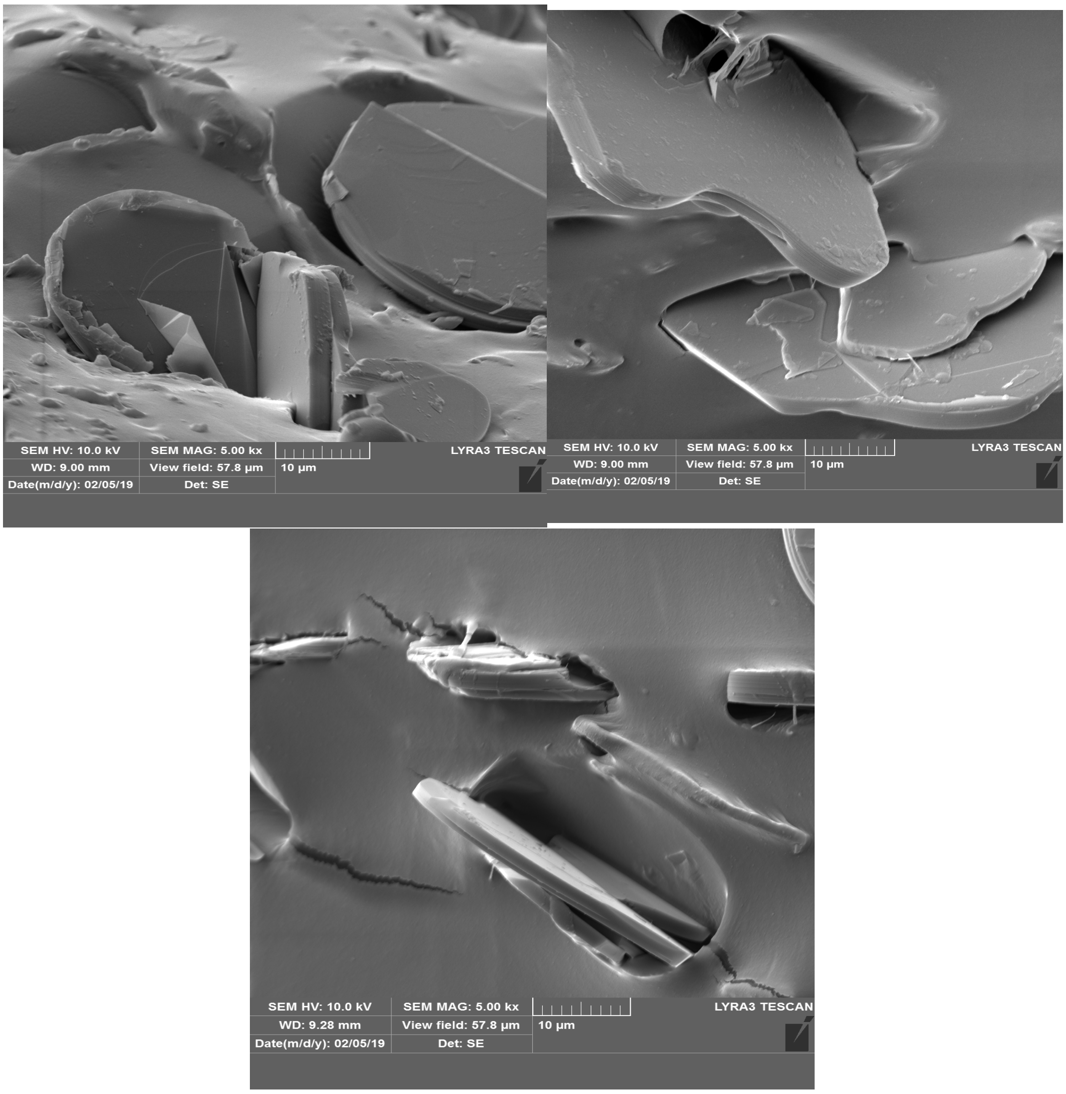

Figure 5. Internal structure of composite R2, with 12% BN platelet (oriented particles, aligned along a chain).

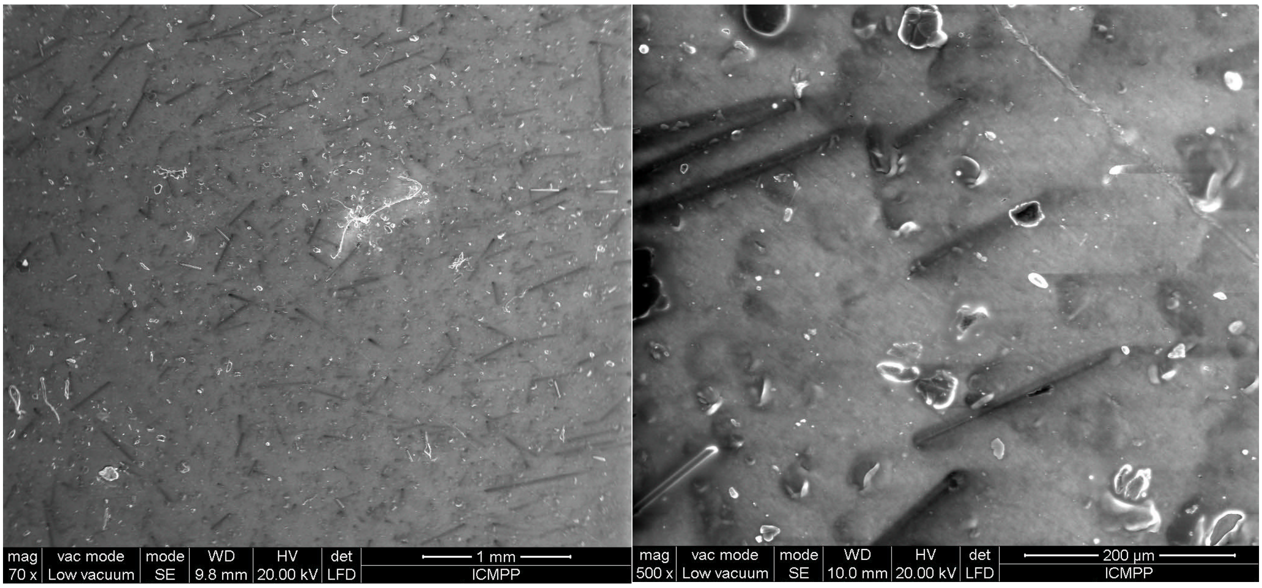

Figure 6. SEM images for sample R3.

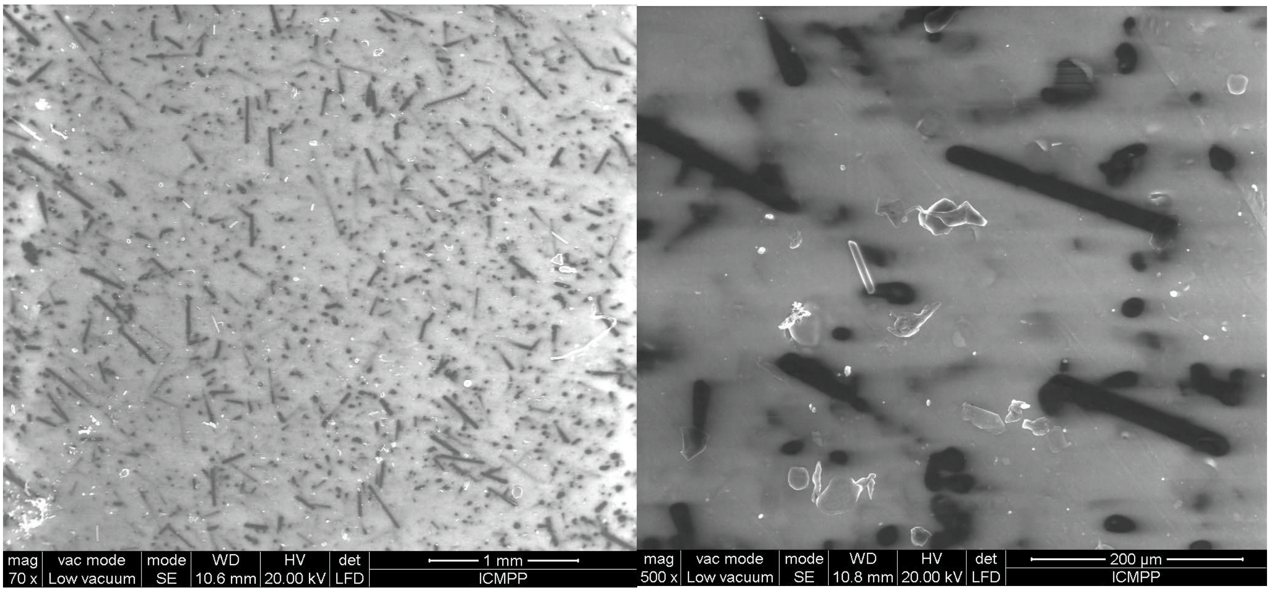

Figure 7. SEM images for sample R4.

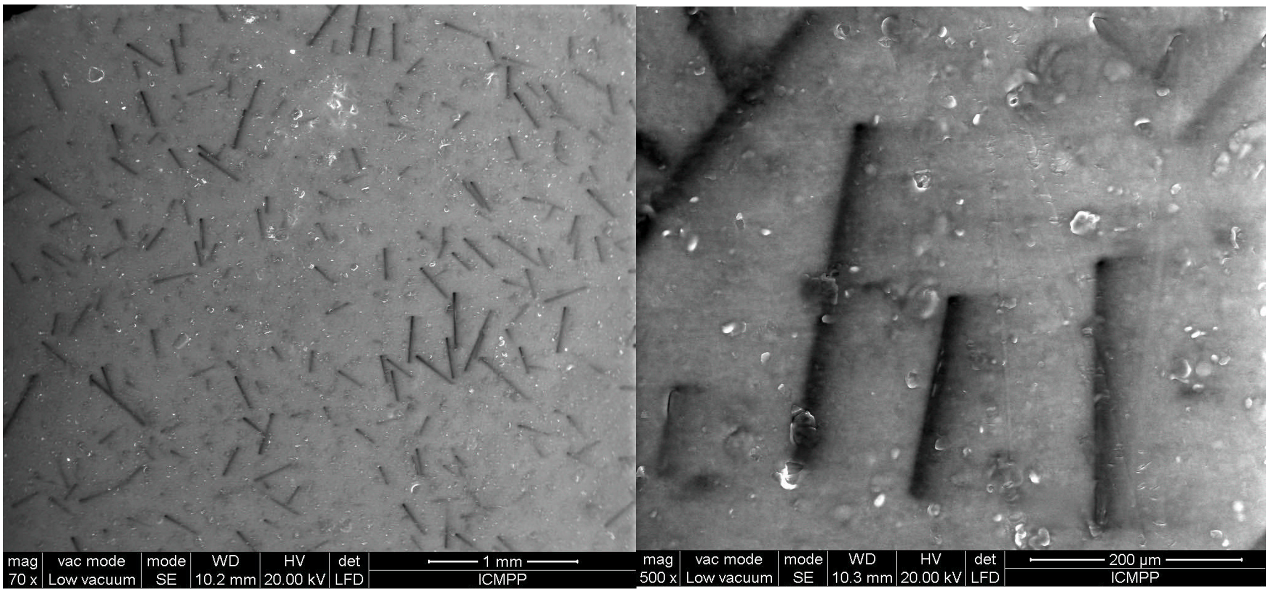

Figure 8. SEM images for sample R5.

Figures 10 and 11 represent samples R9 and R10, containing a greater number of BN platelets (15%) and a lower number of carbon microfibers (0.5%). Through the process of chain formation, we observed that nearly all carbon microfibers were trapped in chains, primarily aligned vertically. In this scenario, the number of chains is higher because of the higher amount of BN, which more easily integrates with the carbon microfibers. Considering the aforementioned findings, it could be observed that the partial incorporation of carbon microfibers into chains is influenced by two factors: the number of fibers, which should be put in relation to the material thickness due to the relatively high fiber length, and the concentration of BN platelets, which aid in the absorption of fibers into chains and facilitate their alignment along the chain. Therefore, assuming a material thickness of 1 mm, the most suitable composition is considered to be a minimum of 15% BN platelets and approximately 0.5% carbon microfibers to achieve a reasonable uniformity in terms of their chain formation and distribution on the material surface.

Seeing the chain formation in composites with BN platelets alone is also beneficial, as shown in Figure 12 for R11 and R12, which have the highest BN content (20%). The even distribution of particles is clearly seen in Figure 12a, while Figure 12b shows the formation of chains that are more uniform and denser than those in composites with carbon microfibers. In general, for all recipes containing oriented particles, it should be noted that the chains are evenly scattered across the sample surface and are fully formed and developed.

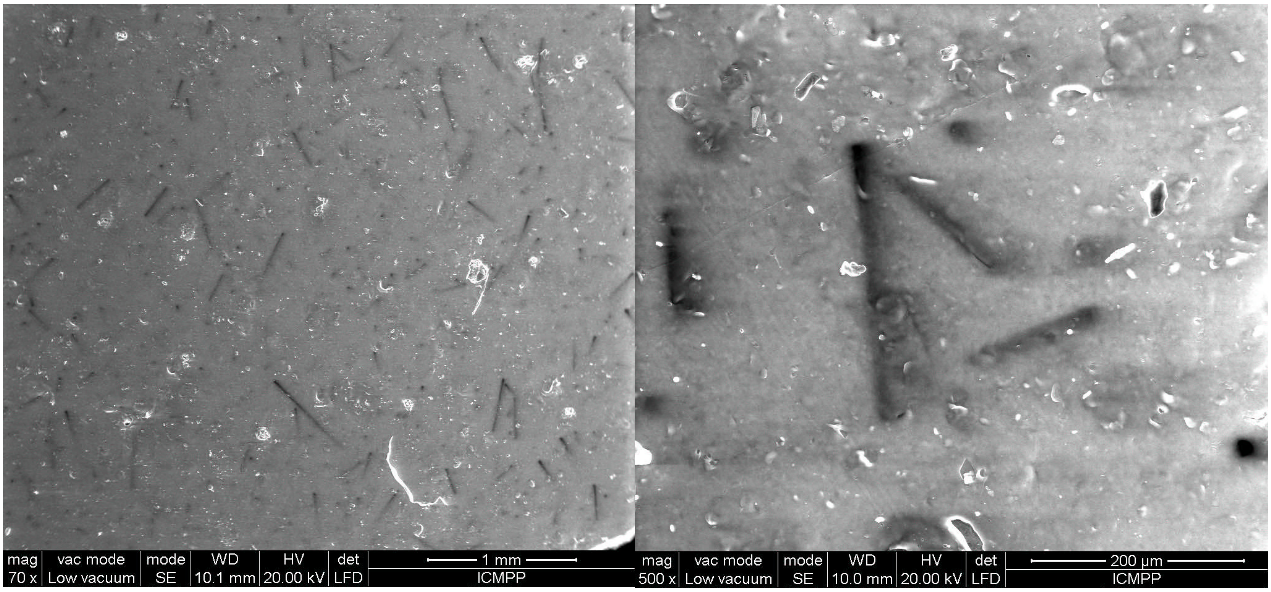

Figure 9. SEM images for sample R6.

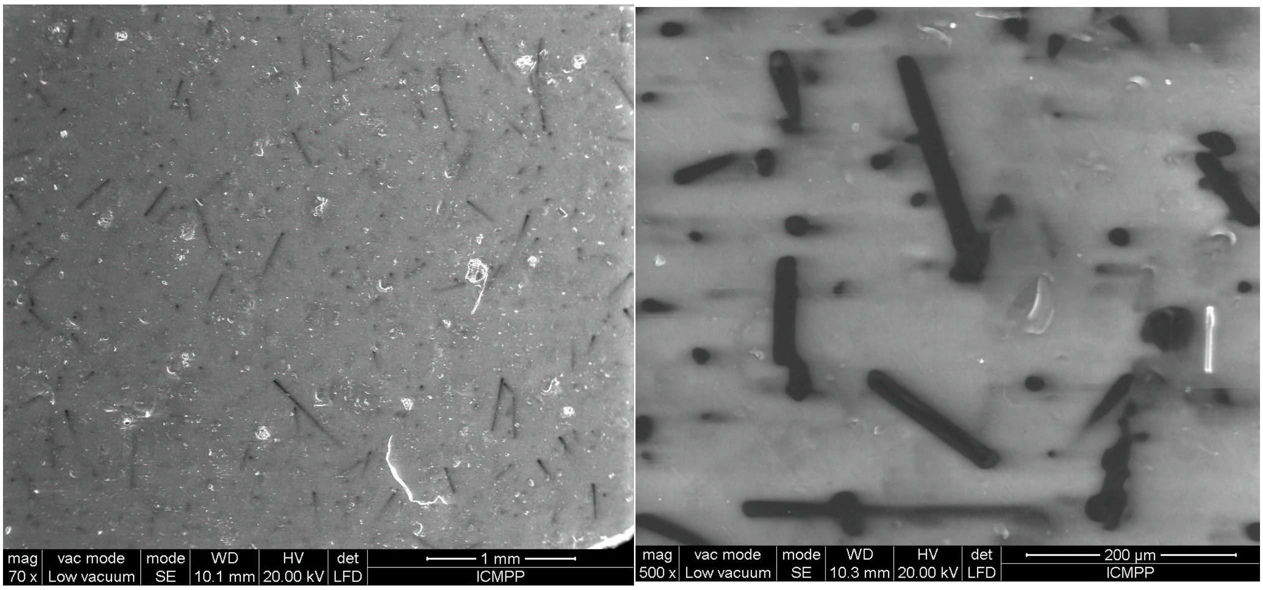

Figure 10. SEM images for sample R9.

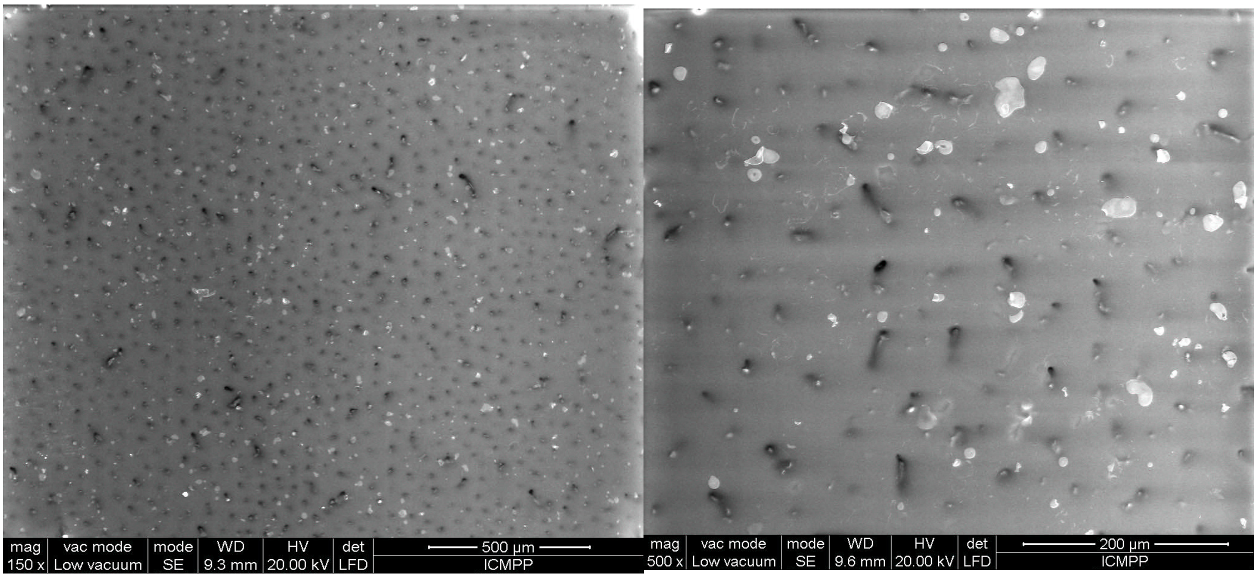

Figure 11. SEM images for sample R10.

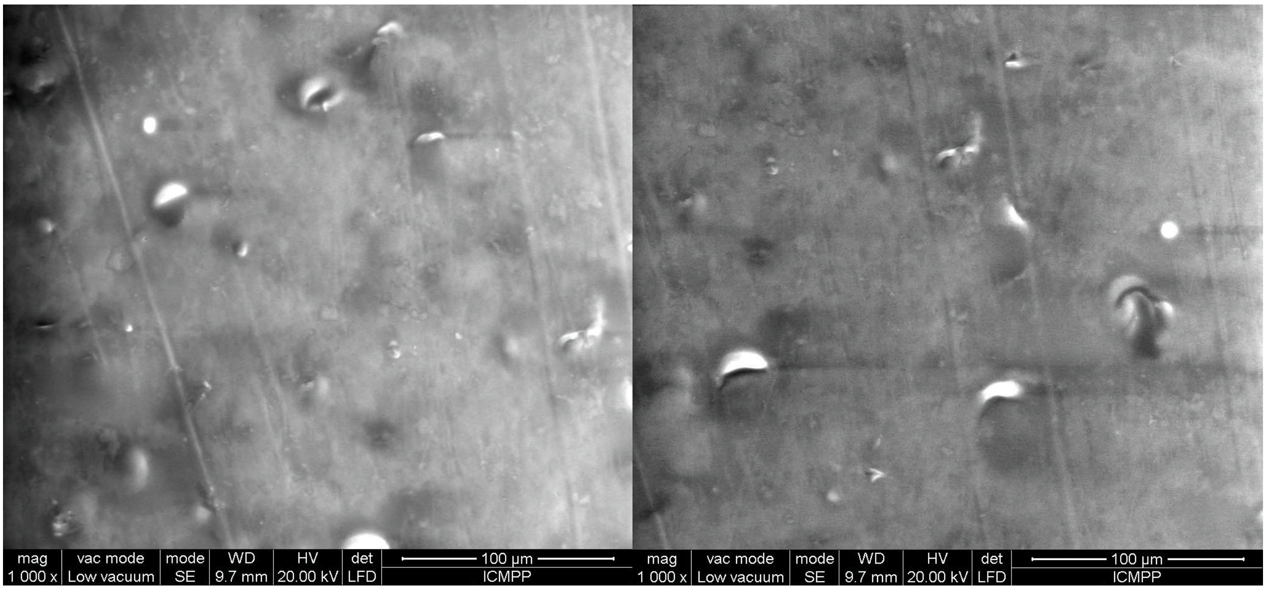

(**a**) (**b**)

Figure 12. Comparative SEM images for samples: (**a**) R11 and (**b**) R12.

3.2. X-Ray Diffraction Analysis

X-ray diffraction analysis certifies the chains' formation by aligning the BN platelets and carbon microfibers in the electrical field direction. The results are presented in Figure 13 for R1 and R2 (containing BN platelets only) and Figure 14 for R5 and R6 (containing BN platelets and carbon microfibers).

It is obvious that for the composites with oriented particles, the intensity of the diffraction maximum (111) of BN is approximately 3.4 times greater than for composites with a uniformly distributed orientation in the case of R2 compared to R1 (Figure 13) and about 2.3 times higher in the case of R6 compared R5 (Figure 14). The texture of the structure is clearly pronounced along the (111) axis, validating the structure seen through scanning electron microscopy. The other picks (for silicon, carbon, etc.) remain unchanged under the alignment process. Regarding BN, the intensity of the diffraction differs from samples R1 to R5 due to a higher content of BN platelets in the case of R5. However, the reduction in diffraction enhancement from R2 (Figure 1) to R6 (Figure 14) is related to the chain architecture modification, because, e.g., in the case of R6, the presence of carbon microfibers partially alters the alignment of BN platelets.

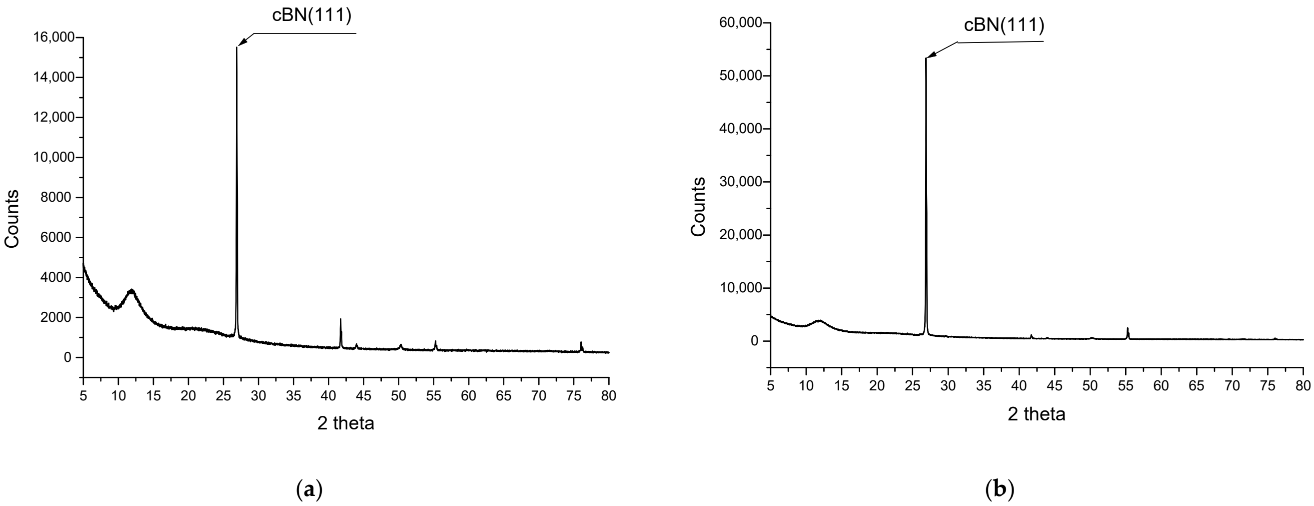

(**a**) (**b**)

Figure 13. Comparative XRD analysis for samples (**a**) R1 and (**b**) R2.

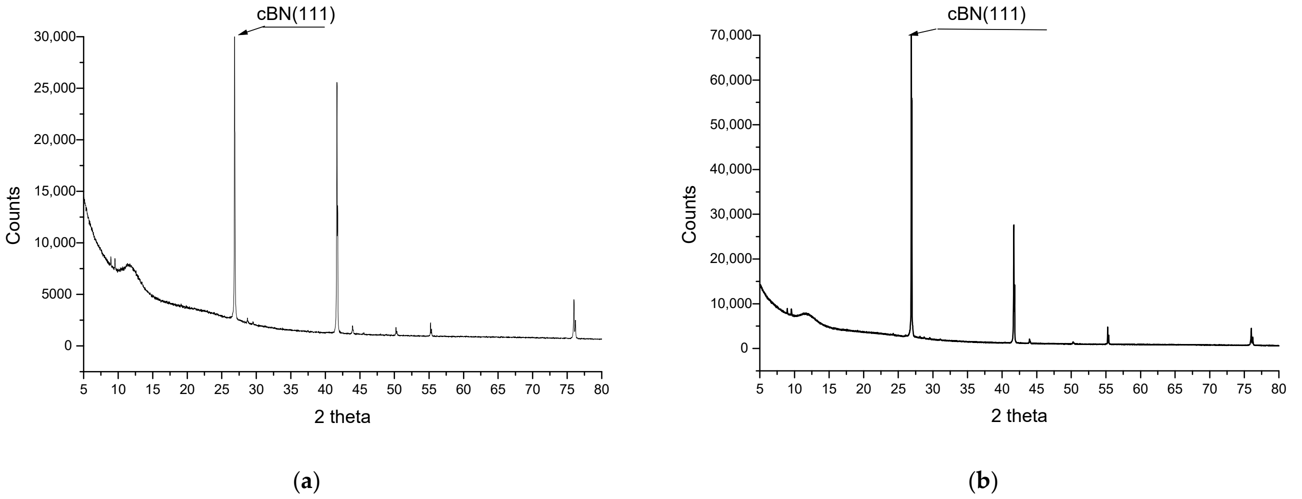

(**a**) (**b**)

Figure 14. Comparative XRD analysis for samples (**a**) R5 and (**b**) R6.

3.3. EDX Analysis

The compositions of the samples were investigated using a scanning electron microscope. Only two samples were included in the results because their composition was very similar, i.e., for R3 (with 10% BN platelet addition and 2% carbon microfiber addition) in Figure 15 and for R5 (with 12.5% BN platelet addition and 1% carbon microfiber addition) in Figure 16. The comparative variations in C and B are emphasized. However, a key finding was that no residual technological impurities such as Al, S, etc., were discovered in the analysis. This outcome enables a more accurate assessment of the analysis of the dielectric parameters that will be further addressed.

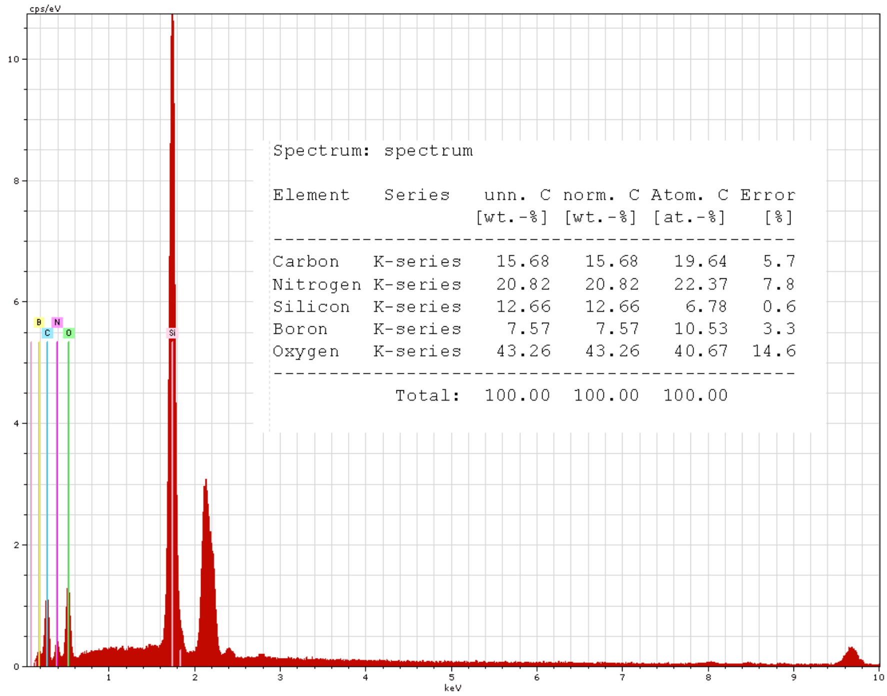

```
Spectrum: spectrum

Element   Series   unn. C norm. C Atom. C Error
                   [wt.-%] [wt.-%] [at.-%]   [%]
-----------------------------------------------
Carbon   K-series   15.68   15.68   19.64   5.7
Nitrogen K-series   20.82   20.82   22.37   7.8
Silicon  K-series   12.66   12.66    6.78   0.6
Boron    K-series    7.57    7.57   10.53   3.3
Oxygen   K-series   43.26   43.26   40.67  14.6
-----------------------------------------------
            Total:  100.00  100.00  100.00
```

Figure 15. EDX results for R3.

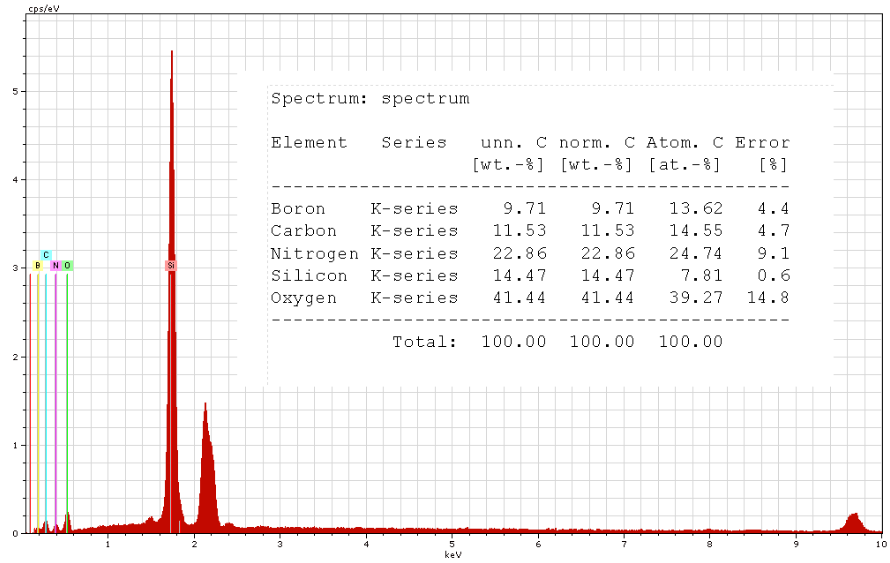

```
Spectrum: spectrum

Element   Series   unn. C norm. C Atom. C Error
                   [wt.-%] [wt.-%] [at.-%]   [%]
-----------------------------------------------
Boron    K-series    9.71    9.71   13.62   4.4
Carbon   K-series   11.53   11.53   14.55   4.7
Nitrogen K-series   22.86   22.86   24.74   9.1
Silicon  K-series   14.47   14.47    7.81   0.6
Oxygen   K-series   41.44   41.44   39.27  14.8
-----------------------------------------------
            Total:  100.00  100.00  100.00
```

Figure 16. EDX results for R5.

3.4. Physical–Mechanical Features

Table 2 presents the various physical and mechanical properties of composites. The density stays the same for both uniform and oriented samples with the same composition. A higher density is linked to a higher number of BN platelets, particularly R11–12, and decreases when there is a lower BN platelet content and more carbon microfibers, eventually reaching its lowest value in samples R3–R4.

The Shore hardness is unexpectedly lower in composites with oriented particles, regardless of their composition, possibly because of the prevalent silicone structure in the sample surface. When the dispersion is uniform, the material with the most BN platelets (specifically R11–12) also has the highest hardness. However, when it comes to materials containing oriented particles, it appears that the number of carbon microfibers has a significant impact; for instance, samples like R4, R6, and R10 show higher values in comparison to R12. Another intriguing finding is that the hardness of samples containing solely BN-oriented particles remains consistently similar, regardless of the particle concentration.

Table 2. Mechanical features of composites.

No.	Density [g cm^{-3}]	Shore Hardness	Tensile Strength [MPa]
R1	1.27	36	2.86
R2		34	2.14
R3	1.26	38	3.85
R4		36	3.23
R5	1.28	40	3.54
R6		37	2.87
R7	1.31	39	2.74
R8		34	2.05
R9	1.30	38	3.32
R10		36	2.59
R11	1.33	42	2.63
R12		34	1.84

The impact of the composition upon tensile strength values is comparable to that upon Shore hardness, with the values being generally reduced in composites with oriented particles, regardless of their composition. The number of carbon microfibers greatly affects the tensile strength of composites with either uniform or particle orientations. The samples containing more carbon microfibers (R3–R4, with 2% content) exhibit the highest tensile strength, followed by R5–R6 (with 1% carbon microfibers' content), which have slightly lower strength values. These tensile strength findings align with the data shown in [50].

3.5. Dielectric Characterization

The permittivity and loss factor (TgDelta) dielectric parameters were calculated based on IEC60250 [53] standards, using a reference frequency of 1 kHz. The data are shown in Table 3. An obvious increase in permittivity values is observed in all composites with aligned particles, regardless of their composition, Figure 17, comparing to Figure 18. An increase in the number of BN platelets leads to a higher level of dielectric permittivity enhancement, though this enhancement is saturated when concentrations surpass 15%. The reason for this is that the dielectric permittivity of bulk BN platelets varies from 3.29 to 3.76 in the out-of-plane direction (with thickness dependency) and remains relatively constant at 6.82 to 6.93 in-plane. Thus, aligning them in the electric field promotes an in-plane orientation within chains, leading to a noticeable increase in permittivity. However, not all platelets in the chain are oriented in-plane. As the concentration of platelets increases, achieving in-plane orientation becomes more difficult. Therefore, at a 15% concentration of BN platelets, we can achieve an optimal orientation. Analyzing the table alone makes it difficult to fully explain the impact of carbon microfibers but comparing samples like R2 and R6 does show a positive effect. Alternatively, the inclusion of carbon microfibers could also positively impact uniform composites when comparing R1 to R3, R5, or R9. To understand how the material's composition affects permittivity, an extended analysis was performed, as shown in Figure 12 (for composites with uniformly dispersed particles) and Figure 13 (for composites with oriented particles). The impact of incorporating carbon microfibers on the dielectric permittivity of homogeneous composites is clearly beneficial, especially when the BN content surpasses 12%. For instance, the permittivity value of a material containing 15.5% BN and 2% carbon microfibers is comparable to that of a material with 20% BN and without fibers. The technological advantage of producing materials with microfibers could be ongoing as the price of BN platelets is at least 10 times greater than carbon microfibers. For composites with oriented particles, the impact of carbon microfiber addition is significant at all concentrations of BN. However, at higher fiber content, the effect becomes more beneficial at higher BN concentrations, which correlates well with the previous SEM observations in Figures 6–12, related to the fact that the integration of carbon microfibers within chains depends on the BN concentration. The impact of incorporating carbon microfibers on the dielectric permittivity is significant, especially when the BN content surpasses 15%. Nonetheless, it can be inferred that a material consisting of 12% BN and 2% carbon microfibers exhibits comparable permittivity to one with 15% BN, or a material comprising 15% BN and 2% carbon microfibers has equivalent permittivity lower than a material with 18% BN, resulting in similar economic implications for materials technology in terms of reducing the costly BN platelet content.

Table 3. Dielectric parameters of composites.

No.	Recipe	Permittivity	TgDelta	Resistivity [Ohm m]	Permittivity Enhancement
R1	12% BN platelet; 2% KH550	3.35	0.0077	4.86×10^{13}	8%
R2		3.62	0.0078	8.21×10^{12}	
R3	10% BN platelet; 2% carbon microfibers; 2% KH550	3.37	0.0098	2.33×10^{8}	6.2%
R4		3.58	0.0102	4.15×10^{5}	
R5	12.5% BN platelet; 1% carbon microfibers; 2% KH550	3.43	0.0086	4.44×10^{9}	8.2%
R6		3.71	0.0088	7.22×10^{6}	
R7	15.5% BN platelet; 2.5% KH550	3.51	0.0076	3.18×10^{13}	9.7%
R8		3.85	0.0077	6.47×10^{12}	
R9	15% BN platelet; 0,5% carbon microfibers; 2.5% KH550	3.54	0.0082	5.27×10^{10}	9.3%
R10		3.87	0.0083	9.53×10^{7}	
R11	20% BN platelet; 2.5% KH550	3.72	0.0075	2.76×10^{13}	9.2%
R12		4.06	0.0076	4.82×10^{12}	

The examination of the dielectric loss factor (TgDelta) indicates a slight distinction between uniformly and particle-oriented composites across all formulations. The findings in reference [54] that aligning the BN platelets can lower dielectric loss by inhibiting defect ions perpendicular to the field direction were not verified; however, this may only hold true at elevated temperatures, which does not apply to our materials. Samples with carbon microfibers show significantly higher dielectric loss compared to samples with only BN, such as reaching 0.0102 for the sample containing 2% microfiber content. Ultimately, the resistivity values were examined. For samples containing only BN, the resistivity decreases slightly as the BN content increases, and there is minimal difference between similar recipes with either uniformly or oriented particles, as also noticed in [55]. Noticeable variations are clearly observed in the samples that have microfibers. In this case, the resistivity is at least 10^4 times less compared to samples containing only BN. Conversely, the alignment of particles once more decreases the resistance by at least 10^3 times. The sample with a 2% concentration of microfibers reached the minimum value of 4.15×10^5 Ohm m. The reason is that with less BN, microfibers align vertically through the BN platelets, creating parallel microconductive areas within the chains and reducing the material's electrical resistance overall.

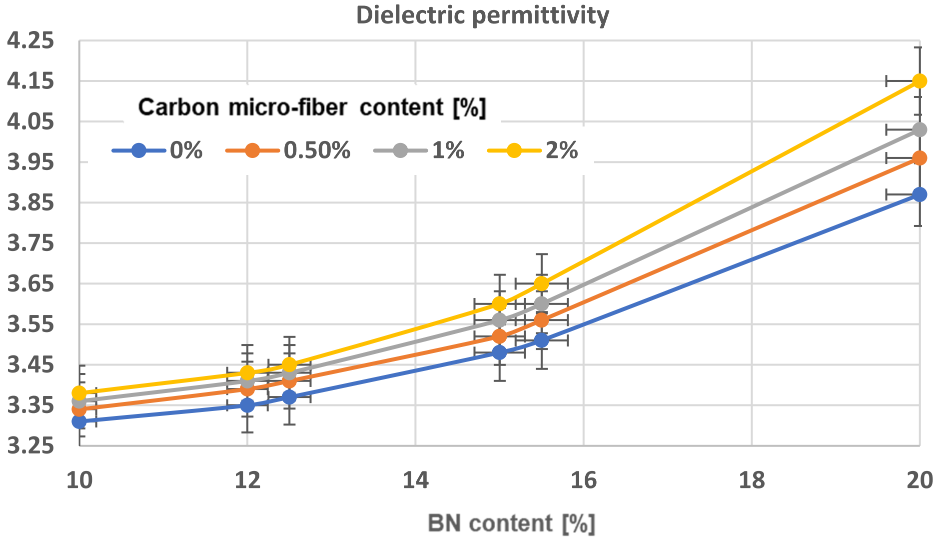

Figure 17. Dielectric permittivity characteristics of composites with uniform dispersion.

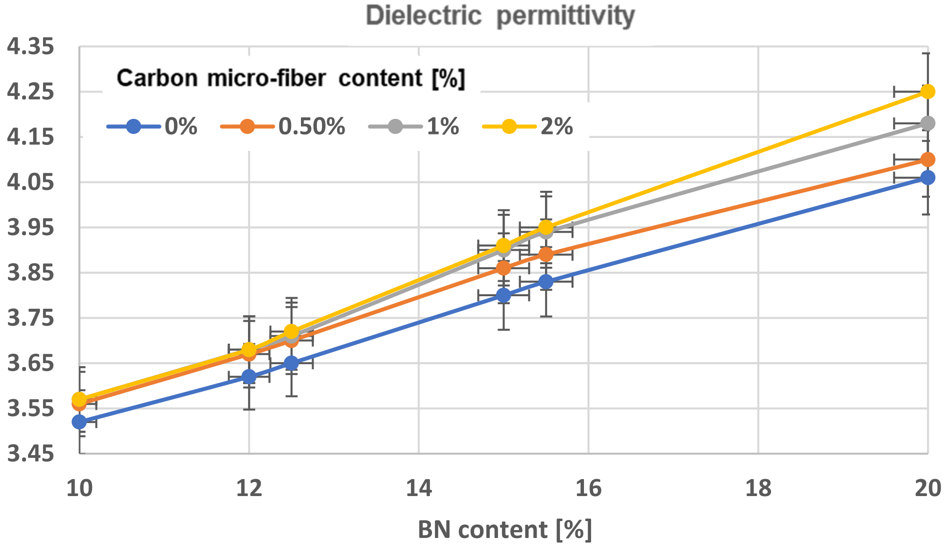

Figure 18. Dielectric permittivity characteristics of composites with oriented particles.

3.6. Thermal Conductivity Analysis

The measurement of thermal conductivity using the Laser Flash Method and its corresponding time–temperature curve is viewed as more effective for analyzing samples with a greater surface area and thickness within the range of the materials presented, in comparison to alternative methods, e.g., the 3ω method [56]. Table 4 displays the thermal conductivity values of composite samples. The difference in thermal conductivity of composites is linked to the architecture of chains when the thermal conductivity of carbon microfibers is similar to boron nitride platelets, as previously discussed in terms of resistivity characteristics. Thermal conductivity was significantly improved in all samples containing aligned particles, regardless of their composition, Figure 19, comparing to Figure 20. Overall, the obtained data align with the findings in, for instance, the study referenced in [42]. The sample with 20% BN platelets content had the highest thermal conductivity value of 1.11 W m^{-1} K^{-1}, while the sample with 2% carbon microfiber content showed the greatest thermal conductivity enhancement. Typically, the thermal conductivity enhancement decreases for composites with higher particle content, despite the fact that thermal conductivity generally increases with higher particle content in absolute terms, meaning that the alignment process remains more relevant at a lower content of particles. The addition of carbon microfibers in composites has a positive impact on enhancing thermal conductivity. In order to analyze how the composition influences the thermal conductivity, an extended analysis was conducted and the findings are displayed in Figure 14 (for uniform composites) and Figure 15 (for composites with aligned particles). For uniform composites, adding carbon microfibers greatly improves thermal conductivity, especially with a BN content of around 15%. The rise continues at a higher BN content but the effect is progressively limited. When oriented particles are present in composites, adding carbon microfibers significantly boosts thermal conductivity, with noticeable enhancements even at a BN content above 12%. The maximum is reached at 15% BN content. However, once the BN content exceeds 15.5%, the impact is progressively limited too. The reason can be found in the architecture of the materials that have microfibers. In instances of even distribution, the microfibers, which are much longer than BN platelets, spread out randomly throughout the material, forming various orientations that help create quicker heat pathways. In this scenario, higher concentrations of microfibers result in increased thermal dissipation. In the case of composites with oriented particles, adding carbon microfibers to chains typically enhances heat transfer pathways by clustering within the chains. With a reduced amount of BN, the microfibers orient vertically between the BN platelets, forming parallel microconductive regions for heat transfer, and additional microfibers enhance this effect. However, when the BN content is increased, a saturation process happens as the concentration of fibers increases because the fibers within chains are only partially oriented vertically, as BN platelets take priority in vertical orientation. These assumptions align perfectly with the observations provided alongside the SEM images in Figures 6–12.

Table 4. Thermal parameters of composites.

No.	Thermal Conductivity K [W m^{-1} K^{-1}]	Thermal Conductivity Enhancement
R1	0.49	63.2%
R2	0.80	
R3	0.53	66%
R4	0.88	
R5	0.64	48.4%
R6	0.95	
R7	0.63	42.9%
R8	0.90	
R9	0.72	40.3%
R10	1.01	
R11	0.84	32.1%
R12	1.11	

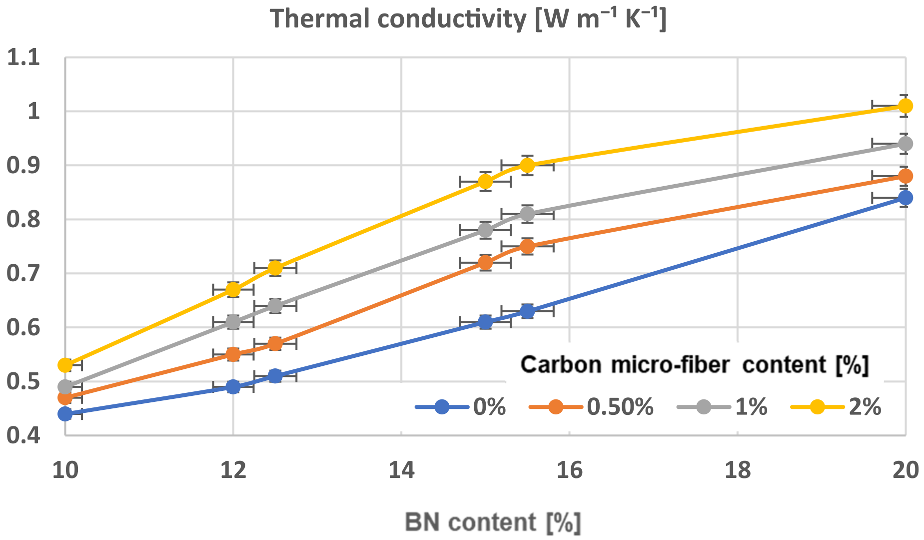

Figure 19. Thermal conductivity characteristics of composites with uniform dispersion.

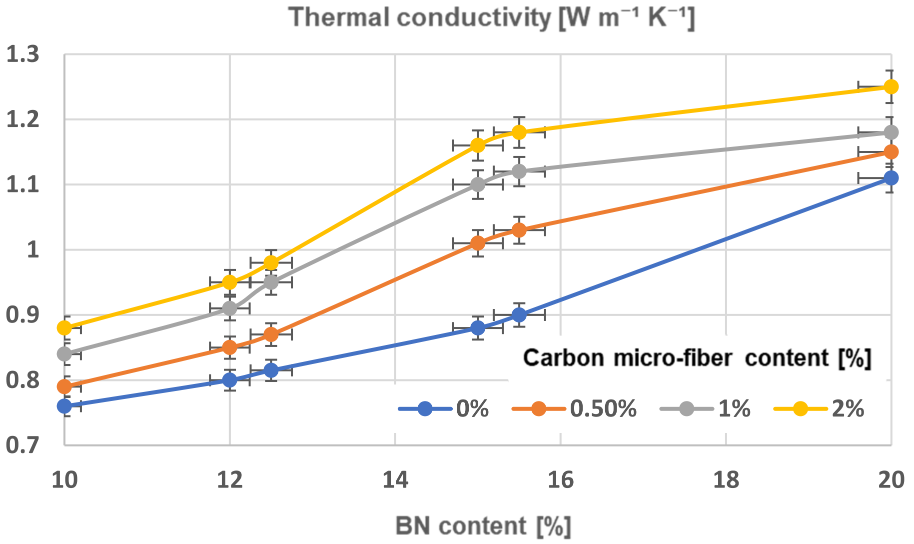

Figure 20. Thermal conductivity characteristics of composites with oriented particles.

The findings in this study showed slightly inferior results for composites with oriented BN platelets and carbon microfibers when compared to previous results presented in the literature, such as those in [57], which described a similar composition and may be the most relevant to our paper but explores a totally different and more complicated chemical–mechanical technology for particle alignment. Similar structures involving BN particles but other types of carbon structures were also thoroughly examined, as noted in references [32,58–64], although comparing their findings to ours is more indicative due to the fact that the proportion of carbon structures is over 15 wt% in those instances. When compared to [58], research that used 10 wt% spherical BN particles and a much higher content of 10–30 wt% carbon microfibers, with a uniform dispersion of additives. In that research, the composite presented a value of thermal conductivity of 1.03 W m^{-1} K^{-1}, similar to the value achieved within our technology at 15 wt% BN and only 0.5 wt% carbon microfibers. It is technically crucial to limit the number of carbon particles or fibers as they can significantly raise the material's dielectric loss and conductivity, thus restricting their use in electronic applications requiring high electrical insulation performance. On the other hand, structures with BN particles exceeding 25% are not advisable for technological and economic reasons. From this perspective, the composites presented could cover a wider range of applications in the thermal management of electronics, mainly due to the continuous miniaturizing of electronic equipment. Compared to actual technologies using homolog materials but with a uniform dispersion of particles, with our technology, ingredient consumption can be reduced by 5–10 times, providing numerous advantages, especially when working with costly powders of certain sizes as they are now organized in chains, ensuring efficient heat transfer in the intended orientation. Ultimately, only the properties of the chain matter for achieving superior electro-thermal properties, compared to materials with evenly dispersed particles.

The main benefit of the study is that the presented technology can be easily expanded for industrial use, it is flexible in terms of ingredients and film thickness, and it can be customized for various thermal management applications in the electronics field. Electronic Thermal Management Materials Market size achieved USD 6.4 billion in 2023 and will grow at 7.5% CAGR from 2024 to 2032 [65], offering clear opportunities. The targeted application of the presented technology is related to, e.g., thermally radiative materials for microelectronics, elastomeric pads for electric autonomous vehicles, interface materials for miniaturized and/or portable healthcare devices, adhesive tapes for thermal interface in telecommunication devices, etc. [66].

When we compare our findings with homolog results from previous studies, such as [45,67–69], the performance demonstrated by the materials we presented is comparable, exhibiting a thermal conductivity of approximately 1 W m^{-1} K^{-1}, yet with a significantly lower content of BN particles. However, the respective technologies, even when employing magnetic fields for the orientation of BN particles, have the limitation of low productivity, questionable reproducibility in larger-scale manufacturing, and no viable equipment to efficiently produce such materials for the market. In our scenario, we showcased a pilot-scale apparatus that can generate substantial numbers of consistent composite forms featuring aligned particles, thus proving its industrial feasibility through a roll-to-roll process. Concerning the environmental impact, the compact nature of our equipment, associated with minimal energy consumption for alignment processes and curing, provides evident advantages for the carbon footprint.

4. Conclusions

This study presents silicone composites with uniform dispersion and electrically oriented boron nitride platelets and carbon microfibers. The technological process included the homogenization and dispersion of nano/microparticles in the liquid polymer, orienting the particles under an electric field, and composite final curing to block particles within chains via the use of IR radiation.

The innovative idea involved using two fields for orienting particles: a higher-voltage stationary field to align the particles in chains and a lower-voltage alternating field at a specific frequency to help move the particles in the polymer and facilitate the orientation, a decisive factor that enhances the uniform spread of carbon microfibers among BN in the created chains.

According to SEM images, it should be noted that the chains are evenly scattered across the sample surface and are fully formed and developed, but their architecture critically depends on the composition. There are fewer chains in the composite with fewer carbon microfibers. The texture of the structure was confirmed through X-ray diffraction analysis, which revealed alignment along the BN(111) axis, supporting the structure observed with scanning electron microscopy.

A higher density is linked to a higher number of BN platelets, which decreases when there is a lower BN platelet content and more carbon microfibers. The Shore hardness is unexpectedly lower in composites with oriented particles, regardless of their composition, possibly because of the prevalent silicone structure in the sample surface. When the dispersion is uniform, the material with the most BN platelets has the highest hardness. The tensile strength values are generally reduced in composites with oriented particles, regardless of their composition. The number of carbon microfibers greatly affects the tensile strength of composites with either a uniform or particle orientation. The samples containing more carbon microfibers exhibit the highest tensile strength.

An obvious increase in permittivity values is observed in all composites with aligned particles, regardless of their composition. The higher the concentration of BN platelets, the greater the enhancement, but the effect decreases gradually after reaching a concentration of 15%. The impact of incorporating carbon microfibers on the dielectric permittivity of homogeneous composites is clearly beneficial, especially when the BN content surpasses 12%. The value of a material containing 15.5% BN and 2% carbon microfibers is comparable to that of a material with 20% BN and without fibers. The technological advantage of producing materials with microfibers could be ongoing as the price of BN platelets is at least 10 times greater than carbon microfibers. The examination of the dielectric loss factor (TgDelta) indicates a slight distinction between uniform and oriented-particle composites across all formulations. For samples containing only BN, the resistivity decreases slightly as the BN content increases, and there is minimal difference between similar recipes with either uniformly or oriented particles. Noticeable variations are clearly observed in the samples that have microfibers, with the resistivity being at least 10^4 times lower compared to samples containing only BN. Conversely, the alignment of particles once more decreases the resistance by at least 10^3 times.

The difference in thermal conductivity of composites is linked to the architecture of chains. Thermal conductivity was significantly improved in all samples containing aligned particles, regardless of their composition. For uniform composites, adding carbon microfibers greatly improves thermal conductivity, especially with a BN content of over 12%. The greatest rise occurred with the addition of carbon microfibers at 2% when the BN content exceeds 15.5%. When oriented particles are present in composites, adding carbon microfibers significantly boosts the thermal conductivity, with noticeable enhancements even at a BN content above 12%. However, once the BN content exceeds 15.5%, the impact becomes less relevant because the fibers within chains are only partially oriented vertically, as the BN platelets take priority in a vertical orientation.

The results of this research demonstrated better outcomes for composites containing BN platelets and carbon microfibers than previous results presented in the literature, while also using a simpler technology for processing the polymer matrix and aligning particles.

Limiting the number of carbon particles or fibers is essential to prevent a notable increase in the material's dielectric loss and conductivity, which hinders their suitability for electronic applications that demand strong electrical insulation. However, it is not recommended to use structures containing more than 25% BN particles for technological and economic purposes.

In contrast to current technologies, by utilizing homologous materials with uniformly dispersed particles, our technology reduces ingredient consumption by 5–10 times. This offers several benefits, particularly when using expensive powders of specific sizes that are now arranged in chains to enhance heat transfer efficiency in the desired direction. We demonstrated a pilot-scale device capable of producing significant quantities of uniform composite structures with aligned particles, thereby confirming its industrial viability via a roll-to-roll method. Regarding the ecological effect, the compact design of our devices, coupled with the low energy usage for alignment and curing, offers clear benefits for the carbon footprint. The presented technology is highly versatile for industrial applications, able to accommodate different ingredients and film thicknesses, and can be tailored for various uses in electronics thermal management, e.g., thermally radiative materials for microelectronics, elastomeric pads for electric autonomous vehicles, interface materials for miniaturized and/or portable healthcare devices, adhesive tapes for thermal interface in telecommunication devices, etc.

Author Contributions: Conceptualization, R.C.C. and C.M.S.; Methodology, R.C.C., M.A. (Magdalena Aflori) and C.M.S.; Validation, R.C.C., C.M.S., M.A. (Mihaela Aradoaei) and D.B.; Formal analysis, M.A. (Magdalena Aflori), C.M.S., M.A. (Mihaela Aradoaei) and D.B.; Investigation, M.A. (Magdalena Aflori), C.M.S., M.A. (Mihaela Aradoaei) and D.B.; Data curation, R.C.C., M.A. (Magdalena Aflori), C.M.S. and M.A. (Mihaela Aradoaei); Writing—original draft, R.C.C. and C.M.S.; Writing—review & editing, R.C.C. and C.M.S. All authors have read and agreed to the published version of the manuscript.

Funding: This research received no external funding.

Institutional Review Board Statement: Not applicable.

Informed Consent Statement: Not applicable.

Data Availability Statement: The original contributions presented in the study are included in the article, further inquiries can be directed to the corresponding author.

Acknowledgments: The findings outlined in the article are an expansion of the research activity conducted within the EU Manunet project AniConFilm/2017-2019.

Conflicts of Interest: The authors declare no conflicts of interest.

References

1. Dhumal, A.; Kulkarni, A.; Ambhore, N. A comprehensive review on thermal management of electronic devices. *J. Eng. Appl. Sci.* **2023**, *70*, 140. [CrossRef]
2. The Essential Guide to Thermal Management of Electronics. Available online: https://magazine.elkem.com/digital-communications/thermal-management-of-electronics/ (accessed on 5 June 2024).
3. Bianco, V.; De Rosa, M.; Vafai, K. Phase-change materials for thermal management of electronic devices. *Appl. Therm. Eng.* **2022**, *214*, 118839. [CrossRef]
4. Chen, H. A new route to fabricate flexible, breathable composites with advanced thermal management capability for wearable electronics. *Flex. Electron.* **2023**, *7*, 24. [CrossRef]
5. Xing, W. Recent Advances in Thermal Interface Materials for Thermal Management of High-Power Electronics. *Nanomaterials* **2022**, *12*, 3365. [CrossRef]
6. Liu, C.; Wu, W.; Drummer, D.; Shen, W.T.; Wang, Y.; Schneider, K.; Tomiak, F. ZnO nanowire-decorated Al_2O_3 hybrids for improving the thermal conductivity of polymer composites. *J. Mater. Chem. C* **2020**, *8*, 5380–5388. [CrossRef]
7. Jiang, H. Unleashing the Potential of Boron Nitride Spheres for High-Performance Thermal Management. *ChemNanoMat* **2024**, *10*, 202300601. [CrossRef]
8. Wu, W.; Zhang, L.; Liu, Y.; Chen, H. Thermally conductive composites based on hexagonal boron nitride nanosheets for thermal management: Fundamentals to applications. *Compos. Part A Appl. Sci. Manuf.* **2023**, *169*, 107533. [CrossRef]
9. Mazumder, R. Boron nitride based polymer nanocomposites for heat dissipation and thermal management applications. *Appl. Mater. Today* **2022**, *29*, 101672. [CrossRef]
10. Bayır, S.; Semerci, E.; Bedri, T. Preparation of novel thermal conductive nanocomposites by covalent bonding between hexagonal boron nitride nanosheet and well-defined polymer matrix. *Compos. Part A Appl. Sci. Manuf.* **2021**, *146*, 106406. [CrossRef]
11. Zhang, Y.; Wang, M.; Li, X.; Liu, J. Fabrication of thermally conductive polymer composites based on hexagonal boron nitride: Recent progresses and prospects. *Nano* **2021**, *2*, 042002. [CrossRef]
12. Yu, C.; Zhao, L.; Wang, Q.; Chen, S. Polymer composites based on hexagonal boron nitride and their application in thermally conductive composites. *RSC Adv.* **2018**, *39*, 21948. [CrossRef] [PubMed]
13. Niu, H.Y.; Guo, H.C.; Ren, Y.J.; Ren, L.C.; Lv, R.C.; Kang, L.; Bashir, A.; Bai, S.L. Spherical aggregated BN/AlN filled silicone composites with enhanced through-plane thermal conductivity assisted by vortex flow. *Chem. Eng. J.* **2022**, *430*, 133155. [CrossRef]
14. Stiubianu, G.T.; Popescu, M.; Vasile, V.; Călin, R. Scalable Silicone Composites for Thermal Management in Flexible Stretchable Electronics. *Batteries* **2022**, *8*, 95. [CrossRef]

15. Zhu, Z.Z.; Li, C.W.; E, S.F.; Xie, L.Y.; Geng, R.J.; Lin, C.T.; Li, L.Q.; Yao, Y.G. Enhanced thermal conductivity of polyurethane composites via engineering small/large sizes Interconnected boron nitride nanosheets. *Compos. Sci. Technol.* **2019**, *170*, 93–100. [CrossRef]
16. Yang, X. Boron Nitride/Polyurethane Composites with Good Thermal Conductivity and Flexibility. *Int. J. Mol. Sci.* **2023**, *24*, 8221. [CrossRef]
17. Wang, T.; Zhang, Y.; Li, J.; Chen, H. Enhanced Thermal Conductivity of Polyimide Composites with Boron Nitride Nanosheets. *Sci. Rep.* **2018**, *8*, 1557. [CrossRef] [PubMed]
18. Ding, D.; Liu, Y.; Zhang, J.; Wang, M. Thermal conductivity of polydisperse hexagonal BN/polyimide composites: Iterative EMT model and machine learning based on first principles investigation. *Chem. Eng. J.* **2022**, *437*, 135438. [CrossRef]
19. Chen, L.; Wang, X.; Zhang, Q.; Zhou, M. Thermal Conductivity Performance of Polypropylene Composites Filled with Polydopamine-Functionalized Hexagonal Boron Nitride. *PLoS ONE* **2017**, *12*, e0170523. [CrossRef] [PubMed]
20. Inagaki, Y. Enhacement of Mechanical Properties of High-Thermal-Conductivity Composites Comprising Boron Nitride and Poly(methyl methacrylate) Resin through Material Design Utilizing Hansen Solubility Parameters. *ACS Appl. Mater. Interfaces* **2024**, *16*, 26653–26663. [CrossRef]
21. Ghosh, B.; Xu, F.; Hou, X. Thermally conductive poly(ether ether ketone)/boron nitride composites with low coefficient of thermal expansion. *J. Mater. Sci.* **2022**, *56*, 10326–10337. [CrossRef]
22. Mohanraman, R. Synergistic Improvement in the Thermal Conductivity of Hybrid Boron Nitride Nanotube/Nanosheet Epoxy Composites. Materials Science 2024. Available online: https://chemrxiv.org/engage/chemrxiv/article-details/65e71e65e9ebbb4db9f27b56 (accessed on 5 June 2024).
23. Moradi, S. Remarkable Thermal Conductivity of Epoxy Composites Filled with Boron Nitride and Cured under Pressure. *Polymers* **2021**, *13*, 955. [CrossRef] [PubMed]
24. Gul, S. Design of Highly Thermally Conductive Hexagonal Boron Nitride-Reinforced PEEK Composites with Tailored Heat Conduction Through-Plane and Rheological Behaviors by a Scalable Extrusion. *ACS Appl. Polym. Mater.* **2022**, *5*, 329–341. [CrossRef]
25. Tang, L. Flexible and Robust Functionalized Boron Nitride/Poly(p-Phenylene Benzobisoxazole) Nanocomposite Paper with High Thermal Conductivity and Outstanding Electrical Insulation. *Nano-Micro Lett.* **2024**, *16*, 38. [CrossRef]
26. Tian, X. Flexible graphene/boron nitride nanosheets paper for thermal management of high-power electronics. *arXiv* **2023**, arXiv:2305.03142.
27. Zhan, Y. An anisotropic layer-by-layer carbon nanotube/boron nitride/rubber composite and its application in electromagnetic shielding. *Nanoscale* **2020**, *12*, 7782–7791. [CrossRef] [PubMed]
28. Wang, Z.; Li, Y.; Zhang, H.; Chen, J. Effective three-dimensional thermal conductivity networks in polystyrene/multi-walled carbon nanotubes/aluminum oxide-hexagonal boron nitride composites based on synergistic effects and isolated structures. *Adv. Compos. Hybrid Mater.* **2023**, *6*, 125. [CrossRef]
29. Badakhsh, A. Preparation of Boron Nitride-Coated Carbon Fibers and Synergistic Improvement of Thermal Conductivity in Their Polypropylene-Matrix Composites. *Polymers* **2019**, *11*, 2009. [CrossRef] [PubMed]
30. Ozbas, R.; Dogu, M.; Derun, E. Enhanced interfacial and mechanical properties of carbon fabric/PA12 composites via grafting silanized nano hexagonal boron nitride onto the fibers. *Compos. Interfaces* **2024**, *31*, 895–917. [CrossRef]
31. Jones, R. Thermal Conductivity of Carbon/Boron Nitride Heteronanotube and Boron Nitride Nanotube Buckypapers: Implications for Thermal Management Composites. *ACS Appl. Nano Mater.* **2023**, *6*, 15374–15384. [CrossRef]
32. Shu, D. Boron Nitride/Carbon Fiber High-Oriented Thermal Conductivity Material with Leaves-Branches Structure. *Materials* **2024**, *17*, 2183. [CrossRef]
33. Cui, Y.; Wang, X.; Liu, Z.; Zhang, Y. Construction of 3D interconnected boron nitride/carbon nanofiber hybrid network within polymer composite for thermal conductivity improvement. *J. Mater. Sci. Technol.* **2023**, *147*, 165–175. [CrossRef]
34. Wang, R. Highly Thermally Conductive Polymer Composite Originated from Assembly of Boron Nitride at an Oil–Water Interface. *ACS Appl. Mater. Interfaces* **2019**, *11*, 42818–42826. [CrossRef]
35. Xia, C. Hybrid boron nitride-natural fiber composites for enhanced thermal conductivity. *Sci. Rep.* **2016**, *6*, 34726. [CrossRef] [PubMed]
36. Zhan, K. Low thermal contact resistance boron nitride nanosheets composites enabled by interfacial arc-like phonon bridge. *Nat. Commun.* **2024**, *15*, 2905. [CrossRef] [PubMed]
37. Cheng, S.; Zhang, L.; Liu, M.; Wang, Y. Enhanced thermal management in electronic devices through control-oriented structures. *J. Mater. Chem. A* **2024**, *12*, 8640–8662. [CrossRef]
38. Niu, H.; Chen, J.; Zhang, X.; Li, D. Highly thermally conductive and soft thermal interface materials based on vertically oriented boron nitride film. *Compos. Part B Eng.* **2024**, *272*, 111219. [CrossRef]
39. Yang, L.; Zhou, Q.; Chen, R.; Xu, J. High thermal conductive polyurethane composite films with a three-dimensional boron nitride network in-situ constructed by multi-folding and multi-laminating. *Compos. Sci. Technol.* **2024**, *245*, 110326. [CrossRef]

40. Liu, J.; Wang, Y.; Zhang, Q.; Zhang, H. A Full-component recyclable Epoxy/BN thermal interface material with anisotropy high thermal conductivity and interface adaptability. *Chem. Eng. J.* **2023**, *469*, 143963. [CrossRef]
41. Geng, Y.; He, H.; Jia, Y.; Peng, X.; Li, Y. Enhanced through-plane thermal conductivity of polyamide 6 composites with vertical alignment of boron nitride achieved by fused deposition modeling. *Polym. Compos.* **2019**, *40*, 3375–3382. [CrossRef]
42. Yue, Y.; Liu, C.; Zhao, Q.; Huang, J. Highly Thermally Conductive Super-Aligned Boron Nitride Nanotube Films for Flexible Electronics Thermal Management. *ACS Appl. Mater. Interfaces* **2024**, *16*, 33971–33980. [CrossRef] [PubMed]
43. Yang, K.; Zhang, X.; Wang, B.; Li, J. Vertically Aligned Boron Nitride Nanosheets Films for Superior Electronic Cooling. *ACS Appl. Mater. Interfaces* **2023**, *15*, 28536–28545. [CrossRef] [PubMed]
44. Yuan, C.; Zhang, Y.; Liu, X.; Li, D. Thermal Conductivity of Polymer-Based Composites with Magnetic Aligned Hexagonal Boron Nitride Platelets. *ACS Appl. Mater. Interfaces* **2015**, *7*, 13000–13006. [CrossRef]
45. Lee, S.; Kim, J.; Choi, H.; Park, J. Vertically-aligned boron nitride composite as a highly thermally conductive material using magnetic field-assisted three-dimensional printing. *Ceram. Int.* **2023**, *49*, 7050–7056. [CrossRef]
46. Tang, B.; Sun, Y.; Zhang, S.; Wang, X. Synthesis of KH550-Modified Hexagonal Boron Nitride Nanofillers for Improving Thermal Conductivity of Epoxy Nanocomposites. *Polymers* **2023**, *15*, 1415. [CrossRef]
47. Wang, Y.; Chen, J.; Liu, H.; Zhang, M. Silane coupling agent and carboxymethyl chitosan co-modified boron nitride for preparing silicone acrylic emulsion-based flame-retarding coatings. *J. Appl. Polym. Sci.* **2023**, *140*, e54286. [CrossRef]
48. Farahani, A.; Jamshidi, M.; Foroutan, M. Effects of functionalization and silane modification of hexagonal boron nitride on thermal/mechanical/morphological properties of silicon rubber nanocomposite. *Sci. Rep.* **2023**, *13*, 11915. [CrossRef] [PubMed]
49. Liu, M.; Zhang, T.; Wang, Y.; Chen, R. Effect of functionalization on thermal conductivity of hexagonal boron nitride/epoxy composites. *Int. J. Heat Mass Transf.* **2024**, *219*, 124844. [CrossRef]
50. Shuilai Qiu, S.; Wu, H.; Chu, F.; Song, L. Boron nitride silicone rubber composite foam with low dielectric and high thermal conductivity. *Chin. J. Chem. Eng.* **2024**, *68*, 224–230. [CrossRef]
51. Condalign, A.S. Anisotropic Conducting Body and Method for Manufacture, EP2446721B1. Available online: https://patents.google.com/patent/EP2446721B1/en (accessed on 5 June 2024).
52. Available online: https://www.arrow.com/en/products/a000073/arduino-corporation (accessed on 5 June 2024).
53. IEC60250: Dielectric Constant and Dissipation Factor. Available online: https://plastics.ulprospector.com/properties/IEC60250 (accessed on 5 June 2024).
54. Niu, B.; Zhang, Z.; Liu, Y.; Wang, H. Reducing high-temperature dielectric loss of h-BN ceramics by orienting grains. *Scr. Mater.* **2023**, *223*, 115098. [CrossRef]
55. Danilov, E.; Ivanov, S.; Petrov, A.; Sokolov, V. Excellent Thermal and Dielectric Properties of Hexagonal Boron Nitride/Phenolic Resin Bulk Composite Material for Heatsink Applications. *J. Compos. Sci.* **2023**, *7*, 291. [CrossRef]
56. Qiu, L.; Wu, S.; Li, X.; Zhang, H. Thermal transport barrier in carbon nanotube array nano-thermal interface materials. *Carbon* **2017**, *120*, 128–136. [CrossRef]
57. Peng, F.; Zhu, Y.; Zhao, Y.; Li, R. Smart polymer composites with vertically oriented boron nitride and carbon fiber for heat management: Magneto-thermal responsiveness. *Compos. Part B Eng.* **2024**, *283*, 111617. [CrossRef]
58. Xie, J.; Li, P.; Wang, H.; Zhang, X. Spherical boron nitride/pitch-based carbon fiber/silicone rubber composites for high thermal conductivity and excellent electromagnetic interference shielding performance. *Appl. Polym. Sci.* **2022**, *139*, e52734. [CrossRef]
59. Bashir, A.; Shah, A.; Liu, Y.; Anis, R. A Novel Thermal Interface Material Composed of Vertically Aligned Boron Nitride and Graphite Films for Ultrahigh Through-Plane Thermal Conductivity. *Small Methods* **2024**, *8*, 2301788. [CrossRef] [PubMed]
60. Wang, J.; Zhou, H.; Yu, Q.; Chen, L. Magnetically Oriented 3D-Boron Nitride Nanobars Enable Efficient Heat Dissipation for 3D-Integrated Power Packaging. *ACS Appl. Nano Mater.* **2023**, *6*, 18508–18517. [CrossRef]
61. Yang, W.; Zhao, Y.; Mi, W.; Shi, J. Improving the thermal conductivity of an epoxy composite with chemically boron nitride-grafted carbon fiber. *Compos. Part A-Appl. Sci. Manuf.* **2024**, *182*, 108192. [CrossRef]
62. Zheng, X.R.; Liu, M.; Yang, H.; Wang, X. Enhancement of thermal conductivity of carbon fiber-reinforced polymer composite with copper and boron nitride particles. *Compos. Part A-Appl. Sci. Manuf.* **2019**, *121*, 449–456. [CrossRef]
63. Wu, Y.H.; Li, J.P.; Chen, L.Y.; Liu, H. Synthesis of multicomponent boron nitride/carbon nanotube conjugated hybrid composite nanosol aqueous sizing agent to improve mechanical properties and thermal conductivity of carbon fiber composites. *Polym. Compos.* **2024**, *45*, 15954. [CrossRef]
64. Uzai, C. Studies on mechanical and thermal properties of cubic boron nitride (c-BN) nanoparticle filled carbon fiber reinforced polymer composites. *Polym.-Plast. Technol. Mater.* **2022**, *61*, 1439–1455. [CrossRef]

65. Global Thermal Interface Materials Market Overview. Available online: https://www.marketresearchfuture.com/reports/thermal-interface-materials-market-3135?utm_term=&utm_campaign=&utm_source=adwords&utm_medium=ppc&hsa_acc=2893753364&hsa_cam=20373674291&hsa_grp=150985931723&hsa_ad=665909881832&hsa_src=g&hsa_tgt=dsa-2089395962584&hsa_kw=&hsa_mt=&hsa_net=adwords&hsa_ver=3&gad_source=1https://www.google.com/search?q=thermally+management+materials++materials+market&sca_esv=bb0627a757e7aa61&ei=flZDZ6vyIcjui-gPxKObyQw&ved=0ahUKEwirqbL0s_WJAxVI9wIHHcTRJskQ4dUDCBA&uact=5&oq=thermally+management+materials++materials+market&gs_lp=Egxnd3Mtd2l6LXNlcnAiMHRoZXJtYWxseSBtYW5hZ2VtZW50IG1hdGVyaWFscyAgbWF0ZXJpYWxzIG1hcmtldDIIEAAYgAQYogRI-x5QtwRYnhtwAXgAkAEAmAHHAaAB5hOqAQQxLjIwuAEDyAEA-AEBmAIKoAKeCMICCxAAGIAEGLADGKIEwgILEAAYsAMYogQYiQXCAggQIRigARjDBMICChAhGKABGMMEGArCAggQABgFGA0YHsICCxAAGIAEGIYDGIoFwgIIEAAYogQYiQWYAwCIBgGQBgSSBwMyLjigB8NM&sclient=gws-wiz-serp (accessed on 5 June 2024).
66. Sun, Z.; Wang, L.; Zhang, Y.; Li, X. Application and Development of Smart Thermally Conductive Fiber Materials. *Nanomaterials* **2024**, *14*, 154. [CrossRef] [PubMed]
67. Luo, W.; Zhao, Y.; Liu, X.; Chen, J. Control of alignment of h-BN in polyetherimide composite by magnetic field and enhancement of its thermal conductivity. *J. Alloys Compd.* **2022**, *912*, 165248. [CrossRef]
68. Kim, K.; Kim, J. Vertical filler alignment of boron nitride/epoxy composite for thermal conductivity enhancement via external magnetic field. *Int. J. Therm. Sci.* **2016**, *100*, 29–36. [CrossRef]
69. Lin, H.; Chen, Q.; Yang, Y.; Wu, X. Thermally Conductive Polydimethylsiloxane-Based Composite with Vertically Aligned Hexagonal Boron Nitride. *Polymers* **2024**, *16*, 3126. [CrossRef] [PubMed]

sustainability

MDPI

Article

Sustainability of the Technology for Obtaining Thermoplastic Building Materials from Non-Recyclable Mixed Plastic–Paper Packaging Waste

Romeo C. Ciobanu [1], Cristina Schreiner [1,*], Alina R. Caramitu [2], Sebastian Aradoaei [1] and Mihaela Aradoaei [1]

[1] Department of Electrical Measurements and Materials, Gheorghe Asachi Technical University, 700050 Iasi, Romania; r.c.ciobanu@tuiasi.ro (R.C.C.); arsete@tuiasi.ro (S.A.); mosneagum@yahoo.com (M.A.)
[2] National Institute for Research and Development in Electrical Engineering ICPE-CA Bucharest, 030138 Bucharest, Romania; alina.caramitu@icpe-ca.ro
* Correspondence: cschrein@tuiasi.ro

Abstract: This paper describes the process used to produce thermoplastic building materials from non-recyclable mixed plastic–paper packaging waste. A first step was dedicated to an innovative and sustainable sterilization technology for non-recyclable waste, based on exposure to microwave radiation in closed air-circulation ovens. Further, composites with different cellulose contents and with two polymer matrices, respectively, were obtained using an injection process, and the samples were subjected to mechanical and physical tests. Due to their superior features, the products based on mixed polypropylene–paper packaging waste may successfully replace the classic polyvinylchloride-based wood–plastic composites. The environmental impact of mixed plastic–paper packaging waste was analyzed, and the sustainability of the thermoplastic technology was demonstrated from an economic and environmental point of view.

Keywords: thermoplastic building materials; mixed plastic–paper packaging; non-recyclable waste; environmental impact indicators; sustainability analysis

Citation: Ciobanu, R.C.; Schreiner, C.; Caramitu, A.R.; Aradoaei, S.; Aradoaei, M. Sustainability of the Technology for Obtaining Thermoplastic Building Materials from Non-Recyclable Mixed Plastic–Paper Packaging Waste. *Sustainability* **2024**, *16*, 3430. https://doi.org/10.3390/su16083430

Academic Editors: Moussa Leblouba, Balaji PS, Muhammad Rahman, Brabha Nagaratnam, Keerthan Poologanathan and Antonio Caggiano

Received: 19 March 2024
Revised: 15 April 2024
Accepted: 17 April 2024
Published: 19 April 2024

1. Introduction

The packaging industry is an essential part of the global economy. The new packaging manufacturing technologies, which confer special properties to packaging, have led to an explosive growth in packaging for specific fields in the food industry, cosmetics, pharmaceuticals, electronics, consumer goods, etc. The packaging market size was valued at USD 1105.6 billion in 2022. The packaging materials industry is projected to grow to USD 1519.97 billion by 2032, exhibiting a CAGR of 3.60% during the forecast period [1]. Unfortunately, a study from 2020 [2] indicated that about 32% of packaging is unsuitable for recycling using actual classical recycling technologies, being either multi-layered and/or mixed plastic–paper packaging. The extensive use of mixed paper and plastic packaging is due to its versatility, as it can be adapted in terms of functional properties to satisfy technical and economic efficiency criteria specific to the use of the individual product. The need for combining plastic and paper within packaging, regardless of the nature and chemical composition of the constituent materials or the field of use of such packaging, lies in the fact that, without exception, they satisfy five important functions [3]: a protective function—the prevention of mechanical damage to the product during distribution (storage, handling, and transport); an isolation function—imposed by the physical form and nature of the product; a conservation function—the prevention or inhibition of changes produced under the action of physical, chemical or biological factors (barrier function against liquids—grease, water etc., gases, UV/light radiation, bacteria/fungus/rodents, etc.); an information function—the transmission of information about the product (legal regulations, composition, instructions for use, expiration date, etc.); and finally, an advertising function—the promotion of products/goods through the generation of a visual impact (packaging with good printing properties).

The main types of non-recyclable combined plastic and paper waste are: wrapping papers, made of laminated/cased paper with films and foils of plastic materials; packaging boxes for different liquids; disposable paper cups for hot or cold drinks; disposable paper plates; containers for frozen food products; photos; and generally water-resistant papers etc. Some of these are included in Group 5 of the special assortments of the European Union classification EN643 [4]: 5.03—cardboard for packaging liquids after use, including cardboard covered with polyethylene, containing at least 50% fiber, while the remainder can be derived from different coatings; and 5.04—craft paper for wrapping, after use, which can be coated with polymers (film or spray), or laminated, but must not contain bitumen or waxy coatings. In the context of a heightened concern for waste management, in which reuse and recycling are the first options in the treatment hierarchy, as described in Waste Framework Directive—WFD 2008/98/EC [5], theoretically, plastic and paper packaging present important advantages because they are obtained from renewable raw materials and are partially biodegradable, so they may be recovered for recycling. Unfortunately, the actual use of non-recyclable mixed plastic–paper (MPP) packaging waste is for incineration for energy recovery because its recycling is not economically beneficial.

The classical collection of the non-recyclable MPP packaging waste comprises mixed collection with household waste, which is the simplest collection system, but this collection method limits the possibilities for further recycling and waste treatment. Additionally, recyclables sorted from household waste can be dirty, wet, or contaminated with dangerous bacteria, which makes them difficult to further process or reuse. Following automatic bacterial identification analyses of four samples of plastic–paper mailing envelopes (a classical packaging which is easy to identified), the presence of pathogenic microorganisms was determined as follows: in sample 1: Enterococcus amnigenus and Eschecrichia coli, bacteria of fecal origin, were identified, indicating that the sample was collected from a highly anthropogenically contaminated location; in sample 2: Enterococcus casseliflavus, Chryseobacterium gambrini, and Escherichia coli were identified, indicating both fecal contamination of the sampling source and contact with yeasts or fermentative substrates; in sample 3: Pediococcus acidilactici and Psychrobacillus psychrotolerans, along with representatives of the Streptococcaceae family, were detected, activated by the waste from biotechnologies or the food industry (as an example, Pediococcus acidilactici is described as a human pathogen that can cause septicemia, liver abscesses, and bacteremia [6]); in sample 4: Psychrobacillus psychrotolerans, Chryseobacterium caini, bacteria from the genus Bacillus, and Salmonella enterica, microorganisms that indicate the high level of contamination with fecal matter and fermentative representatives of biofilms, were identified. It must be noted that the presence of bacteria from the genus Bacillus (Bacillus acidiceler and Bacillus subtilis) in sample 4 casts doubt on the efficiency of the use of classical chemical or thermal processes for sterilization/decontamination, some of them even destroying the initial plastic structure [7–9]. In conclusion, any technological process aimed at recycling MPP packaging waste towards innovative products must be based on and initiated with an efficient mixed drying/sterilization process other than the current classical energy consuming and/or destructive methods. The authors have developed a sustainable sterilization technology for non-recyclable MPP packaging waste obtained either from household bins or municipal waste landfills, which will be presented in this paper.

Based on treated raw material from recyclable MPP packaging waste, the authors developed a technology for obtaining thermoplastic building materials, which is similar to the classical technology used for wood-plastic composites (WPC). The WPC technology uses also cellulose-derived materials, but in a primary form, i.e., wood fibers, or wood flour, and thermoplastic matrices such as polyethylene, polypropylene, or polyvinylchloride, etc., which can be also obtained from recycled sources [10–12].

An advantage of using MPP packaging for defining composite technologies is related to their preliminary polyethylene and/or polypropylene content, which can be further supplemented with similar matrices from recycled sources. The use of cellulosic fibers recovered from waste paper in the manufacture of such composites is considered very advantageous, suggested by the strength properties that can be substantially improved by substituting, e.g., wood flour, used in the case of WPC compositions. WPCs products exhibit a growing market and various potential applications, i.e., a value of USD 7.5 billion in 2023, projected to grow to USD 11.9 billion by 2028, exhibiting a CAGR of 9.80% during the forecast period [13].

In general, WPCs are obtained with a wood flour usage weight of up to 50%. The analysis of the composition of the MPP packaging demonstrated values of up to 80% of paper/cellulose fibers and a percentage of about 20% of polyethylene and/or polypropylene. In this situation, a technology similar to WPCs technology can be developed by: 1. preparing the MPP packaging waste as a raw material containing a high percentage of cellulose (this must be performed after drying and sterilization using a specialized drying technology), and 2. correcting the recipe until a cellulose content of up to 50% is reached by adding, e.g., polyethylene and/or polypropylene pellets obtained from recycled sources related to the recycling of other plastic packaging types.

2. Sustainable Sterilization of Non-Recyclable Mixed Plastic–Paper Packaging Waste

The authors have developed an innovative and sustainable sterilization technology for non-recyclable MPP packaging waste based on exposure to microwave radiation in closed air-circulation ovens. Various samples of MPP packaging waste were collected directly from a municipal waste landfill, with a tested minimum humidity of 70%. The samples were subjected to a combined drying-sterilization process, carried out until the cellulosic material presented a minimal residual humidity. It must be noted that the classical cellulose products used for, e.g., printing purposes, normally present a residual humidity of approximately 8% to ensure the optimal intrinsic properties of the paper, but for other uses, such as classical packaging boxes, it may be higher [14]. The exposure to microwave radiation was performed at several power stages between 200–1200 × 10^3 W/kg and at preselected durations of up to 10 min, but only the most relevant results are presented (with lower power vs. lower exposure time). For the analysis of sterility control, four samples of MPP waste were subjected to different microwave exposures, starting from a reference sample with about 74% humidity before the application of the microwave treatment. The results are presented as experiments Exp1–Exp 4, with data related to exposure time and the efficiency of the technological variants, Table 1.

Table 1. Technological variants of microwave sterilization.

Exp 1			**Exp 2**			**Exp 3**			**Exp 4**		
Power (10^3 W/kg)	**Time (min)**	**Weight (g)**	**Power (10^3 W/kg)**	**Time (min)**	**Weight (g)**	**Power (10^3 W/kg)**	**Time (min)**	**Weight (g)**	**Power (10^3 W/kg)**	**Time (min)**	**Weight (g)**
400	0	0.986	400	0	0.994	800	0	0.997	800	0	1.014
	1	0.397		3	0.270		0.5	0.380		1	0.321
Mass loss		61%	Mass loss		73%	Mass loss		62%	Mass loss		68%
Residual humidity		14%	Residual humidity		2%	Residual humidity		12%	Residual humidity		6%

It can be noted that the driest sample is obtained at 400 × 10^3 W/kg over a duration of 3 min, because the residual humidity reached 2%, less than that in other experiments. Similar results can be obtained in the case of exposure to 800 × 10^3 W/kg during a duration of time slightly exceeding 1 min. The use of higher energy or longer exposure periods is needed to assure an efficient sterilization because, as it can be observed, only a minimal exposure at a lower microwave power would be enough to assure a reasonable drying of the waste to approximately 10% humidity, in which case, only a drying process would be achieved.

A concurrent experiment was performed to assess the sterilization efficacy of the composite plastic–paper waste subsequent to microwave treatment, achieved by inoculating the reference sample with about 74% humidity in a growth medium. This method involved utilizing culture media. To verify the efficacy of the sterilization procedures, both chemical and biological indicators, such as Bacillus stearothermophilus, were employed. After the designated incubation period, turbidity became evident, indicating the presence of microorganisms. The determination of the total colony was achieved following the guidelines outlined in SR EN ISO 6222:2004 (adapted from [15]). Consequently, 1 mL of suspension and 1 mL of each sequential dilution (1/10, 1/100, and 1/1000) were inoculated from every turbid vial onto Petri plates coated with 15–20 mL of yeast extract agar medium, which were then preheated and cooled to 45 ± 1 °C. The colonies on each plate were enumerated, and the colony-forming units (CFU) were determined, taking into account the dilution factor. The aggregate count of colonies grown at 37 °C for the reference samples ranged from 7865 to 8230 CFU/mL.

In interpreting the results, sterilization efficiency is defined as the proportion of bacteria eliminated due to microwave exposure, relative to the total number of bacteria identified within each unexposed sample. The intricate bacterial automated detection system comprised an incubator/reader interfaced with computerized software. Upon insertion, the plates underwent a 22 h incubation period at 33 °C and were automatically scanned using a micro camera. The sterilization efficiency values for the four samples treated with microwaves were determined as follows: Exp. 1–16.6%; Exp. 2–25.5%; Exp. 3–31.6%; Exp. 4–42.9%, with the entire process being described in Ref. [16].

It is observed that the sterilization effectiveness increases with the duration of microwave exposure, but a much greater efficacy is observed at higher energy levels. For 400×10^3 W/kg, by increasing the exposure time from 1 min to 3 min, the sterilization efficacy increases by over 50%. By increasing the exposure power form 400×10^3 W/kg to 800×10^3 W/kg, after 1 mi of exposure, the sterilization efficacy increases by about 160%. In fact, in reality, the efficiency is expected to be much higher because the collateral drying of waste accelerates the sterilization process, an effect that cannot be achieved using the standardized method described above.

3. Technology for Obtaining Composite Materials from Non-Recyclable Mixed Plastic–Paper Packaging Waste

3.1. Materials and Preparation Methods

The MPP packaging waste was processed by dry grinding/milling in two stages, yielding a mixed powder with final dimensions under 1 mm, by use of a high efficiency plastic shredder machine (Henan Gomine Industrial Technology Co., Zhengzhou, China) and a pulverizer–milling machine (Jiangsu Xinhe Intelligent Equipment Co., Ltd., Taizhou, China).

The PP/HDPE waste may be processed either by grinding in one stage to yield mixed flakes with dimensions under 3 mm, as described above, using a plastic shredder machine (Henan Gomine, China), or alternatively, by using preprocessed pellets from PP/HDPE waste with dimension of 2–3 mm, obtained from third parties. In this paper, we used only in-house-made raw materials as mixtures of ground plastic waste and MPP packaging waste, obtained by grinding the waste to form of flakes with dimensions under 3 mm and powder with dimensions under 1 mm.

In order to define the composite structures, the following sample codes were used:

- Materials collected as MPP packaging waste (from unselective collecting):

P1—paper envelopes with a plastic window inside (contains high density polyethylene), containing about 95% paper;

P2—large boxes with plastic applied externally (contains low density polyethylene), containing about 85% paper/board;

P3—blend of MPP packaging (contains mixtures of polypropylene and polyethylene), containing about 80% cellulose derived materials.

- Raw materials as mixtures of ground plastic waste and MPP packaging waste (raw materials prepared for thermoplastic process):

P4—ground high-density polyethylene (HDPE) waste, with 25% MPP packaging waste (containing about 20% cellulose derived materials), as powder;

P5—ground polypropylene (PP) waste, with 25% MPP packaging waste (containing about 20% cellulose derived materials), as powder.

- Thermoplastic composites obtained by injection:

P6—composite material derived from the injection of HDPE waste and 25% MPP packaging waste (containing about 20% cellulose derived materials);

P7—composite material derived from the injection of HDPE waste and 40% MPP packaging waste (containing about 32% cellulose derived materials);

P8—composite material derived from the injection of PP waste and 25% MPP packaging waste (containing about 20% cellulose derived materials);

P9—composite material derived from the injection of PP waste and 40% MPP packaging waste (containing about 32% cellulose derived materials).

Before the injection process, the mixed flakes and powder, in different proportions, were subjected to specialized equipment (Ningbo Lvhua Rubber & Plastic Machinery Industry, Yuyao, China) for final dehumidification, homogenization, and thermal pre-compatibilization with various additives, mainly dispersion additives and anchoring additives for the polymers to create interfacial bonds between the hydrophobic matrix and the cellulose-derived powder in order to improve the mechanical properties (composite stabilizer: HL-604 (Jiaxu Development Industrial Co., Beijing, China), 3%; azodicarbonamide blowing agent: AC7000 (WSD Chemical, Shengzhou, China), 1.2%; foam regulator: ZB-530 (Zibo Hailan Chemical Co., Zibo, Shandong, China), 0.5%; modifier/coupling agent: Jiaxu Development Co. stabilizer, 0.4% and lead stearate, 0.2%).

The injection of composites from flakes was conducted using a Dr. Boy 35A injection molding machine from Germany, featuring the following specifications: a screw diameter of 28 mm, an L/D ratio of 18.6 mm, an injection capacity of 58.5 cm^3 (calculated), a maximum material pressure of 2200 bar, and a minimum real injection capacity of 500 mm. Considering the nature of the polymer matrices (polyethylene and polypropylene, respectively), the following operating parameters were selected: pressure: 550 bars; subsequent pressure: 1000 bars; back pressure: 90 bars; mold temperature: 15–20 °C. The interface of the injection machine utilized for producing composite materials and the temperature regime across the cylinder areas of the injection machine, progressively adapted for each type of polymer matrix for finally obtaining the optimal parameters of the process, are briefly presented in Figure 1 and Table 2. The injection process is ideal for generating standard samples of composites for the mechanical and physical tests.

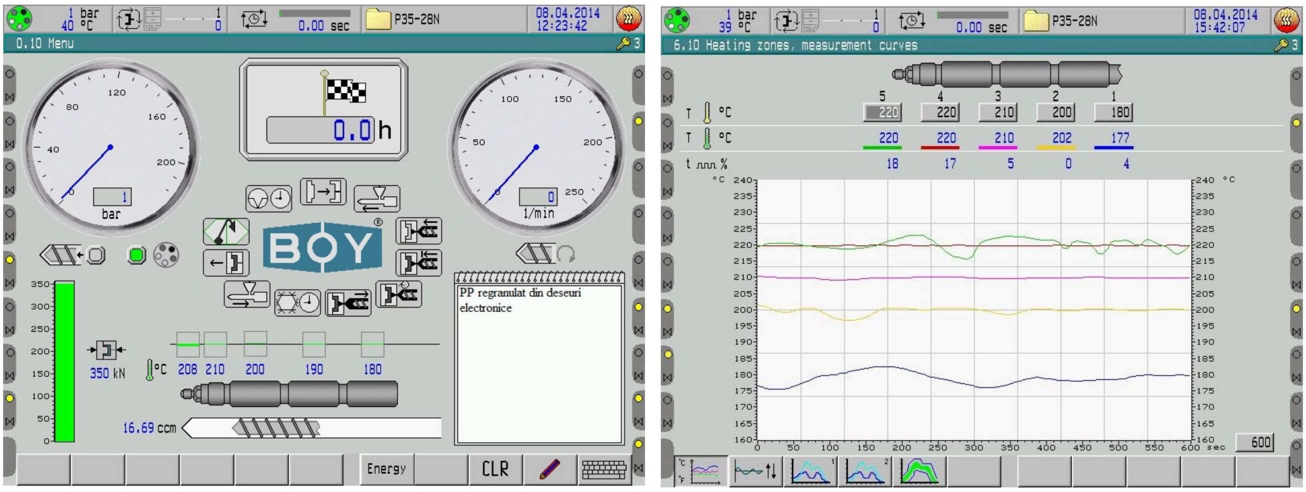

Figure 1. The interface with thermal diagrams of the injection machine.

Table 2. Optimal temperatures of the five heating zones of the injection machine cylinder.

Zone	5	4	3	2	1
HDPE (°C)	200	190	180	172	162
PP (°C)	220	210	201	192	178

3.2. Characterization Equipment

- Optical scanning microscopy SEM was performed with a field emission and focused ion beam scanning electron microscope (SEM), model Tescan Lyra III XMU (Libušina tř. 21 623 00, Brno-Kohoutovice, Czech Republic).
- The hydrostatic density is determined utilizing the XS204 Analytical Balance, characterized by the following specifications: maximum capacity of 220 g, precision of 0.1 mg, linearity of 0.2 mg, internal calibration, equipped with a density kit for solids and liquids, and an RS 232 interface. The measurements were conducted at a temperature of 25 °C.
- Shore hardness measurements were performed with a common Shore "D" digital durometer.
- The equipment for determining the mechanical features was a specialized PC-controlled universal tensile testing machine (Qiantong, Changshu, China), with nominal force: min. 20 kN, allowing measurement of tensile strength and elongation.
- The LFA 447 Nanoflash apparatus (Netzsch, Selb, Germany) was employed to quantify thermal conductivity and thermal diffusivity, as described in [17]. A potent xenon lamp served as the radiation energy source, with an irradiation time of 0.18 ms on the sample's front face. Each temperature was analyzed three times. The rise in temperature on the opposite surface of the sample was gauged using an InSb-type infrared (IR) detector. Thermal diffusivity, a thermophysical characteristic delineating the velocity of heat transmission via conduction during temporal temperature fluctuations, was determined. Greater thermal diffusivity in a material denotes accelerated heat propagation. The methodology and mathematical model of thermal analysis are taken from Ref. [18].
- The swelling capacity is assessed based on the volume of liquid that the material can uptake upon immersion. In this study, water and toluene were selected as the liquid swelling agents. Methodology: 1. Around 1 g of the composite material was weighed and deposited into plastic ampoules; two sample groups were arranged: one designated for evaluating the extent of swelling in water and the other in a solvent, here toluene; 2. The vials containing the material were filled with double-distilled water and solvent (toluene), respectively, and then held for variable durations (up to 576 h)

at ambient temperature [19]. The subsequent equation was employed to ascertain the extent of swelling:

$$Q = \frac{X_2 - X_1}{X_1} \times 100 \quad (1)$$

where: Q—the degree of swelling; X_2—the mass of the swollen material; X_1—the mass of the dry material.

- The metal content in the leachates was assessed using an inductively coupled plasma mass spectrometer (ICP-MS 7900, Agilent Technologies, Santa Clara, CA, USA). Sulfate and chloride anion concentrations were determined by employing a Dionex ICS-3000 ion chromatograph (Dionex, Sunnyvale, CA, USA.) equipped with an AG23 Dionex column and suppressed conductivity detection. Dissolved organic carbon (DOC) levels were analyzed using a nitrogen/carbon analyzer (N/C 3100, Analytik Jena, Jena, Germany).

3.3. Results and Discussion

3.3.1. SEM Analysis

The magnitude of 1000× was chosen to analyze the composites structure, being correlated to the theoretical dimension of cellulose-derived fibers from the milling process.

Figure 2a,b emphasizes the cellulose fiber transformation from packaging towards ground raw material. In larger boxes made of cardboard, P2, the fibers are larger compared to those in the paper in the envelopes, P1. This difference is not as obvious after the grinding of the mixed cellulose packaging, but the ground plastic seems different, i.e., the polyethylene looks more acicular, P4, and polypropylene appears spheroidal, P5, Figure 2c,d.

Figure 2e–h shows that the injected samples with both matrices present a homogeneous structure, with the paper particles/cellulose fibers uniformly distributed and well embedded within the polymer matrix. Clearer images for the cellulose fibers, which seem to be a bit scattered, is observed where the fibers content is higher, i.e., for P8 and P9, Figure 2g,h. The imprint of the injection mold (inclined stripes) can also be noted.

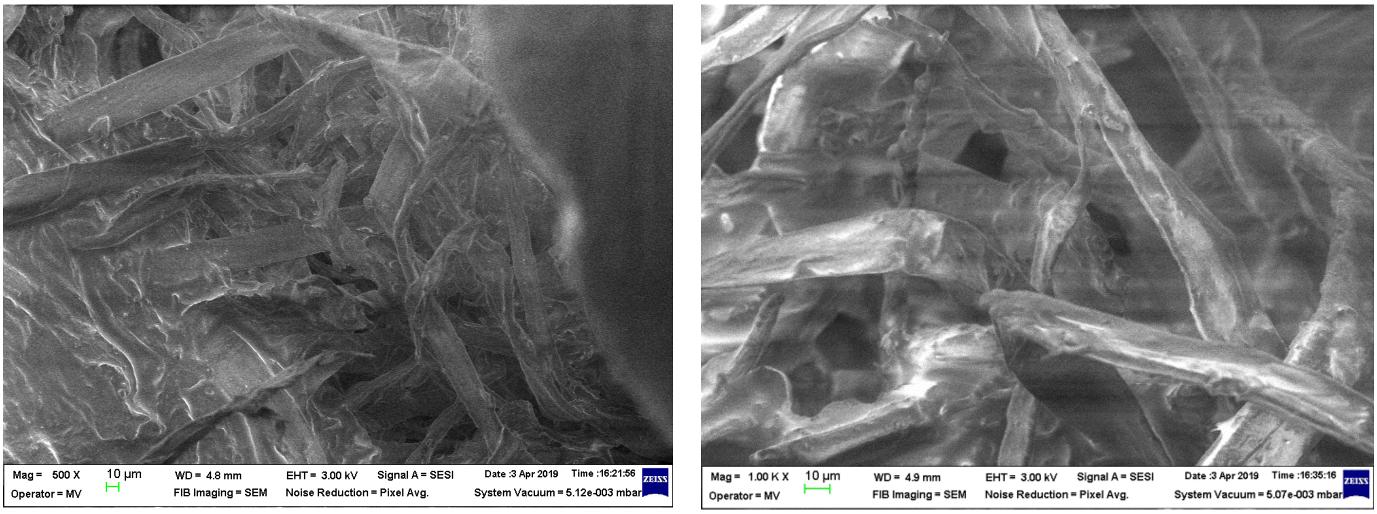

(**a**) (**b**)

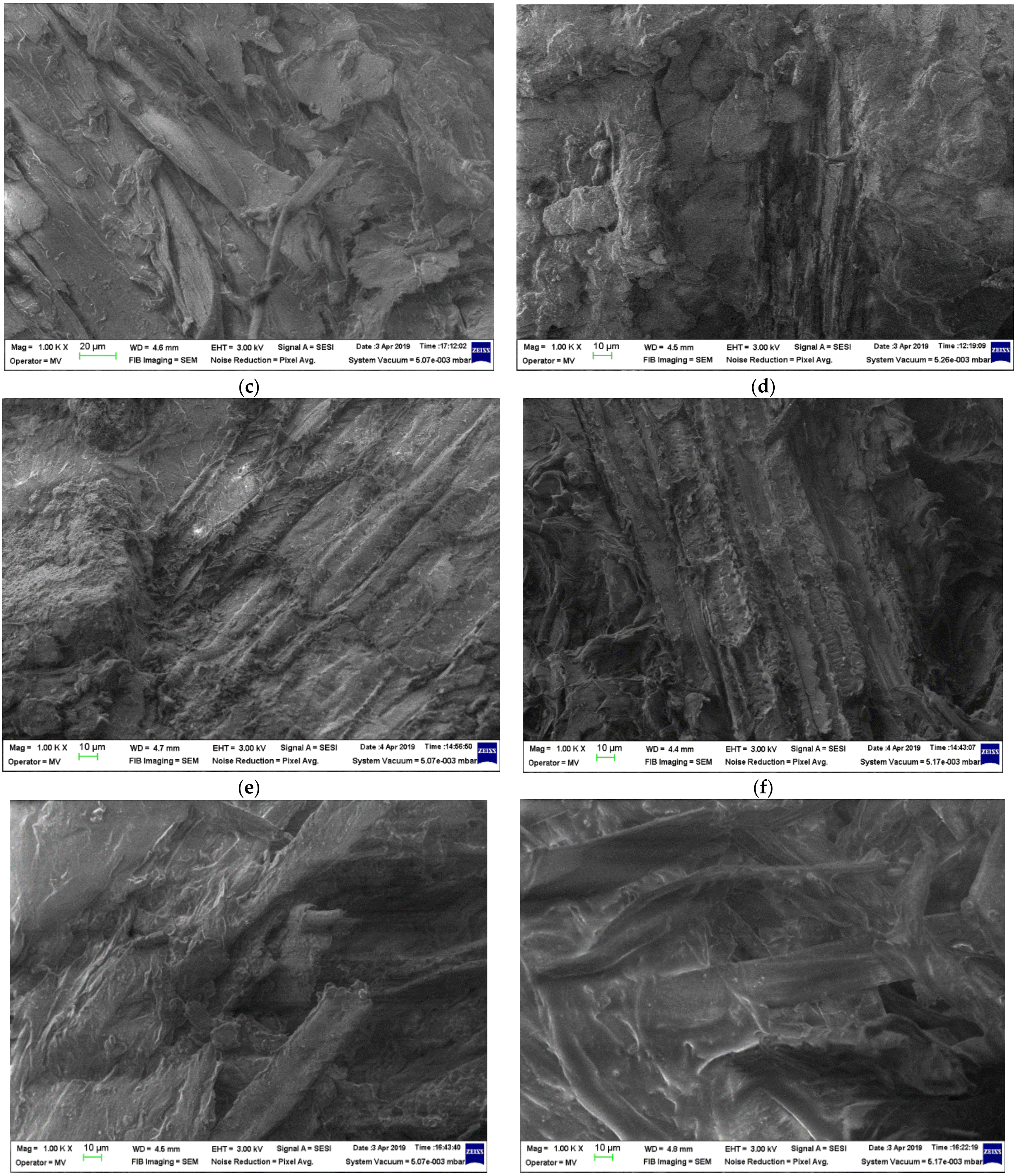

(**c**) (**d**)

(**e**) (**f**)

(**g**) (**h**)

Figure 2. SEM images of samples: (**a**). P1, (**b**). P2, (**c**). P4, (**d**). P5, (**e**). P6, (**f**). P7, (**g**). P8, and (**h**). P9.

3.3.2. Evaluation of Hydrostatic Density

The results are presented in Table 3. A lower density of composites with polypropylene compared with the composites with polyethylene was noticed, mainly due to the lower density of the polypropylene matrix. A higher content of cellulose in the composites leads to a slightly higher value for hydrostatic density, for both polymer matrices. The data are in line with those for similar characteristics of classical WPC, as in Refs. [20,21].

Table 3. Hydrostatic density values.

Sample	Hydrostatic Density [g/cm^3]
P6	0.955
P7	0.964
P8	0.925
P9	0.940

3.3.3. Evaluation of Mechanical Characteristics

Shore hardness and mechanical characteristics are presented as the average of six measurements, Table 4, and exhibit higher values for the polypropylene composites compared to those of the polyethylene composites. A higher content of cellulose in the composites leads to a slightly higher value for the mechanical characteristics, for both polymer matrices. On the other hand, it was noticed that the mechanical characteristics are clearly better when compared to those of similar wood–plastic or paper–plastic composites [20–24], an effect explained by a more fine preparation of cellulose fibers obtained from mixed paper–plastic waste, especially in a dry state, accelerating paper defibration and generating fibers with about 1 mm length, finally leading to a more homogeneous structure of the composites.

Table 4. Mechanical characteristics of composites.

Sample	Cellulose Content [%]	SHORE Hardness [MPa]	Tensile Strength [MPa]
P6	20	68	33.7
P7	32	69	37.2
P8	20	74	40.5
P9	32	73	43.3

3.3.4. Evaluation of Thermal Features

The results are presented in Table 5. For building purposes, the thermal conductivity usually needs to be lower, so that the absorption and release of heat is synchronized with the building's heating and cooling cycle. In our case, the increase in the cellulose content leads to a lower thermal insulation. By using cellulose derived for MPP packaging, the thermal features of the composites are about 10% superior to the homologue data for commercial WPC [10,25,26]. On the other hand, the composites based on polyethylene present superior thermal characteristics compared to the those from the polypropylene matrix. It is known that WPC based on the polyvinylchloride matrix present better thermal features compared to those of WPC based on polypropylene matrix, but recently, the production and use of polyvinylchloride-based products has been restricted due to their environmental impacts. Taking into account that the composites corresponding to P6–P7 samples, based on the polypropylene matrix, present similar features to those of WPC based on the polyvinylchloride matrix, the technology proposed in this paper, based on the polypropylene matrix, may successfully replace the polyvinylchloride-based WPC.

Table 5. Thermal conductivity of composites.

Sample	Thermal Conductivity [W/(m × K)]
P6	0.254
P7	0.297
P8	0.288
P9	0.311

3.3.5. Determination of the Degree of Swelling in Water and Solvent

Due to the high content of cellulose fibers in the materials, the degree of swelling in water represents an important parameter, which can be further related to the environmental stability and reliability of the products based on such materials. The experimental results obtained at the laboratory level are presented in Figure 3 and Table 6, with all samples P1–P9 being investigated. In regards to the degree of swelling in a solvent, only the injected composites samples were considered, i.e., P6–P9, and at a shorter time period of 24 h due to less technical exposure to such conditions in engineering practice, Table 7. With a confidence level of 95%, the degree of swelling was computed as the mean of five measurements conducted on five distinct samples, excluding any outlying values. Based on the experimental findings, the degree of swelling in water is much larger for raw materials with a larger quantity of cellulose, reaching about 70% after approximately 500 h, e.g., for P2 and P3. Regarding the sample made by injection-molding, the fibers are more compact, and the degree of swelling in water is about 20% after 500 h. The samples with polypropylene present a lower swelling behavior in water. The increasing of the cellulose content in the injected samples minimally increase the value of the extent of water absorption, e.g., P6 compared with P7, or P8 compared with P9 (an increase of 60% of cellulose in the samples leads to only a 10% increase in the extent of swelling in water). Thus, after an exposure of over 500 h, the degree of swelling in water reaches saturation for all analyzed samples.

Table 6. Degree of swelling in water.

Sample	Q_{H2O} [%]						
	72 h	**168 h**	**240 h**	**336 h**	**408 h**	**504 h**	**576 h**
P1	12.26	18.76	29.33	40.13	50.599	60.72	60.85
P2	11.44	26.22	38.52	45.34	57.97	69.47	69.78
P3	9.44	25.24	37.88	44.22	56.68	68.37	68.37
P4	8.54	12.29	17.16	25.73	30.22	38.38	37.50
P5	7.43	11.36	18.09	24.94	31.65	37.37	37.59
P6	4.02	7.01	11.64	14.19	18.64	20.98	20.98
P7	4.13	9.56	14.75	15.92	19.52	23.67	23.77
P8	3.15	6.13	9.34	13.22	16.39	19.99	19.99
P9	3.12	8.38	12.62	14.62	18.84	22.72	22.78

Table 7. Degree of swelling in water and solvents, at 24 h.

Sample	Q_{H2O} [%]	$Q_{solv.}$ [%]
	24 h	**24 h**
P6	2.74	3.30
P7	3.13	7.51
P8	2.26	5.69
P9	2.65	9.34

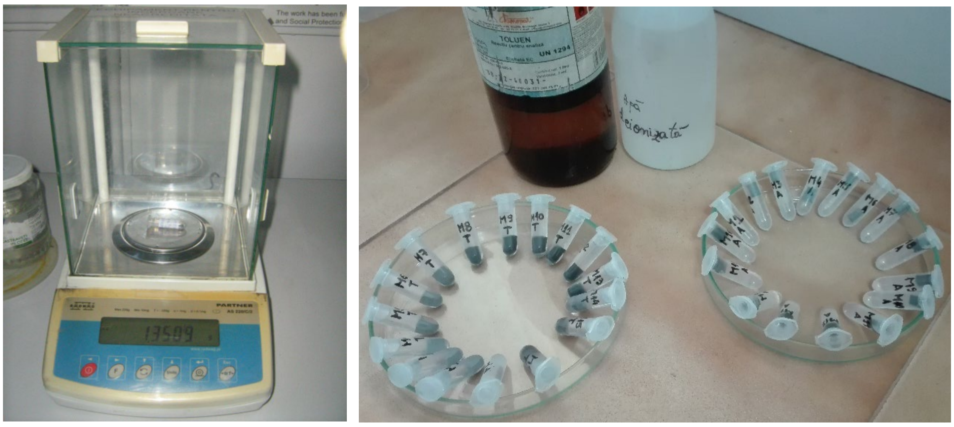

Figure 3. Experiment for the evaluation of the degree of swelling.

When comparatively addressing the degree of swelling in water and solvents, at 24 h, we noticed that the solvent activity was increased compared to that of water, with the swelling degree reaching up to three times higher. The samples with a higher content of cellulose present a higher swelling degree in solvent, for both matrices. Contrary to the behavior related to water immersion, the immersion in solvent seems to affect the samples with polypropylene matrix more significantly when compared to the samples with a polyethylene matrix. This effect can be explained by the grinding process of the matrices from waste plastic, which may also impact the internal structure of the injected composites, an outcome also observed when analyzing SEM images, e.g., Figure 2c,d.

4. Technology for Obtaining Thermoplastic Building Materials from Non-Recyclable Mpp Packaging Waste

Profiles for building purposes were obtained by the extrusion of flakes of HDPE waste and 40% MPP packaging waste, obtained as powder, by use of a POEX T40 twin screw extruder (Turkey), using different molds. The extruder with two corotating screws presents the following characteristics: capacity: 150–250 kg/h; main engine: 75 kW, 1500 rpm; heating power: 16 kW; a temperature control system with 12 temperature adjustment zones, with a separate control for each section. The flakes/powders were preliminary subjected to a specialized device for final dehumidification, homogenization, and thermal pre-compatibilization with various additives (Ningbo Lvhua, Ningbo, China). The miscellaneous additives were in proportion of up to 8% and included a composite stabilizer: Jiaxu Development Co. HL-604, 2.6%; an azodicarbonamide blowing agent: WSD Chemical AC7000, 1.2%; a foam regulator: Shandong Zibo ZB-530, 0.4%; and a modifier/coupling agent: Jiaxu Development Co. stabilizer, 0.4%; lead stearate, 0.2%; calcium carbonate and talc concentrate 4:1, with fineness of 800 mesh or more, 3.1%; inorganic pigments for uniform brown color, UV stabilization additives and flame retardant additives, 0.1% in all. An example of a resulted profile for flooring/decking is presented in Figure 4.


(**a**) (**b**)

Figure 4. Thermoplastic building material. (**a**) Composite semi-finished material, before passing through the mold. (**b**) Example of profile obtained from the extrusion equipment.

It was noticed that the applied extrusion technology led to qualitative and versatile products, with features similar to those of products currently on the market, obtained by classical WPC technology, e.g., deck floors, fences, landscaping items, cladding and siding, park benches, window and door frames, indoor furniture, etc., [24,25]. A comparison among some technical characteristics of the building profile realized from non-recyclable MPP packaging waste and a homologues profile realized as WPC with polyvinylchloride base (but containing about 11% calcium carbonate) is presented in Table 8.

Table 8. Comparative technical characteristics.

Technical Characteristic	HDPE Profile with MPP Packaging Waste	WPC Profile with Polyvinylchloride Base
Density [g/cm^3]	0.966	0.998
Shore hardness [MPa]	69	71
Tensile strength [MPa]	39	42
Thermal conductivity [W/(m × K)]	0.294	0.366

As expected, a better thermal conductivity can be noticed for the panel realized with the technology presented in the paper. Regarding the slightly higher values for the density and for the mechanical characteristics of commercial WPC with a polyvinylchloride base, the explanation would be related to the higher content of calcium carbonate.

5. Sustainability of the Technology Which Uses Non-Recyclable MPP Packaging Waste

The materials corresponding to the P1–P9 samples were subjected to a leaching process following the procedure described in Refs. [27,28] to determine the impact of critical dangerous metals. The leachates acquired were characterized by assessing the environmental impact indicator values related to the procedures for waste storage considered permissible within each waste landfill category [29]. Upon scrutinizing the outcomes, it was observed that samples P3, P4, and P5 exhibited a remarkably elevated zinc content (i.e., 109.21, 74.33, and 57.769 mg/kg DW, respectively, compared to 50 mg/kg DW—the limit value for accepting waste in non-hazardous waste deposits). However, they remained below the threshold designated for admission to hazardous waste repositories. Thus, the method of collecting the MPP packaging waste seems to be very important. Even if samples P1–P3 seem to be similar, the method of collecting them is different. P1 and P2 come from selective recycling, but P3 is obtained directly from the landfill, where a possible contamination with leakage from batteries or other related items containing Zn is obvious.

The effect remains, even though it is slightly diminished, when grinding the mixture of packaging with plastic waste, as in the case of P4 and P5. It must be noted that, in spite of exhibiting similar percentages of plastic matrices, the Zn content remains higher in the case of polyethylene, P4, compared to polypropylene, P5. This can explain the higher affinity of polyethylene for Zn, when it comes in contact with landfill leakage. Ultimately, considering the other analyzed elements (i.e., As, Ba, Cd, Cr, Cu, Hg, Mo, Ni, Pb, Sb, Se), the environmental impact of non-recyclable MPP packaging waste and its related products was minor.

Here, we must emphasize that by thermoplastic processing, i.e., injection of samples—the case for P6–P9, even if the raw material was from P4 or P5 sources, with a high Zn content, the environmental impact, including Zn impact, was clearly diminished due to the fact that the leaching process is limited for compact thermoplastic products. Obviously, the samples related to polyethylene, coming, e.g., from P4, continue to present a higher quantity of Zn compared to that of the products from polypropylene, e.g., from P5. In addition, the Zn impact slightly increases when using larger quantities of cellulose-based raw material for injected products, i.e., when comparing the results of P6 with P8, respectively, or of P7 with P9. In summary, in regards to both chloride and sulfate indicators, the values acquired for all samples were significantly beneath the prescribed limit values of 500 mg/kg DW for waste acceptance at non-hazardous waste disposal sites. Even so, the P4 and P5 materials processed by injection to produce P6 and P8 exerted a diminished impact for the chloride ion levels by at least nine times and the sulphate ion values by about four times.

The sustainability of a technology can be oriented towards three directions: substituting non-renewable with renewable resources, including from waste sources; the prevention or elimination of potential contamination, as well of other negative environmental impacts; and efficiency in terms of the use of resources.

By using raw materials from waste sources, i.e., non-recyclable MPP packaging waste, our paper mainly addresses the improvement of the environmental impact, partially solved by the proposed technology, in addition to improved efficiency in terms of the use of resources. It also indirectly addresses the carbon footprint reduction and raw materials depletion through the use of waste materials instead of virgin resins for the same technological purpose.

In regards to the elimination of a potential contamination of the environment, beyond the results presented above, concerning the reduction and stabilization of the analyzed elements, two more indicators were analyzed, i.e., dissolved organic carbon (DOC) and total dissolved solids (TDS). The TDS indicator values were assessed using a standardized analytical technique [30,31]. DOC is an important indicator which may be related to global change and sustainability [32,33]. As presented in Table 9, the situation is concerning, and was observed for all samples P1 to P5, where both DOC and TDS values surpassed the limit set for acceptance, even for hazardous waste deposits.

Regarding the DOC indicator, the increase is from 4 to 10 times, and regarding the TDS indicator, the increase is from 2 to 7 times. A preliminary conclusion should lead to the decision to forbid the storage of combined plastic and paper waste, which is dangerous and un-recyclable, or to send it to a non-hazardous landfill. The decision could also be made not to use such raw materials coming from hazardous waste deposits, resulting in a negative impact on the environment due to the high content of organic compounds sensitive to the leaching effect, e.g., as P3, which presents the highest values.

The good news is that through the thermoplastic processing of non-recyclable MPP packaging waste, even coming from the landfill, the sustainability indicators are very low, meaning that such a technology is sustainable. Here, it is once again noted that the values are slightly larger for polyethylene-related products, compared to those for polypropylene-related products due to the matrix features. Hence, the conversion of raw materials classified as P4 and P5 through injection and/or extrusion processes into final products (composite materials designated for construction applications) is indicated for stabilizing and consuming potentially dangerous waste. Taking into account that the related extruded products have a clear market in the building industry; that they are self-recyclable using the same technology, if collected as building waste and re-processed by grinding and extrusion, etc.; and are in accordance with the actual European regulations for building material recycling [34], the sustainability of the technology using non-recyclable MPP packaging waste is also fully demonstrated from the point of view of life cycle assessment, and related implementation standards may successfully apply to this technology [35].

Table 9. Technology sustainability indicators.

Sample	**Indicator**	
	DOC (mg/kg DW) Accepted Limit 1000	**TDS (mg/kg DW) Accepted Limit 4000**
P1	**3970**	**8600**
P2	**4650**	**15,920**
P3	**10,020**	**28,080**
P4	**3790**	**11,280**
P5	**2390**	**10,880**
P6	43	200
P7	70.1	80
P8	55.7	400
P9	135.8	120

6. Conclusions

The paper describes the process used to produce thermoplastic building materials from non-recyclable MPP packaging waste. A first step was dedicated to an innovative and sustainable sterilization technology for non-recyclable waste, based on exposure to microwave radiation in closed air-circulation ovens. It is observed that the sterilization efficiency rises with the extension of the microwave exposure duration, but the efficiency is better when using higher energy.

Further, composites with different cellulose content and with two polymer matrices (polyethylene and polypropylene), respectively, were obtained using the injection process. The samples present a homogeneous structure, with the paper particles/cellulose fibers uniformly distributed and well embedded within the polymer matrix. A lower density of composites with polypropylene compared with the composites with polyethylene was observed, due mainly to the lower density of the polypropylene matrix. A higher content of cellulose in the composites leads to a slightly higher value for hydrostatic density, for both polymer matrices. Higher values of mechanical strength for the polypropylene composites, compared to those of the polyethylene composites, were noticed. A higher content of cellulose in the composites leads to a slightly higher value for the mechanical characteristics, for both polymer matrices. The increase in the cellulose content decreases the thermal features of the composites. On the other hand, the composites based on polyethylene present superior thermal characteristics when compared to those of the polypropylene matrix.

The degree of swelling in water is much larger at the raw materials level, with a larger quantity of cellulose, reaching about 70% after about 500 h, but in regards to the samples obtained by injection molding, these are more compact, and their degree of swelling in water is about 20% after 500 h. The samples with a higher cellulose content present a higher swelling degree in the solvent, for both matrices. In contrast to the behavior related to water immersion, the immersion in solvent seems to affect more samples with a polypropylene matrix than those with a polyethylene matrix.

The applied extrusion technology led to qualitative and versatile products, with features similar to those of products currently on the market, which were obtained by classical WPC technology. Moreover, due to their superior features, the products based on mixed polypropylene–paper packaging waste may successfully replace the classical polyvinylchloride-based WPC.

The MPP packaging waste coming directly from landfill is affected by a possible contamination by leakage from batteries or other related items containing Zn, leading to a dangerously high Zn content in the leaching tests. The effect remains, although slightly diminished, when grinding the packaging mixture with plastic waste. However, using thermoplastic processing, the environmental impact, including Zn impact, was clearly diminished due to the fact that the leaching process is limited regarding compact products. Ultimately, considering the other analyzed potentially dangerous elements, the environmental impact of non-recyclable MPP packaging waste and its related products is minor.

The sustainability of using non-recyclable MPP packaging waste is evaluated by analyzing indicators as: dissolved organic carbon (DOC) and total dissolved solids (TDS). The situation is critical, mostly in terms of the TDS indicator, in the case of raw materials based on non-recyclable MPP packaging waste, for which both DOC and the TDS values surpass the threshold set for acceptance in hazardous waste deposits by 5 to 11 times. However, when considering the transformation of raw materials by injection and/or extrusion into finished products (composite materials intended for construction fields), the sustainability indicators return to normal, indicating a successful consuming and stabilization of potentially dangerous waste.

In our case, the materials were collected from the city dump, as such materials currently have no direct recycling route. In most cases, such materials occurring when the selective collecting is completed, and is mixed either with paper or plastic waste. When speaking about paper waste, such mixed packaging is selected, separated, and sent to the city dump. When speaking about plastic waste, it depends on the destination of plastic. If designated for recycling towards new plastic products, such mixed packaging is selected, separated, and sent to the city dump. If it is intended to be burned for energy production, the mixed paper–plastic waste is directly used for this purpose, without being separated. Consequently, the most feasible and economic method of separating such mixed paper–plastic waste is automatic separation from the classical selective collecting of both paper and/or plastic waste. The minimal effect upon the environment is assured when selecting occurs during the early stages of such mixed paper–plastic waste, as described above, subjecting the waste to a thermoplastic process to obtain new products.

As long as such thermoplastic products are self-recyclable using the same technology, if collected as building waste and re-processed by grinding and extrusion, etc., in terms of actual European regulations for building materials recycling, the sustainability of the technology, which uses non-recyclable MPP packaging waste, is also fully demonstrated from the point of view of life cycle assessment.

Author Contributions: Conceptualization, C.S.; methodology, R.C.C., C.S. and A.R.C.; validation, R.C.C., C.S. and A.R.C.; formal analysis, A.R.C., S.A. and M.A.; investigation, R.C.C., C.S., A.R.C., S.A. and M.A.; data curation, R.C.C., C.S. and A.R.C.; writing—original draft preparation, C.S. and R.C.C.; writing—review and editing, R.C.C., C.S., S.A. and M.A.; visualization, R.C.C., C.S. and A.R.C.; supervision, C.S. and R.C.C. All authors have read and agreed to the published version of the manuscript.

Funding: This research received no external funding

Institutional Review Board Statement: Not applicable.

Informed Consent Statement: Not applicable.

Data Availability Statement: The data presented in this study are available on request from the corresponding author.

Acknowledgments: The research was based on the preliminary results of the Project ID P_40_300, SMIS 105581, Operational Program Competitiveness 2014–2020, Subsidiary Contract 15351/13.09.2017.

Conflicts of Interest: The authors declare no conflicts of interest.

References

1. Available online: https://www.marketresearchfuture.com/reports/packaging-material-market-12385?utm_term=&utm_campaign=&utm_source=adwords&utm_medium=ppc&hsa_acc=2893753364&hsa_cam=20543884685&hsa_grp=153457592316&hsa_ad=673752668768&hsa_src=g&hsa_tgt=dsa-2246460574313&hsa_kw=&hsa_mt=&hsa_net=adwords&hsa_ver=3&gad_source=1 (accessed on 16 February 2024).
2. Available online: https://zerowasteeurope.eu/wp-content/uploads/2021/09/Analysis-of-non-recyclable-waste-in-lightweight-packaging_case-study.pdf (accessed on 16 February 2024).
3. Han, J. (Ed.) *Innovations in Food Packaging*, 1st ed.; Academic Press: Cambridge, MA, USA, 2005; ISBN 9780080455174.
4. Available online: https://www.letsrecycle.com/prices/waste-paper/paper-grades-and-en643/ (accessed on 16 February 2024).
5. Available online: https://www.eumonitor.eu/9353000/1/j4nvk6yhcbpeywk_j9vvik7m1c3gyxp/vitgbgip5dwf (accessed on 16 February 2024).
6. Sarma, P.; Mohanty, S. *Pediococcus acidilactici* Pneumonitis and bacteriemia in a pregnant woman. *J. Clin. Microbiol.* **1998**, *36*, 2392–2393.
7. Brown, R.M.; Hoover, A.N.; Klinger, J.L.; Wahlen, B.D.; Hartley, D.; Lee, H.; Thompson, V.S. Decontamination of Mixed Paper and Plastic Municipal Solid Waste Increases Low and High Temperature Conversion Yields. *Front. Energy Res.* **2022**, *10*, 834832. https://doi.org/10.3389/fenrg.2022.834832.
8. Alkhursani, S.A.; Ghobashy, M.M.; Alshangiti, D.M.; Al-Gahtany, S.A.; Meganid, A.S.; Nady, N.; Atia, G.A.N.; Madani, M. Plastic waste management and safety disinfection processes for reduced the COVID-19 Hazards. *Int. J. Sustain. Eng.* **2023**, *16*, 1–14. https://doi.org/10.1080/19397038.2023.2188396.
9. Belbessai, S.; Azara, A.; Abatzoglou, N. Recent Advances in the Decontamination and Upgrading of Waste Plastic Pyrolysis Products: An Overview. *Processes* **2022**, *10*, 733. https://doi.org/10.3390/pr10040733.
10. Najafi, S.K. Use of recycled plastics in wood plastic composites—A review. *Waste Manag.* **2013**, *33*, 1898–1905.
11. Shettigar, Y.P.; Kumar, N.; Aveen, K.P.; Hebbale, A.M.; Karinka, S. Mechanical characterization of Waste Plastic and Waste Paper Composites (WPWPC). *Mater. Today Proc.* **2022**, *52*, 2154–2159.
12. Wanske, M.; Weber, P.G.; Großmann, H.; Siwek, S.; Jornitz, F.; Wagenführ, A. Paper-Polymer-Composites (PPC): Added value through recycling. *Sci. Technol. Das Pap.* **2013**, 11–12. https://www.researchgate.net/publication/293144561_Paper-Polymer-Composites_PPC_Added_value_through_recycling (accessed on 16 February 2024).
13. Available online: https://www.marketsandmarkets.com/Market-Reports/wood-plastic-composite-market-170450806.html?gad_source=1&gclid=CjwKCAiA0bWvBhBjEiwAtEsoW8NFBPr0tYAaU1XtUQHVYm0mYpZVOQHxei6k7fw1wgovZvOrvWrE9xoC8GEQAvD_BwE (accessed on 16 February 2024).
14. Banik, G.; Brückle, I. Principles of water absorption and desorption in cellulosic materials. *Restaurator* **2010**, *31*, 164–177, https://doi.org/10.1515/rest.2010.012.
15. Available online: https://www.iso.org/standard/28960.html (accessed on 16 February 2024).
16. Ciobanu, R.C.; Ursan, G.A.; Aradoaei, M.; Batrinescu, G.; Banciu, A.R. Specific Tests Concerning Microwave Sterilization Efficiency of Combined Plastic and Paper Waste. In Proceedings of the 2018 International Conference and Exposition on Electrical And Power Engineering (EPE), Iasi, Romania, 18–19 October 2018; pp. 1000–1003. Available online: https://ieeexplore.ieee.org/abstract/document/8559931 (accessed on 16 February 2024).
17. *ASTM E-1461-07*; Standard Test Method for Thermal Diffusivity by the Flash Method. ASTM International: West Conshohocken, PA, USA, 2012. Available online: https://www.astm.org/e1461-07.html (accessed on 16 February 2024).
18. Aradoaei, M.; Ciobanu, R.C.; Schreiner, C.; Ursan, A.G.; Hitruc, E.G.; Aflori, M. Thermoplastic Electromagnetic Shielding Materials from the Integral Recycling of Waste from Electronic Equipment. *Polymers* **2023**, *15*, 3859. https://doi.org/10.3390/polym15193859.
19. *SR EN ISO 175:2011*; Plastics—Methods of Test for the Determination of the Effects of Immersion in Liquid Chemicals. Romanian Standards Association: Bucureşti, Romania, 2011. Available online: https://e-standard.eu/en/standard/186982 (accessed on 16 February 2024).
20. Gozdecki, C.; Wilczyński, A.; Kociszewski, M.; Tomaszewska, J.; Zajchowski, S. Mechanical properties of wood–polypropylene composites with industrial wood particles of different sizes. *Wood Fiber Sci.* **2012**, *44*, 14–21.
21. Murayama, K.; Ueno, T.; Kobori, H.; Kojima, Y.; Suzuki, S.; Aoki, K.; Ito, H.; Ogoe, S. Mechanical properties of wood/plastic composites formed using wood flour produced by wet ball-milling under various milling times and drying methods. *J. Wood Sci.* **2019**, *65*, 5.

22. Arnandha, Y.; Satyarno, I.; Awaludin, A.; Irawati, I.S.; Prasetya, Y.; Prayitno, D.A.; Winata, D.C.; Satrio, M.H.; Amalia, A. Physical and Mechanical Properties of WPC Board from Sengon Sawdust and Recycled HDPE Plastic. *Procedia Eng.* **2017**, *171*, 695–704.
23. Li, J.; Huo, R.; Liu, W.; Fang, H.; Jiang, L.; Zhou, D. Mechanical properties of PVC-based wood–plastic composites effected by temperature. *Front. Mater.* **2022**, *9*, 1018902. https://doi.org/10.3389/fmats.2022.1018902.
24. Ciobanu, R.C.; Batrinescu, G.; Ursan, G.A.; Caramitu, A.R.; Marinescu, V.; Bors, A.M.; Lingvay, I. Mechanical and Morphostructural Characteristics of Composite Materials Performed by Recycling Mixed Waste of Plastic and Paper. *Mater. Plast.* **2019**, *56*, 475–478.
25. Available online: https://wpcproducts.com/ (accessed on 16 February 2024).
26. Available online: https://www.sundi-wpc.com/wpc-products/ (accessed on 16 February 2024).
27. *SR EN 12457-2:2003*; Characterisation of Waste—Leaching. European Standards: Plzen, Czech Republic, 2003. Available online: https://www.en-standard.eu/une-en-12457-2-2003-characterisation-of-waste-leaching-compliance-test-for-leaching-of-granular-waste-materials-and-sludges-part-2-one-stage-batch-test-at-a-liquid-to-solid-ratio-of-10-l-kg-for-materials-with-particle-size-below-4-mm-without-or-with-size-/ (accessed on 16 February 2024).
28. Batrinescu, G.; Cristea, I.; Badescu, V.; Ciobanu, R.C.; Ursan, G.A.; Aradoaei, M. The Induced Impact on the Environment by Combined Plastic and Paper Waste before and after Recovery. *Rev. Chim.* **2019**, *70*, 4579–4583.
29. ORDER 95/2005, The Criteria for the Acceptance and Preliminary Acceptance Procedures for Waste at Storage and National List of Waste Accepted in Each Class of Waste Landfill, Official Monitor of Romania, Part 1, No. 452/27.05.2005. Available online: https://www.ecotic.ro/wp-content/uploads/2015/07/1e62400fcaa487767564187df6343e669b6f36ad.pdf (accessed on 16 February 2024).
30. Batrinescu, G.; Cristea, I.; Badescu, V.; Ciobanu, R.C.; Ursan, G.A.; Aradoaei, M. Induced environmental impact of combined plastic and paper wastes before and after valorization. In Proceedings of the International Symposium "The Environment and the Industry", SIMI 2019, Bucharest, Romania, 26–27 September 2019. https://doi.org/10.21698/simi.2019.ab20.
31. Available online: https://www.alsglobal.com/es/News-and-publications/2022/11/Enviromail-42-Canada-Accurate-TDS-Measurement (accessed on 16 February 2024).
32. Available online: https://www.sciencedirect.com/science/article/pii/S0048969717303595 (accessed on 16 February 2024).
33. Available online: https://www.ncbi.nlm.nih.gov/pmc/articles/PMC6616961/ (accessed on 16 February 2024).
34. Available online: https://single-market-economy.ec.europa.eu/news/eu-construction-and-demolition-waste-protocol-2018-09-18_en (accessed on 16 February 2024).
35. Available online: https://www.iso.org/standard/37456.html (accessed on 16 February 2024).

crystals

MDPI

Article

Technology for Obtaining Sintered Components with Tailored Electromagnetic Features by Selective Recycling of Printed Circuit Boards

Romeo Cristian CIOBANU *, Mihaela Aradoaei and Cristina SCHREINER

Department of Electrical Measurements and Materials, Gheorghe Asachi Technical University, 700050 Iasi, Romania; mosneagum@yahoo.com (M.A.); cschrein@tuiasi.ro (C.S.)
* Correspondence: r.c.ciobanu@tuiasi.ro

Abstract: The paper presents a technological approach for obtaining sintered components with tailored electromagnetic features from electromagnetically active powders through the selective recycling of electronic waste, in particular scrap electronic components. Printed circuit board (PCB) scraps were submitted to a succession of grinding processes, followed by progressive magnetic and electrostatic separation, resulting two final fractions: metallic particles and non-metallic particles including different metallic oxides. Three types of powders were analyzed, i.e., powder after fine grinding, after magnetic separation and after electrostatic separation, which were further processed within a spark plasma sintering furnace in order to obtain solid disk samples. All samples contained several classes of oxides, and also residual metals, leading to specific thermal decomposition processes at different temperatures, depending on the nature of the oxides present in the studied materials. The chemical analysis of powders, via spectrometry with X-ray fluorescence—XRF, emphasized the presence of a mixture of metal oxides and traces of metals (mainly Ag), with concentrations diminishing along with the purification process. The most important analysis was related to dielectric parameters, and it was concluded that the powders obtained by the proposed technology could efficiently substitute scarce raw materials actually used as additives in composites, coatings and paints, mainly due to their high permittivity (above 6 in all frequency domains) and, respectively, dielectric loss factor (above 0.2 in all cases, in all frequency domains). We estimate that the technology described in this paper is a sustainable one according to the concept of circular economy, as it could reduce, by a minimum of 15%, the embodied GHG emissions generated from information and communications technology (ICT) devices by advanced recycling.

Keywords: selective recycling; electronic waste; electromagnetically active powders; sintered components with tailored electromagnetic features; circular economy

Citation: CIOBANU, R.C.; Aradoaei, M.; SCHREINER, C. Technology for Obtaining Sintered Components with Tailored Electromagnetic Features by Selective Recycling of Printed Circuit Boards. *Crystals* **2024**, *14*, x. https://doi.org/10.3390/xxxxx

Academic Editor(s): Name

Received: 13 August 2024
Revised: 6 September 2024
Accepted: 9 September 2024
Published: date

1. Introduction

The European Union unites the waste issue with actual policies for the use of material resources in the "Thematic Strategy on waste prevention and recycling" [1] and in the "Thematic Strategy on the use of natural resources" [2], aiming to decouple the use of resources from the production of waste and the associated negative effects on the environment. In addition, the application of the concept of "waste hierarchy" is encouraged, which classifies the different waste management options from the best to the least good for the environment. Priority is given to the prevention of waste generation, the minimization of the amount and degree of danger, followed by reuse, recycling, energy recovery and, finally, disposal by incineration or storage. In applying the waste hierarchy, the options that produce the best overall environmental result should be adopted. This may require that certain specific waste streams move away from the hierarchy; this is determined by analyzing the entire life cycle regarding the global effects of the generation and management of that waste. Waste policies can primarily reduce three types of pressure on the environment: emissions from waste treatment/disposal facilities, irrational exploitation of natural resources, and air pollution and greenhouse gas emissions caused by the consumption of energy and fuels in the waste management process.

Electrical and electronic equipment waste represents the waste of equipment that operates on the basis of electric current or electromagnetic fields and the equipment for generating, transporting and measuring these currents and fields, intended for use at a voltage lower than or equal to 1000 volts alternating current and 1500 volts direct current. The main objectives of Directive 2002/96/EC regarding electrical and electronic equipment waste—WEEE [3]—with subsequent amendments and additions are: 1. preventing the production of electrical and electronic equipment waste, as well as their reuse, recycling and other forms of valorization, so as to reduce the volume of disposed waste; and 2. improving the performance regarding the environment and the health of the population of producers, importers, distributors, consumers and especially of the economic operators who collect, treat, recycle, valorize or dispose of WEEE.

According to the latest UN's General E-Waste Monitor, in 2022, 62 million tons of E-waste were generated globally. The quantity of e-waste is expected to rise to 82 million tons by 2030 [4]. Starting with 2016, the European Union will oblige member countries to collect, recycle and reuse at least 85% of used electronic equipment. Currently, each member of the European Union is obliged to recycle 4 kg/inhabitant of waste from WEEE [5].

In general, WEEE is composed of metals (40%), plastic materials (30%) and refractory oxides (30%) [6,7]. Regarding metals, WEEE generally contains average quantities of copper (20%), iron (8%), tin (4%), nickel (2%), lead (2%), zinc (1%), silver (0.02%), gold (0.1%) and palladium (0.005%) [8,9]. Polyethylene, polypropylene, polyesters and polycarbonates typically constitute plastic components.

In the European Union, the disposal of WEEE is closely controlled by Directive 2003/108 [10] of the European Commission, which requires that WEEE be collected selectively, broken down separately into each type of material (e.g., plastics and metals) and then recycled. The current technologies for recycling electrical waste and electronic equipment create an important advantage for the recovery of metallic components. Separating metals from WEEE is a simpler task, as each respective metal can be easily identified and dismantled, being in a quasi-pure state without being mixed with other components. On the other hand, the separation of thermoplastic components of WEEE is also relatively facile, involving mainly packaging or support items for other components; here, it is also possible that some plastic types are partially mixed, making their separation and recycling more difficult. The most problematic subject, with severe limitation regarding recycling, is represented by the content of non-metallic components. The non-metallic section of electronic waste—especially printed circuit boards (PCBs) with scrap electronic components—represents one of the major problems facing consumer societies in Europe, Japan, and North America. Such components are practically inseparable from thermorigid organic materials, traces of precious metals, semiconductors as crystals and metal oxides. However, the recycling of non-metallic components of WEEE is particularly problematic because they also contain special additives, such as heavy metals (Hg, Pb, Cd and hexavalent chromium) and halogenated flame retardants, which have a negative impact on the environment (according to restrictions from Directive 2002/95/CE—RoHS, [11]). In combination with plastic, halogen compounds may form volatile metal halides, which further perform a catalytic effect with the formation of dioxins and furans, dangerous for people and the environment, [12].

Along with the established raw materials to be recovered from non-metallic components of WEEE, research was oriented with priority in the direction of the recovery of precious metals, towards sustainable business [13,14]. But in the last 20 years, electronic technology has advanced with new types of electronic components with better integration and very limited use of precious metals, so the problem related to the recycling of scrap electronic components remains conceptually and technologically unsolved and has rarely been targeted by the scientific literature. In analyzing the evolution of electronic technology, one can identify the following: 1. electronic equipment produced before the 1990s, where there is a significantly large number of passive components (capacitors, resistors, coils with ferrimagnetic cores, etc.) of a volume comparable to that of the active components (such as diodes/transistors and some integrated circuits of large areas), with a below-average degree of integration, all disposed of on PCBs of large surfaces, with a high quantity of soldering alloys; 2. electronic equipment produced between the 1990s and 2010s, with a higher degree of integration, where there is a significantly large number of integrated-circuit-type active components, and passive ones are present with less than 30% of the volume of active ones, but are still of a large volume, all disposed of on PCBs of smaller surfaces, eventually within a predefined spatial architecture, with soldering alloys still largely being used; and 3. electronic equipment produced after the 2010s, with a very high degree of integration, miniaturized integrated circuits—microprocessors predominating, with a negligible volume of passive components and negligible PCB areas—based on new methods of soldering, without alloys. As the years pass, it is becoming more evident that WEEE recycling technologies must keep up with technological development, i.e., with new concepts of electronic technology, because classic waste with large amounts of metals and thermoplastic components present before the 2000s is on its way to becoming extinct. Accordingly, the legislative Decree n. 49 of 2014 represents the reference legislation of EC regarding Waste Electrical and Electronic Equipment towards implementing the European Directive 2018/849, present in the Circular Economy Package [15].

The primary issue with PCB recycling is their complicated structure and material combination. Actual technologies presume either thermal processing, chemical treatment, or mechanical non-thermal processing, including disassembly, separation and shredding techniques. The actual purpose of PCB recycling is to recover approximately 99% of precious and scarce metals, mainly Cu, Ag and Au, but this also depends on their purity and amount. Other fractions are ignored and/or sent either to damping or to high-temperature thermal processing for energy purposes.

This paper's novelty lies in showcasing the technology used to produce electromagnetically active powders by selectively recycling electronic waste, specifically scrap electronic components—as detailed in [16]—aligning with current electronic technology and the principles of the circular economy. These powders could replace expensive conductive materials currently used in EMC/EMI composites, coatings, and paints. This study aimed to show how sintered materials could be used as more affordable electromagnetic shielding systems by utilizing powders from the new recycling concept.

2. Materials and Methods

2.1. Manufacturing and Characterization Equipment

- Sintering was performed by use of the Spark plasma sintering furnace HHP D (FCT Systeme Gmbh, Rauenstein, Germany).
- A simultaneous thermal analyzer—Thermogravimetry (TG)/Differential Scanning Calorimetry (DSC) type STA 449 F3 Jupiter, (NETZSCH, Selb, Germany)—allowed the determination of mass variations and thermal changes for different types of materials, including inhomogeneous materials.
- Hydrostatic density was determined utilizing XS204 Analytical Balance, characterized by the following specifications: maximum capacity of 220 g, precision of 0.1 mg, linearity of 0.2 mg, internal calibration, equipped with a density kit for solids and liquids, and an RS 232 interface. The measurements were conducted at a temperature of 25 °C.
- Chemical analysis was performed by use of the XRF spectrometer model WD-XRF S8 TIGER-1 kW (Bruker AXS GmbH, Berlin, Germany).

- Structural characterization was carried out by X-ray diffraction (XRD) using CuKα radiation ($\lambda = 0.154$ nm) with Ni filter Bruker AXS D8 Advance (Bruker AXS, Billerica, MA, USA). Diffraction patterns were recorded at room temperature in Bragg–Brentano geometry at an angle 2θ from 20° to 65° at a rate of 0.6°/min (2θ)/min.
- Scanning electron microscopy (SEM) was performed with a field emission and focused ion beam scanning electron microscope (SEM) model Tescan Lyra III XMU (Brno-Kohoutovice, Czech Republic).
- Shore hardness tests were performed with a common Microdurometer Vickers FM700 (Future-Tech Corp, Tokyo, Japan).
- Dielectric analysis was performed via broadband dialectic spectroscopy, by use of a Turn Key Dielectric Spectrometer BDS 40BDS (frequency band 3 μHz–3 GHz), with variable temperature control (Novocontrol Gmbh, Montabaur, Germany).

2.2. Powder Manufacturing Process

The manufacturing process starts with the selective dismantling and selection of PCBs with electronic components (integrated circuits, but with the presence of minoritarian quantities of diodes, metallic film resistors and ceramic capacitors). Initially, the PCBs were submitted to an extraction process of copper wires, ferritic elements, metallic carcasses and radiators, and most of the solder alloys, etc. These kinds of PCB scraps constitute the non-metallic WEEE category that is considered non-recyclable. The respective scraps were submitted to dimensional reduction till reaching 3 × 3 cm^2, performed with a mini-breaker, and further to a succession of grinding processes, as suggested in Figure 1, which were carried out with two types of mills, the RETSCH SM 2000 knife cutting mill and the RETSCH RS100 vibrating disc mill (both from Retsch Gmbh, Haan, Germany). The first milling process can be adjusted by changing the grinding size by the use of interchangeable sieves with different dimensions, to be adapted according to the type and technological age of the PCBs to be processed. After the first milling process of 10 min was completed., the resulting granules were passed through a vibrating sieve to separate the fraction with a size greater than 0.8 mm (basically till a maximum of 2.5 mm), a fraction practically formed by pieces of PCBs without a significant quantity of electronic components (eventually with some pieces of capsule of such components). This first fraction can be processed by classical chemical recycling technologies in order to recover Cu [17,18], and it is not the purpose of our study. The second fraction, with a size smaller than 0.8 mm, represents the concentrated part, containing in large proportion the electronic components, and this was submitted to a second milling process for 15–20 min. The new powder, with a particle size of up to 10 microns, is presented in Figure 2. This powder was finally submitted to magnetic separation to select the magnetic fractions from non-magnetic fractions (the magnetic fraction may include Fe, Ni, but also NiO, Cr_2O_3 and ferrite powders), performed using a Carpco MIH 111-5 laboratory magnetic separator (IMSC Group, Jacksonville, FL, USA), using an average magnetic field of 6000 G. This dry separator was considered the most adequate for the type of powder to be processed. Further, it was submitted to a final electrostatic separation performed by a EHTP 111-15 laboratory electrostatic separator (Sepor Inc., Los Angeles, CA, USA) to remove most of the metallic particles from the remaining non-magnetic fraction. The following parameters were set: ionizing electrode: distance to rotor = 25 cm; static electrode: distance to rotor = 25 cm; rotor speed: 80 rpm; and high tension average value: 45 kV.

The separation processes results and yield values are similar to the ones described, e.g., in [19], and the average fraction distribution was, in our case, of about 13% of the magnetic fraction, about 23% of the metallic non-magnetic fraction, and about 64% of remaining powder requiring further analysis. We note that some small quantities of non-magnetic metallic powders were still trained by a magnetic separator (mainly Cu and Sn), and some residual magnetic powders were present in the fraction that resulted after electrostatic separation (e.g., Fe_2O_3). We note further that some quantities of metallic and magnetic components remained in the powder of study after the separation processes.

Accordingly, it is difficult at this moment to evaluate a precise recovery rate of the separation processes, but it is estimated to be over 97% for all metals, and notably, about 99% for Cu.

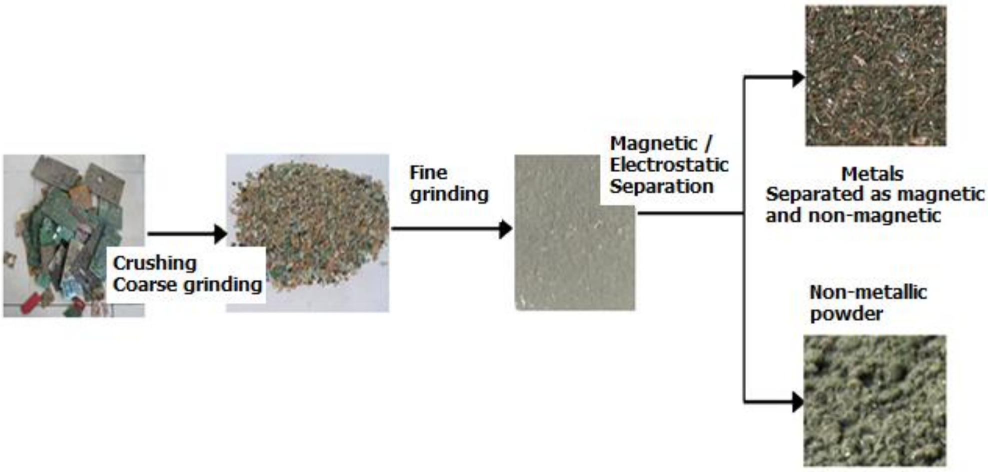

Figure 1. Technological flow for obtaining non-metallic powder from processed PCBs.

Figure 2. Image of non-metallic powder/fraction with particle size of up to 10 microns.

Hence, after the separation processes were finalized, we obtained three main final fractions: magnetic particles (Fe, Ni, etc., with residues of ferritic powders), those associated with metallic non-magnetic particles (Cu, Sn, Pb, Au, Ag, etc.)—which both have a classical route of valorization—depending on their concentration and purity, and the powder of non-metallic particles (of our direct interest, which will be analyzed further), as presented in Figure 1.

The second step was related to the sintering of the powder material (4 g of powder per sample) in order to obtain solid samples with a diameter of 12 mm and a thickness between 2 and 3 mm. The spark plasma sintering process was performed within a spark plasma sintering furnace. The direct heating of the mold–sample–piston system allowed high temperature-increase speeds (50–130 °C/min) and short sintering times, in the order of tens of minutes. The equipment is presented in Figure 3, and the resulting samples are shown in Figure 4. The mold and the sample were heated by the direct passage of a pulsating electric current of low voltage, which propagated through the piston–sample–mold system, with cycle times in the order of several minutes. The processing data were preselected; in the case of Figure 3, a thermal cycle of 15 min is presented, with a maximal temperature exposure equivalent to 1000 °C for 5 min.

Above 600 °C, the mixture of heterogeneous (inhomogeneous) powders went through a pre-sintering process, finalized at 800 °C with slight compaction.

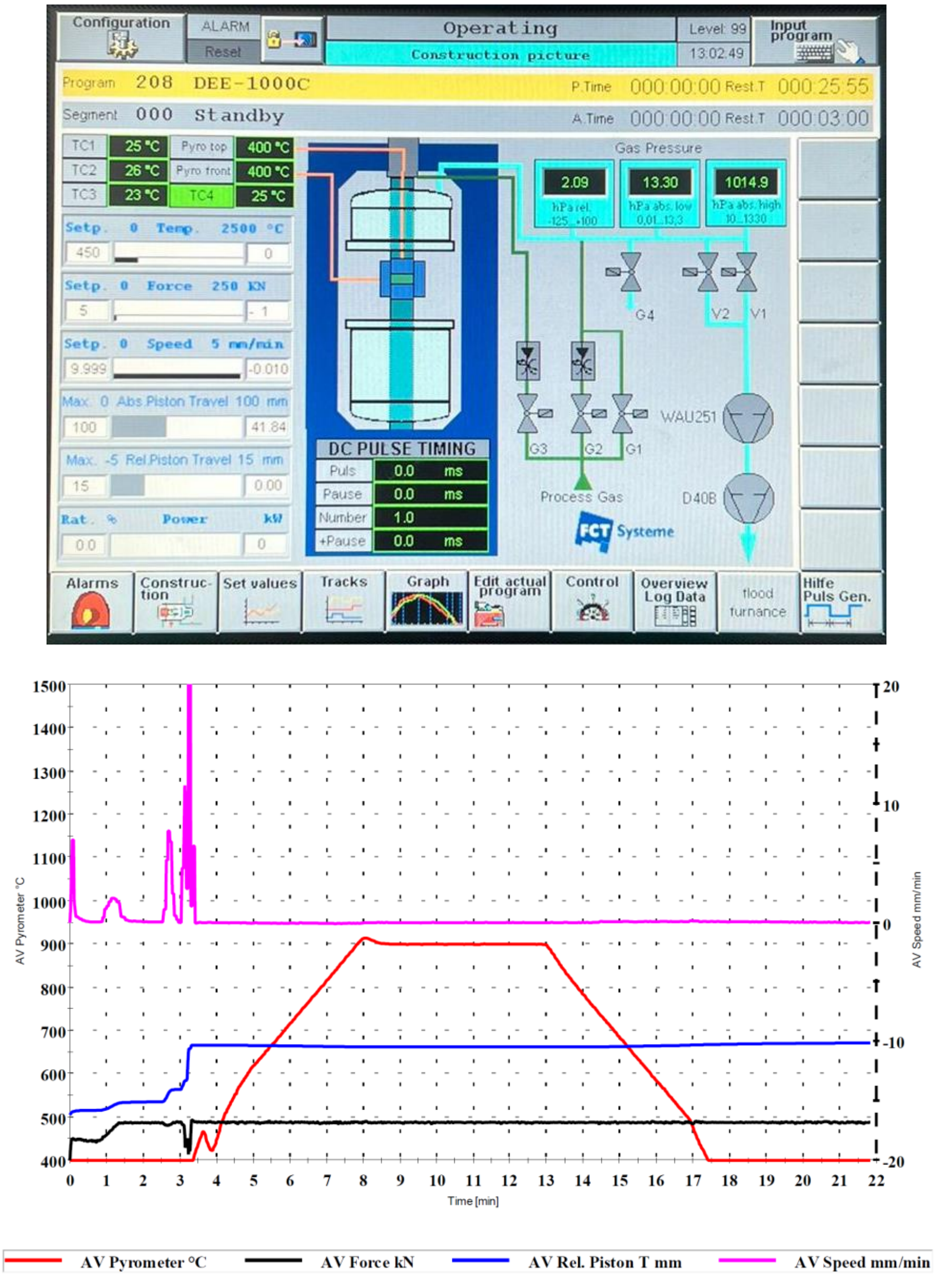

Program 208 DEE-1000C P.Time 000:00:00 Rest.T 000:25:55

Segment 000 Standby A.Time 000:00:00 Rest.T 000:03:00

TC1 25 °C Pyro top 400 °C

TC2 26 °C Pyro front 400 °C

TC3 23 °C TC4 25 °C

Setp. 0 Temp. 2500 °C 450 0

Setp. 0 Force 250 KN 5 -1

Setp. 0 Speed 5 mm/min 9.999 -0.010

Max. 0 Abs.Piston Travel 100 mm 100 41.84

Max. -5 Rel.Piston Travel 15 mm 15 0.00

Rat. % Power kW 0.0 0

Gas Pressure 2.09 hPa rel. -125...+100 13.30 hPa abs. low 0.01...13.3 1014.9 hPa abs. high 10...1330

DC PULSE TIMING Puls 0.0 ms Pause 0.0 ms Number 1.0 +Pause 0.0 ms

Figure 3. Spark plasma sintering equipment and template with heating and cooling zones.

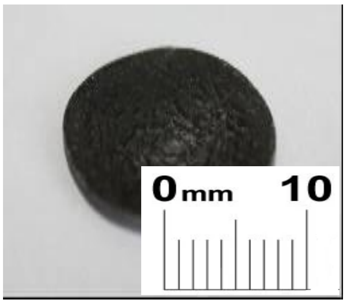

Figure 4. Sintered disk from WEEE powder.

3. Results and Discussion

The tests were performed on both powders and sintered disks from respective powders. Three types of powders were analyzed, i.e., powder after fine grinding (P1), after magnetic separation (P2) and after electrostatic separation (P3).

3.1. Thermal Analysis for Powders

The results are presented in Figures 5–7.

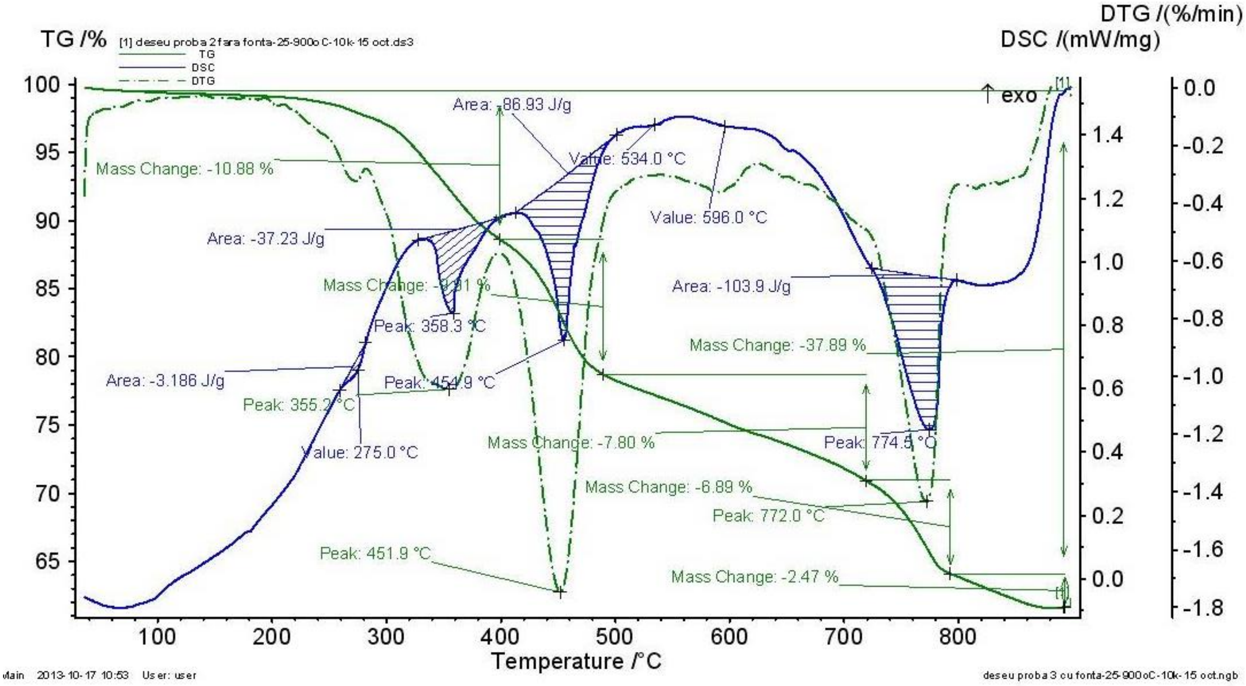

Figure 5. TG/DTG characteristics of P1.

For P1, Figure 5, four thermal processes were identified in the studied temperature range 25–900° C.

Process I (green TG line)—mass loss (on the green curve—TG): 10.88% (25–400 °C), 9.85% (400–48 0 °C), 7.80% (480–780 °C), 6.89% (720–780 °C), and 2.47% (780–800 °C); the total mass loss in the studied temperature range 25–800 °C was 37.89%.

Process II (blue line—DSC)—mass loss at 84.8 °C and an endothermic process of melting of thermoplastic polymers at 182 °C.

Process III (dotted green DTG line)—a two-step oxidation reaction is observed (exothermic process), possibly due to the presence of oxygen in the material, with a minimum at 260 °C and a maximum at 290.7 °C

Process IV—includes the decomposition of the products resulting from the delamination of printed PCBs based on epoxy resin. During these decomposition processes, enthalpies with high values of 37.23 J/g, 86.93 J/g and 103.9 J/g appeared.

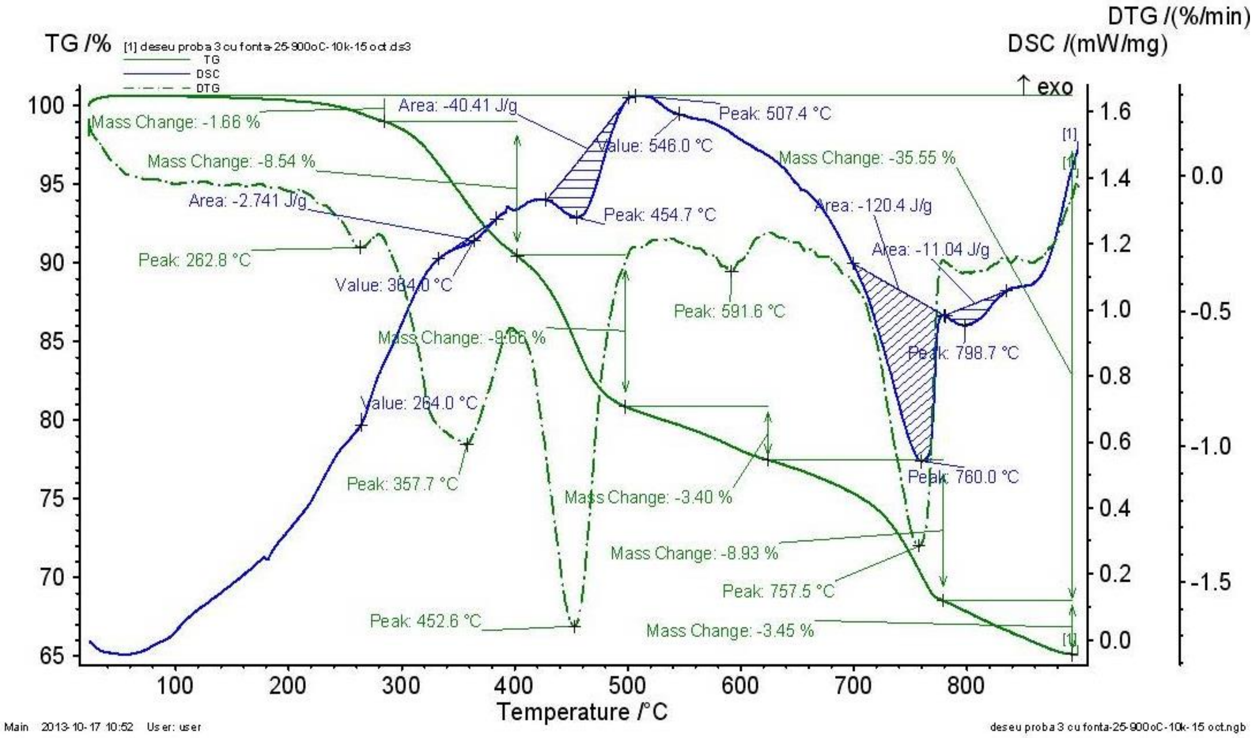

Figure 6. TG/DTG characteristics of P2.

For P2, Figure 6, several processes of decomposition were also recorded.

Process I (green TG line)—mass loss (on the green curve—TG): 1.66% (25–300 °C), 8.54% (300–420 °C), 9.57% (420–500 °C), 3.4% (500–640 °C), 8.93% (640–780 °C) and 3.45% (780–800 °C); the total mass loss over the studied temperature range 25–800 °C was 35.55%.

Process II (blue line—DSC)—mass loss at 84.8 °C and an endothermic melting process of thermoplastic polymers at 182 °C.

Process III (dotted green DTG line)—a two-step oxidation reaction is observed (exothermic process), possibly due to the presence of oxygen in the material, with a minimum at 262.8 °C and a max. at approx. 280 °C.

Process IV—includes the decomposition of the products resulting from the delamination of printed PCBs based on epoxy resin. During these decomposition processes, enthalpies with values of 40.41 J/g and 11.04 J/g appeared.

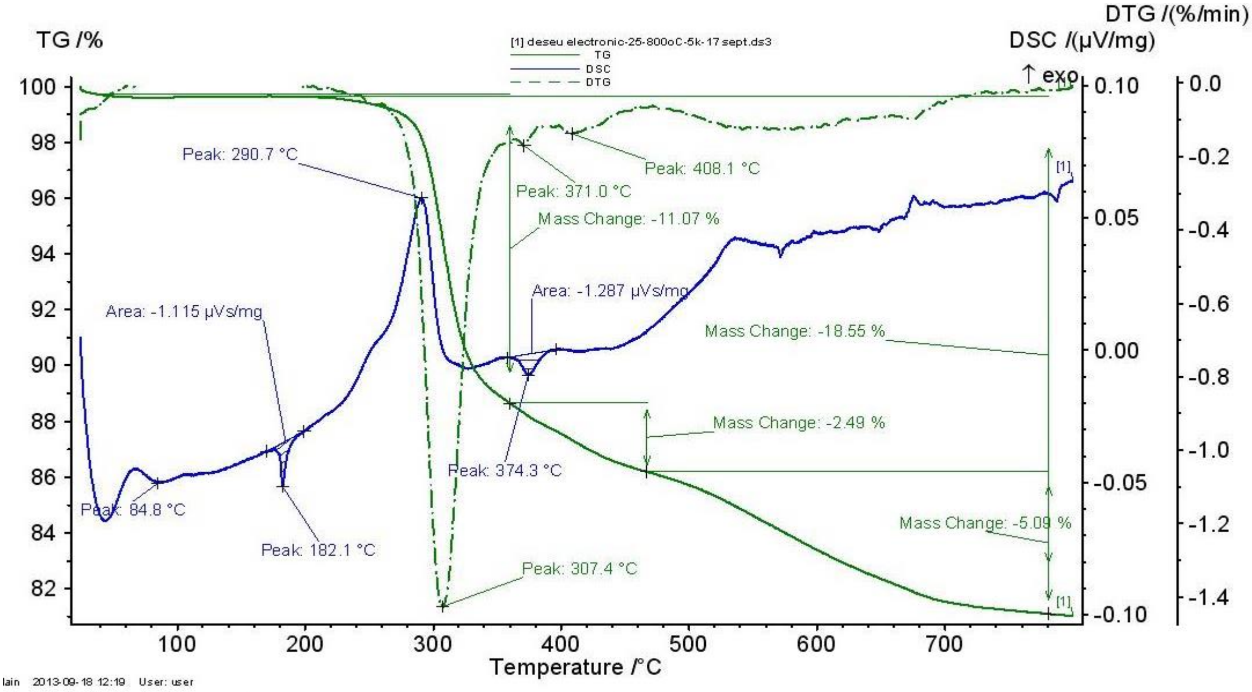

Figure 7. TG/DTG characteristics of P3.

In the case of P3, Figure 7, four thermal processes may be identified:

Process I (green line TG)—loss of water (bound and unbound). It is found that three losses of water occur: 11.07% (25–350 °C), 2.49% (350–460 °C) and 5.09% (460–800 °C); the total mass loss in the studied temperature range 25–800 °C was 18.65%.

Process II (blue line—DSC)—includes a mass loss corresponding to a temperature of 84.8 °C and an endothermic process of melting thermoplastic polymers at 182 °C.

Process III (dotted green DTG line)—a two-step oxidation reaction is observed (exothermic process), possibly caused by the presence of oxygen in the material, with a maximum of 290.7 °C.

Process IV—includes the decomposition of the products resulting from the delamination of printed PCBs based on epoxy resin. During these decomposition processes, enthalpies with high values of 37.23 J/g, 86.93 J/g and 103.9 J/g appeared.

3.2. Evaluation of Hydrostatic Density of Powders before Sintering Process

The freely poured density was determined according to the standard ISO 3923-2 [20], when the powder flowed freely in a collector cylinder with volume of 4.5167 cm^3. The results are presented in Table 1 as an average of five measurements (eliminating the lowest and highest values), with a standard deviation of under 1% [20]. Table 1 offers a preliminary view of the sintered samples' characteristics following the separation processes.

Table 1. Hydrostatic density of powders.

Sample	ϱ [g/cm^3]
P1	0.6630
P2	0.6338
P3	0.6242

The highest diminution of density was noticed after the magnetic separation process, where magnetic fractions of higher mass were excluded from the powder.

3.3. Chemical Analysis of Powders via Spectrometry with X-ray Fluorescence—XRF

The results are presented in Tables 2–4 and Figures 8–10.

As regards P1, it was found that the composition was a mixture of complex structures based on metallic oxides (mainly of Fe, Si, Cu, Ca Pb, Sn, etc.) and some traces of metals (mainly Ag); the concentrations of metals are given in Table 2. The total concentration of metallic compounds was approximately 98.32%. The remainder is expected to be polymeric components, as it comprised integrated circuits (thermoplastic) and PCBs (mainly epoxy-derived resins). XRF equipment cannot identify carbon compounds.

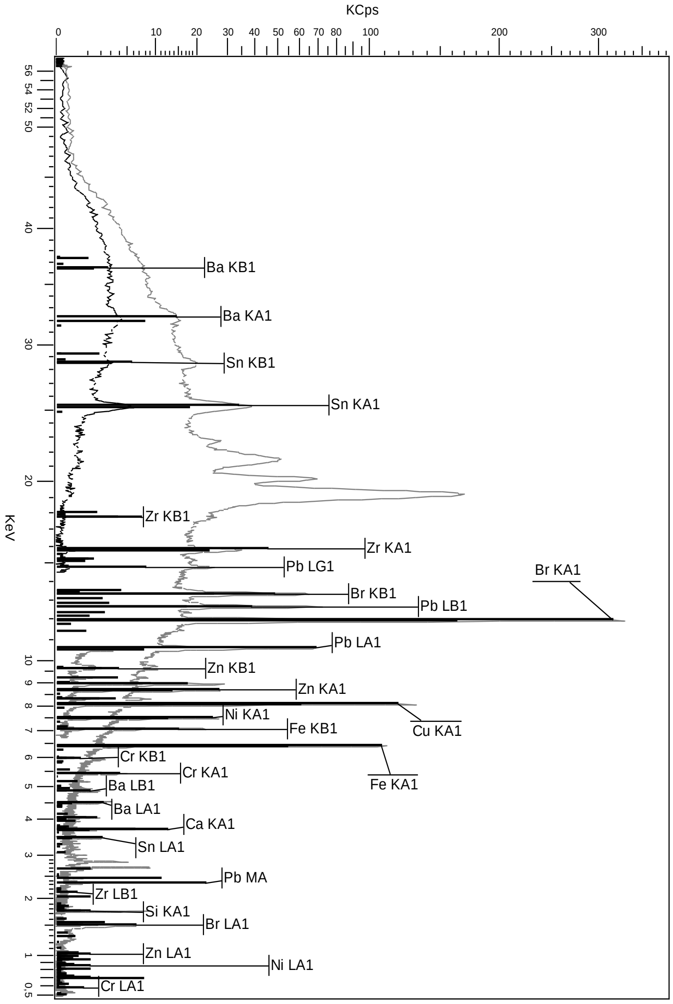

Figure 8. XRF spectrum for P1.

Table 2. Composition of P1.

Element	Concentration (%)
Fe	17.96
Si	17.62
Br	17.21
Cu	13.46
Ca	8.91
Pb	8.28
Sn	7.37
Ba	3.20
Ni	1.76

Zr	1.55
Zn	1.51
Cr	1.17

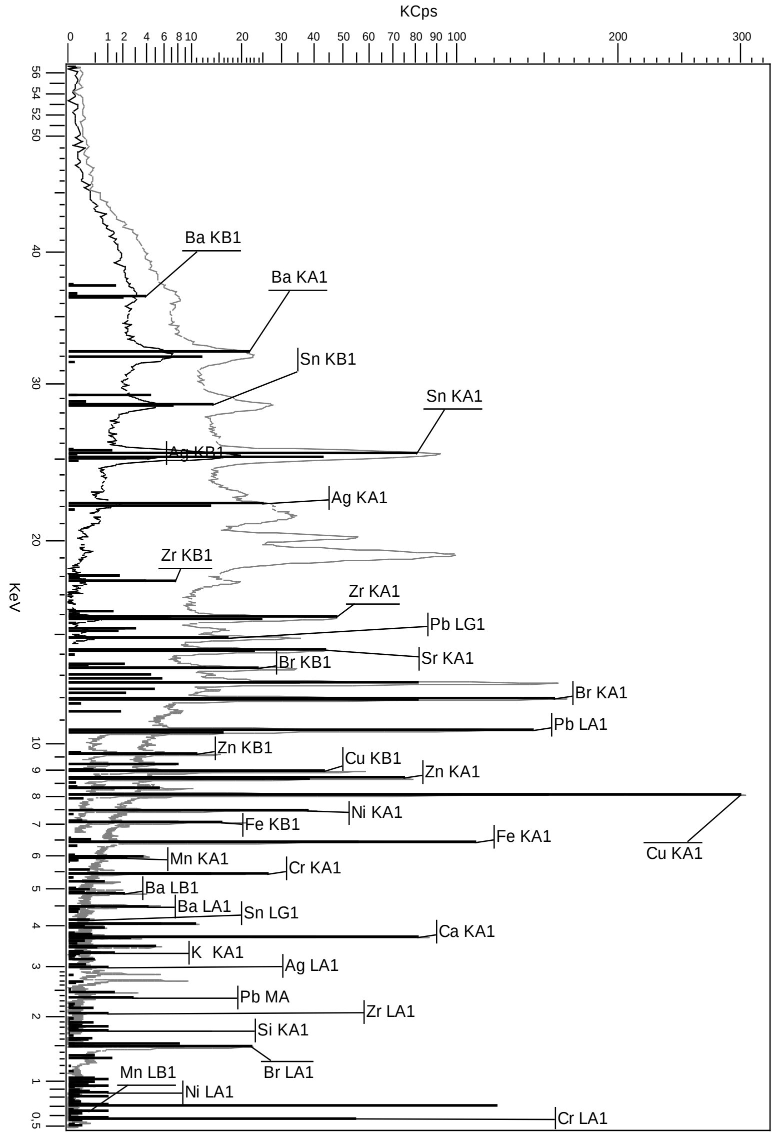

Figure 9. XRF spectrum of P2.

Table 3. Composition of powder P2.

Element	Concentration (%)
Ca	25.16
Fe	15.72
Cu	13.91
Si	12.69
Sn	7.93
Pb	7.68
Ba	3.39
Br	3.10
Cr	2.68
Zn	2.61

Mn	1.88
Ni	1.57
Zr	0.69
Sr	0.61
Ag	0.38

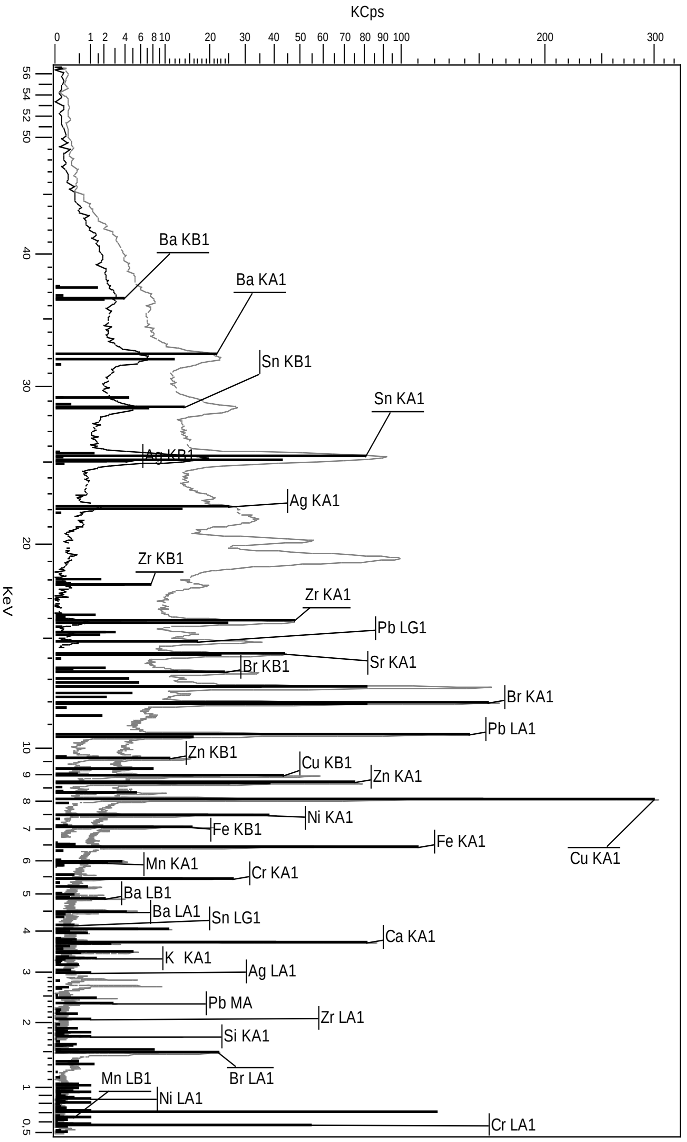

Figure 10. XRF spectrum of P3.

Table 4. Composition of P3.

Element	Concentration (%)
Ca	27.19
Cu	14.55
Si	13.43
Sn	9.93
Fe	9.30
Pb	8.84
Ba	3.80
Br	3.42

Cr	3.07
Zn	2.31
Ni	1.59
Zr	0.88
Sr	0.70
Ag	0.49
K	0.36
Mn	0.14

As regards P2, it was found that the powder consisted of a mixture of complex structures based on metallic oxides (mainly of Ca, Cu, Si, Sn, Fe, etc.) and metallic traces; the concentrations of metals are given in Table 3. The total concentration of metallic compounds was approximately 83.42%, the remainder being a polymeric component. It is obvious that the concentrations of certain metals (and related metallic oxides) with magnetic properties, mainly Fe, Ni, and Cr, were significantly reduced by magnetic separation.

As regards P3, it was found that the powder consisted of a mixture of complex structures based on metallic oxides (mainly of Ca, Cu, Si, Sn, Pb, Ba, Zn, etc.); the concentrations of metals are given in Table 4. The total concentration of metallic compounds was approximately 78,65%. The remainder is expected to be a polymeric component. It was noticed that the main separation of metallic oxides is assured by magnetic separation, and following the metallic compound separation, the concentration of polymeric components progressively increased. This aspect is in line with the thermal analysis. More details regarding the composition of samples P1–P3 are presented in Section 3.4.

Please note that the results presented above cannot be directly correlated with the results from powder separation processes, because the results from Tables 2–4 refer to the samples that were sintered, when most metals reacted to become oxides and related complexes.

A comparative overview of the variation of powder components along the separation processes is presented in Figure 11. As we can see, a significant reduction in Fe, Ni and Cr oxides is noticed, occurring mainly after magnetic separation. The relative stationary percentages of Sn, Pb and Ag are not related to weak performance of the electrostatic separation, but to the fact that the remaining compounds after each separation step constituted a lower quantity of remaining powder.

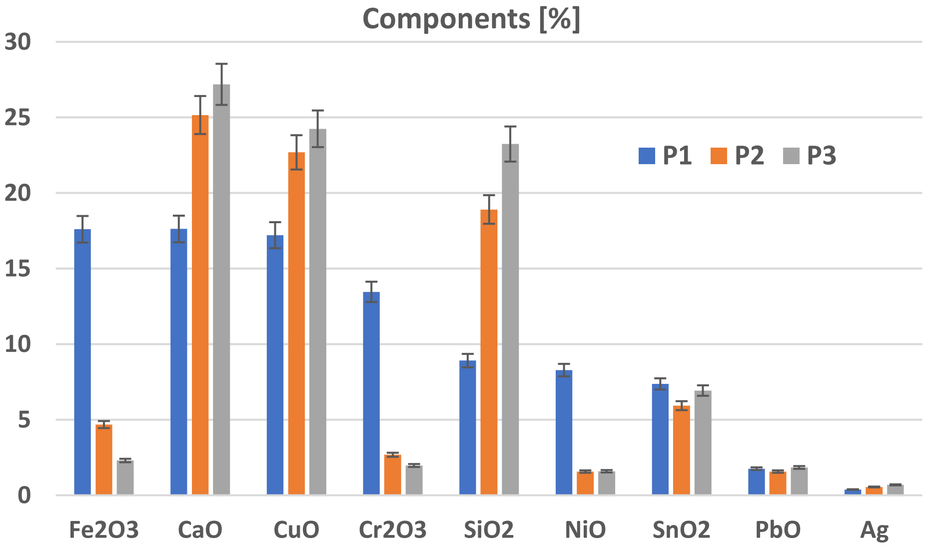

Figure 11. Component evolution vs. separation technology.

3.4. X-ray Diffraction (XRD) Analysis of Disks

Analysis via X-ray diffraction (XRD) of sintered disks from the powders P1–P3 is presented in Figures 12–14. The results largely confirmed the composition presented in Tables 2–4, obtained by spectrometry with X-ray fluorescence. After sintering, some new complex inorganic compounds were formed, based on some metallic ions. As the samples contained many elements, the peaks related to XRD analysis overlap, and therefore, the diffractograms are highly loaded.

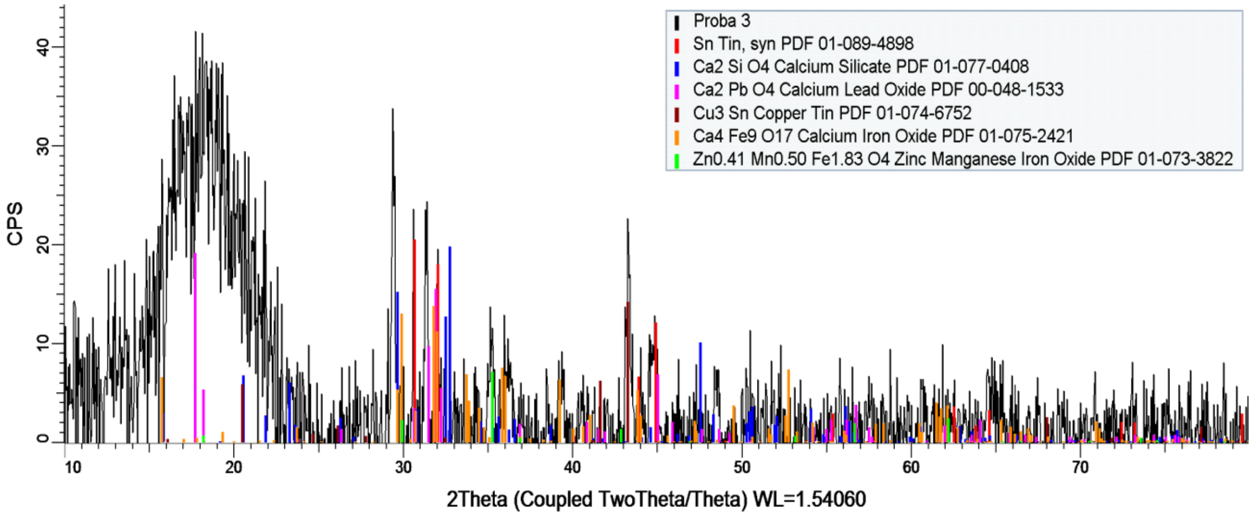

Figure 12. XRD analysis of disk from P1.

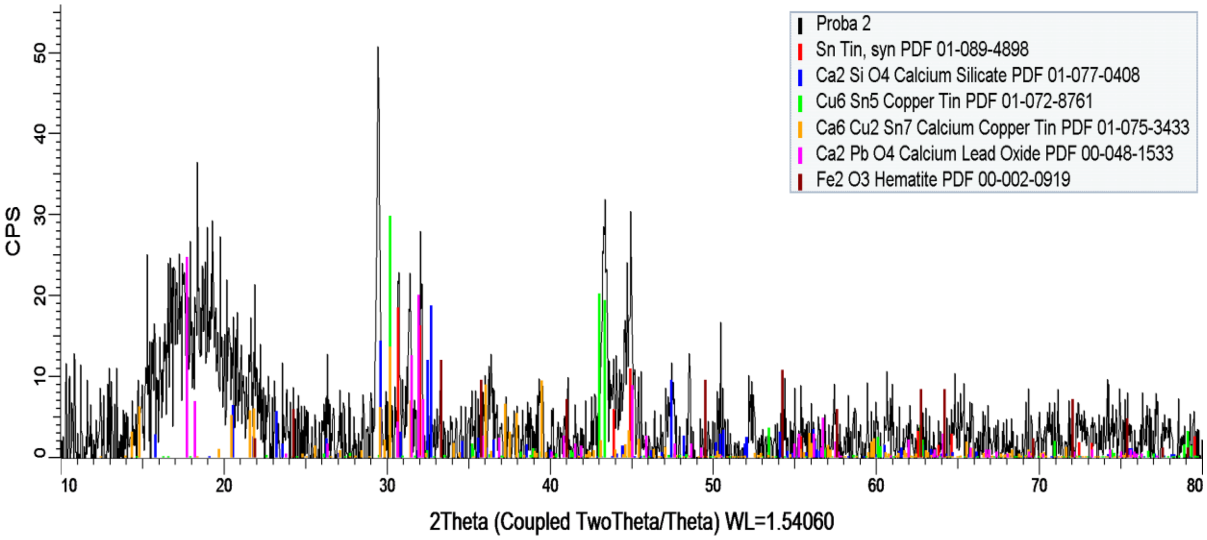

Figure 13. XRD analysis of disk from P2.

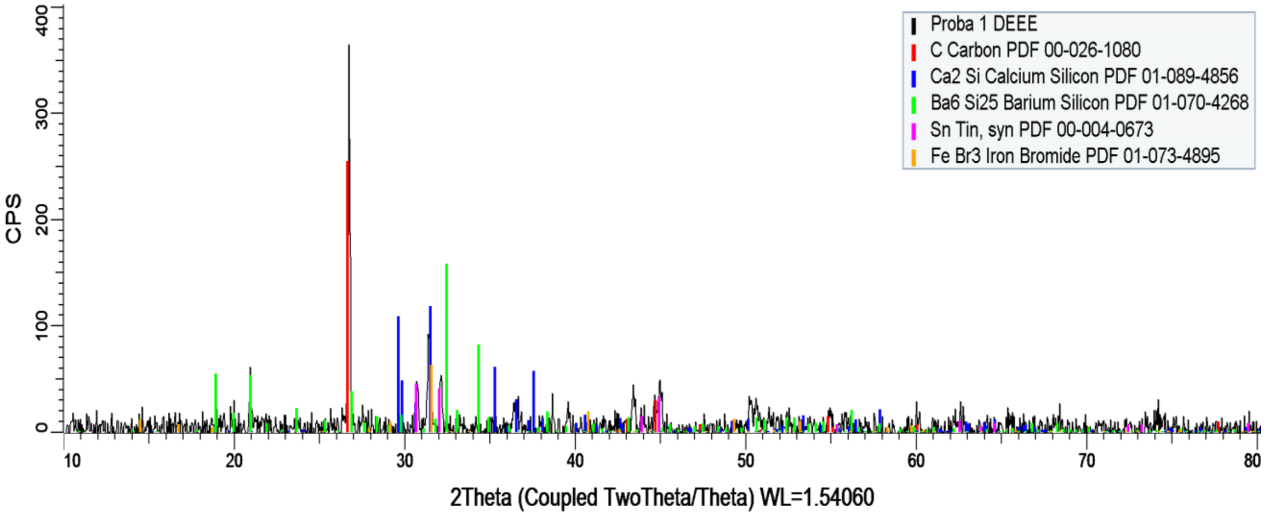

Figure 14. XRD analysis of disk from P3.

P1 (Figure 12) and P2 (Figure 13) contained mixed compounds based mainly on Ca, Si, Pb, Sn, Cu and Fe. Three common crystallographic phases were clearly identified in these samples: Ca_2SiO_4, Ca_2PbO_4 and Sn (in a tetragonal crystallization system). P1 additionally contained a crystalline phase based on ZnMnFe ($Zn_{0.41}Mn_{0.5}Fe_{1.83}O_4$, 2θ = 35.2°). From the analysis of the diffractograms of P1 and P2, it can be seen that the peaks of sample P1 have a higher intensity than those for sample P2, a fact to be further confirmed by the calculation of the degree of crystallinity, as presented in Table 5.

As regards the disk from P3, Figure 14, the presence of carbon can be noticed, due to the larger quantity of polymeric residues, reduced to residual carbon, fixed within the inorganic complexes. Accordingly, a very high intensity of the C peak can be observed (2θ = 26.5°) in relation to the other peaks, explained by texturing (preferential orientation in the 0 0 4 direction). In addition, crystallographic phases related to some types of compounds based on Ca, Si, Sn, Fe, Ba, Br, etc., were highlighted.

Compared to P2 and P3, P1 (Figure 15) showed the highest degree of crystallinity (59%) (Table 5).

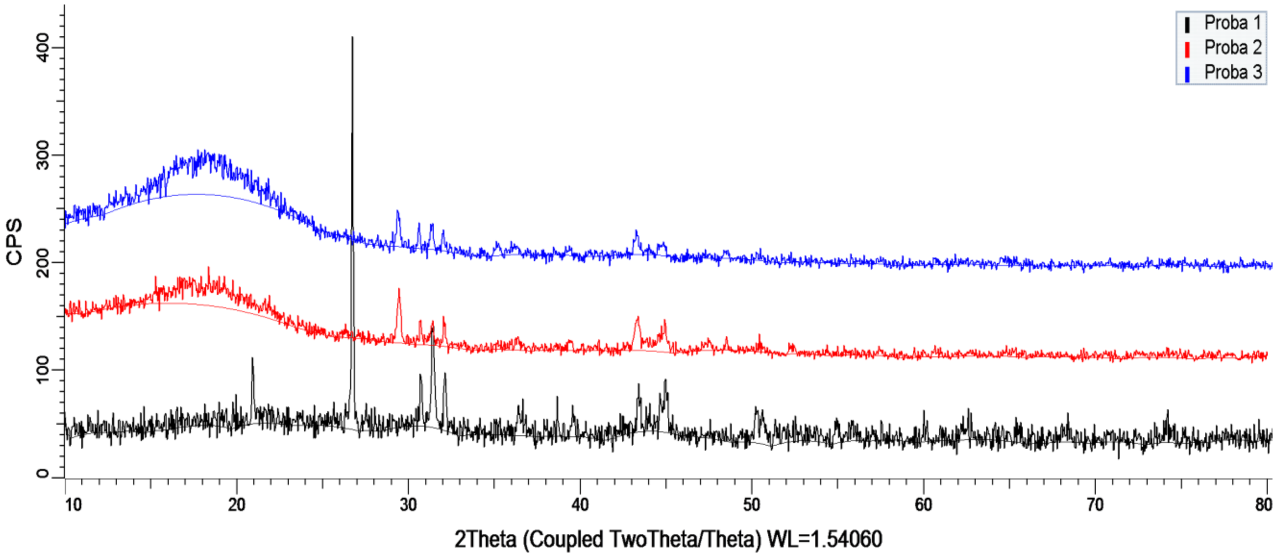

Figure 15. Comparative XRD analysis of P1–P3.

Table 5. Crystallinity degree of samples.

Sample	Crystallinity Degree [%]
P1	59
P2	35.4
P3	16.8

3.5. Evaluation of Vickers Hardness of Disks

Vickers hardness results are presented in Table 6 as an average of five measurements (eliminating the lowest and highest values), with a standard deviation under 5%.

The hardness seems to diminish with the increase in the concentration of the polymeric component. Accordingly, an increase in disks fragility was noticed when a lower percentage of metallic compounds was present.

Table 6. Vickers hardness results.

Sample	HV 0.1/10 [kgf/mm^2]
P1	15.91
P2	13.64
P3	11.28

The results are in line with and can be justified by the results from Section 3.2, this time referring to sintered powders. Sintered materials coming from powders with higher density present a higher hardness.

3.6. SEM Images and Evaluation of the Chemical Composition of Disks Carried Out by the Use of the EDS Probe

SEM images of samples with powders P1–P3 (at 5.000 magnitude) and related analysis (eight areas taken into account) are presented in Figures 16–18. A reasonable homogeneity of the investigated areas was noticed, meaning that the powders are relatively uniform in composition, and the sintering process was fairly performed. On the other hand, by analyzing the SEM images, it is obvious that the opacity (darker color) and granule dimensions increase with the increase in the quantity of polymeric residues, e.g., in P2 and P3, i.e., due to the presence of more residual carbon, fixed within the inorganic complexes.

When analyzing the centralized values for the concentration of each element in Figures 16–18, it is obvious that these results are in line with chemical analyses presented above, i.e., the concentrations of Fe, Cr and Ni are clearly diminishing, mainly by magnetic separation, when comparing the results for P1 with P2, and further with P3.

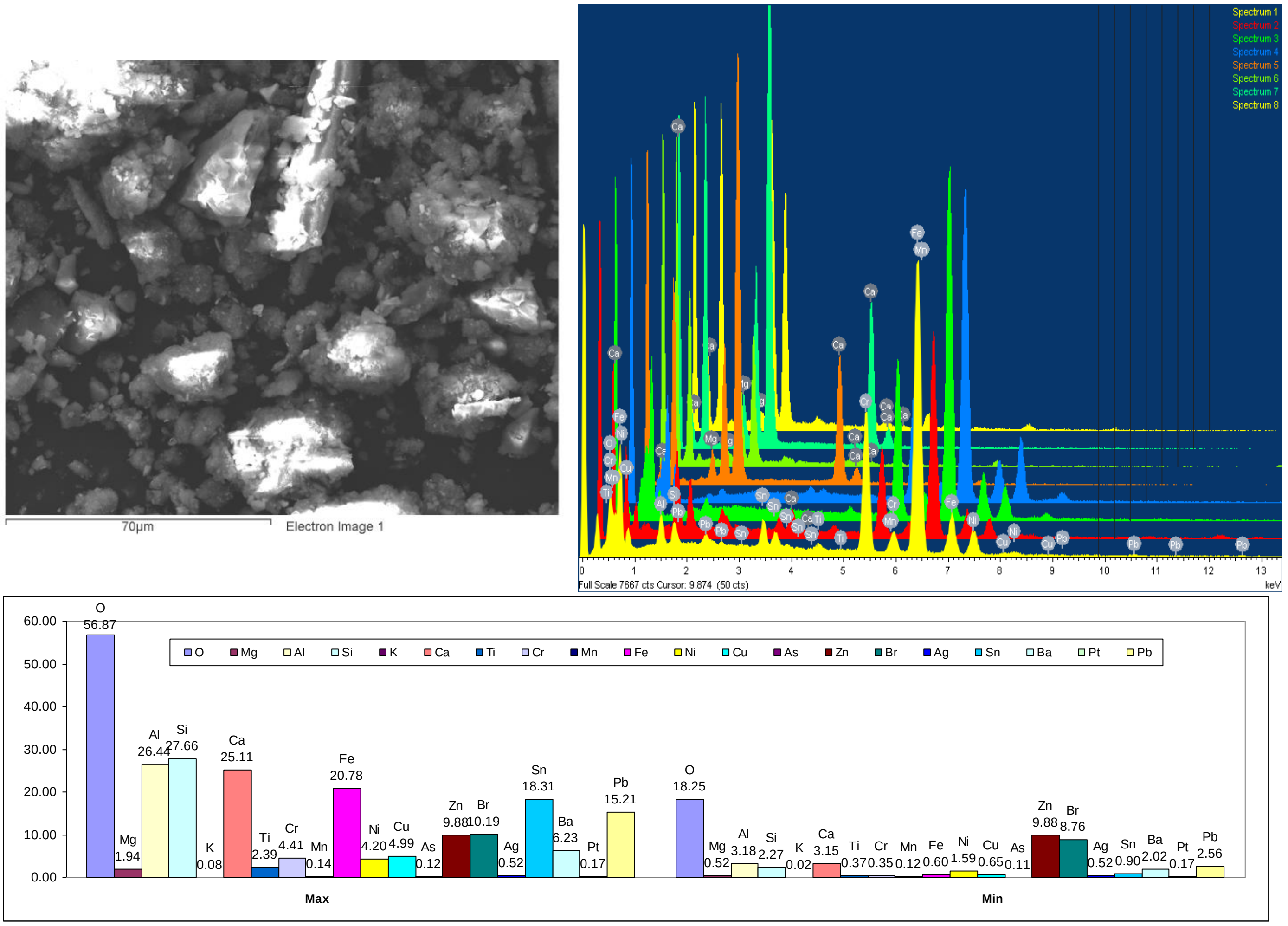

Figure 16. SEM image of P1 and related analysis.

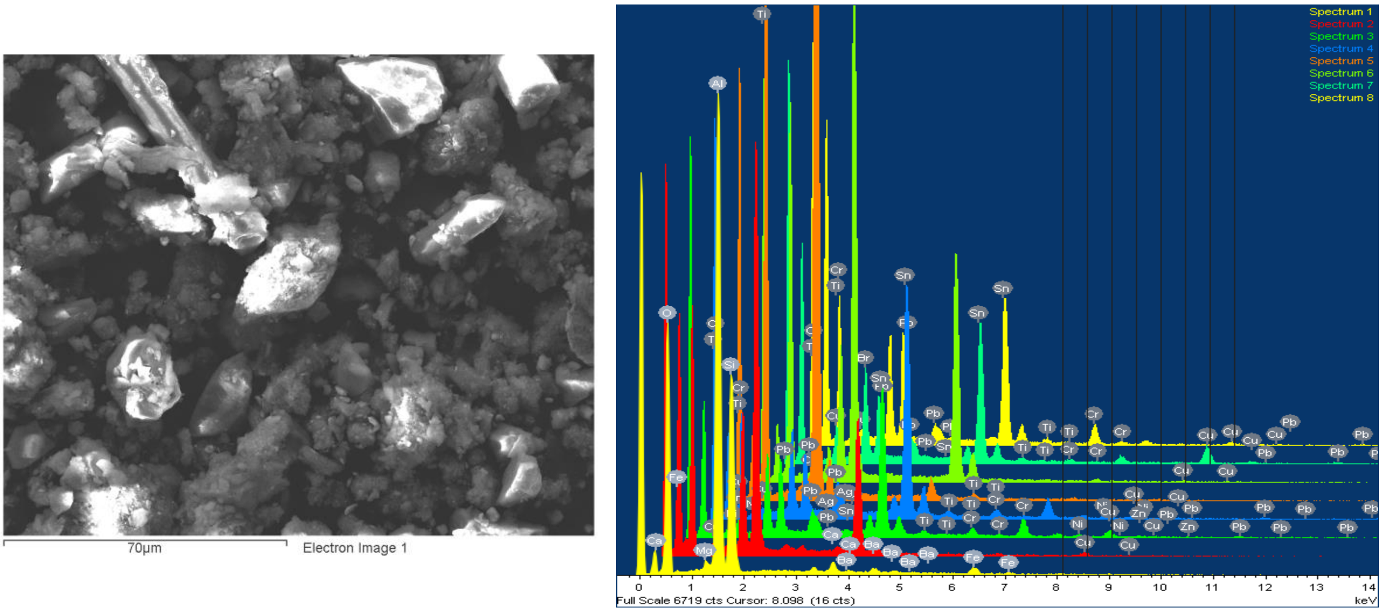

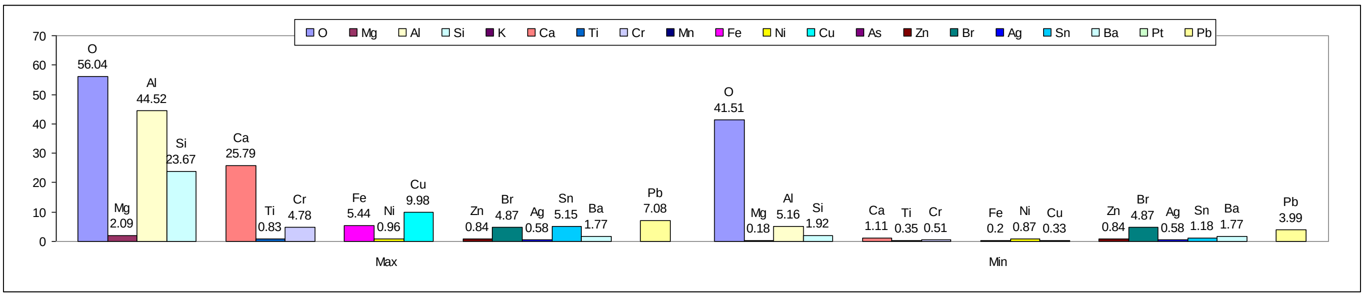

Figure 17. SEM image of P2 and related analysis.

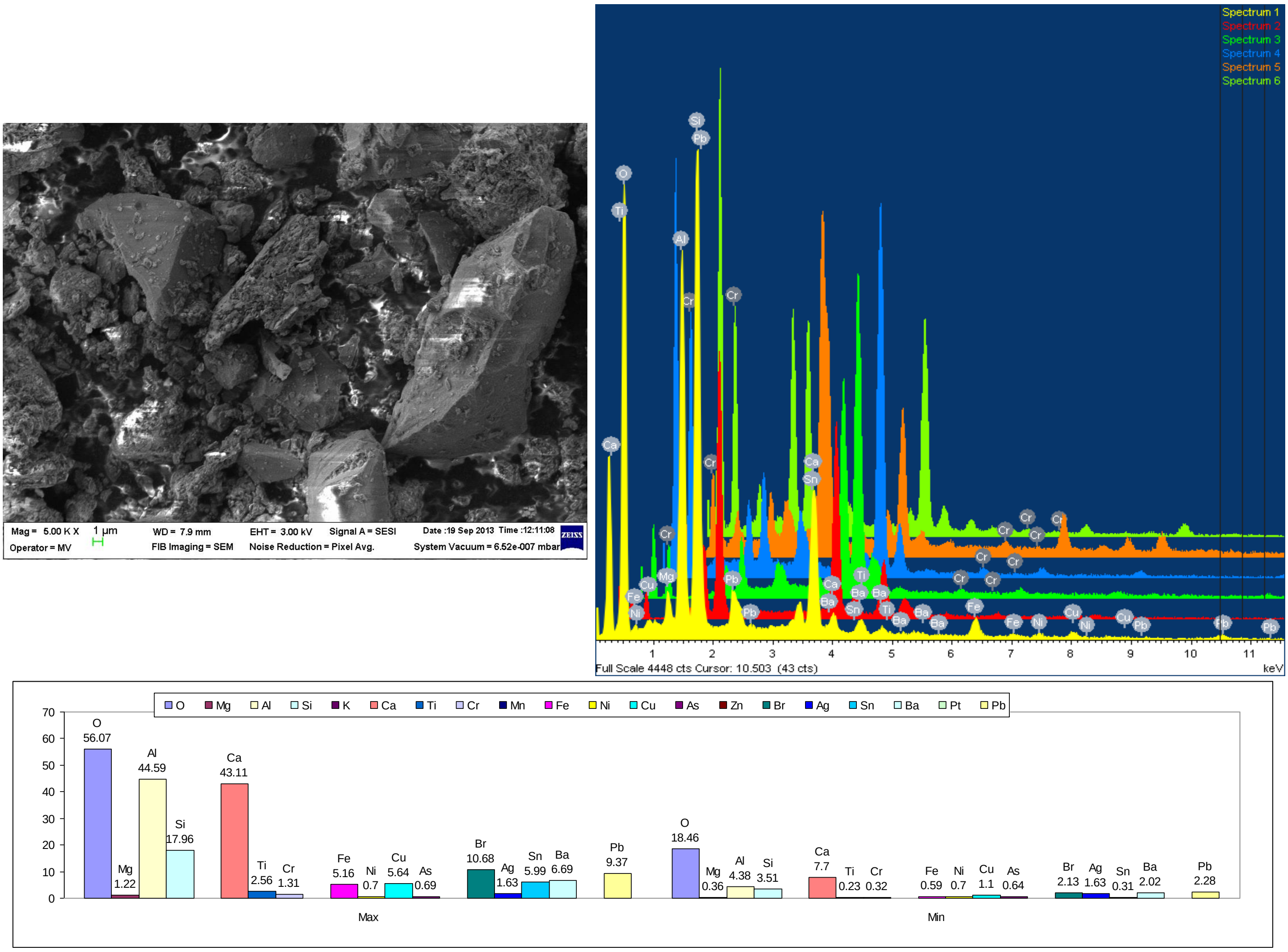

Figure 18. SEM image of P3 and related analysis.

Analyzing the maximum values obtained for each component element of the P1–P3 disk samples for the areas taken into account, it can be observed, in Figures 16–18:

– The elements Al, Si, Ca, Cu, Mg, Fe, Cr, Ni, Sn and Pb were identified in all disk samples in all areas, e.g., Al (with a maximum percentage of 44.59% in the case of area 2 of P2, a value close to the maximum also being identified in the case of area 5 of P1, namely 44.52%); Si (with a maximum percentage of 47.42% in the case of area 2 of P3); Cr (with a maximum percentage of 18.9% in the case of area 3 of P1); Fe (with a maximum percentage of 68.09% in the case of area 5 of P1, and 62.37% in the case of area 7 of P1); Ni (with a maximum percentage of 19.96% in the case of area 2 of P1); and Cu (with a percentage of 9.98% in the case of area 1 of P3).

- There are elements that appear only in limited areas: Ti, with a maximum percentage of 5.86% in the case of area 2 of P2; Zn, with a maximum percentage of 8.43% in the case of area 1 of P3; K, which appears only in the case of, e.g., area 1 of P2 with a percentage of 0.48%; Mn, which appears only in the case of, e.g., area 3 of P1 in a percentage of 0.85%; Al, which appears only in the case of, e.g., area 2 of P3 with a percentage of 0.63%; and Br, with a maximum percentage of 5.57% in the case of area 1 of P1.
- The presence of precious metals is also found, such as the following: Ag, in all areas, with a minimum percentage of 0.59%, e.g., in P1—area 1, and a maximum percentage of 1.63% in P3—area 2; Pt, only in limited areas, with a maximum percentage of 0.89%, e.g., in the case of P1—area 2; and Au, in many areas, with a maximum percentage of 0.96%, e.g., in the case of P3—area 5.

3.7. Dielectric Tests

Dielectric analysis for the three types of disks is presented in Figures 19–21.

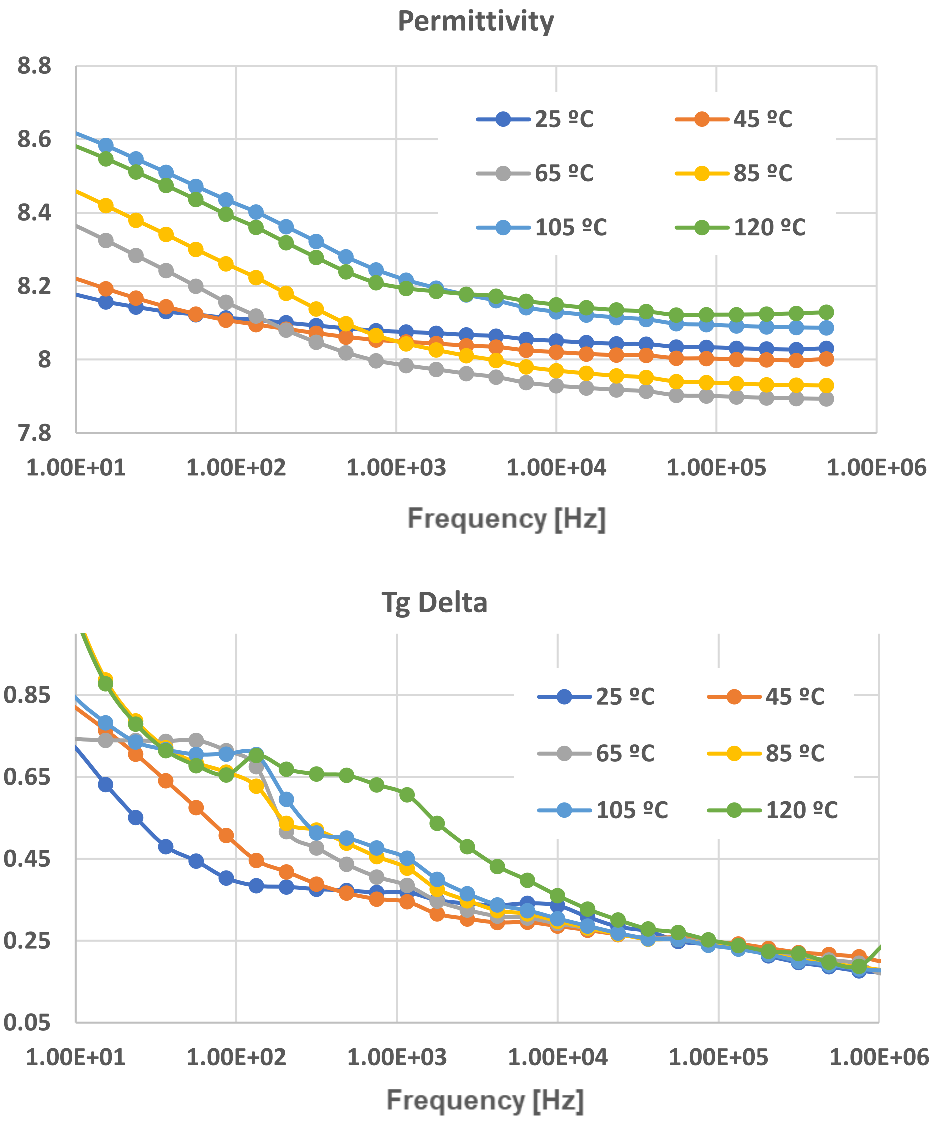

Figure 19. Dielectric properties of P1.

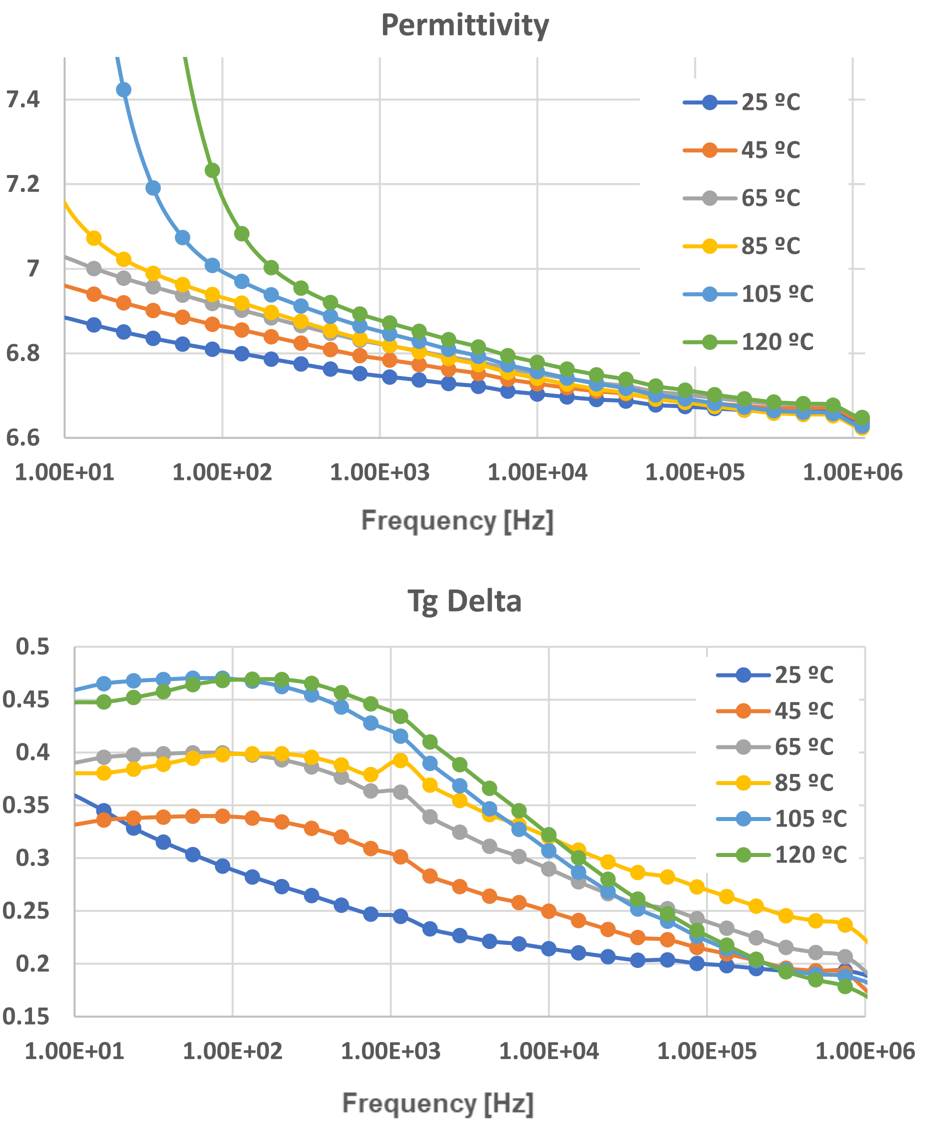

Permittivity

Tg Delta

Figure 20. Dielectric properties of P2.

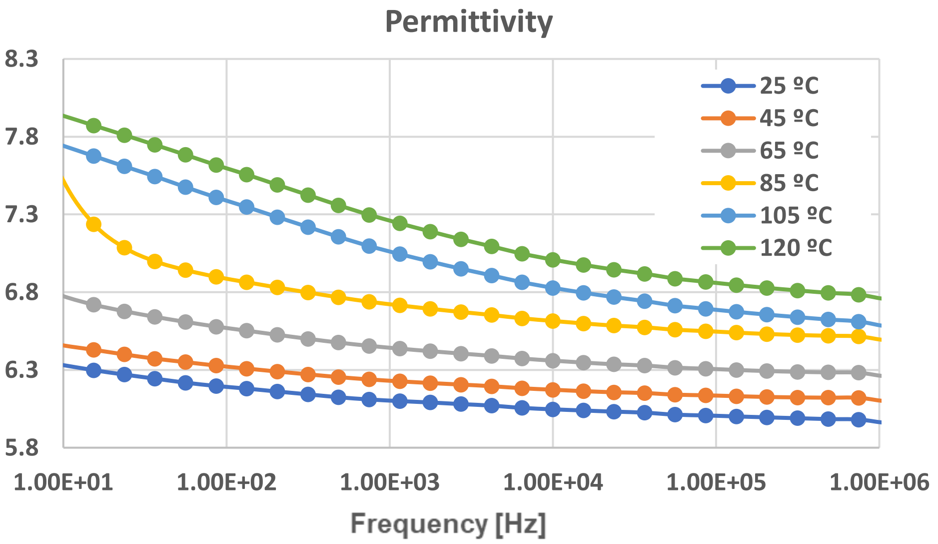

Permittivity

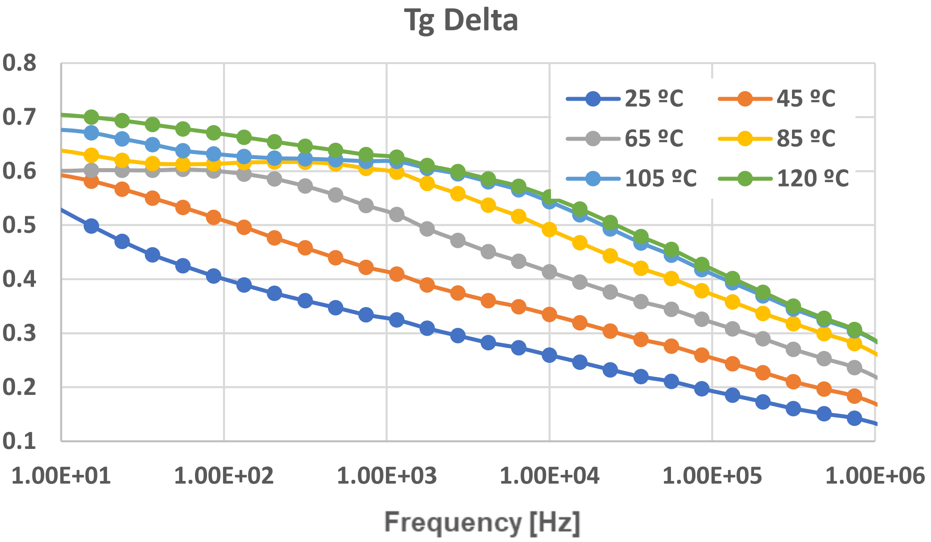

Figure 21. Dielectric properties of P3.

The characteristics taken into account were dielectric permittivity, dielectric loss factor (tangent delta) and conductivity. The highest values of permittivity and loss factor were reached by P1, followed by P2. The variation in the dielectric characteristics with temperature for P1 is specific to the composites with interfacial–ionic polarization processes, i.e., an increase with temperature at lower frequencies, followed by a progressive decrease with temperature at higher frequencies, explained by the initial activation of polarization of orientation, followed by a saturation process (Figure 19). At temperatures over 85 °C, due to the agitation of electric charges, the permittivity increases again. As regards P2 and P3 (Figures 20–21), the evolution of the dielectric loss factor is different from that of P1 due to the presence of more residues of polymeric components and an increased quantity of residual carbon, which is conductive matter. The polarization in this case is more interfacial–dipolar, and we noticed an important increase with temperature, especially at lower frequencies for the permittivity, where the interfacial effect is predominant. On the other hand, an increase at lower frequencies and a decrease at higher frequencies was noticed at higher temperatures for the dielectric loss factor, an aspect that confirms the influence of dipolar polarization, mainly for P3. As regards the conductivity values, they are not so different between the three samples, but P3 presents slightly higher values due to the presence of a larger content of residual carbon.

Taking into account all the results presented above, especially the values of the dielectric parameters, one can notice the economic value of such powders as additives in composites for electromagnetic shielding purposes. They can efficiently substitute scarce raw materials actually used as additives in composites, coatings and paints, mainly due to their high permittivity (above 7.5 for P1 and above 6 for P2 and P3, in all frequency domains) and dielectric loss factor (above 0.2 in all cases, in all frequency domains).

End-of-life mobile phones, smart devices, laptops and tablets constitute one of the fastest growing electrical and electronic equipment waste streams in the world (e.g., about 5.3 billion mobile phones became waste in 2022 only). EC recommended new strategies for improving the rate of return and recycling of used and waste mobile phones, tablets and laptops [21]. Unfortunately, the actual circuit board processing from WEEE, [22–24] is still not selective, i.e., is performed only for precious metal recovery by melting entire PCBs or chemical treatment/leaching in acid solutions, all of which are polluting technologies that lead to a large quantity of non-recyclable waste, under which circumstances many valuable components are lost. In [25], a brief calculus related to the global WEEE recycling estimated an increase of 3 million new job opportunities per year under the circumstances that the environmental load (i.e., the cost required to offset the environmental impacts) was estimated up to 9 USD/kg, so new approaches must be taken into account aimed at reducing the related carbon emissions.

It was estimated that between 2014 and 2020, embodied GHG emissions generated from information and communications technology (ICT) devices increased by 53%, up to 580 million metric tons (MMT) of CO_2 emitted in 2020. That is why the purpose of the research was also to outline the technological evolution in the domain of ICT devices. This presumes less metal use, better integration of electronic components and other technologies for connecting (eventually soldering) the electronic parts. The way we approached the PCB selection and primary dismantling of some classical components, along with ferritic and metallic powders separation, is in line with newer electronic technologies, which progressively eliminates such components. The importance of integrating in fabrication circuits made of such powders with special electromagnetic features lies also in the fact that statistics show that nowadays, the recovery of electronic parts comprises about 20% of WEEE, and recovered metals from WEEE constitute under 9%, from which only 3–4% come from electronic parts (wt%), even if the recovery rate is high, as presented above. Consequently, over 90% of electronic part scrap represents the origin of the powder studied in the paper, up to now destined to be dumped.

The technology described in this paper allows, beyond the classical recovery of useful metals, here with an average recovery rate of over 97% (e.g., in line with the data presented in [26]), a potential exploitation of remaining powder as raw material for sintered electromagnetic devices. The use of such semiconducting fillers for, e.g., hybrid materials for electromagnetic shielding—in fact, the use of electromagnetically active inorganic matters—is meeting rising interest nowadays [27]. According to the achieved features of the sintered discs from the P3 residual powder, described above, mainly the dielectric ones, the following applications may become possible, to be fabricated by spark plasma sintering: hard composites with high electromagnetic shielding efficiency, as in [28]; electromagnetic interference and RFID absorbers and related gaskets, as in [29,30]; microwave absorbers, as in [31]; radar emission absorbers, as in [32]; high-k dielectric devices; high-Q dielectric resonators; and other related devices for electromagnetic applications.

Another important application of the powders is as ingredients/pigments in electromagnetic shielding paints and primers, due mainly to the actual pressure of reducing the quantity of scarce metal powders (mainly Ag, Cu and Ni), nanocarbon or ferrite powders, which are common ingredients in such paints [33]. A homologue application, but with lower technical impact, related to electromagnetic shielding systems in building areas, is presented in [34], along with a preliminary life cycle analysis.

The recent literature generally addresses the environmental impact assessment of WEEE and management strategies towards industrially integrating WEEE [35–37], but without offering global sustainable solutions, other than metal recovery, as in [24,25,38], or eventually waste plastic recovery, as in [34,39]. The application of circular economy practices in WEEE management represents a new scientific trend, as presented, e.g., in [40–46], but in all actual publications, the concept is described too generally, without a clear example of technological circuits to be recommended, and practically recommending sending non-metallic residual powders to dumps after metal extraction.

We present below a practical analysis of the technological sustainability of the studied powders derived from WEEE, in terms of a circular economy [47]. The final purpose would be “Zero Waste Recycling of PCBs”, a concept preliminary described in [48]. The principle of this concept is shown in Figure 22.

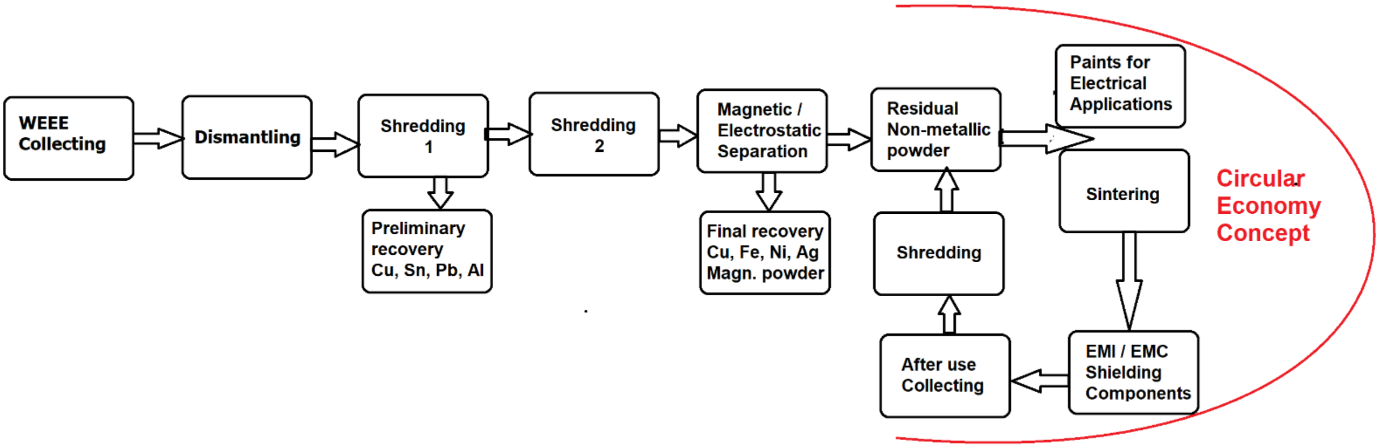

Figure 22. Circular economy scheme for zero-waste recycling of PCBs.

The technological stages follow the classical recycling circuit, i.e., electronic waste collection and dismantling (of large components, metallic parts as radiators, etc., coils/transformers, cables, etc.) till the remaining PCBs have mostly small electronic components, first-stage shredding of PCBs (with separation of large items without components—sent to preliminary recovery of metals such as Cu, Sn, Pb, and Al), second-stage shredding of PCBs to create a powder, described as P1 in this paper; magnetic separation of the powder, described as P2 in this paper (resulting in a mixture of Fe, Ni and magnetic powders as metallic oxides); and electrostatic separation of the residual powder, described as P3 in this paper (resulting in a mixture of metals such as Cu, Sn, Pb, Ag, and Au). In classical technologies, the residual powder is sent to a dump, but in our case, it follows the concept of the circular economy, being used for innovative high-value products: as ingredients for paints with electrical applications, or for advanced hard components with specialized electromagnetic features after a sintering process. These paints may follow the already-established recycling process under the circular economy concept, as described in [49]. The hard components are self-recyclable by the same technology, being suitable for specialized shredding processes and reintegrated within residual powder, because they have the same composition. In this way, the concept is ‘cradle to cradle’ and tends to zero-waste recycling within a closed-loop system in order to optimize resource efficiency. The proposed model of re-using metal and non-metal fractions of PCBs may lead to new business models for residual powder integration within electromagnetic components technologies, and new markets for the respective components. Benefits of the proposed recycling scheme include financial and environmental gains, since large quantities of powders do not go to landfills, and a reduced chemical pollution of WEEE, initially leading to harming soil and aquatic life.

When producing new electromagnetic shielding systems from powders from recycled WEEE components, only 10% of the original CO_2 emissions are released in the process. Accordingly, we estimate that the technology described in the paper could be able to reduce, by a minimum of 15%, the embodied GHG emissions generated from ICT devices by advanced recycling under the circular economy concept, and reduce by 90% the carbon footprint related to the processing of inorganic ingredients to be used in composites or paints for electromagnetic shielding purposes, without speaking about their economic benefit, under the circumstances that the powders obtained by recycling are at least 10 times cheaper than virgin raw materials.

By tending to the desiderates of “no net emissions of greenhouse gases by 2050” and of “economic growth decoupled from scarce resource use”, the proposed technology is also in line with The European Green Deal strategy [50].

4. Conclusions

This paper presents a technological approach for obtaining electromagnetically active powders and related sintered components by the selective recycling of electronic PCB waste, in particular scrap electronic components, in line with actual electronic technology and under the circular economy concept.

PCB scraps were submitted to a succession of grinding processes, followed by progressive magnetic and electrostatic separation, resulting in two final fractions: metallic particles (with residues of ferritic powders) and non-magnetic/non-metallic particles including different metallic oxides. Three types of powders were analyzed, i.e., powder after fine grinding, after magnetic separation and after electrostatic separation. Finally, the powder material was processed within a spark plasma sintering furnace in order to obtain solid samples with a diameter of 12 mm and a thickness between 2 and 3 mm.

The results of the thermal analysis outlined for all samples specific decomposition processes, at temperatures depending on the nature of the residual metals/metallic oxides.

The chemical analysis of powders, via spectrometry with X-ray fluorescence (XRF), emphasized the presence of a mixture of metal oxides (mainly CaO, Fe_2O_3, CuO, Cr_2O_3, SiO_2, SnO_2, NiO, ZrO_2, PbO, and ZnO) and traces of metals (mainly Ag), with concentrations diminishing along with the purification process, from 98.32% after fine grinding till 78,65% after electrostatic separation.

The EDS analysis revealed that there was a relatively uniform composition of disks in all analyzed areas, the sintering process being effectively performed. By analyzing the SEM images, it is noticed that the opacity (darker color) and granule dimensions increase with the increase in the quantity of polymeric residues, mainly in the samples from powders after electrostatic separation, due to the presence of more residual carbon, fixed within the inorganic complexes.

The most important analysis was related to dielectric parameters, mainly permittivity and loss factor. It was concluded that the powders obtained by the proposed technology could efficiently substitute scarce raw materials actually used as additives in composites, coatings and paints, mainly due to their high permittivity (above 6 in all frequency domains) and dielectric loss factor (above 0.2 in all cases, in all frequency domains).

The technology described in the paper allows the recovery of precious metals, but also allows the recovery of powders with special electromagnetic features, under the circumstances that electronic parts in all comprise about 20%, and recovered metals from WEEE comprise under 9%, from which only 3–4% is from the electronic parts (wt%). Accordingly, we estimate that the technology described in this paper is a sustainable one, as it could be able to reduce by a minimum of 15% the embodied GHG emissions generated from ICT devices by advanced recycling under the circular economy concept, and reduce by 90% the carbon footprint related to the processing of inorganic ingredients to be used in composites or paints for electromagnetic shielding purposes, without speaking about their economic benefit, under the circumstances that the powders obtained by recycling are at least 10 times cheaper than the homologous virgin raw materials.

Author Contributions: Conceptualization, C.S.; methodology, R.C.C., C.S. and M.A.; validation, R.C.C., C.S. and M.A.; formal analysis, M.A. and C.S.; investigation, R.C.C., C.S. and M.A.; data curation, R.C.C., C.S. and M.A.; writing—original draft preparation, C.S. and R.C.C.; writing—review and editing, C.S.; visualization, R.C.C., C.S. and M.A.; supervision, C.S. and R.C.C. All authors have read and agreed to the published version of the manuscript.

Funding: No financial support.

Data Availability Statement: The data are included in this study.

Conflicts of Interest: The authors declare no conflicts of interest.

References

1. Available online: https://www.eea.europa.eu/policy-documents/thematic-strategy-on-the-prevention (accessed on 06. June 2024).
2. Available online: https://www.eea.europa.eu/policy-documents/thematic-strategy-on-the-sustainable (accessed on 06. June 2024).
3. Directive 2002/96/EC Regarding Electrical and Electronic Equipment Waste. Available online: https://www.eumonitor.eu/9353000/1/j4nvk6yhcbpeywk_j9vvik7m1c3gyxp/vitgbgibgvwc (accessed on 06. June 2024).
4. Available online: https://weee-forum.org/iewd-about/#:~:text=According%20to%20the%20latest%20UN's,82%20billion%20kg%20by%202030 (accessed on 06. June 2024).
5. Directive 2012/19/EU on Waste Electrical and Electronic Equipment (WEEE). Available online: https://eur-lex.europa.eu/legal-content/EN/TXT/PDF/?uri=CELEX:32012L0019 (accessed on 06. June 2024).
6. Martinho, G.; Pires, A.; Saraiva, L.; Ribeiro, R. Composition of plastics from waste electrical and electronic equipment (WEEE) by direct sampling. *Waste Manag.* **2012**, *32*, 1213–1217.
7. Gerne, G.; Carbajosa, J.R. *Electrical and Electronic waste (E-Waste) Dismantling and Recycling Manual*; Technical Report; United Nations Development Programme: New York, NY, USA, 2022. https://doi.org/10.13140/RG.2.2.23420.21129.
8. Vermeșan, H.; Tiuc, A.E.; Purcar, M. Advanced Recovery Techniques for Waste Materials from IT and Telecommunication Equipment Printed Circuit Boards. *Sustainability* **2020**, *12*, 74; https://doi.org/10.3390/su12010074.
9. Chen, M.; Avarmaa, K.; Taskinen, P.; Klemettinen, L.; Michallik, R.; O'Brien, H.; Jokilaakso, A. Handling trace elements in WEEE recycling through copper smelting-an experimental and thermodynamic study. *Miner. Eng.* **2021**, *173*, 107189.
10. Directive 2003/108/EC on Waste Electrical and Electronic Equipment (WEEE). Available online: https://leap.unep.org/en/countries/eu/national-legislation/directive-2003108ec-european-parliament-and-council-amending (accessed on 06. June 2024).
11. Directive 2002/95/EC. Available online: https://www.analytice.com/en/directive-2002-95-ec-also-known-as-the-rohs-directive/ (accessed on 06. June 2024).
12. Ghulam, S.; Abushammala, H. Challenges and Opportunities in the Management of Electronic Waste and Its Impact on Human Health and Environment. **2***Sustainability* **023**, *15*, 1837; https://doi.org/10.3390/su15031837.
13. Hea, Y.; Xu, Z. Recycling gold and copper from waste printed circuit boards using chlorination process. *RSC Adv.* **2015**, *12*, 8957–8964.
14. Lossless Recycling of E-Waste Into Additive Manufacturing Powders. Available online: https://www.additivemanufacturing.media/articles/lossless-recycling-of-e-waste-into-additive-manufacturing-powders (accessed on 06. June 2024).
15. European Recycling Platform: Recycling of Waste Electrical and Electronic Equipment. Available online: https://erp-recycling.org/en-it/consorzio/collective-schemes/weee/ (accessed on 06. June 2024).
16. European Recycling Platform: Streams—WEEE. Available online: https://erp-recycling.org/en-se/what-we-cover/streams/weee/ (accessed on 06. June 2024).
17. Rajahalme, J.; Perämäki, P.; Budhathoki, R.; Väisänen, A. Effective Recovery Process of Copper from Waste Printed Circuit Boards Utilizing Recycling of Leachate. *Adv. Process Metall.* **2021**, *73*, 980–987.
18. Recycling Copper from Printed Circuit Boards. Accessible online: https://www.rigiflex.com/blog/recycling-copper-from-printed-circuit-boards/ (accessed on 06. June 2024).
19. Veit, H.M.; Diehl, T.R.; Salami, A.P.; Rodrigues, J.S.; Bernardes, A.M.; Tenório, J.A.S. Utilization of magnetic and electrostatic separation in the recycling of printed circuit boards scrap. *Waste Manag.* **2005**, *25*, 67–74.
20. ISO 3923-2:1981: Metallic Powders—Determination of Apparent Density. Available online: https://www.iso.org/standard/9559.html (accessed on 6 June 2024).
21. Commission recommendation (EU) 2023/2585 on Improving the Rate of Return of Used and Waste Mobile Phones, Tablets and Laptops. Available online: https://eur-lex.europa.eu/legal-content/EN/TXT/PDF/?uri=OJ:L_202302585 (accessed on 06. June 2024).
22. Bruno, M.; Sotera, L.; Fiore, S. Analysis of the influence of mobile phones' material composition on the economic profitability of their manual dismantling. *J. Environ. Manag.* **2022**, *309*, 114677.
23. Fontana, D.; Pietrantonio, M.; Pucciarmati, S.; Rao, C.; Forte, F. A comprehensive characterization of End-of-Life mobile phones for secondary material resources identification. *Waste Manag.* **2019**, *99*, 22–30.
24. Gulliani, S.; Volpe, M.; Messineo, A.; Volpe, R. Recovery of metals and valuable chemicals from waste electric and electronic materials: A critical review of existing technologies. *RSC Sustain.* **2023**, *1*, 1085–1108. https://doi.org/10.1039/D3SU00034F.
25. Yang, W.D.; Sun, Q.; Ni, H.G. Cost-benefit analysis of metal recovery from e-waste: Implications for international policy. *Waste Manag.* **2021**, *123*, 42–47.
26. Bizzo, W.A.; Figueiredo, R.A.; de Andrade, V.F. Characterization of printed circuit boards for metal and energy recovery after milling and mechanical separation. *Materials* **2014**, *7*, 4555–4566. https://doi.org/10.3390/ma7064555.
27. Zachariah, S.M.; Grohens, Y.; Kalarikkal, N.; Thomas, S. Hybrid materials for electromagnetic shielding: A review. *Polym. Compos.* **2022**, *43*, 2507–2544. https://doi.org/10.1002/pc.26595.
28. Long, L.; Xiao, P.; Luo, H.; Zhou, W.; Li, Y. Enhanced electromagnetic shielding property of cf/mullite composites fabricated by spark plasma sintering. *Ceram. Int.* **2019**, *45*, 18988–18993.
29. Available online: https://hollandshielding.com/en/emi-rfid-absorbers-ferrites-pyramids?gad_source=1&gclid=Cj0KCQjwhb60BhClARIsABGGtw_NS58kj2Zc0jgZgpQakmxvVO-RmdZuIz-cWdkMJSE8c2ngNYRbVnOUaAgFsEALw_wcB (accessed on 06. June 2024).

30. Available online: https://www.solianiemc.com/en/cp/emi-rfi-shielding-gasket/ (accessed on 06. June 2024).
31. Li, X.; Zhu, L.; Su, Z.; Li, X.; Yu, W.; Liu, J.; Lv, C. Microwave absorbing performance and temperature resistance of multifunctional foamed ceramics prepared by the sintering method. *Ceram. Int.* **2023**, *49 Pt A*, 34992–35000.
32. Afanasiev, A.; Bakhracheva, Y. Analysis of the Types of Radar Absorbing Materials. *NBI Technol.* **2019**, *13*, 35–38. https://doi.org/10.15688/NBIT.jvolsu.2019.2.6.
33. EMF and RFI Shielding with Conductive Paints. Available online: https://www.antala.uk/emf-and-rfi-shielding-with-conductive-paints/ (accessed on 30 June 2024).
34. La Rosa, A.D.; Grammatikos, S.A.; Ursan, G.A.; Aradoaei, S.; Summerscales, J.; Ciobanu, R.C.; Schreiner, C.M. Recovery of electronic wastes as fillers for electromagnetic shielding in building components: An LCA study. *J. Clean. Prod.* **2021**, *280 Pt 2*, 124593.
35. Xiang, D.; Mou, P.; Wang, J.; Duan, G.; Zhang, H.C. Printed circuit board recycling process and its environmental impact assessment. *Int. J. Adv. Manuf. Technol.* **2007**, *34*, 1030–1036. https://doi.org/10.1007/s00170-006-0656-6.
36. Ismail, H.; Hanafiah, M.M. An overview of LCA application in WEEE management: Current practices. *J. Clean. Prod.* **2019**, *232*, 79–93. https://doi.org/10.1016/j.jclepro.2019.05.329.
37. Ikhlayel, M. An integrated approach to establish e-waste management systems for developing countries. *J. Clean. Prod.* **2018**, *170*, 119–130. https://doi.org/10.1016/j.jclepro.2017.09.137.
38. Priya , A.; Hait, S., Comprehensive characterization of printed circuit boards of various end-of-life electrical and electronic equipment for beneficiation investigation. *Waste Management* **2018**, *75*, 103–123. https://doi.org/10.1016/j.wasman.2018.02.014.
39. Wagner, F.; Peeters, J.R.; De Keyzer, J.; Janssens, K.; Duflou, J.R.; Dewulf, W. Towards a more circular economy for WEEE plastics—Part A: Development of innovative recycling strategies. *Waste Manag.* **2019**, *100*, 269–277.
40. De Meester, S.; Nachtergaele, P.; Debaveye, S.; Vos, P.; Dewulf, J. Using material flow analysis and life cycle assessment in decision support: A case study on WEEE valorization in Belgium. *Resour. Conserv. Recycl.* **2019**, *142*, 1–9.
41. Bressanelli, G.; Saccani, N.; Pigosso, D.; Perona, M. Circular Economy in the WEEE industry: A systematic literature review and a research agenda. *Sustain. Prod. Consum.* **2020**, *23*, 174–188.
42. Ghisellini, P.; Quinto, I.; Passaro, R.; Ulgiati, S. Circular Economy Management of Waste Electrical and Electronic Equipment (WEEE) in Italian Urban Systems: Comparison and Perspectives. *Sustainability* **2023**, *15*, 9054; https://doi.org/10.3390/su15119054.
43. Awasthi, A.K. Circular economy of the WEEE: A potential waste resource. *Waste Manag. Res.* **2023**, *41*, 1601–1602. https://doi.org/10.1177/0734242X231202199.
44. Pan, X.; Wong, C.; Li, C. Circular economy practices in the waste electrical and electronic equipment (WEEE) industry: A systematic review and future research agendas. *J. Clean. Prod.* **2022**, *365*, 132671.
45. Ahmadinia, M.; Setchi, R.; Evans, S.L.; Baker, T.; Gregory, S.; Cox, J.; Rodriguez, L.G.; Giblin, S.; Clode, S.; Litos, L.; et al. Transforming E-Waste into Value: A Circular Economy Approach to PCB Recycling. In *Sustainable Design and Manufacturing*; Springer: Singapore, 2023; pp. 275–285. https://doi.org/10.1007/978-981-99-8159-5_24.
46. Cozza, G.; D'Adamo, I.; Rosa, P. Circular manufacturing ecosystems: Automotive printed circuit boards recycling as an enabler of the economic development. *Prod. Manuf. Res.* **2023**, *11*, 2182837. https://doi.org/10.1080/21693277.2023.2182837.
47. Available online: https://www.circularise.com/blogs/r-strategies-for-a-circular-economy (accessed on 06. June 2024).
48. Copani, G.; Colledani, M.; Brusaferri, A.; Pievatolo, A.; Amendola, E.; Avella, M.; Fabrizio, M. Integrated Technological Solutions for Zero Waste Recycling of Printed Circuit Boards (PCBs). In *Factories of the Future*; Springer: Cham, Switzerland, 2019; pp. 149–169. Available online: https://re.public.polimi.it/retrieve/handle/11311/1075132/338855/Integrated%20Technological%20Solutions%20for%20Zero%20Waste%20Recycling%20of%20Printed%20Circuit%20Boards%20%28PCBs%29.pdf (accessed on 06. June 2024).
49. Paint Industry and Circular Economy. 2022. Available online: https://www.paintsforlife.eu/en/blog/paint-industry-and-circular-economy-it-possible (accessed on06. June 2024).

50. The European Green Deal. Available online: https://commission.europa.eu/strategy-and-policy/priorities-2019-2024/european-green-deal/delivering-european-green-deal_en (accessed on 06. June 2024).

polymers

MDPI

Article

Thermoplastic Composite Hot-Melt Adhesives with Metallic Nano-Particles for Reversible Bonding Techniques Utilizing Microwave Energy

Romeo Cristian Ciobanu *, Mihaela Aradoaei and George Andrei Ursan

Department of Electrical Measurements and Materials, Gheorghe Asachi Technical University, Boulevard D. Mangeron 71, 700050 Iasi, Romania; mosneagum@yahoo.com (M.A.); andrei_urs@yahoo.com (G.A.U.)
* Correspondence: r.c.ciobanu@tuiasi.ro

Abstract: This study investigated the creation of nano-composites using recycled LDPE and added 7.5 wt% nanofillers of Al and Fe in two varying particle sizes to be used as hot-melt adhesives for reversible bonding processes with the use of microwave technology. Reversible bonding relates to circular economy enhancement practices, like repair, refurbishment, replacement, or renovation. The physical–chemical, mechanical, and dielectric characteristics were considered to determine the impact of particle size and metal type. Through the investigation of electromagnetic radiation absorption in the composites, it was discovered that the optimal bonding technique could potentially involve a frequency of 915 MHz and a power level of 850 × 10^3 W/kg, resulting in an efficient process lasting 0.5 min. It was ultimately proven that the newly created hot-melt adhesive formulas can be entirely recycled and repurposed for similar bonding needs.

Keywords: nano-composites; hot-melt adhesives; reversible bonding; microwave technology

check for updates

Citation: Ciobanu, R.C.; Aradoaei, M.; Ursan, G.A. Thermoplastic Composite Hot-Melt Adhesives with Metallic Nano-Particles for Reversible Bonding Techniques Utilizing Microwave Energy. *Polymers* **2024**, *16*, 3496. https://doi.org/10.3390/polym16243496

Academic Editors: Silvia González Prolongo and Antonio Vázquez-López

Received: 1 November 2024
Revised: 7 December 2024
Accepted: 13 December 2024
Published: 15 December 2024

1. Introduction

Bonding technologies are commonly used in various industries, particularly in sectors like automotive, naval, and aerospace, where composite materials, metals, and plastics are employed. Such materials are commonly joined during the manufacturing processes with mechanical fasteners, welding, or adhesive bonding techniques. The first process is slow, costly, labor-consuming, and sometimes non-esthetic. The latter two processes have many benefits over mechanical fastening, such as a faster process speed, weight-saving properties, less material demand, and cost effectiveness. These techniques are currently increasingly used for assembling processes; however, they have the most important drawback of being irreversible. Disbonding or, more advantageous, reversible bonding are new ideas connected to circular economy, primarily driven by the European Community's recycling plan in different industries, such as the automotive sector, which follows the End-of-Life Vehicles Directive [1]. Reversible bonding may be necessary to separate a temporary structure or a previously bonded assembly for activities such as repair, refurbishment, replacement, or renovation. Streamlined disbanding processes also make it easier to recycle materials and components from items and structures that are bonded with adhesive. Salvageable components must be recovered without any harm in bonded composite structures for successful debonding. Frequently, saving medium-cost components can be profitable in order to decrease assembly or lead time expenses. After removing the components, one can proceed with reattaching or reassembling them so that the bonded product can be put back into use.

Nowadays, hot-melt bonding techniques play a vital role with a relevant market impact (the hot-melt adhesives industry is projected to grow from USD 10.07 billion in 2024 to USD 13.42 billion by 2032 at a CAGR of 4.33% during the forecast period) [1]. Hot-melt adhesives, which are polymer-based glues that are applied in a molten state, change from a liquid state at high temperatures to a solid state at low temperatures over a small temperature range. Once the hot melt cools down, it becomes solid and creates a sticky connection between two selected surfaces [2]. Hot-melt adhesives are very beneficial for mass production, with low expenses due to ease of application, quick bonding, and the use of a single component without needing additional materials or catalysts for bonding. Hot melts have the ability to stick to a range of materials, such as plastics, paper, wood, metal, and fabrics, allowing for diverse application options. They are considered environmentally friendly since they do not include solvents or volatile organic compounds (VOCs), decreasing their impact on the environment. Unlike solvent-based adhesives, hot melts present lower health hazards, too [3]. The reversible bonding techniques involving hot melts need to employ approaches that can be categorized based on the energy types involved and how the bonding is disrupted. In order to break the connection created by a regular hot-melt adhesive, the bond must be heated to a temperature higher than the adhesive's melting point. In reality, it is frequently not feasible to administer enough heat to a sizable bonded unit or to bonded components that are sensitive to temperature. Determining how easy the hot melt is to remove depends on the method of removal chosen, the time taken for removal, and the equipment used. It is important to choose a method that requires minimal disassembly time in order to prevent extended downtime.

Traditional methods of bonding with hot melt can involve thermal, electrical, or laser processes used alone or together. Thermal processes consist of exposing materials to heat from sources like pressurized steam or hot air, either directly or by using hot plates that come into contact with the surfaces being bonded [4,5]. Certain drawbacks are clear and restrict the application of these thermal techniques: ununiform heating of surfaces leading to ununiform bonding, inducing internal mechanical residual stress or deformation, collateral effects related to the difference of dilatation—with limitations in performance, insufficient heat resistance, limited bonding strength, high energy consumption, and a longer bonding process time. The hot melt may not be adequately heated, which affects not only the bonding strength but also the efficiency and quality of the debonding process. Laser bonding involves laser treatment with UV and IR radiation of the surfaces to be bonded, but it has low efficiency and no relevant industrial applications because it is normally associated with thermal bonding [6]. Finally, adhesive bonding technology activated by electromagnetic fields is innovative and an alternative to the thermal bonding technologies used today in manufacturing sectors. The main advantage lies in the heating of the hot melt before heating the bonding surfaces, resulting in the hot melt being sufficiently heated.

There are three main directions of electrical bonding: by thermal effects of conduction in direct current (direct resistance heating and/or partial discharging), as described in [7–11], which is associated with electrochemical effects at the interfaces [12]; induction bonding under alternating field, as described in [11,13–19], which exploits either the dielectric or hysteresis properties of adhesives mainly under 400 kHz frequency; and, finally, a newer approach of using microwave exposure at frequencies exceeding 1 GHz [20–22]. The challenge of these technologies is to develop new multifunctional and highly reliable hot-melt materials and related processes capable of providing a strong and energy-efficient joint, which can be reversed to disassemble the components by a specific trigger of an electromagnetic field. The formulation of innovative hot-melt adhesives manufactured with functional micro/nanosized fillers, opportunely functionalized depending on the adhesive matrix used, may lead to an increase in the mechanical performance in terms of the intrinsic mechanical resistance of the adhesive, improvement of the mechanical performance of the joints (shear stress, flexural stress, and compression stress of joints), and improvement of adhesion to different typologies of substrates, but it also assures an increased heating rate by applying electromagnetic fields. Depending on the heating principle to be used (dielectric or hysteresis) and to the frequency to be applied, different functional particles can be employed, e.g., conducting particles (graphite or metallic powders, carbon nano-tubes, etc.), or particles with ferritic properties (iron oxides, nickel oxides, etc.); in rare cases, conducting polymers may be additionally introduced [15,18,19,21,22]. The amount of the heat generated depends on the nature, percentage and morphology of the particles, and the dissipated heat is able to quickly reach the melting temperature of the thermoplastic polymeric matrix in order to activate the adhesive for a rapid assembling or disassembling process, as presented in Figure 1.

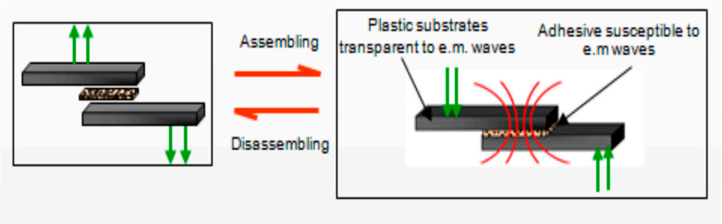

Figure 1. Assembling/disassembling process under electromagnetic field (marked in red).

The hot-melt adhesives formulation can also include oligomers, plasticizers, etc., which exhibit polar properties, adding new advantages to the bonding process under an electromagnetic field. It is beneficial for the hot-melt adhesive if the oligomers that coordinate ionic species are able to mix well in their molten state with functional particles, acting as a supplementary tackifier for the adhesive composition [23–31].

Recent research has focused on evaluating the environmental impact of electrically activated hot-melt adhesives, highlighting their lower impact during manufacturing and reduced energy requirements compared to thermal processes [32,33]. There is potential for further improvement by implementing innovative materials and electromagnetic equipment to increase efficiency and productivity and to decrease electricity consumption during application.

Currently, there is no research on utilizing MW-activatable adhesives with functional particles, and the study presented shows that incorporating metal particles into thermoplastic formulations to make MW-activatable adhesives reduces energy consumption by allowing for a quick activation time of only a few seconds. This paper addresses, with priority, the development of polyethylene-based hot-melt adhesives due to their various benefits, such as excellent life stability, better thermostability, a wider bonding range, and lack of tendency to char or to create unpleasant smells. In 2018, the European Commission approved a European plastics strategy as a component of the EU's circular economy action plan [34]. The objective was to aid, enhance, and speed up the execution of actions to decrease plastic waste. Another important goal is the mandate that by 2030, all plastic packaging sold in the EU must either be reusable or economically recyclable [35]. For such reasons, the MW-activatable adhesives manufacturing used a polyethylene matrix from recycled sources. In this way, the innovation involves creating new adhesive formulations that are eco-friendly and can be fully recycled and reused for similar bonding needs.

2. Materials and Methods

2.1. Materials

Composites containing recycled LDPE powder as the polymer matrix incorporated nanofillers of Al and Fe in two different particle sizes at the nanoscale: 50 nm and 800 nm. The main characteristics of the spherical-shaped metallic powders of Al and Fe and their dimensional distribution are presented elsewhere [36]. It was shown that the variance in the particle dimensions (larger for Fe particles) benefits adhesive manufacturing because the larger distribution lowers the particle costs by approximately tenfold compared to narrower distributions and offers increased conductivity and superior dielectric loss—dielectric characteristics expected with higher values for MW-activatable adhesives.

To produce the samples for the experiments, the polymer and the nano-conductive powder were mixed together for 15 min in a TURBULA T2F cylindrical mixer from Artisan Technology Group (Champaign, IL, USA). The mixer has a 1.3 L capacity mixing basket and a rubber-ring-based clamping device, with a rotation speed of 40 rpm. Finally, the composite materials were produced using the Dr. Boy 35A injection machine (Dr. Boy GmbH & Co. K, Neustadt-Fernthal, Germany) with a screw diameter of 28 mm, L/D ratio of 18.6 mm, calculated injection capacity of 58.5 cm^3, maximum material pressure of 2200 bar, and minimum real injection capacity of 500 mm. In all the experimental models, a 3% ratio of compatibilizing agents was employed, including Poly(ethylene glycol) methacrylate at 1%, an Ethylene Acrylic Acid Copolymer at 1%, and Tegomer® E 525 (Evonik Operations GmbH, Essen, Germany) at 1% (wt%). Table 1 shows the optimal temperature range for the injection cylinder's five heating zones during the injection process for LDPE composites containing Al and Fe. Figure 2 shows the control monitor with the temperatures set for the five heating zones of the injection machine for the Al- and Fe-containing composites. Slightly higher temperatures for the Fe-containing composites were needed. The recipes' descriptions are given in Table 2. The optimal value of 7.5 wt% metallic powder was determined after an extended simulation using specialized software for S parameters and absorbed microwave energy in polymeric nano-composites containing 5–10 wt% iron and aluminum powder of two particle sizes within the frequency range of 0.1–3 GHz.

Table 1. Temperature regime for rLDPE (°C).

Heating Zone	5	4	3	2	1
rLDPE—Al	190	186	180	175	170
rLDPE—Fe	195	193	185	180	176

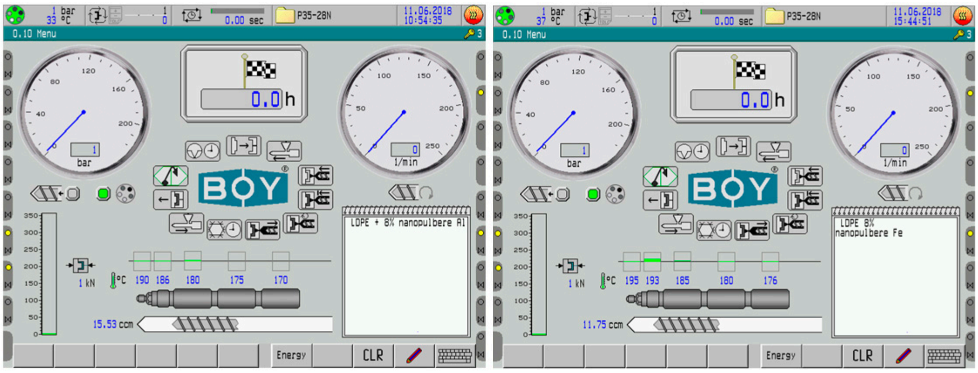

(**a**) (**b**)

Figure 2. The control monitor of the injection machine for composites containing (**a**) Al and (**b**) Fe.

Table 2. Recipes' descriptions (addition in wt%).

Sample Code	Formulation
M1	rLDPE + 7.5% Al/800 nm
M2	rLDPE + 7.5% Al/50 nm
M3	rLDPE + 7.5% Fe/800 nm
M4	rLDPE + 7.5% Fe/50 nm

2.2. Characterization Methods and Related Equipment

(i) Electron scanning microscopy SEM was performed with a field emission and focused ion beam scanning electron microscope (SEM), model Quanta FEG 250, with STEM and EDX detectors (Thermo Fisher Scientific Inc., Waltham, MA, USA). The analysis method was LowVac, with water vapor, which does not allow the samples to be damaged. The SEM charging occurrence was significantly reduced due to the low vacuum in the specimen chamber of the SEM.

(ii) A Netzsch STA PC 409 thermal analyzer (Erich NETZSCH B.V. & Co. Holding KG, Selbwas, Germany) was used for thermogravimetric analysis. The working atmosphere was synthetic air, 100 mL/min in alumina crucibles. The heating program was 35–1200 °C, with a heating speed of 10 °C/min.

(iii) The hydrostatic density was determined utilizing an XS204 Analytical Balance (Mettler-Toledo, Columbus, OH, USA), characterized by the following specifications: maximum capacity of 220 g, precision of 0.1 mg, linearity of 0.2 mg, internal calibration, equipped with a density kit for solids and liquids and an RS 232 interface (Mettler-Toledo, Columbus, OH, USA). The measurements were conducted at a temperature of 21 °C, with three consecutive repetitions, and the error was calculated. The density was determined as the mean value between the three consecutive repeated measurements.

(iv) Shore hardness measurements were taken with a common Shore "D" digital durometer, as the mean of 5 measurements.

(v) The equipment for determining the mechanical features was a specialized PC-controlled universal tensile testing machine (Qiantong, China), with nominal force: min 20 kN, allowing measurement of tensile strength and elongation.

(vi) Microindentation tests were performed with the use of a compact open platform equipped with a Nano/Micro Indentation Tester and a Micro Scratch Tester, from CSM Instruments SA, Peseux, Switzerland. The mechanical tests were performed at ambient temperature, as 5 measurements on each sample, with the average of the obtained values and their standard deviation being reported.

(vii) The degree of swelling was determined by measuring the variation in the mass of the samples at predefined immersion intervals, utilizing the XS204 Analytical Balance.

(viii) The dielectric properties were carried out using a Broadband Dielectric Spectrometer (Novocontrol GMBH, Montabaur, Germany) encompassing an Alpha frequency response analyzer and a Quattro temperature controller, with tailored measurement cells up to 40 GHz.

3. Results and Discussion

3.1. SEM and X-Ray Fluorescence (XRF)

Micrographs were taken at 20,000 magnification to assess how the metallic particles were incorporated into the LDPE matrix in the produced composite materials. The examination of the compositions shows that Al, depicted in Figure 3, is associated with smooth powder particles, while Fe, shown in Figure 4, is linked to rough spherical particles in both size dimensions. However, it was observed that the Al particles behaved differently compared to the Fe particles, as they are mostly exposed rather than being covered by the polymer matrix, showing a stronger connection. Choosing different additives for the compatibility of composite components can enhance the compounding process of aluminum. Furthermore, it has been observed that the most uniform samples are produced with 50 nm particles, regardless of their metal type, especially for M4, where the dispersion of Fe particles is technologically optimized.

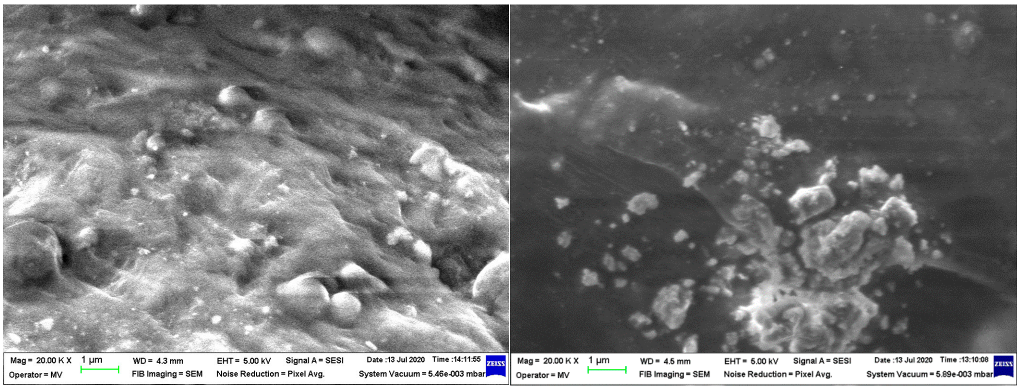

(**a**) (**b**)

Figure 3. SEM images for Al-containing composites: (**a**) M1 and (**b**) M2.

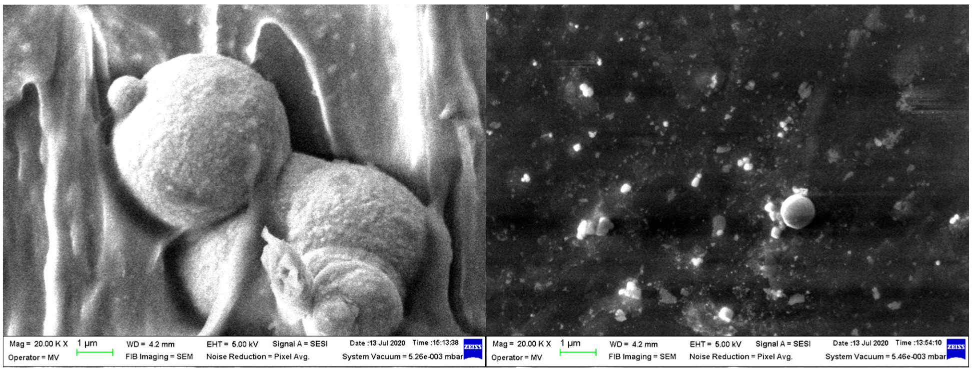

(**a**) (**b**)

Figure 4. SEM images for Fe-containing composites: (**a**) M3 and (**b**) M4.

The results obtained as XRF characteristics, shown in Figures 5 and 6, confirm the nature and percentages of the nano-powder in the composite materials, as described in Tables 3 and 4.

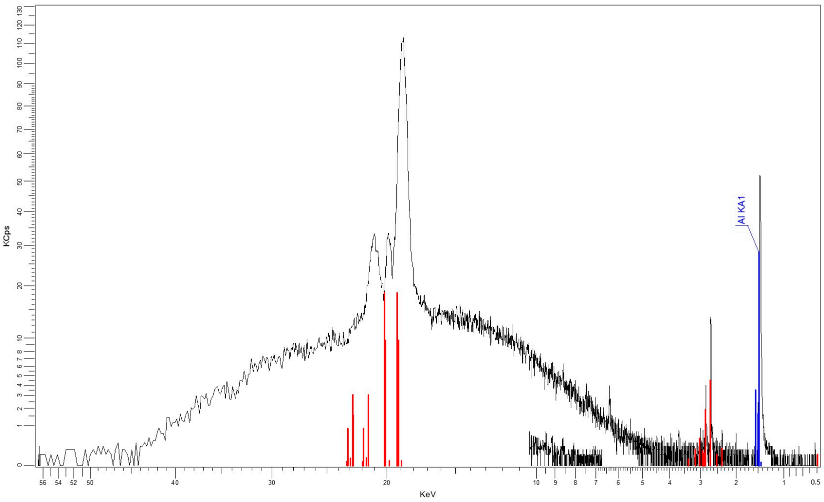

Figure 5. XRF spectrum for M1.

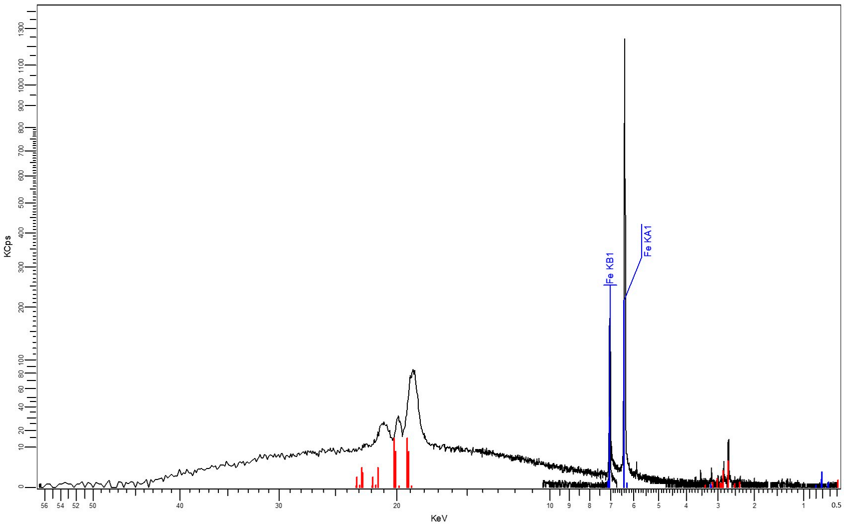

Figure 6. XRF spectrum for M3.

Table 3. Composition of M1.

Formula	Z	Concentration	Most Intense Spectral Line	Statistical Measurement Error	Thickness of the Analyzed Layer
CH_2	-	92.73%	Organic matter	-	-
Al	13	7.19%	Al KA1-HR-Tr	9.70%	11.8 µm

Table 4. Composition of M3.

Formula	Z	Concentration	Most Intense Spectral Line	Statistical Measurement Error	Thickness of the Analyzed Layer
CH_2	-	92.64%	Organic matter	-	-
Fe	26	7.35%	Fe KA1-HR-Tr	2.06%	0.95 µm

3.2. Results Obtained from Micro-Indentation Tests

Table 5 presents the results of H_{IT}, HV, E_{IT}, S, $W_{elastic}$, $W_{plastic}$. W_{total} and η_{IT} obtained from the microindentation tests for the composite samples tested, as presented in ASTM E2546-15 with the Oliver–Pharr calculus method [37]. The mechanical characteristics, mainly, indented hardness H_{IT} and Vickers hardness HV, are slightly higher for the composites containing smaller metallic particles, regardless of the metal type. The highest values were reached by M4. A reduced modulus of elasticity E_{IT} was found to be identical for all the samples. The elastic indentation work $W_{elastic}$ and reversible elastic deformation work show higher values for samples with larger-sized powders, with slightly increased values for composites containing Al, e.g., M1. As regards the mechanical plastic deformation of indentation $W_{plastic}$, slightly increased values were found for composites containing larger-sized Fe powder, e.g., M3. The examination showed distinct variations in the sample structure on the surface, linked to the type and size of metallic additives and their impact on the interaction with the matrix during compounding. These results will be connected to other characteristics for further discussion, but initially, the composites containing aluminum appeared to have a more flexible surface compared to those containing iron.

Table 5. Results of parameters obtained from microindentation tests.

Sample	H_{IT} (MPa)	HV	E_{IT} (GPa)	S (N/µm)	h_{max} (µm)	$W_{elastic}$ (µJ)	$W_{plastic}$ (µJ)	W_{total} (µJ)	η_{IT} (%)
M1	19.2 ± 0.2	1.8 ± 0.1	0.1 ± 0.01	0.04 ± 0.01	66.9 ± 0.5	16.9 ± 0.1	9.3 ± 0.3	26.1 ± 0.3	65.0 ± 0.6
M2	20.0 ± 1.1	1.9 ± 0.1	0.1 ± 0.02	0.04 ± 0.01	65.4 ± 0.3	16.6 ± 0.3	9.1 ± 0.2	25.7 ± 0.5	64.6 ± 0.2
M3	19.0 ± 0.5	1.8 ± 0.4	0.1 ± 0.02	0.04 ± 0.01	65.3 ± 0.4	15.8 ± 0.2	9.6 ± 0.1	25.4 ± 0.3	62.1 ± 0.2
M4	21.2 ± 1.3	2.0 ± 0.1	0.1 ± 0.01	0.04 ± 0.01	61.0 ± 1.8	14.3 ± 0.4	9.0 ± 0.1	23.3 ± 0.4	61.2 ± 0.5

3.3. Results Obtained from Density Analysis

The hydrostatic density results from Table 6 show close values, which can be attributed to the high polymer content. In theory, if the metal powder content is consistent in all the samples, the discrepancy may be attributed to the variance in atomic mass between aluminum and iron, resulting in a clear difference in density between M1 and M3, or M2 and M4. However, we also observed variances between M1 and M2, as well as between M3 and M4, despite containing identical metallic particles, possibly due to the way the particle size influences the composite structure. The composites containing 50 nm particles may have a lower density because of the looser connection between LDPE matrix elements, which is a result of the more evenly spread particles. This supports the findings of the SEM analysis.

Table 6. Results obtained from density analysis.

Sample	Density [g/cm^3]
M1	0.933
M2	0.928
M3	0.960
M4	0.937

The composite material M3 had the greatest density, while M2 had the smallest when compared to the other composite materials acquired.

3.4. Results Obtained from Shore Hardness Tests

The shore hardness was determined in accordance with ASTM D2240-00 [38], and the results are displayed in Table 7.

Table 7. Results obtained from shore hardness tests.

Sample	Shore Hardness [MPa]
M1	58
M2	64
M3	59
M4	69

The hardness of samples M2 and M4 was higher than that of M1 and M3, respectively, because the metallic particles with a 50 nm dimension are better dispersed, resulting in lower surface roughness. The slightly elevated values of the Fe-containing composites in comparison to the Al-containing composites may be attributed to the increased attraction of Fe particles to the polymer matrix, leading to a more robust bond between the polymer and particles, as supported by the SEM analysis results.

3.5. Results Obtained from the Mechanical Tests

The mechanical tests were carried out according to the SR EN ISO 527-2:2000 standard [39], on five samples each. The statistical interpretation of the results consisted in determining the average value of five measurements, excluding values outside the range, with a confidence level of 95%, Table 8. Once the metallic powder was added to the polymer matrix, the composite material became more rigid, showing a rise in mechanical strength but a decrease in flexibility and elasticity. The resistance increase was greater, while the elongation was lower in the Fe-containing composites and overall, in the composites with smaller particle dimensions that are more evenly distributed. Therefore, M4 had the highest mechanical resistance value, while M1 had the lowest. In terms of flow resistance, materials with larger particle dimensions were favored, such as M1, and the type of metal had little impact upon flow resistance.

Table 8. Experimental data obtained for the mechanical tests.

Sample	Mechanical Resistance [MPa]	Flow Resistance [MPa]	Elongation [%]	Young's Modulus [GPa]
M1	5.12	0.17	133	0.01
M2	7.42	0.14	100	0.03
M3	6.74	0.18	104	0.01
M4	8.93	0.15	96	0.03

3.6. Results Obtained for the Degree of Swelling

The procedure was carried out according to SR EN ISO 175/2011 [40], and the results are presented in Table 9, for immersion in water, and in Table 10, for immersion in solvent, here, toluene. Essentially, mixing metallic nano-particles with polymer matrices can create micro-voids during the melt process, affecting the surface roughness of the samples and determining liquid attraction and insertion potential. With regards to water absorption, as shown in Figure 7, it was observed that the swelling degree remained low until 400 h of immersion, after which it rapidly increased until reaching a saturation point at around 600 h. The level of swelling was greater in the composites with Al, as well as in the composites with smaller particles because they have more micro-voids in the materials. After 400 h of immersion time, the composites with smaller particle dimensions exhibited an intriguing phenomenon where the swelling degree appeared to be nearly identical, regardless of the type of metallic particle present.

Table 9. Degree of swelling in water, at different immersion times [%].

Sample	72 h	168 h	240 h	336 h	408 h	504 h	576 h
M1	4.4147	4.5314	5.2729	5.8699	7.3488	8.7460	8.7460
M2	6.1095	6.8577	7.1886	7.5236	8.3946	10.9999	10.9999
M3	0.6470	2.2700	2.6299	4.8786	6.1141	6.6090	6.6095
M4	1.9535	2.8318	3.8943	6.0172	8.0319	11.0827	11.0844

Table 10. Degree of swelling in toluene, at different immersion times [%].

Sample	72 h	168 h	240 h	336 h	408 h	504 h	576 h
M1	7.9868	8.6907	8.8797	9.5472	10.4701	10.7932	10.8056
M2	8.1148	8.8822	9.5250	9.6802	10.5641	10.9785	10.9908
M3	8.2854	9.3585	9.5383	10.2608	10.9119	11.0490	11.0613
M4	9.1654	9.6462	9.9119	10.7267	11.0407	11.1217	11.1341

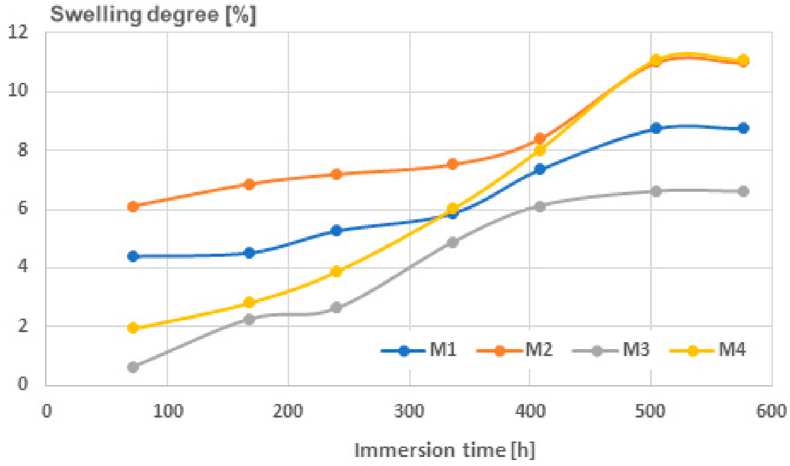

Figure 7. Swelling degree for water.

In relation to the level of swelling with toluene, shown in Figure 8, it was observed that because of toluene's attraction to the matrix, the values were elevated even with shorter immersion times. The overall trend holds true: the composites with aluminum had a greater degree of swelling, as did the composites with smaller particles. For the solvent, saturation happened sooner, around 450 h, and the degree of swelling was similar for all the composites, showing that toluene absorption is not greatly affected by the number or size of micro-voids. A noteworthy observation was made about the ultimate swelling saturation levels in water and toluene, which were nearly identical at around 11%, specifically for samples M2 and M4. This indicates a total filling of the micro-voids, which are evidently more abundant and smaller in size compared to M1 and M3.

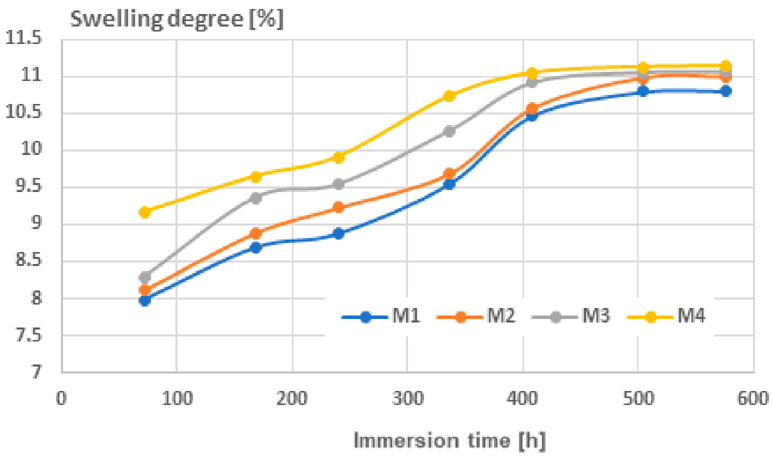

Figure 8. Swelling degree for toluene.

3.7. *Results Obtained from Thermal Analysis*

The TG/DSC characteristics of the composite samples are presented in Figures 9–12.

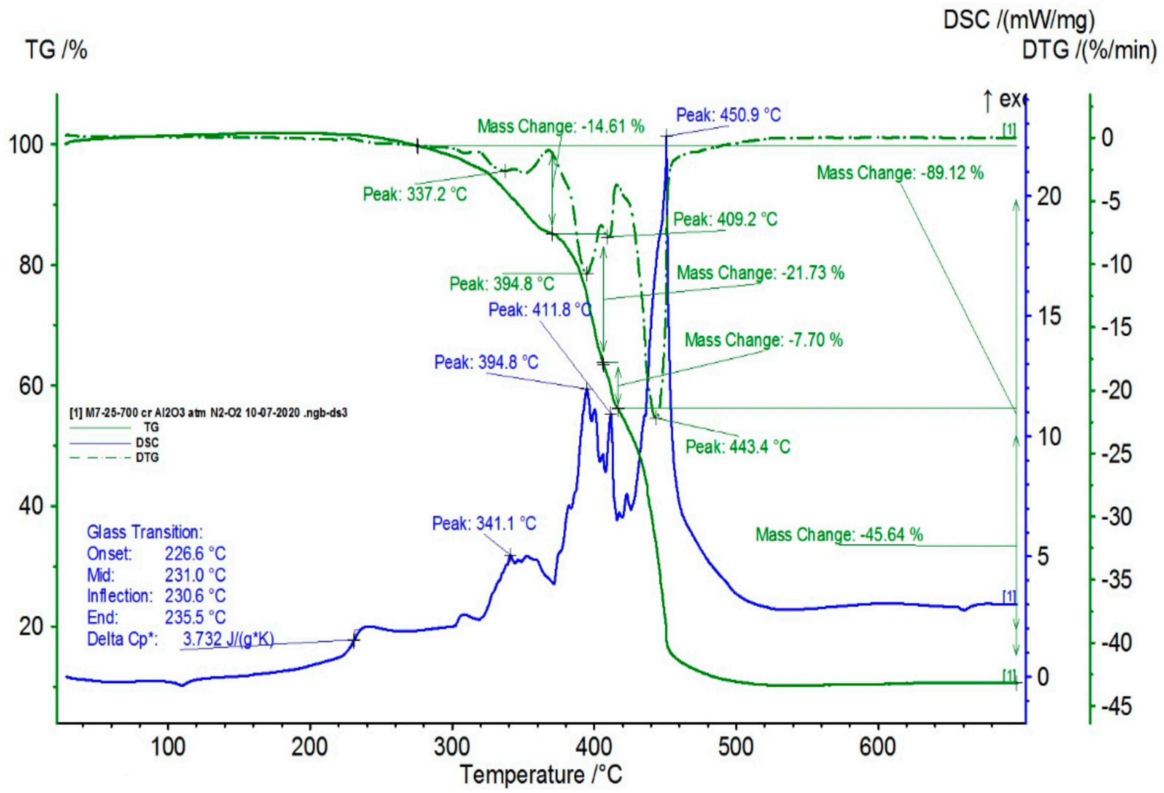

Figure 9. Thermal characteristics obtained for M1.

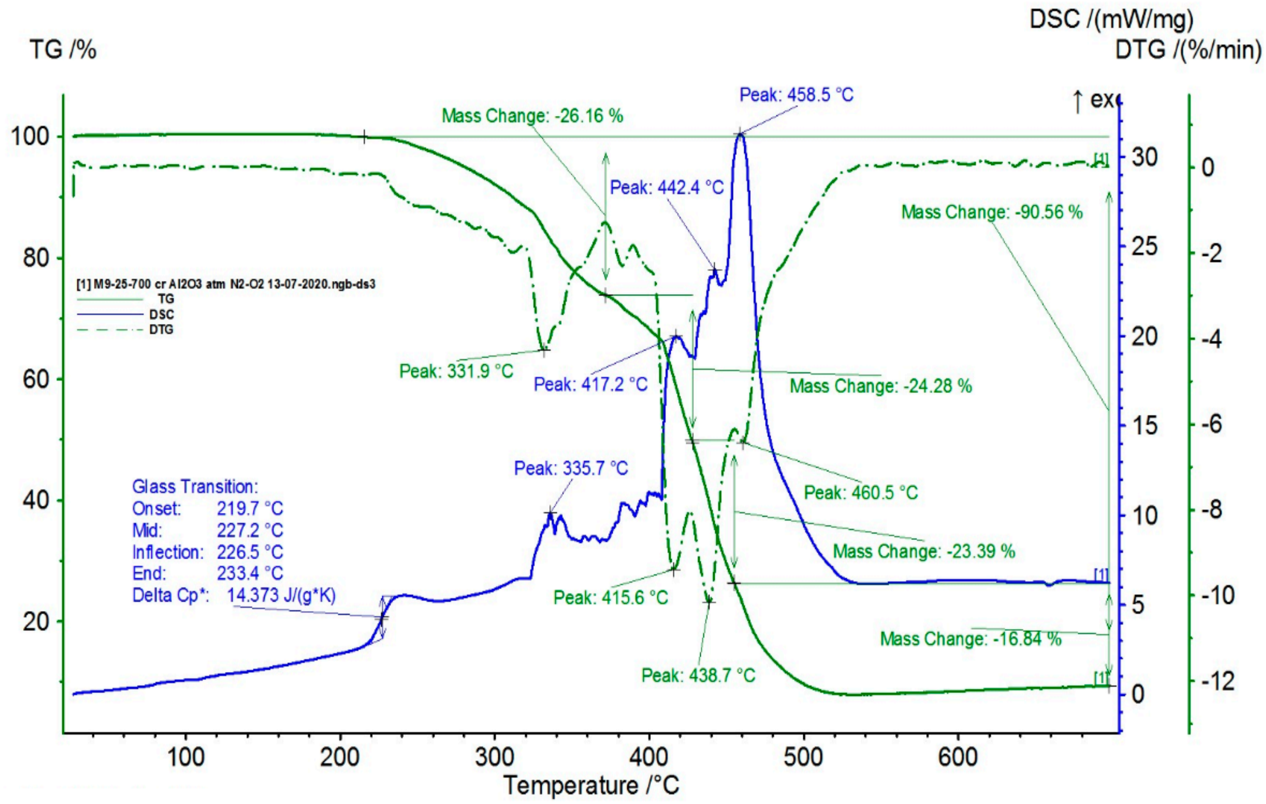

Figure 10. Thermal characteristics obtained for M2.

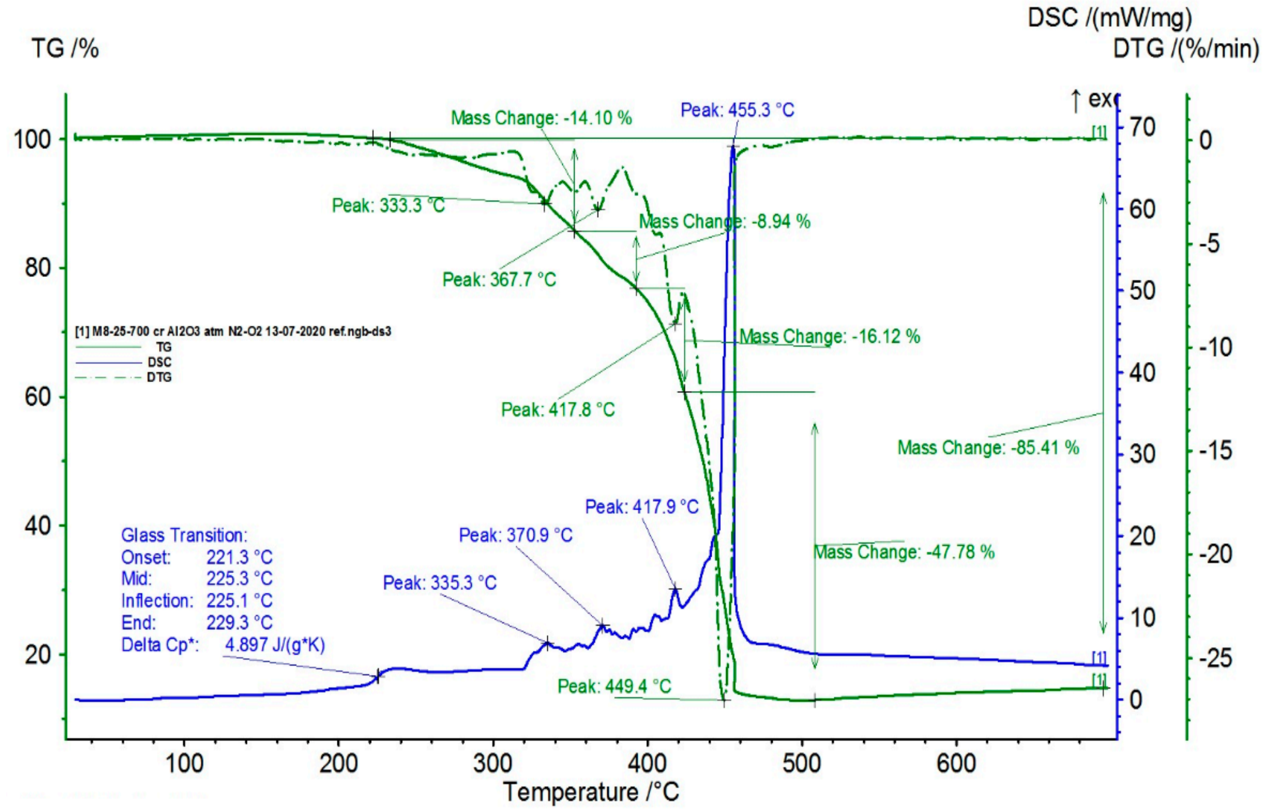

Figure 11. Thermal characteristics obtained for M3.

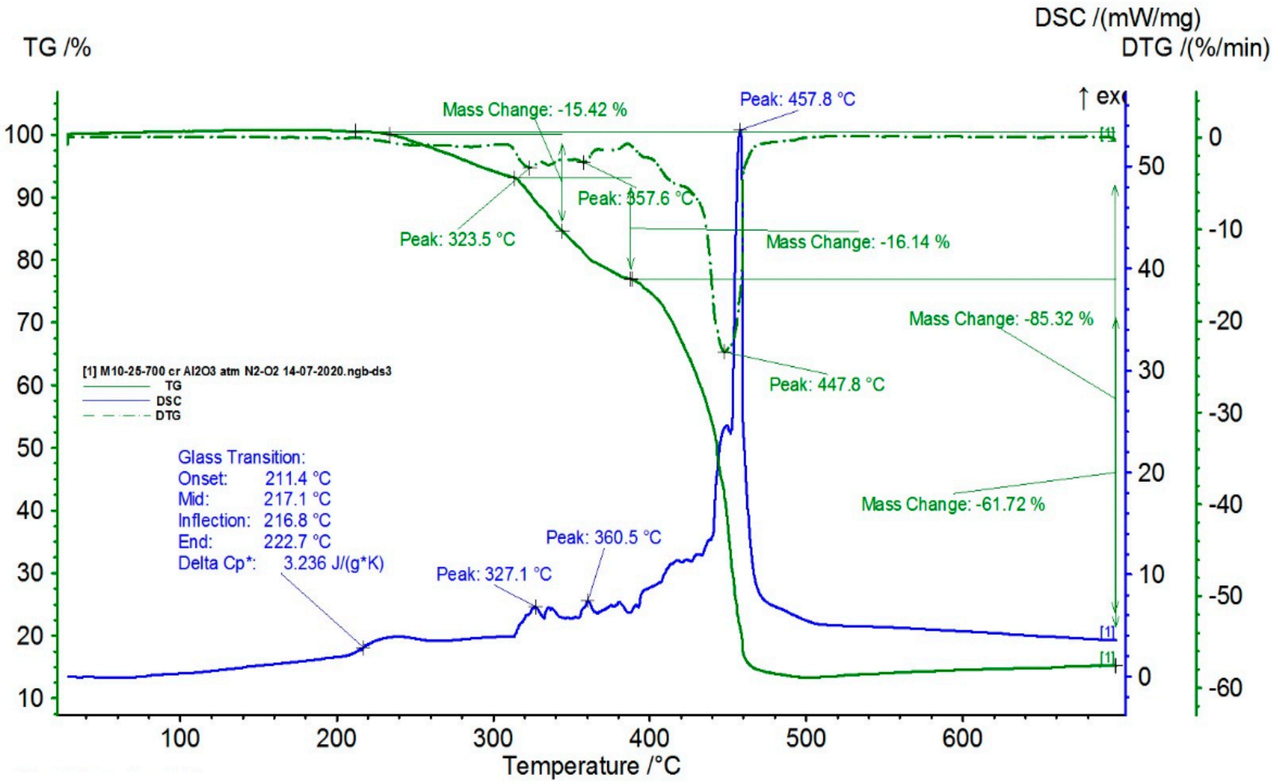

Figure 12. Thermal characteristics obtained for M4.

From the statistical interpretation of the obtained results, it was found that for the composite materials with the LDPE polymer matrix, the melting temperatures were very close due to the majority concentration of the base polymer, varying in the range of 103–106 °C—the specific melting temperature of LDPE. It was noticed that the composites with lower-dimension metallic particles presented slightly higher melting temperature values. The respective results are in line with similar findings in [41–44]. The temperatures of the start of the first oxidation process (OOT_1) varied in the range of 190–215 °C, and the temperatures of the start of the second oxidation process (OOT_2) varied in the range of 250–315 °C, Table 11. Heating further led to thermo-oxidative processes until complete destruction of the polymer matrix. Other specific values of the DSC parameters are presented in Table 11. It was noticed that the composites with lower-dimension metallic particles presented slightly lower values of oxidation processes.

Table 11. Determined DSC parameters.

Sample	T_t (°C)	ΔH_t (J/g)	χ_{cr} (%)	OOT_1 (°C)	OOT_2 (°C)
M1	103.7	40.1	14.9	212	315
M2	104.5	36.4	13.5	209	307
M3	102.9	46.3	17.2	204	251
M4	104.5	40.1	14.3	188	239

3.8. Results Obtained for Dielectric Properties

The primary dielectric properties that were examined included dielectric permittivity (eps′) and the dielectric loss factor (Tan(Delta)). The frequency domain was selected based on the main frequencies used in industrial microwave technologies. Figure 13 illustrates the findings for the composites containing Al, while Figure 14 demonstrates the results for the composites containing Fe. Regardless of the type of metal, there was a consistent increase in both characteristics versus frequency, beginning at 0.8 GHz and peaking at around 1.4 GHz for Tan(Delta) in every scenario. Particle size had a minimal effect, even though it appears that compounds with larger particles may have shown slightly increased parameters values across all the frequency ranges, regardless of the metal type. Considering that Tan(Delta) is a critical factor in converting microwave energy into heat through dielectric loss, the frequency range of 0.9–1.7 GHz is the most effective for such materials.

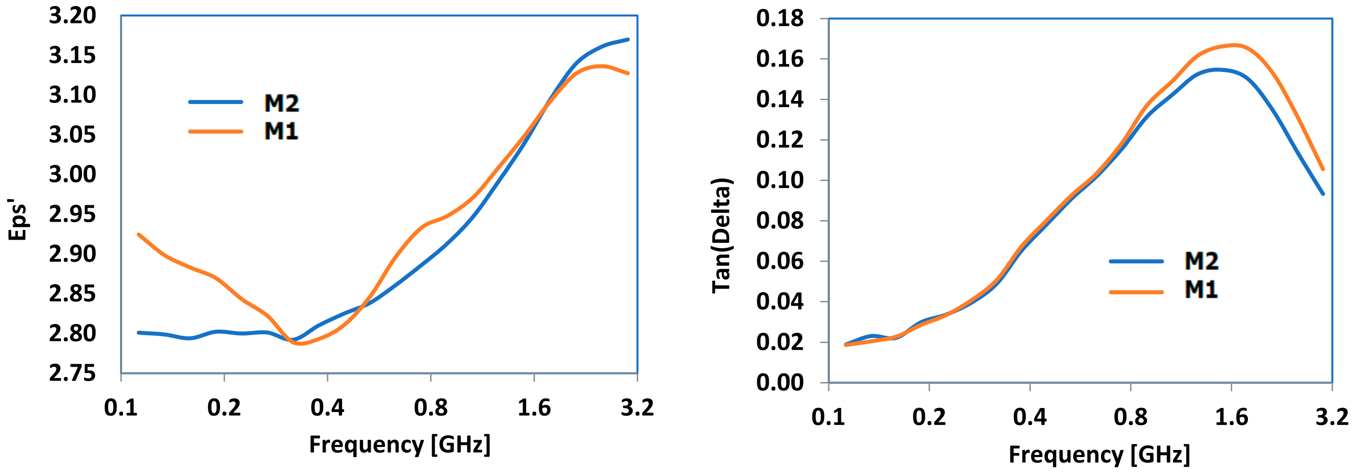

Figure 13. Dielectric properties of Al-containing composites.

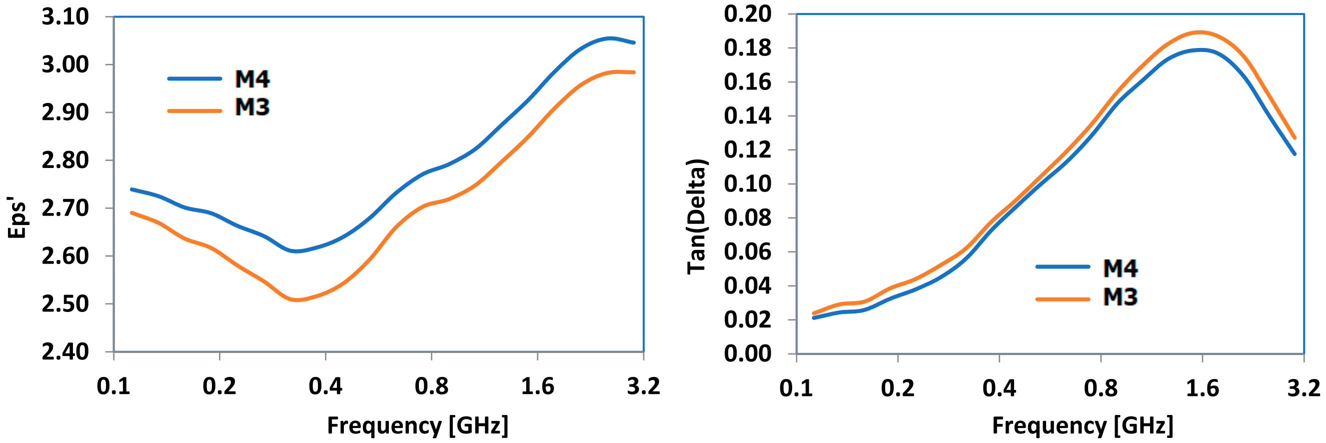

Figure 14. Dielectric properties of Fe-containing composites.

3.9. Results Obtained for Electromagnetic Radiation Attenuation

The dielectric properties obtained need to be verified by examining how electromagnetic radiation is absorbed in materials, which is a crucial factor for how well they function as hot melts, as they should retain as much microwave energy as they can. Figure 15 shows the features of M1 and M3, which are considered the most suitable as a recipe according to the previous observations. The attenuation reached a peak at approximately 0.9 GHz, while showing a unique shape at frequencies above 1 GHz, resulting in reduced attenuation levels. The sharp decrease found around 1.15 GHz is specific to microwave waveguides, where the peculiar spacing of particles favors the transmission of microwaves through the material within a narrow frequency range. Considering all the findings from studying microwave effects, it can be determined that the optimal frequency range for maximizing hot melt usage is 0.9–1 GHz. Thankfully, there are currently large industrial/commercial microwave ovens utilizing 915 MHz, making it possible to develop bonding technologies using the achieved composites as hot melts at the same frequency.

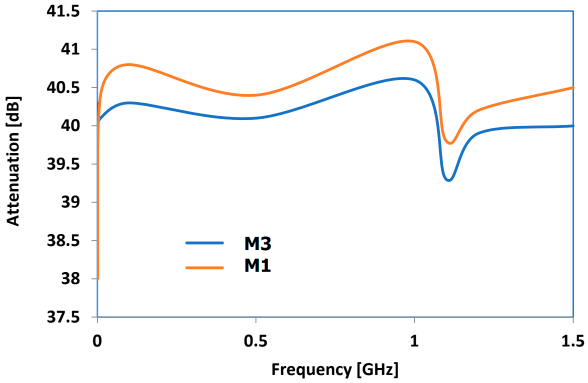

Figure 15. Comparative electromagnetic radiation attenuation of M1 and M3 composites.

3.10. Tests upon the Feasibility of Reversible Bonding Techniques Utilizing Microwave Energy

Experiments were conducted to test the feasibility of bonding methods using microwave energy at 915 MHz, with varying emission power levels ranging from 100 to 1000 × 10^3 W/kg. Figure 16 displays a sample subjected to microwave heating, exhibiting a slight change in color at elevated temperatures, attributed to the aluminum's coloring effect.

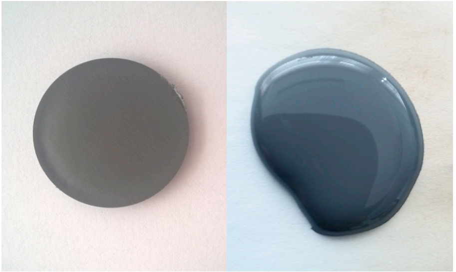
(**a**) (**b**)

Figure 16. Images of hot-melt composite M1: (**a**) before exposure and (**b**) after exposure to microwaves.

Figure 17 shows the heating properties of microwave exposure on the Al-containing composites at different power levels (140, 280, 570, and 850 × 10^3 W/kg), while Figure 18 represents the same for the Fe-containing composites.

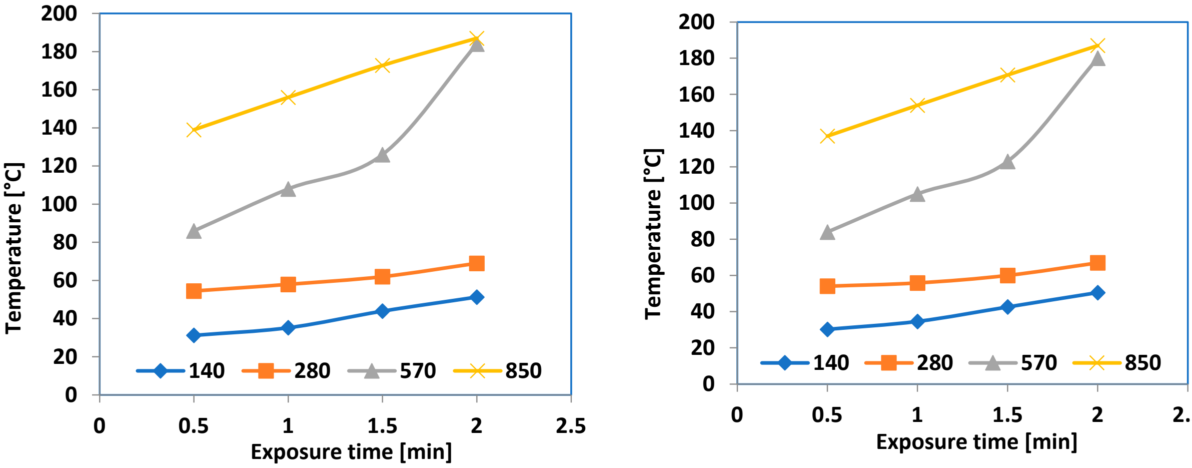

(**a**) (**b**)

Figure 17. Heating characteristics at different power values (10^3 W/kg) of microwave exposure for hot-melt composites (**a**) M1 and (**b**) M2.

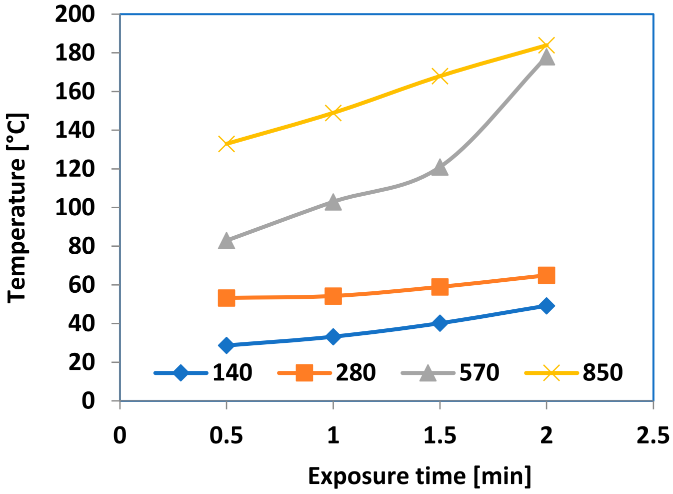

(**a**) (**b**)

Figure 18. Heating characteristics at different power values (10^3 W/kg) of microwave exposure for hot-melt composites (**a**) M3 and (**b**) M4.

Upon initial observation, it became clear that energy levels below 400 × 10^3 W/kg could not adequately raise the temperature of the composites to a significant degree within a reasonable timeframe, with the temperature not exceeding 60 °C. The effectiveness of 570 × 10^3 W/kg power utilization was achieved after the samples had been exposed for over 1.5 min, regardless of the type of sample. When a power of 850 × 10^3 W/kg was used, the efficiency of the process increased, even with lower exposure times, starting from 0.5 min. A notable phenomenon was noticed, i.e., the temperature reached after 2 min of exposure was quite similar at both 570 and 850 × 10^3 W/kg powers for all the samples. This occurrence is not caused by an electromagnetic impact but by a distinct effect in the melted composites, as 180 °C represents a high fluid state of the composites, regardless of their receipt, a temperature that should not be reached in bonding technologies utilizing this type of hot melt.

A more in-depth evaluation was conducted on the actual heating efficiency of microwave exposure for the hot-melt composites, at 570 × 10^3 W/kg power compared to 850 × 10^3 W/kg power, as shown in Figure 19.

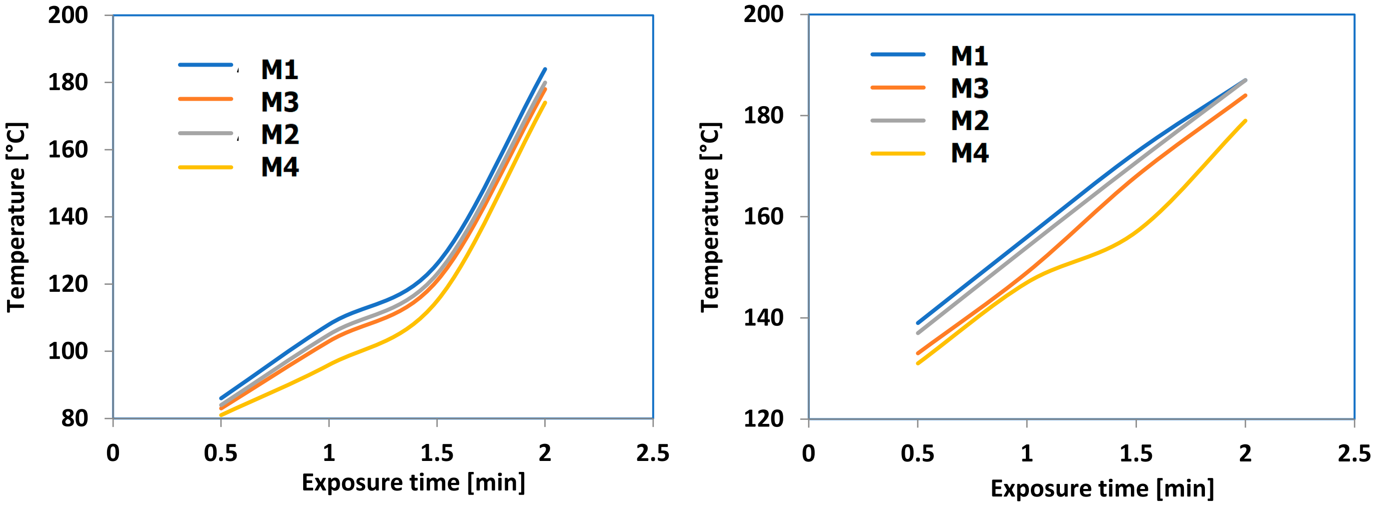

(**a**) (**b**)

Figure 19. Heating efficiency of microwave exposure for hot-melt composites (**a**) at 570 × 10^3 W/kg power and (**b**) at 850 × 10^3 W/kg power.

The optimal temperature for the hot-melt composites to become functional for bonding processes was considered approximately 5 °C higher than the melting point of LDPE composites, which is about 135 °C. This reduced application temperature represented a significant benefit of the hot melts examined compared to traditional hot melts used in thermal processes, such as thermoplastic rubber around 200 °C and polyurethane or polyamide exceeding 250 °C.

Based on Figure 19, regarding the exposure time when the temperature level of 140 °C was reached, it took over 1.5 min at 570×10^3 W/kg, and only 0.5 min at 850×10^3 W/kg. Accordingly, the energy needed for bonding activities was about double when operating at 570×10^3 W/kg, with the efficiency being roughly three times lower when compared with operating at 850×10^3 W/kg. In present hot melt uses, a 0.5 min exposure is appropriate and may be equivalent to the typical thermal method with a similar duration. The M1 formula is suggested as the most efficient hot-melt option available. In this situation, it is not necessary to use metallic powders smaller than 800 nm or with limited dimensional range, or in higher amounts within composites. This provides a significant cost advantage, as powders sized 50 nm are at least five times more costly than those sized 800 nm.

An illustration of the bonding testing is shown below, where Figure 20 depicts the bonding arrangement as a longitudinal joint of the samples by overlapping them at the ends. The mechanical tests were carried out according to the SR EN ISO 527-2:2000 standard [39], on five samples each. The overlap was of a length of three times the width of the items to be joined. The statistical interpretation of the results consists in determining the average value of five measurements, excluding values outside the range, with a confidence level of 95%. For the preliminary study, based on the materials typically used for bonding in the automotive industry, the main focus was on testing the bonding of low- and high-density polyethylene (LDPE and HDPE) and polypropylene (PP), with the results shown in Table 12. The test was conducted using the M1 and M3 hot melt samples, with the thickness being roughly 20% of the bonded item's thickness, applying a pressure of 200 kPa, a minimal value needed to counteract the separation for the plastic items. The exposure was 0.5 min at 850×10^3 W/kg. In every instance, a curing duration of approximately 1 min was noticed when the hot melt temperature dropped below 70 °C. A high cohesion of materials was observed in all the cases, but the bonding strength relies on the type of material and the hot melt composition. The peak value was reached with the LDPE + LDPE/M1 setup, while the lowest value occurred with the PP + PP/M1 configuration. The minimum elongation occurred with the PP + PP setup for both types of adhesives. The efficiency of the M1 formula was once again demonstrated.

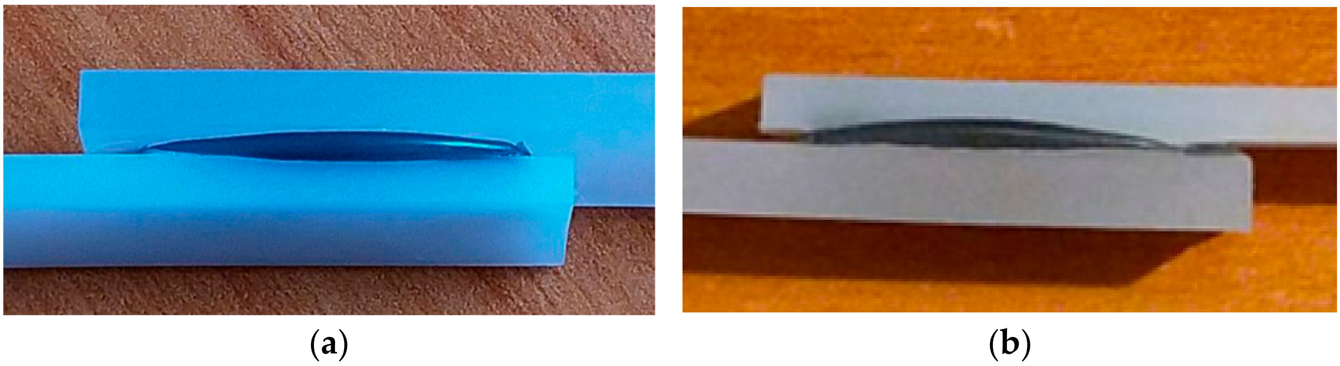

Figure 20. Examples of bonding configuration: (**a**) LDPE + LDPE/M1; (**b**) PP + PP/M3.

Table 12. Experimental data obtained for the bonding process.

Bonded Items	Hot Melt Sample	Mechanical Resistance [MPa]	Elongation [%]
LDPE + LDPE	M1	11.38	33
LDPE + HDPE	M1	10.84	28
LDPE + PP	M1	11.11	31
HDPE + PP	M1	10.75	25
PP + PP	M1	10.31	21
LDPE + LDPE	M3	11.12	32
LDPE + HDPE	M3	10.78	27
LDPE + PP	M3	10.93	28
HDPE + PP	M3	10.83	24
PP + PP	M3	10.68	21

Overall, microwave bonding offers considerable benefits compared to traditional thermal polymer-to-polymer bonding methods. The heating procedure initiates from the inside to the outside of the hot melt and is consistent, not impacting the materials to be joined, even regarding expansion or internal mechanical stresses. The energy consumption is greatly reduced, and the microwave bonding process efficiency may be finally improved by using a green electric supply, hence reducing CO_2 emissions [45,46]. Conversely, the equipment size and complexity are minimized with microwave technology, making it readily suitable for robotic and remote operation. Furthermore, reheating and subsequently resealing or reconfiguring the items in the event of process failure is also practical. On the other hand, no volatile organic compounds are released during microwave exposure, ensuring a safer work experience. A case study upon the efficiency of using microwave technology, with a brief cost analysis emphasizing the impact of cost elements, such as energy, processing speed, product quality, equipment cost vs. power, operating cost, and payback period, is presented in [47], concluding that the average repayment period is about four times shorter compared to conventional thermal process.

Ultimately, the final assessment would focus on the recyclability of these hot melts within the framework of the circular economy. As previously stated, the manufacture of MW-activatable adhesives utilized polyethylene matrix from recycled materials, a topic extensively covered in [48–50] as regards the sources and specific characteristics of such matrices. In contrast to commonly used, mostly non-recyclable hot-melt adhesives, our suggested composites can be recycled entirely using microwaves to separate the materials and gather them for future use. Accordingly, the recycling procedure includes item sorting and dismantling, hot melt gathering, and grinding. However, it should be noted that recycling hot-melt adhesives does not imply their immediate reuse after the recycling process. The obtained powder is meant to be incorporated into new hot melts in a ratio of up to 25%. The process relies solely on extrusion to create materials like films for new bonding processes. As long as LDPE reprocessing through extrusion is widely known, recycled materials can be reprocessed right away using the same extrusion method, possibly with the addition of small amounts of additives to complete their formula. This innovation entails developing eco-friendly hot-melt adhesive formulations that can be completely recycled and reused for similar bonding requirements. Additionally, using reversible bonding techniques with microwave energy is advantageous, especially in the automotive and construction industries. The bonding process is carried out in industrial settings where the temperature must not surpass 30 °C and the humidity is strictly controlled, where the robotization process efficiently and economically integrates the heating equipment using microwave energy, which offers reduced size, increased dependability, and energy-efficient characteristics.

Recycling hot-melt adhesives is crucial in these areas, as European regulations mandate thorough and specific recycling of all related components or materials [1,51].

4. Conclusions

This study presents the development of composites using recycled LDPE and 7.5% nanofillers of Al and Fe in two varying particle sizes (800 nm and 50 nm) to be potentially used as hot-melt adhesives for reversible bonding processes with the use of microwave energy. Microwave bonding provides significant advantages over conventional thermal polymer-to-polymer bonding techniques. The heating process begins from the core to the surface of the hot melt and is uniform, not affecting the materials being bonded, including aspects like expansion or internal mechanical stresses. The energy usage is significantly lowered since only the hot melt is heated in an inefficient manner.

As regards the mechanical features of these hot melts, the rise in mechanical resistance is more significant, whereas the elongation is reduced in the Fe-based composites, particularly in those with smaller particles that are distributed more uniformly. Regarding flow resistance, materials with larger particle sizes are preferred, and the metal type has a minimal effect on flow resistance.

Concerning water absorption, it was noted that the swelling degree stayed minimal until 400 h of immersion, after which it rapidly escalated until achieving a saturation point at approximately 600 h. The extent of swelling was higher in the composites containing Al and in those with smaller particles due to the presence of more micro-voids within the materials. Following 400 h of immersion, the composites with smaller particle sizes displayed a particular occurrence where the degree of swelling seemed to be almost the same, irrespective of the type of metallic particle involved. Regarding the extent of swelling with toluene, it was noted that due to toluene's affinity for the matrix, the values increased, even with briefer immersion durations. The composites containing Al experienced more swelling, as did those with finer particles. In the case of the solvent, saturation occurred earlier, at approximately 450 h, and the extent of swelling was comparable across all the composites, indicating that the absorption of toluene is not significantly influenced by the quantity or dimensions of micro-voids. An interesting finding was noted regarding the final swelling saturation levels in water and toluene, which were almost the same, of approximately 11%, suggesting a complete filling of micro-voids after an immersion time exceeding 500 h.

No matter the metal type, there was a steady rise in dielectric permittivity and dielectric loss factor properties with respect to frequency, starting at 0.8 GHz and reaching a peak approximately at 1.4 GHz for Tan(Delta) in all cases. The size of the particles had little impact, although it seems that compounds with larger particles might exhibit slightly higher parameter values across all the frequency ranges, irrespective of the type of metal. Given that Tan(Delta) plays a crucial role in transforming microwave energy into heat via dielectric loss, the frequency range of 0.9–1.7 GHz is considered optimal for use as the hot melt of these materials. Taking into account all the research on how materials absorb electromagnetic radiation, it is possible to conclude that the best frequency range for maximizing hot melt usage is 0.9–1 GHz. This range is feasible because many industrial/commercial microwave ovens currently operate at 915 MHz, allowing for the development of bonding technologies using these composites as hot melts at the same frequency.

In order to reach the optimal temperature level of 140 °C for bonding using the developed composites, the process requires more than 1.5 min at 570×10^3 W/kg microwave energy and just 0.5 min at 850×10^3 W/kg. As a result, bonding activities require twice as much energy when running at 570×10^3 W/kg, while the efficiency is approximately three times worse compared to operating at 850×10^3 W/kg. For current hot-melt applications, a 30 s exposure is recommended and is comparable to the usual thermal technique, which costs at least ten times more. Finally, it was shown that it is not required to utilize metallic powders smaller than 800 nm or with a restricted dimensional range, or in larger quantities within the composites in this scenario. This offers a substantial cost benefit, since 50 nm sized powders are at least five times more expensive than those sized 800 nm.

The entirety of the presented hot-melt composites can be recycled through microwave technology to separate the elements, enabling them to be collected and reprocessed immediately by a grinding step. The obtained powder is meant to be incorporated into new hot melts in a ratio of up to 25%, to be processed by the same extrusion technique, potentially incorporating minimal additives to enhance their composition for subsequent reuse in similar bonding applications. Furthermore, the utilization of reversible bonding methods with microwave power is beneficial, particularly in the automotive and construction sectors, where the incorporation of heating equipment using microwave energy into the robotization process is efficient and cost-effective, resulting in a smaller size, enhanced reliability, and energy efficiency.

Future research directions will involve experimental data on bonding conditions and bonding resilience under environmental conditions, the recyclability of hot melts, and the reprocessing effect upon the hot melt features.

Author Contributions: Conceptualization, R.C.C.; methodology, R.C.C.; investigation and formal analysis, G.A.U., R.C.C., and M.A.; validation M.A. and R.C.C.; writing—original draft preparation, R.C.C. All authors have read and agreed to the published version of the manuscript.

Funding: This research received no external funding.

Institutional Review Board Statement: Not applicable.

Data Availability Statement: The data are presented in this study.

Conflicts of Interest: The authors declare no conflicts of interest.

References

1. End of Life Vehicles Directive. Available online: https://environment.ec.europa.eu/topics/waste-and-recycling/end-life-vehicles_en (accessed on 28 October 2024).
2. Global Hot Melt Adhesives Market Overview. Available online: https://www.marketresearchfuture.com/reports/hot-melt-adhesives-market-4640?utm_term=&utm_campaign=&utm_source=adwords&utm_medium=ppc&hsa_acc=2893753364&hsa_cam=20373674291&hsa_grp=150985931723&hsa_ad=665909881832&hsa_src=g&hsa_tgt=dsa-2089395910984&hsa_kw=&hsa_mt=&hsa_net=adwords&hsa_ver=3&gad_source=1 (accessed on 28 October 2024).
3. What Is Hot Melt Made Of? Available online: https://www.hotmelt.com/blogs/blog/what-is-hot-melt?srsltid=AfmBOookNMHynvS8fmmLcf9jTMsXJid6Iv4_yc5m7DRh_2YPKojEEcfH (accessed on 28 October 2024).
4. Gharde, S.; Sharma, G.; Kandasubramanian, B. Hot-Melt Adhesives: Fundamentals, Formulations, and Applications: A Critical Review. In *Progress in Adhesion and Adhesives*; Mittal, K.L., Ed.; Scrivener Publishing LLC: Austin, TX, USA, 2021; Available online: https://onlinelibrary.wiley.com/doi/pdf/10.1002/9781119846703.ch1 (accessed on 28 October 2024).
5. Budhe, S.; Banea, M.D.; de Barros, S.; da Silva, L.F.M. An updated review of adhesively bonded joints in composite materials. *Int. J. Adhes. Adhes.* **2017**, *72*, 30–42. [CrossRef]
6. Amend, P.; Frick, T.; Schmidt, M. Experimental Studies on Laser-based Hot-melt Bonding of thermosetting Composites and Thermoplastics. *Phys. Procedia* **2011**, *12*, 166–173. [CrossRef]
7. Gilbert, M.D. Electrically Disbonding Materials. U.S. patent 6620308, 16 September 2003.
8. Gilbert, M.D. Electrically Disbonding Adhesive Compositions and Related Methods. U.S. patent 20080196828, 21 August 2008.
9. Anduix-Canto, C.; Peral, D.; Pérez-Padilla, V.; Diaz-Rovira, A.M.; Lledó, A.B.; Orme, C.A.; Petrash, S.; Engels, T.; Chou, K.W. Unraveling the mechanism of electrically induced adhesive debonding: A spectro-microscopic study. *Adv. Mater. Interfaces* **2022**, *9*, 2101447. [CrossRef]
10. Springer, M.; Bosco, N. Environmental Influence on Fracture and Delamination of Electrically Conductive Adhesives. In Proceedings of the 47th IEEE Photovoltaic Specialists Conference (PVSC), Calgary, Canada, 15–21 August 2020. [CrossRef]
11. Bibi, I.; Ahmad, H.; Farid, A.; Iqbal, H.; Habib, N.; Atif, M. A comprehensive study of electrically switchable adhesives: Bonding and debonding on demand. *Mater. Today Commun.* **2023**, *35*, 106293. [CrossRef]
12. Lupi, S.; Forzan, M.; Aliferov, A. *Induction and Direct Resistance Heating: Theory and Numerical Modeling*; Springer International Publishing: Cham, Switzerland, 2015; pp. 1–22. [CrossRef]
13. Leijonmarck, S.; Cornell, A.; Danielsson, C.-O.; Åkermark, T.; Brandner, B.D.; Lindbergh, G. Electrolytically assisted debonding of adhesives: An experimental investigation. *Int. J. Adhes. Adhes.* **2012**, *32*, 39–45. [CrossRef]
14. Ciardiello, R. The Mechanical Performance of Re-Bonded and Healed Adhesive Joints Activable through Induction Heating Systems. *Materials* **2021**, *14*, 6351. [CrossRef]

15. Ciardiello, R.; Belingardi, G.; Martorana, B.; Brunella, V. Physical and mechanical properties of a reversible adhesive for automotive applications. *Int. J. Adhes. Adhes.* **2019**, *89*, 117–128. [CrossRef]
16. Ciardiello, R.; Tridello, A.; Brunella, V.; Martorana, B.; Paolino, D.S.; Belingardi, G. Impact response of adhesive reversible joints made of thermoplastic nanomodified adhesive. *J. Adhes.* **2017**, *94*, 1051–1066. [CrossRef]
17. Verna, E.; Cannavaro, I.; Brunella, V.; Koricho, E.G.; Belingardi, G.; Roncato, D.; Martorana, B.; Lambertini, V.; Neamtu, V.A.; Ciobanu, R. Adhesive joining technologies activated by electro-magnetic external trims. *Int. J. Adhes. Adhes.* **2013**, *46*, 21–25. [CrossRef]
18. Ciardiello, R.; Belingardi, G.; Litterio, F.; Brunella, V. Effect of iron oxide and graphene particles on joint strength and dismounting characteristics of a thermoplastic adhesive. *Int. J. Adhes. Adhes.* **2021**, *107*, 102850. [CrossRef]
19. Salimi, S.; Babra, T.S.; Dines, G.S.; Baskerville, S.W.; Hayes, W.; Greenland, B.W. Composite polyurethane adhesives that debond-on-demand by hysteresis heating in an oscillating magnetic field. *Eur. Polym. J.* **2019**, *121*, 109264. [CrossRef]
20. Liebezeit, S.; Mueller, A.; Leydolph, B.; Palzer, U. Microwave-induced interfacial failure to enable debonding of composite materials for recycling. *Sustain. Mater. Technol.* **2017**, *14*, 29–36.
21. Hellmann, H.; Krieger, R. Microwave-Activatable Hot-Melt Adhesive. US patent 4906497A, 4 November 1988.
22. Roth, M.; Padurschel, P.; Niehaus, E.; Hoffmann, G. Hot Melt Adhesive for Microwave Heating. Patent WO2008071469, 19 June 2008.
23. Czakaj, J.; Sztorch, B.; Romanczuk-Ruszuk, E.; Brząkalski, D.; Przekop, R.E. Organosilicon Compounds in Hot-Melt Adhesive Technologies. *Polymers* **2023**, *15*, 3708. [CrossRef]
24. Plasticisers: A Challenge for Bonding. 2024. Available online: https://www.buehnen.de/international/blog/2024/06/18/plasticisers-a-challenge-for-bonding/ (accessed on 25 October 2024).
25. Chabert, F.; Tournilhac, F.; Sajot, N.; Tencé-Girault, S.; Leibler, L. Supramolecular polymer for enhancement of adhesion and processability of hot melt polyamides. *Int. J. Adhes. Adhes.* **2010**, *30*, 696–705. [CrossRef]
26. Malysheva, G.V.; Bodrykh, N.V. Hot-melt adhesives. *Polym. Sci. Ser.* **2011**, *4*, 301–303. [CrossRef]
27. Secrist, K.E.; Gray, S.D.; Hussein, N. Tackifier-Free Hot Melt Adhesive Compositions Suitable for Use in a Disposable Hygiene Article. Patent WO2021011390A1, 21 January 2021.
28. Chou, R. Hot Melt Adhesive Composition. Patent WO2007079092A1, 12 July 2007.
29. Nakatani, H.; Yamanoue, T. Hot-Melt Adhesive Composition. Patent EP 3 839 002 A1, 23 June 2021.
30. Hu, Y.; Desai, D.R.; Chen, J.; Sharak, M.L. Hot Melt Adhesive Composition and Use Thereof. Patent EP 3 271 436 B1, 21 August 2019.
31. Li, D.; Ye, X.; Shi, J. Hot Melt Adhesive Composition. Patent EP 4 186 956 A1, 31 May 2023.
32. Srinivasan, D.V.; Idapalapati, S. Review of debonding techniques in adhesively bonded composite structures for sustainability. *Sustain. Mater. Technol.* **2021**, *30*, e00345. [CrossRef]
33. La Rosa, A.D.; Ursan, G.-A.; Aradoaer, M.; Ursan, M.; Schreiner, C. Life Cycle Assessment of Microwave Activated Hot-Melt Adhesives. In Proceedings of the 2018 International Conference and Exposition on Electrical and Power Engineering (EPE), Iasi, Romania, 19–19 October 2018. [CrossRef]
34. European Commission. *A European Strategy for Plastics in a Circular Economy. Communication from the Commission to the European Parliament, the Council, the European Economic and Social Committee and the Committee of the Regions*; European Commission: Brussels, Belgium, 2018; Available online: https://eur-lex.europa.eu/legal-content/EN/TXT/?uri=COM:2018:28:FIN (accessed on 28 October 2024).
35. European Commission. Report from the Commission to the European Parliament, the Council, the European Economic and Social Committee and the Committee of the Regions on the Implementation of the Circular Economy Action Plan. Available online: https://eur-lex.europa.eu/legal-content/EN/TXT/?uri=CELEX:52019DC0190 (accessed on 28 October 2024).
36. Ciobanu, R.C.; Damian, R.F.; Schreiner, C.M.; Aradoaei, M.; Sover, A.; Raichur, A.M. Simulation of Dielectric Properties of Nanocomposites with Non-Uniform Filler Distribution. *Polymers* **2023**, *15*, 1636. [CrossRef]
37. *ASTM E2546-15*; Standard Practice for Instrumented Indentation Testing. ASTM: West Conshohocken, PA, USA, 2015. Available online: https://www.astm.org/e2546-15.html (accessed on 25 October 2024).
38. *ASTM D2240-00*; Standard Test Method for Rubber Property—Durometer Hardness. ASTM: West Conshohocken, PA, USA, 2021. Available online: https://www.smithers.com/en-gb/services/testing/standard/astm/astm-d2240 (accessed on 25 October 2024).
39. *SR EN ISO 527-2:2000*; Plastics—Determination of Tensile Properties—Part 2: Test Conditions for Injection and Extrusion Plastics. ISO: Geneva, Switzerland, 2012. Available online: https://cdn.standards.iteh.ai/samples/56046/c5c3ec20cc0741289bf6def861e0a40b/ISO-527-2-2012.pdf (accessed on 25 October 2024).
40. *SR EN ISO 175/2011*; Plastics—Methods of Test for the Determination of the Effects of Immersion in Liquid Chemicals. ISO: Geneva, Switzerland, 2010. Available online: https://www.en-standard.eu/une-en-iso-175-2011-plastics-methods-of-test-for-the-determination-of-the-effects-of-immersion-in-liquid-chemicals-iso-175-2010/ (accessed on 25 October 2024).
41. Meraje, W.C.; Huang, C.-C.; Ahmad, N.; Dewangga, G.R.S.; Kuo, C.-F.J. Hybrid sol-gel-derived method for the synthesis of silicon rubber composites with hBN for characteristic applications in elastomeric thermal pads. *Text. Res. J.* **2022**, *92*, 11–12. [CrossRef]

42. Doner, S.; Paswan, R.; Das, S. The influence of metallic particulate inclusions on the mechanical and thermal performance of 3D printable acrylonitrile-butadiene-styrene/thermoplastic polyurethane fused polymer blends. *Mater. Today Commun.* **2023**, *35*, 106111. [CrossRef]
43. Zaaba, N.F.; Ismail, H.; Saeed, A.M. A Review: Metal Filled Thermoplastic Composites. *Polym. Plast. Technol. Mater.* **2021**, *60*, 1033–1050. [CrossRef]
44. Leon, A.; Perez, M.; Barasinski, A.; Abisset-Chavanne, E.; Defoort, B.; Chinesta, F. Multi-Scale Modeling and Simulation of Thermoplastic Automated Tape Placement: Effects of Metallic Particles Reinforcement on Part Consolidation. *Nanomaterials* **2019**, *9*, 695. [CrossRef] [PubMed]
45. Lei, K.F.; Ahsan, S.; Budraa, N.; Li, W.J.; Mai, J.D. Microwave bonding of polymer-based substrates for potential encapsulated micro/nanofluidic device fabrication. *Sens. Actuators A Phys.* **2004**, *114*, 340–346. [CrossRef]
46. Holmes, R.J.; McDonagh, C.; McLaughlin, J.A.D.; Mohr, S.; Goddard, N.J.; Fielden, P.R. Microwave bonding of poly(methylmethacrylate) microfluidic devices using a conductive polymer. *J. Phys. Chem. Solids* **2011**, *72*, 626–629. [CrossRef]
47. Hasna, A. Microwave Processing Applications in Chemical Engineering: Cost Analysis. *J. Appl. Sci.* **2011**, *11*, 3613–3618. [CrossRef]
48. Epure, E.-L.; Cojocaru, F.D.; Aradoaei, M.; Ciobanu, R.C.; Dodi, G. Exploring the Surface Potential of Recycled Polyethylene Terephthalate Composite Supports on the Collagen Contamination Level. *Polymers* **2023**, *15*, 776. [CrossRef]
49. Ciobanu, R.C.; Schreiner, C.; Caramitu, A.R.; Aradoaei, S.; Aradoaei, M. Sustainability of the Technology for Obtaining Thermoplastic Building Materials from Non-Recyclable Mixed Plastic–Paper Packaging Waste. *Sustainability* **2024**, *16*, 3430. [CrossRef]
50. Aradoaei, M.; Ciobanu, R.C.; Schreiner, C.; Ursan, A.G.; Hitruc, E.G.; Aflori, M. Thermoplastic Electromagnetic Shielding Materials from the Integral Recycling of Waste from Electronic Equipment. *Polymers* **2023**, *15*, 3859. [CrossRef] [PubMed]
51. EU Construction and Demolition Waste Protocol and Guidelines. Available online: https://single-market-economy.ec.europa.eu/news/eu-construction-and-demolition-waste-protocol-2018-09-18_en (accessed on 25 October 2024).

coatings

MDPI

Article

Endurance to Multiple Factors of Water-Based Electrically Conductive Paints with Metallic Microparticles

Alina Ruxandra Caramitu [1], Romeo Cristian Ciobanu [2,*], Mihaela Aradoaei [2], Magdalena Valentina Lungu [1], Nicoleta Oana Nicula [1] and Eduard Marius Lungulescu [1]

[1] National Institute for Research and Development in Electrical Engineering ICPE-CA Bucharest, 030138 Bucharest, Romania; alina.caramitu@icpe-ca.ro (A.R.C.); magdalena.lungu@icpe-ca.ro (M.V.L.); nicoleta.nicula@icpe-ca.ro (N.O.N.); marius.lungulescu@icpe-ca.ro (E.M.L.)

[2] Department of Electrical Measurements and Materials, Gheorghe Asachi Technical University, 700050 Iasi, Romania; mihaela.aradoaei@academic.tuiasi.ro

* Correspondence: r.c.ciobanu@tuiasi.ro

Abstract: The paper describes the innovative adaptation of some specific environmental tests from general organic coatings towards newly developed water-based composite paints with metallic particles (Al and Fe), with a high content of metal (10% and respectively 20%) for electromagnetic shielding applications. Electrical conductivity is the most affected dielectric parameter under both by UV radiation and thermal exposure. The paints with 20% metallic powder are more sensitive to environmental factors, and the influence of metal type could also be emphasized in relation to the dielectric feature evolution vs. exposure time. The action of mold significantly decreases the dielectric features of paints, but the weathering aging effect is much more enhanced if the samples are cumulatively submitted to thermal aging and respectively UV exposure, along with the action of mold. The potential application of the study is related mainly to the development of new autonomous electric cars, which need special conditions of electromagnetic shielding, under the circumstances that the conductive paint layers are normally very sensitive to environmental factors, affecting the equipment performance and security.

Keywords: composite paints; metallic nano-particles; dielectric tests; environmental tests; lifetime

check for updates

Citation: Caramitu, A.R.; Ciobanu, R.C.; Aradoaei, M.; Lungu, M.V.; Nicula, N.O.; Lungulescu, E.M. Endurance to Multiple Factors of Water-Based Electrically Conductive Paints with Metallic Microparticles. *Coatings* **2024**, *14*, 1016. https://doi.org/10.3390/coatings14081016

Academic Editors: Indrani Coondoo and Mikhaïl Rodionovich Baklanov

Received: 27 June 2024
Revised: 30 July 2024
Accepted: 8 August 2024
Published: 10 August 2024

1. Introduction

Electrically conductive paint is commonly created by blending an electrically conductive pigment with a non-conductive resin binder. Potential uses for these paints include electromagnetic shielding, circuit prototyping, repairing, guarding against electrostatic discharge, and preventing galvanic corrosion. The binder preserves the paint's quality and helps it stick to surfaces, while the conductive pigment enables electrical current to flow through. Metallic particles like copper, silver, and other soft malleable metals are very conductive and enable the current to transmit efficiently in liquid media with solvents. These particles are extremely fine to maintain the wetting and adhesion qualities that regular paints are known for. Electric charges flow through the conductive fillers by making brief jumps between particles in the matrix. This process works best with densely packed fillers in the form of flakes or tubes. Spherical particles may not be the best for achieving maximum conductivity, but when paired with flakes, they can offer a better finish and enhanced conductivity. Besides shape, fillers also vary significantly in electrical conductivity, corrosion resistance, and cost. Actual technologies and related conductive paint products on the market use a limited number and low content of pigments, including branched carbon powder, nickel flakes, silver coated copper flakes, and/or silver flakes, e.g., [1–8], and most of them are based on non-conductive resin binder and organic solvents, which are not environmentally friendly. Water-based electrically conductive paints are specialized coatings that use water as the primary solvent. They are designed to provide electrical conductivity and to be environmentally friendly, representing a versatile solution for situations where traditional solvent-based conductive paints are impractical or environmentally harmful. Water-based conductive paints are used in a variety of industries, including electronics, automotive, and energy, being applied to surfaces for electromagnetic interference (EMI) shielding, antistatic coatings, or other uses that require electrical conductivity on non-metallic substrates. Although they have considerable potential for use, almost no research has examined the reliability of paint films on plastic substrates, although such evaluations would be essential, especially for automotive equipment operating in diverse environments and even in severe conditions.

In current practice for aerospace or construction applications, specific tests have been described to evaluate, for example, the effect of solar absorption, in order to develop infrared-reflective paints [9–11] or solar-absorbing paints on metal support [12,13]. However, there are no similar tests defined for conductive paints. On the other hand, some researchers have examined the antifouling properties of electrodes printed with conductive paints [14], but these studies have only focused on improving the printing technology, not evaluating the reliability of the paints. The methodology for testing for endurance of multilayer water-based electrically conductive paints to multiple factors may be based on related research on environmental effects upon composite organic coatings, e.g., in [15–17].

The novelty of the presented research consists in the adaptation of some specific environmental tests from general organic coatings towards newly developed water-based composite paints with metallic particles (Al and Fe). The originality of the presented recipes lies in the fact that they include a high content of metal (10% or 20%) and special additives to allow them to offer high electromagnetic shielding features and high reliability on different plastic substrates. All ingredients used in paint formulation respects the European Union regulatory framework related to REACH (Registration, Evaluation, Authorization and Restriction of Chemical Substances) in terms that no "Substances of Very High Concern" (SVHCs) were used. The potential application is related mainly in the development of new autonomous electric cars, which need special conditions of electromagnetic shielding to avoid interference and protect the large quantity of sensors and IoT-related devices, but the electromagnetic shielding efficiency is normally very sensitive to environmental factors, which can deteriorate the conductive paint layers and so affect the equipment performance and security.

2. Preparation of Paints with Large Quantities of Metallic Microparticles

2.1. Materials and Methods

The research was oriented towards water-based acrylic paints, which are versatile in applications, offering good water resistance; a wide range of color shades—if necessary to embed; resistance to algae and mold growth; good vapor permeability; resistance to environmental phenomena; high elasticity of the film; high coverage; and easy application (allowing mechanical application by spraying—ideal for the electronic or automotive industry). The basic formula of the water-based acrylic paint is pigment—here also metallic powder, binder (resin), solvent—water, and additives.

2.1.1. Raw Materials

The raw materials for obtaining the paints that are the subject of this work were:

- Polyoxyethylene (25) octyl phenyl ether, butyl acrylate, vinyl acetate, dibutyl phthalate, sodium dodecyl sulfate. All these substances are procured from authorized distributors;
- Microparticles powders (source: Laiwu Powder Material Co. Ltd., Shanghai, China).

2.1.2. Testing Equipment and Methods

Two types of paints were obtained, coded as V1 and V2, with the following composition: V1—Solvent—water 42%; Polyoxyethylene (25) octyl phenyl ether—surfactant and buffer 2%; butyl acrylate and vinyl acetate—binder 43%; Dibutylphthalate—plasticizer 1%; sodium dodecyl sulfate—antiagglomerant and compatibilizer 1%; initiator, reducing agent, defoamer, preservative and crosslinking polymer—all 1%, metallic powder 10% (two variants, with Al and respectively Fe powder); and V2—Solvent—water 37%; Polyoxyethylene (25) octyl phenyl ether—surfactant and buffer 2%; butyl acrylate and vinyl acetate—binder 38%; Dibutylphthalate—plasticizer 1%; sodium dodecyl sulfate—antiagglomerant and compatibilizer 1%; initiator, reducing agent, defoamer, preservative and crosslinking polymer—all 1%, metallic powder 20% (two variants, with Al and Fe powder), as described in [18].

To homogenize the paints and avoid the agglomeration of the Al and Fe powders, an ultrasonication was applied for 30 min when mixing the metallic powders with the solvent, another 15 min when adding the binder and additives, and finally for 5 min before applying the paints upon support. The ultrasonication of paint mixtures was made in the USC-T type VWR ultrasonic bath: capacity 2.8 L; frequency 45k Hz; size of the tub: 237 × 134 × 100 mm (VWR International—Avantor Inc., Radnor, PA, USA). The paints were deposited on polycarbonate support, which was preliminarily sandblasted. The sandblasting process was performed with an Eco Pressure 80–140 P Sandblasting Booth (Sablast Techn., Targu Mures, Romania), maximum pressure: 10 bar, loading capacity: 350 Kg, abrasive grit: max. 1.5 mm; degree of sandblasting: SA-3 [18].

The composite samples obtained were coded as M1 for V1 + Al, M2 for V2 + Al, M3 for V1 + Fe, and M4 for V2 + Fe.

For the powders used, SEM structural analyses were initially carried out to verify the morphology and particle sizes. The equipment with which the SEM structural analyses were carried out was a scanning electron microscope with field emission source and focused ion beam from ZEISS. This equipment is dedicated to the study of microscopic structures and inorganic and organic surfaces. The images were taken at an acceleration voltage of 5 kV with a working distance of 4.3–4.5 mm. The detector used was the secondary electron detector of the Everhart Thornley type with the Faraday cup in the sample chamber, resulting in micrographs that highlight the morphology and topography of the analyzed surfaces. Also, we employed an active load compensation system (local) with N2 gas was used on the surface of the analyzed sample (CC—charge compensation).

The FTIR spectra of the paint samples were recorded with a Jasco 4200 spectrometer (Jasco International Co., Ltd., Tokyo, Japan) coupled with the accessory ATR (Attenuated Total Reflectance) Jasco Pro 470-H. The samples were measured directly by placing them on the crystal of the ATR device and by pressing with a controlled force, and the spectra recording conditions were as follows: spectral range: 4000–500 cm^{-1}; resolution: 4 cm^{-1}; number of scans/spectrum: 50.

The determination of the thickness of the paint layers (average of 3 measurements) was made with the PosiTector® 200 tester (DeFelsko Corporation, Ogdensburg, NY, USA).

The hydrodynamic diameter (D_{hd}), also known as the effective diameter (D_{eff}) of Al and Fe particles, as well as polydispersity, particle size distribution, and mean diameter (Multimodal Size Distribution—MSD) by volume, were determined by Dynamic Light Scattering (DLS) using a 90Plus particle size analyzer (Brookhaven Instruments Corporation, Holtsville, NY, USA). The analyzer was equipped with a solid-state laser with a wavelength of 660 nm and an output power of 32 kW. Ten measurements were conducted per sample at a temperature of 25 °C and a light scattering angle of 90°. A 10 mm pathlength plastic cell filled with 3 mL of 0.1 wt % Al or Fe particle aqueous suspension was used for the measurements.

To determine the topography of the surface of the samples, a high-precision interferometric WYKO NT 1100 microscope (Veeco, Tucson, AZ, USA) was used, with a resolution of up to 0.2 nm on the Oz axis. The derived parameters are Ra—arithmetic average of the deviation values from the average profile, on the scanned surface; Rq—root mean square roughness; Rt—total roughness in μm (difference of measured values between the highest point and the deepest point of the scanned surface). The roughness parameters were determined as the average value of 3 measurements performed on the same sample in its central area at a focal distance of 90 μm.

The UV irradiation exposure was performed using a Kolorlux Blacklight UV lamp (wavelength of 365 nm) Mercury HGW 160 W/27 230–240 V (GE Lightening, East Cleveland, OH, USA) with a dose of 150 mW/m^2 per hour at a temperature of 40 °C and humidity of 60%.

The dielectric properties were determined using broadband dielectric spectroscopy method with a Solartron 1260A dielectric spectrometer (Solartron Analytical, Farnborough, UK).

3. Results and Discussion

3.1. Structural Analyses

Figure 1 shows the micrographs, with the identification of the particle size, for the two powders used.

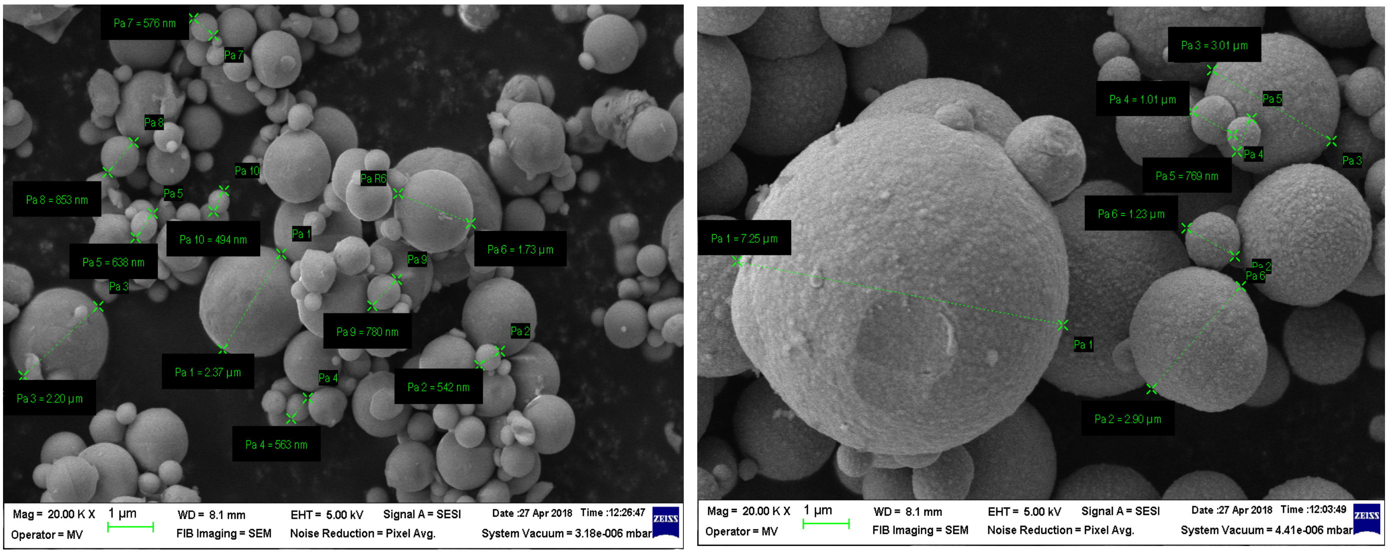

(**a**) (**b**)

Figure 1. SEM micrographs for (**a**) Al powder 800 nm and for (**b**) Fe powder 790 nm [19].

From the micrographs in Figure 1, a large dispersion of particle sizes is observed. This was highlighted by making 10 measurements of Al 800 nm powder particles, and the following values resulted: 2.37 µm, 542 nm, 638 nm, 1.73 µm, 576 nm, 853 nm, 780 nm and 494 nm. This powder has an average size of 798 nm. And in the case of Fe powder, the following values are obtained after six measurements: 7.25 µm, 2.9 µm, 3.01 µm, 1.01 µm, 769 nm, and 1.23 µm, for an average size of 2.78 µm.

3.2. ATR/FTIR Analysis

The ATR/FTIR spectra presented below were selected and reprocessed for the data presented in [20]. The ATR/FTIR spectra recorded on the two analyzed paint samples, before the metallic powder addition, is presented in Figure 2 (where V2 has a lower concentration of binder).

The spectral display absorption bands represent various functional groups present in the chemical composition of the samples being analyzed, as mentioned in references [20–22]: 3100–3600 cm^{-1}, peaking around 3390 cm^{-1}, specific to the stretching vibration of hydroxyl groups (–OH); 2700–3000 cm^{-1}, specific to the stretching vibrations of the –CH-type groups; 2951 and 2925 cm^{-1} (CH_3 asymmetric stretching vibration), 2854 cm^{-1} (for CH_2 stretching vibration); 1610–1780 cm^{-1}, the typical carbonyl group band, showing a primary peak at approximately 1721 cm^{-1} (resulting from the stretching vibration of the C–O group) and a faintly distinguishable peak at around 1715 cm^{-1} from the vibration of a ketone-type C=O, while 1500–1570 cm^{-1} has a peak around 1536 cm^{-1}, specific to the C=O vibration;

1430–1500 cm^{-1}, peaking at around 1464 cm^{-1}, is caused by C–H bending vibrations (CH_2, CH_3); 1330–1420 cm^{-1}, peaking at 1387 cm^{-1}, indicates symmetrical deformation of CH_2; 1258 cm^{-1} signifies characteristic C–O–C of ester type; 1000–1180 cm^{-1} displays multiple peaks (1040, 1070, and 1128 cm^{-1}) characteristic for the vibration modes of C–O.

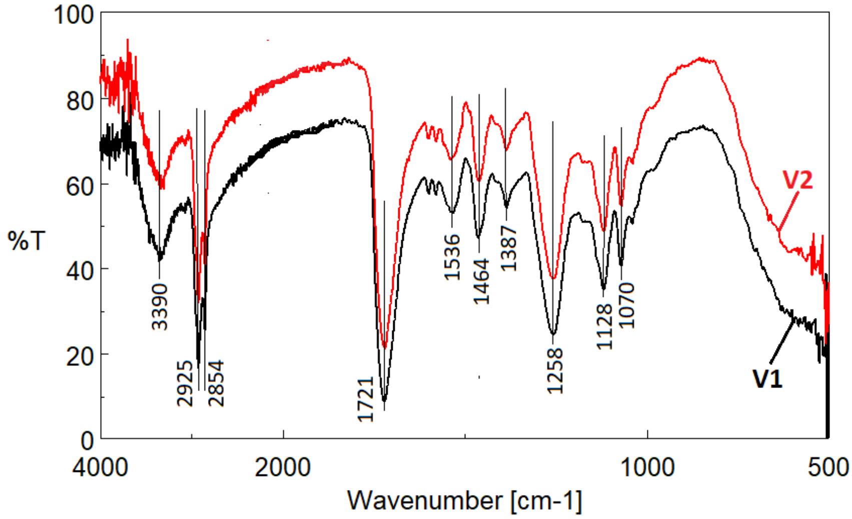

Figure 2. ATR/FTIR spectra recorded before metallic powder addition [20].

The characteristic features of acrylic-type compounds include the intense peak at 1258 cm^{-1} and the doublet at 1128 and 1170 cm^{-1} [23]. By comparing the data gathered, along with the information that bands within the ranges of 2700–3000 cm^{-1}, 1610–1780 cm^{-1}, 1430–1500 cm^{-1} are associated with methyl-methacrylate compounds [23], we can deduce that both types of paints studied are indeed acrylic in nature. However, it is clear that the ATR/FTIR spectra of both paint samples are nearly identical, indicating that the two paints being analyzed share the same fundamental chemical composition. Figure 3 shows ATR/FTIR spectra of metal powders, with notable peaks near the 2200 cm^{-1} band, yet all metallic powders are considered to be infrared-inactive substances. Finally, the comparative ATR/FTIR spectra recorded on V1 and V2 paints after the addition of metal fillers are presented in Figure 4.

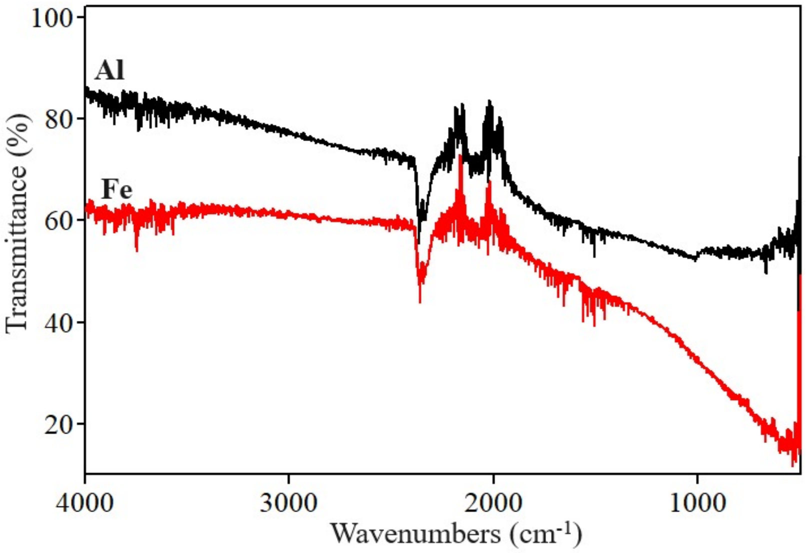

Figure 3. Comparative ATR/FTIR spectra recorded on metal powders [20].

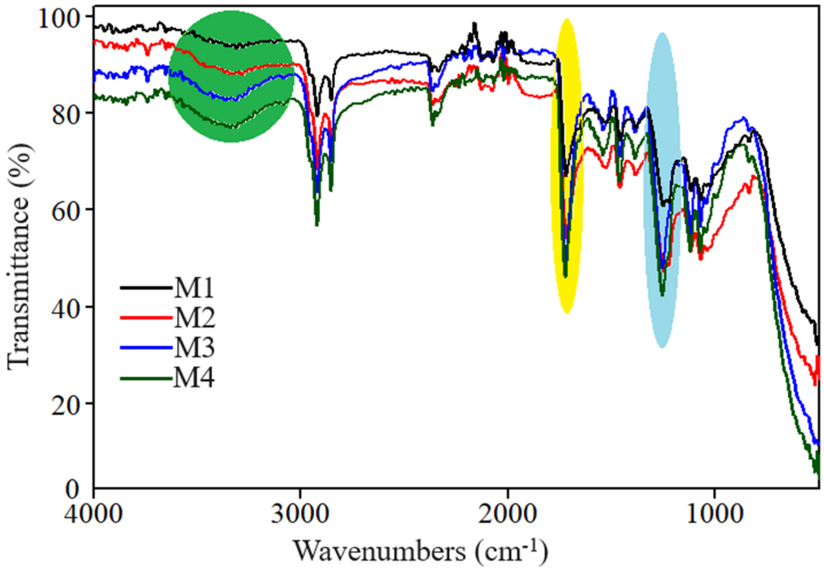

Figure 4. Comparative ATR/FTIR spectra recorded on paints with different metal fillers [20].

Adding metal powders results in a significant alteration in the appearance of bands representing C=O groups in the 1610–1780 cm^{-1} region (band widens), as well as C–O–C at 1258 cm^{-1} (band widens and gains a multi-peaked structure). The intensity of the band characteristic of hydroxyl groups at 3390 cm^{-1} decreases with the presence of metal powder. The presence of electrostatic interactions between the acrylic matrix of the paint and the metal particles, potentially forming hydrogen bonds, contributes to this phenomenon [24]. The band specific for metallic particles identified in Figure 2 can be also identified in Figure 3. Regarding the transmittance level, the paints containing Al present a higher transmittance comparing to the paints containing Fe. On the other hand, it is obvious, for both paint types with metallic additives, that the transmittance decreases with the increase in the metallic particle content.

3.3. DLS Study

The results are presented in Figures 5 and 6, and respectively in Table 1. G(d) represents the relative percentage contribution of the particle size range, and C(d) denotes the cumulated percentage contribution.

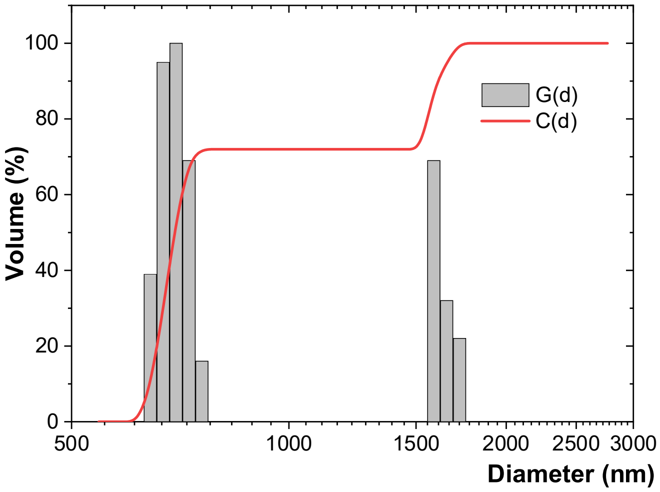

Figure 5. Particle size distribution histogram (MSD) of Al particles by volume.

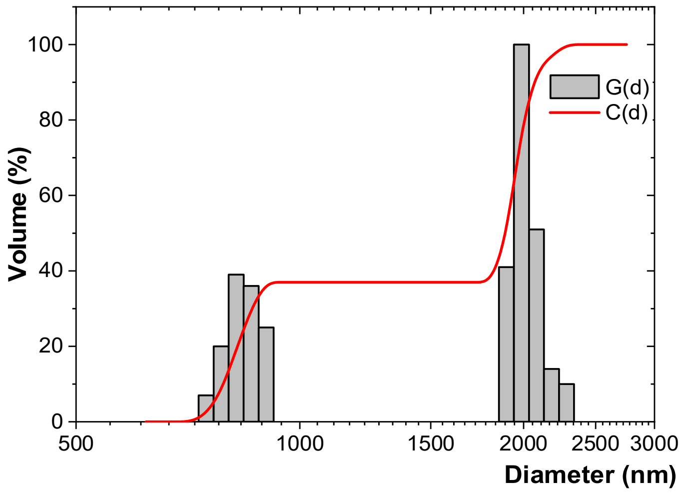

Figure 6. Particle size distribution histogram (MSD) of Fe particles by volume.

Table 1. DLS results for Al and Fe particles dispersed in aqueous suspensions at a concentration of 0.1 wt %.

Sample	Hydrodynamic Diameter (nm)	Polydispersity Index (PDI)	MSD by Volume		
			Mean Diameter (nm)	Relative Variance	Skew
Al particles	896.4 ± 35.6	0.113 ± 0.058	951.4	0.196	0.999
Fe particles	1317.3 ± 71.4	0.126 ± 0.022	1580.5	0.133	−0.484

Both Al and Fe particles dispersed in aqueous suspensions at a concentration of 0.1 wt % revealed PDI values indicative of polydisperse particles (Table 1, Figures 5 and 6). The PDI measures the width of the particle size distribution and is derived from the cumulants analysis of the DLS data.

The relative variance, a statistical measure used to describe the distribution of particle sizes within a sample, correlates with the PDI. It indicates the degree of polydispersity and how widely the particle sizes vary around the mean size (Table 1).

The mean and standard deviation of the hydrodynamic diameter were lower for Al particles (896.4 ± 35.6 nm) compared to Fe particles (1317.3 ± 71.4 nm). This indicates the coherence of the granulometric dimensions of the metallic powder-additive system within the binder and solvent. The Fe-based systems exhibited larger dispersion, a higher hydrodynamic diameter, and a larger mean diameter by volume compared to the Al systems. This observation is in agreement with the SEM analysis (Figure 1). Moreover, the particle size determined by DLS analysis is typically higher than that obtained by SEM or TEM analysis, as DLS considers the size of the inorganic particle core along with its surrounding adsorbed molecular layer from the aqueous suspension. Both Al and Fe particles dispersed in aqueous suspensions exhibited bimodal size distributions by volume. The Al particle suspension featured a predominant population of smaller particles (642.7–757.6 nm) with a C(d) of 9%–72%, and a second population of coarser particles (1587.4–1723.4 nm) with a C(d) of 88%–100% (Figure 5). In contrast, the Fe particle suspension had a first population of smaller particles (748.0–901.0 nm) with a C(d) of 2%–37%, and a dominant population of larger particles (1896.4–2284.1 nm) with a C(d) of 49%–100% (Figure 6).

The particle size distribution for Al particles was right-skewed, while that for Fe particles was left-skewed (Table 1), indicating deviations from a symmetrical distribution.

The bimodal characteristics of both Al and Fe particle size distributions can be attributed to the presence of both primary and agglomerated particles in the aqueous suspensions. However, no additional population of aggregates with higher particle sizes was observed in either suspension. Furthermore, deagglomeration of Al and Fe particles can be achieved through sonication or stirring, and the addition of additives within the binder and solvent prevented particle flocculation and sedimentation.

3.4. Determination of Thickness and Surface Topography (Roughness) of Paint Layers

The results are summarized in Table 2 and Figures 7 and 8. The roughness of the paint layers with more metal particles content is about 30%–35% higher compared to the layers with less metal particle content, regardless the metal type. The roughness of the paint layers containing Al is at least 2.5 times higher compared to the paint layers containing Fe, an aspect which could be explained by a better formulation of paints containing Fe, in terms of dispersibility of metallic particles and/or affinity to the compatibilization additives, but also based on the granulometric results for the metallic systems.

Table 2. Average surface roughness of paint layers.

Roughness (µm)	Thickness of Paint Layer (µm)	Ra	Rq	Rt
M1	19.96	2.95	3.73	25.65
M2	25.87	3.78	4.82	30.16
M3	20.49	1.01	1.25	8.39
M4	26.20	1.34	1.66	10.91

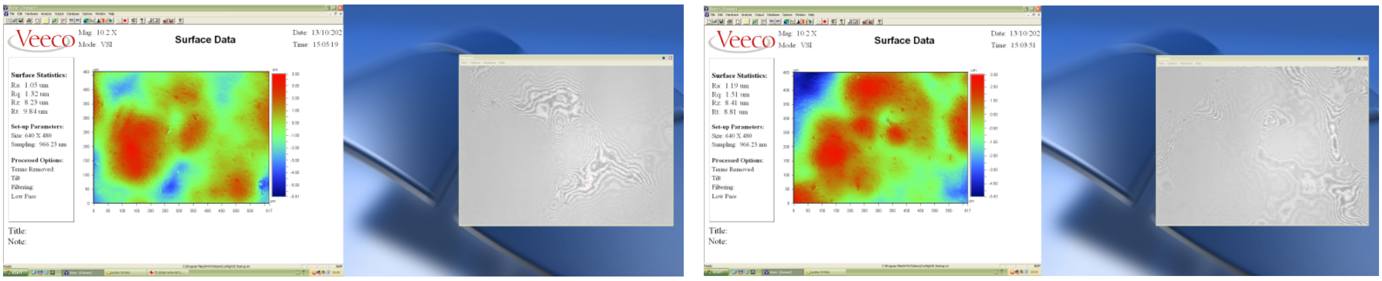

Mag: 10.2 X
Mode: VSI
Date: 13/10/202
Time: 15:05:19

Surface Statistics:
Ra: 1.05 um
Rq: 1.32 um
Rz: 8.23 um
Rt: 9.84 um

Set-up Parameters:
Size: 640 X 480
Sampling: 966.23 nm

Processed Options:
Terms Removed:
Tilt
Filtering:
Low Pass

Title:
Note:

Mag: 10.2 X
Mode: VSI
Date: 13/10/202
Time: 15:03:51

Surface Statistics:
Ra: 1.19 um
Rq: 1.51 um
Rz: 8.41 um
Rt: 8.81 um

Set-up Parameters:
Size: 640 X 480
Sampling: 966.23 nm

Processed Options:
Terms Removed:
Tilt
Filtering:
Low Pass

Title:
Note:

Figure 7. Roughness analysis for M1 and M2.

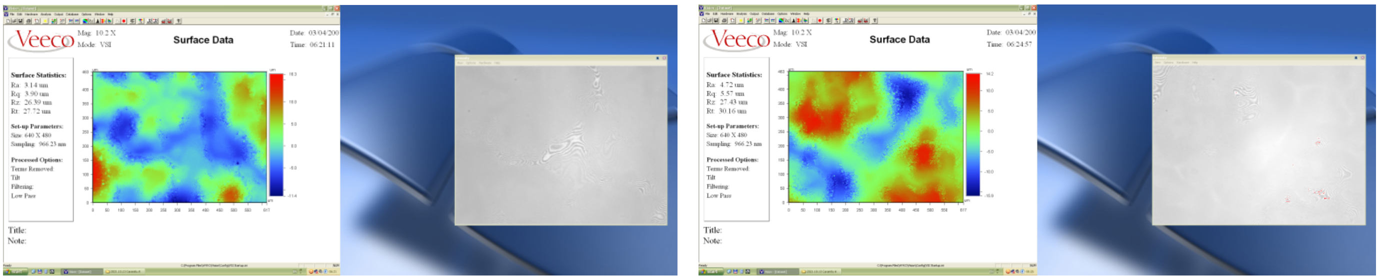

Mag: 10.2 X
Mode: VSI
Date: 03/04/200
Time: 06:21:11

Surface Statistics:
Ra: 3.14 um
Rq: 3.90 um
Rz: 26.39 um
Rt: 27.72 um

Set-up Parameters:
Size: 640 X 480
Sampling: 966.23 nm

Processed Options:
Terms Removed:
Tilt
Filtering:
Low Pass

Title:
Note:

Mag: 10.2 X
Mode: VSI
Date: 03/04/200
Time: 06:24:57

Surface Statistics:
Ra: 4.72 um
Rq: 5.57 um
Rz: 27.43 um
Rt: 30.16 um

Set-up Parameters:
Size: 640 X 480
Sampling: 966.23 nm

Processed Options:
Terms Removed:
Tilt
Filtering:
Low Pass

Title:
Note:

Figure 8. Roughness analysis for M3 and M4.

3.5. Resistance to Water and Solvent (Isopropyl Alcohol)

The water/solvent (here isopropyl alcohol—specific for water-based paints) resistance of composite materials is determined by the amount of liquid that the material can absorb when immersed in water/solvent, according to SR EN ISO 175/2011 [25]. Approx. 0.1 g of each paint material was weighed and placed in plastic ampoules with tight lids (tubes for microcentrifuges with a diameter of 10 mm and a length of 40 mm). The ampoules with composite material were filled with deionized water and respectively with solvent (isopropyl alcohol) and then were kept for cycles of 72 h for a total duration of 360 h at a temperature of 22 °C (atmospheric) and an average humidity of 40%. The following

Formula (1) was used to determine the resistance to the action of water/solvent (degree of swelling):

$$c = \frac{m_2 - m_1}{X m_1} \times 100 \tag{1}$$

where:

c—degree of swelling;
$m_{2,3,4}$—mass of inflated/swollen material (after each 72-h cycle); X_1—mass of initial—dry material.

The experimental results for the resistance to the action of water and the resistance to the action of alcohol are presented in Figure 9.

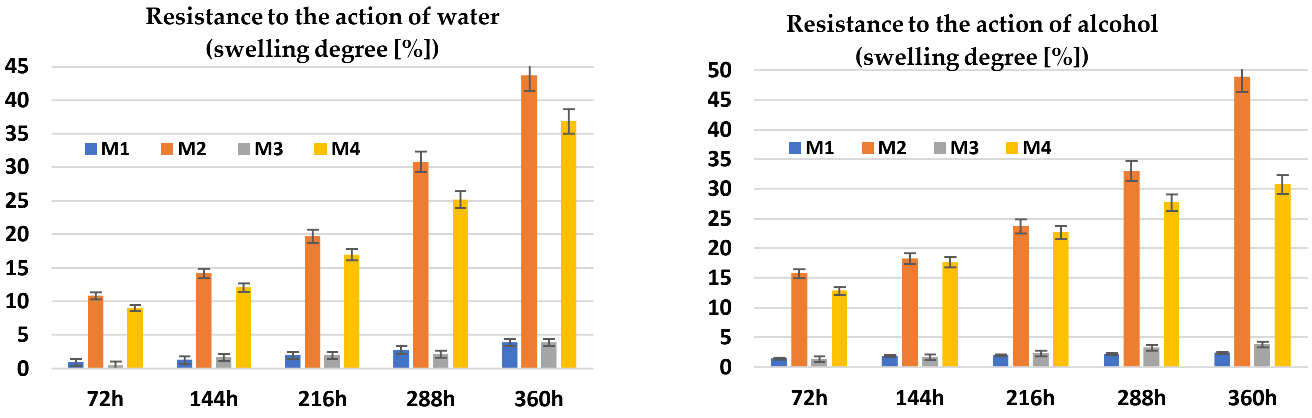

(**a**) (**b**)

Figure 9. Resistance to the action of (**a**) water, (**b**) isopropyl alcohol.

The hygroscopicity, as well as the dissolution in isopropyl alcohol, can be justified by the fact that the acrylic groups, existing in the paint, present functional groups that form hydrogen bonds with the water/alcohol they absorb. The dissolution occurs due to the fact that the solvent changes the spacing of the macromolecular chains and reduces intermolecular forces so much that a polymer solution is obtained.

Due to the higher inhomogeneity, and to the action of metallic particles mainly in the presence of water, the paints with a higher percent of metallic particles exhibited an expected higher swelling degree, but the value itself was remarkable high, i.e., the swelling degree of paints with 20% metallic powder was about 10 times higher than the one for the paints with 10% metallic powder. Regarding the influence of the type of added metal, the paints with Al present a higher swelling degree, at about 20%, compared to the paints with Fe. In all, the swelling degree seems to increase linearly with time in the case of water, but in the case of alcohol, it increases more rapidly in the first period, until 9 days of exposure, and then the increase is slower, due probably to the saturation of functional groups of the binder.

3.6. Resistance to the Action of UV Radiation and Lifetime Evaluation

The samples of paint films were subjected to exposure to UV radiation cycles of 72 h for a total duration of 360 h, according to ISO 4892-3:2016 [26,27].

It could be noticed that until 144 h of UV radiation exposure, the samples did not suffer any visible change; starting at 216 h, the samples M2 and M4 presented some micro-cracks, and after 288 h, the crack phenomenon intensified for all samples, leading to partial exfoliation from support after 360 h of exposure.

Due to the fact that for the proposed application of electromagnetic shielding, the main dielectric feature to be maintained was dielectric loss factor—Tg(Delta)—this was mainly analyzed, as presented in Figure 10.

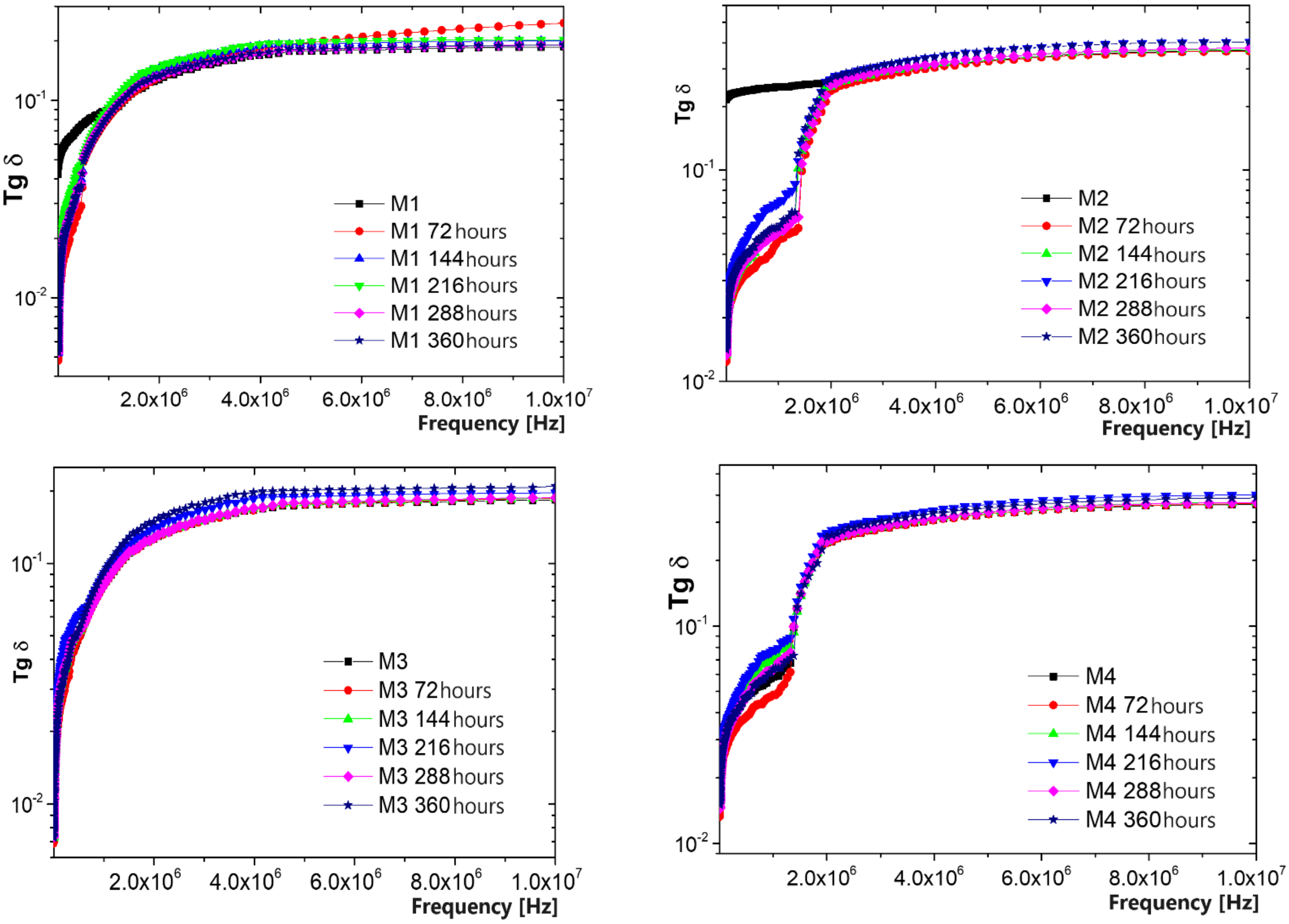

Figure 10. Tg(Delta) variation vs. time at UV radiation exposure.

When analyzing the initial values, it was noticed that the paint samples with higher metallic content present a higher loss factor, at about 20%, and a higher conductivity, about 10 times higher. The influence of metallic particles type is insignificant, even if the paints with Fe seem to present slightly higher values. Regarding the influence of exposure time, tg(Delta) presents a higher stability for all samples, even if some variations are noticed at lower frequencies, mainly for the paints with higher metallic content. The conductivity seems to be more affected by UV radiation, especially for the paints with higher metallic content. Here also the influence of metal type could be noticed, i.e., the conductivity of paints with Fe content is more sensitive to UV exposure compared to that of paints with Al content, meaning that Fe may catalyze some destruction processes at binder level.

On the other hand, some specific extra-polymerization phenomena under UV exposure were noticed, leading, e.g., to an increase in conductivity, mainly for M2 and M4, until 72 h of exposure, followed by the normal decrease after 144 h, a phenomenon in line with other related phenomena as in [26].

Finally, the estimated remaining lifetime was calculated, considering that the exposure to UV radiation continues, following the methodology in [27]. Here, the analyzed characteristic was the electrical resistivity (inverse of conductivity). The variation in the electrical resistivity according to the time of exposure to UV radiation is presented in Figure 11, and the functions that describe the trend of the variation curve were determined.

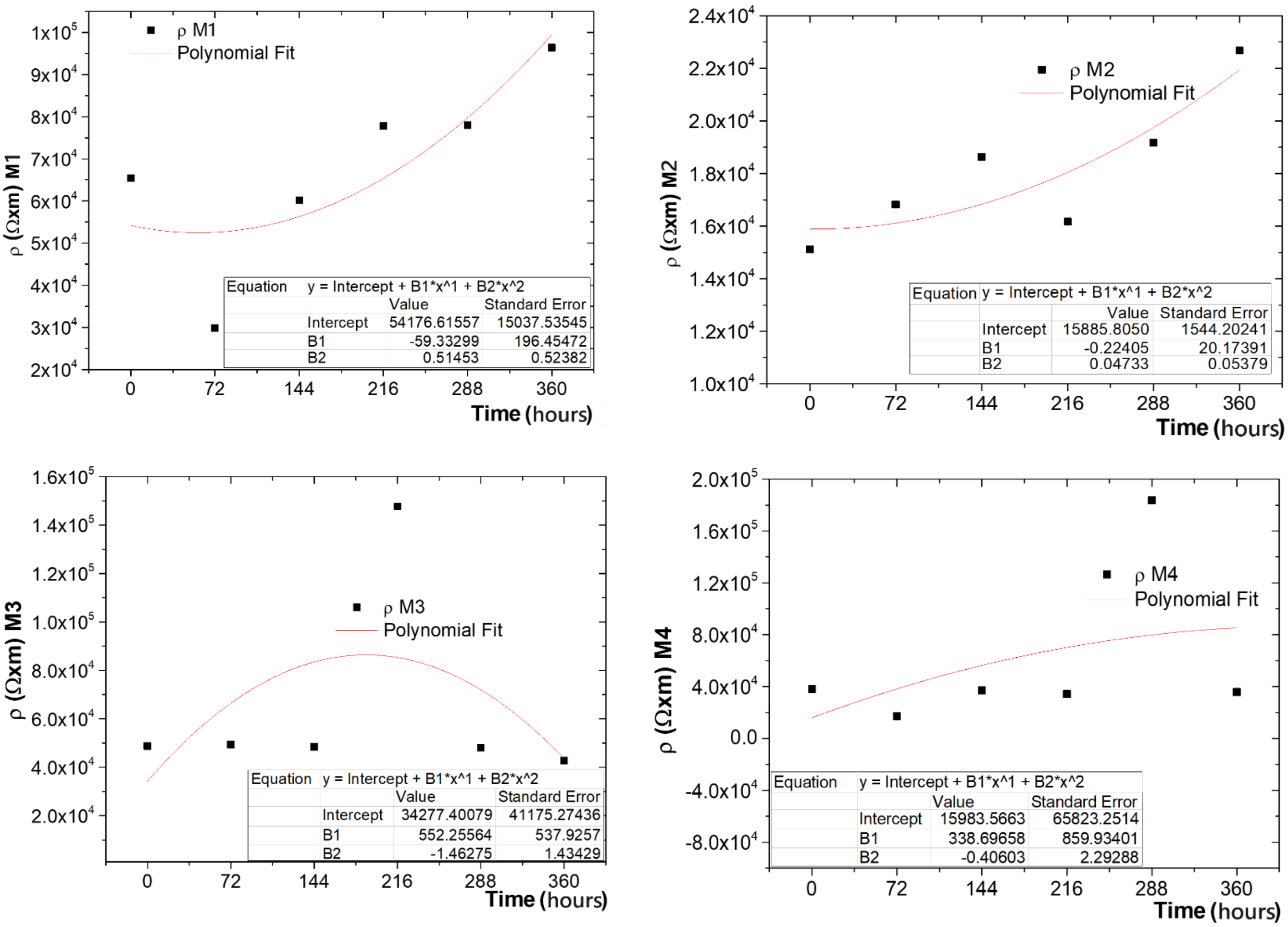

Equation	y = Intercept + B1*x^1 + B2*x^2	
	Value	Standard Error
Intercept	54176.61557	15037.53545
B1	-59.33299	196.45472
B2	0.51453	0.52382

Equation	y = Intercept + B1*x^1 + B2*x^2	
	Value	Standard Error
Intercept	15885.8050	1544.20241
B1	-0.22405	20.17391
B2	0.04733	0.05379

Equation	y = Intercept + B1*x^1 + B2*x^2	
	Value	Standard Error
Intercept	34277.40079	41175.27436
B1	552.25564	537.9257
B2	-1.46275	1.43429

Equation	y = Intercept + B1*x^1 + B2*x^2	
	Value	Standard Error
Intercept	15983.5663	65823.2514
B1	338.69658	859.93401
B2	-0.40603	2.29288

Figure 11. Lifetime evaluation results for UV radiation exposure.

The critical value of the electrical resistivity at which the material can be considered to be degraded was chosen as a 30% variation from the initial value, and we could identify at what number of hours of UV radiation exposure the material should be replaced, i.e., M1 after 472 h, M2 after 360 h, M3 after 445 h, and M4 after 332 h, confirming the conclusions presented above, related to the higher stability of paints with lower metallic content, and respectively with Al insertions, but generally, the lifetime differences are not so high among the analyzed paints.

3.7. *Resistance to the Action of Temperature and Lifetime Evaluation*

The samples of paint films were placed in a Memmert UF30 oven with forced convection (Humeau, Couëron, France), at a temperature of 100 °C and maintained for cycles of 72 h for a total duration of 360 h, according to SR EN 60216-3:2007 [28,29]. The results for the investigated dielectric parameters are presented in Figure 12 and the lifetime evaluation in Figure 13.

It can be noticed that until 144 h of thermal exposure, the samples do not suffer any visible change, but starting at 216 h, the samples present visible yellow traces, which indicates that the binder is starting to be affected by the temperature. After 288 h, the crack phenomenon occurs for all samples, but no exfoliation process was identified, even after 360 h of exposure. It seems that the paints are more sensitive to long-time UV radiation exposure than to thermal exposure.

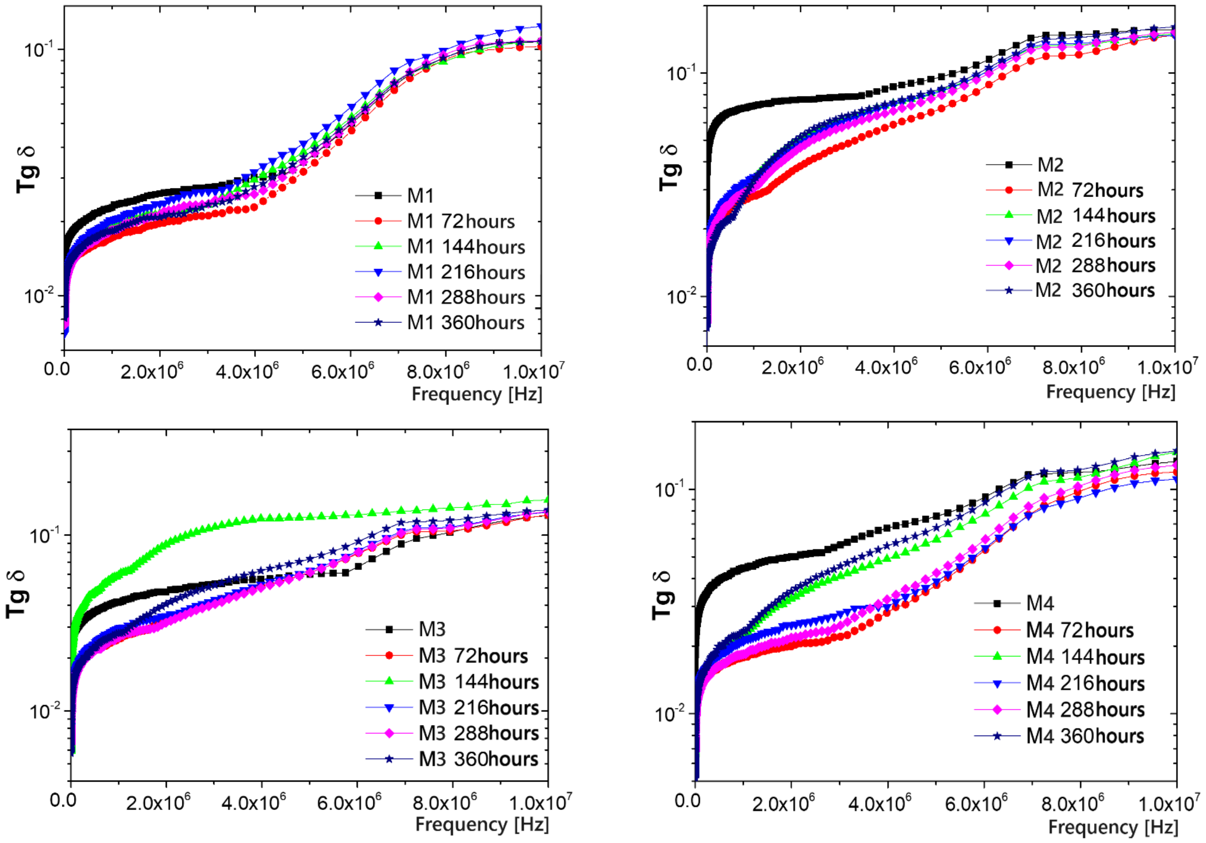

Figure 12. Tg(Delta) variation vs. time at thermal exposure.

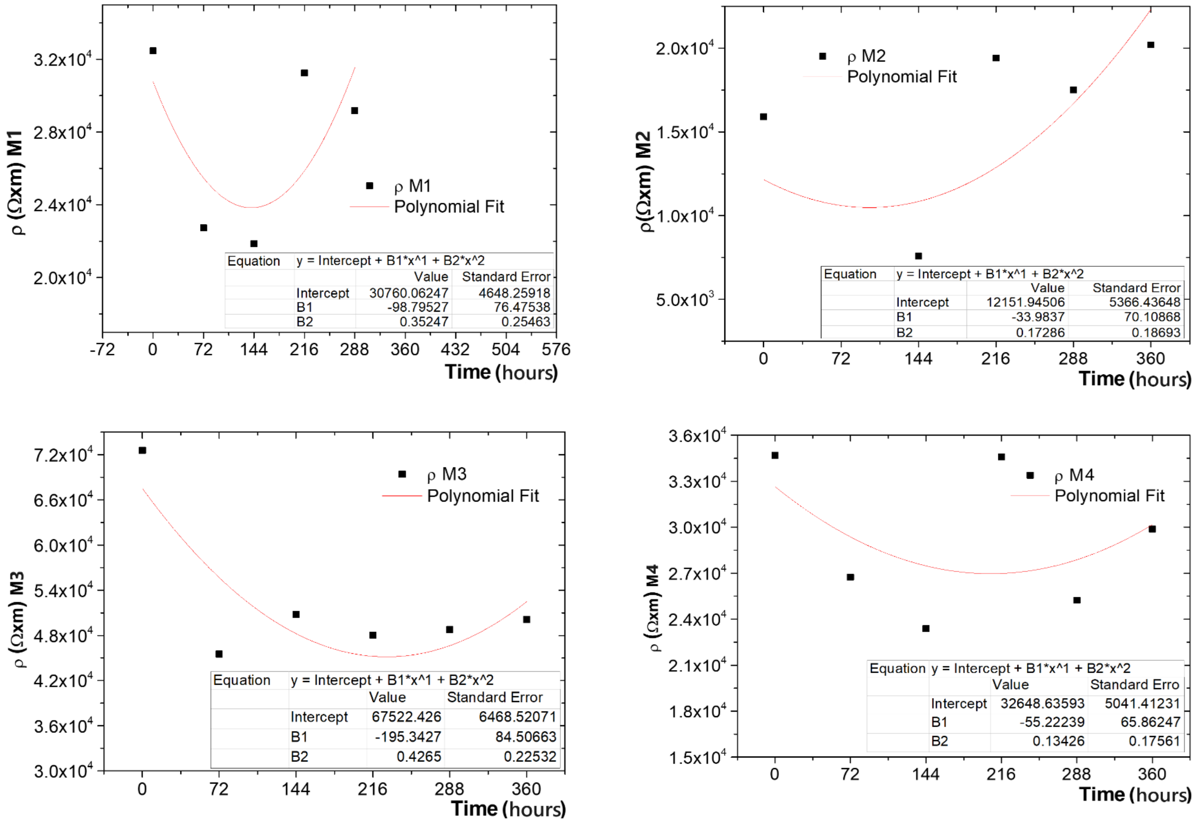

Equation	y = Intercept + B1*x^1 + B2*x^2		
		Value	Standard Error
	Intercept	30760.06247	4648.25918
	B1	-98.79527	76.47538
	B2	0.35247	0.25463

Equation	y = Intercept + B1*x^1 + B2*x^2		
		Value	Standard Error
	Intercept	12151.94506	5366.43648
	B1	-33.9837	70.10868
	B2	0.17286	0.18693

Equation	y = Intercept + B1*x^1 + B2*x^2		
		Value	Standard Error
	Intercept	67522.426	6468.52071
	B1	-195.3427	84.50663
	B2	0.4265	0.22532

Equation	y = Intercept + B1*x^1 + B2*x^2		
		Value	Standard Erro
	Intercept	32648.63593	5041.41231
	B1	-55.22239	65.86247
	B2	0.13426	0.17561

Figure 13. Lifetime evaluation results for thermal exposure.

When analyzing the influence of exposure time, tg(Delta) presents a continuous decrease in value, mainly at lower frequencies, and a more pronounced decrease for the paints with higher metallic content. The conductivity seems to be very affected by the thermal exposure, with an unexpected high increase of values, especially after 144 h of exposure, and more pronounced for the paints with higher metallic content. Here also the influence of metal type could be noticed, i.e., the conductivity of paints with Al content is more sensitive to thermal exposure compared to that of paints with Fe content, meaning that in this case, Al is the main factor that may catalyze some destruction processes at the binder level.

Finally, the estimated remaining lifetime was calculated, considering that the thermal exposure continues, following the methodology in [29]. The variation in the electrical resistivity according to the time of thermal exposure is presented in Figure 13, and the functions that describe the trend of the variation curve were determined. The critical value of the electrical resistivity at which the material can be considered to be degraded was chosen as a 30% variation from the initial value, and we could identify at what number of hours of thermal exposure the material should be replaced, i.e., M1 after 562 h, M2 after 641 h, M3 after 447 h, and M4 after 476 h, confirming the conclusions presented above, related to the higher stability of paints with lower metallic content, and respectively with Fe insertions. The lifetime differences are not so high at higher metallic contents, but remain high enough at lower metallic contents when comparing the paints with Al and Fe.

3.8. Resistance to the Action of Molds

The tests were performed according to EN 60068-2-10:2005 [30] and consisted in exposing the samples to the action of the fungal strains, in the presence of a nutrient medium (with sucrose as additional carbon source), in Petri dishes. The samples were applied to the agarized Czapek–Dox medium and inoculated by spraying with mixed spore suspensions (prepared in a nutrient solution of mineral salts). The tested molds were especially Trichoderma viride, Aspergillus flavus, and Aspergillus niger, the most aggressive species considered for the dedicated application of paints for electromagnetic shielding carcasses for automotive electronics. To ensure favorable conditions for spore germination and fungal development, the samples were incubated in a thermostat with humidification, at a temperature of 30 ± 2 °C and approximately 90% RH for 28 days.

The resistance to the action of molds was comparatively analyzed taking into account the initial paint samples and aged samples (thermal aging—1776 h in dry heat at 100 °C and then UV aged—432 h exposed to UV radiation of 100 W/m^2), because the stabilization and destructive effect of molds may be enhanced on aged paint samples. In our case, the study was much more expanded comparing to homologue research results presented e.g., in [30,31].

The preliminary visual analysis upon the initial samples reveled that:

- After 3 days of exposure, no zone of mold growth was observed on the paint samples, but a very dense growth of mold could be observed around the paint on the plastic sample support, and there were very few fungal colonies starting to penetrate the edge of the paint samples.
- After 7 days of exposure, mold colonies were noticed on the samples, but they did not cover more than 20% of the sample surface, under the circumstances that massive mold colonies were growing around the paint samples.
- After 14, 21, and 28 days of exposure, the mold colonies persisted on the paint samples, but they were found at the same stage of development as for 7 days, i.e., the degree of coverage remained unchanged at about 25% of the paint sample surface.

The maximum paint surface covering was noticed for M3 sample (25%), and the minimal effect for M2 (about 14%).

Taking into account homologous research upon acrylic paints [30], we can preliminarily estimate that the high content of metallic particles within the paints limits the extension of molds on paints, compared to homologue paints without metallic particle content, and the effect is remarkable, mostly because the added metallic particles are not from the classical category recognized for their anti-mold effect, such as Ag or Ni. On the other hand, the host and infestation area for mold activity remains the plastic support for paint deposition.

From the three mold types tested, only Aspergillus niger and Aspergillus flavus occurred on the paint surface, an example being indicated in Figure 14.

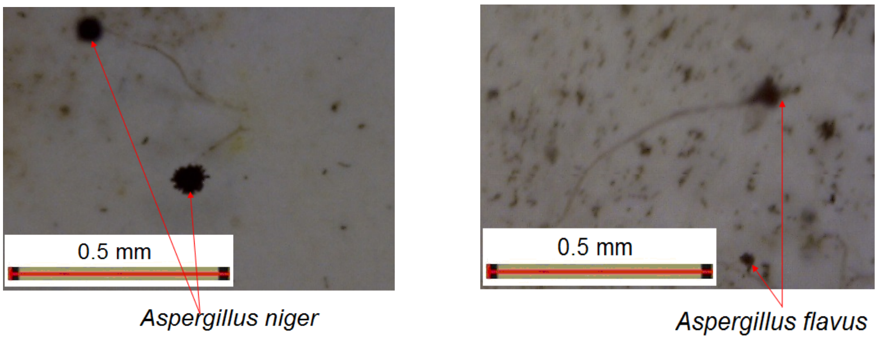

Figure 14. Molds occurrence on M2, after 7 days of exposure [30].

The similar observations upon paint samples thermally aged revealed that the results were similar to those for initial samples, i.e., after 28 days of exposure the mold colonies maintained on the paint samples do not cover more than 25% of the sample surface, even if massive mold colonies were growing around the paint samples.

When analyzing the UV-aged paint samples, some new aspects were revealed:

- After 3 days of exposure, no large zones of mold growth were observed on the paint samples, but some few fungal punctual colonies were noticed, along with a very dense growth of mold observed around the paint samples and on the paint edges.
- After 7 days of exposure, a consistent growth of fungal colonies on the paint samples were noticed, this time especially Trichoderma viride, mainly along with Aspergillus niger, exceeding 25% of the paint.
- After 14, 21, and 28 days of exposure, the mold colonies were constantly developing upon the paint samples, but much more slowly, the degree of coverage remaining under 35% of the paint sample surface after 28 days, an example being indicated in Figure 15.

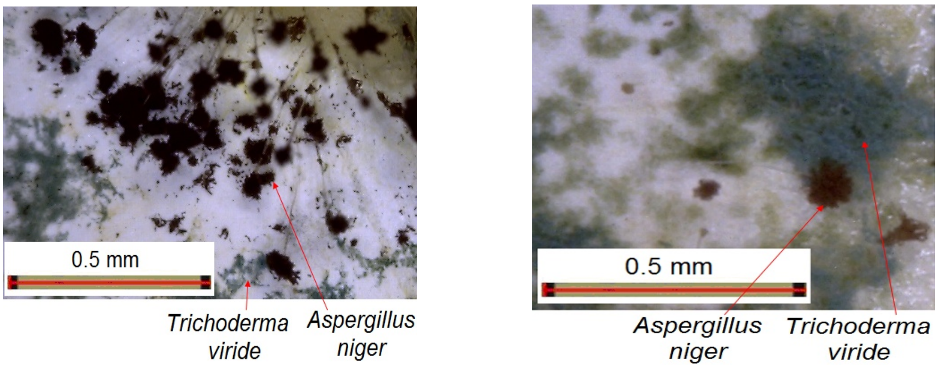

Figure 15. Mold occurrence on M3, after 7 days and, respectively, 28 days of exposure [30].

In this case, the maximum paint surface covering was noticed also for the M3 sample (over 35%), and the minimal effect for M2 (about 22%).

It is obvious that the UV aging effect is the most destructive also from the point of view of mold action. In order to assure a higher stability of paints, along with the limitation of the fungal effect, two strategies should be taken into account: addition of UV protection additives to the paint, and most relevant, addition of fungal protection additives within the plastic carcasses (the most sensitive to weathering conditions) which are supposed to be submitted to paint covering for electromagnetic shielding features. So the inhibition of molds at plastic surface is considered essential, because the mold action begins with a dense growth of mold around the paint on the plastic sample support, followed by a later penetration of the paint layer, forming the edge of the paint samples.

Taking into account that the most important characteristic of paint which assures the electromagnetic shielding features is the dielectric loss factor Tg(delta), the variation in this parameter was analyzed for combined cumulative action of molds, dry heat, and UV radiation. The results are presented in Figure 16.

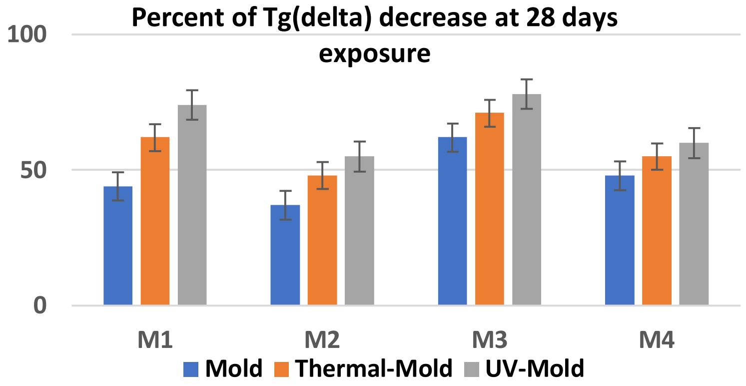

Figure 16. Tg(delta) variation at combined action of molds, dry heat, and UV radiation.

It is obvious that the mold action significantly decreases the dielectric features of paints, when compared to the results under Sections 3.6 and 3.7 for the aging of initial samples, but the weathering aging effect is much more enhanced if the samples are cumulatively submitted to thermal aging and then UV exposure, along with the mold action. The aging effect due to mold action is diminished for the paints with a higher metallic particle content, in all cases, even if those paints are more aged when exposed to thermal or UV aging alone. This aspect confirms synergetic effects of aging under thermal–mold and/or UV–mold action. The Tg(delta) factor diminishing is quite high, reaching about 80% for M1 and M3 under UV–mold exposure, M3 being, in fact, the most sensitive sample of all.

The conclusions for the weathering tests presented above are coherent with the ones presented in the literature for homologous coatings, e.g., [31–33], but in our case, the experiments emphasized with priority the evolution of dielectric parameters, which are the relevant parameters for the proposed application, and the remaining lifetime was predicted starting from these parameters, thus treating the material more as a polymeric insulation coating than a normal paint coating, which is a novelty in the domain.

4. Conclusions

This paper describes the innovative adaptation of some specific environmental tests from general organic coatings towards newly developed water-based composite paints with metallic particles (Al and Fe). The originality of the presented recipes lays in the fact that they include a high content of metal (10% and 20%) and special additives to allow them to offer high electromagnetic shielding features and high reliability on different plastic substrates.

Due to the higher inhomogeneity, and to the action of metallic particles mainly in the presence of water, the paints with a higher percent of metallic particles exhibit an expected higher swelling degree, but the value itself was remarkable high, i.e., the swelling degree of paints with 20% metallic powder was about 10 times higher than that of the paints with 10% metallic powder. Regarding the influence of the type of added metal, the paints with Al presented a higher swelling degree, at about 20%, compared to the paints with Fe.

The conductivity seems to be more affected by UV radiation, especially for the paints with higher metallic content. Here the influence of metal type could be noticed, i.e., the conductivity of paints with Fe content is more sensitive to UV exposure compared to that of paints with Al content, meaning that Fe may catalyze some destruction processes at the binder level.

The conductivity is also affected by the thermal exposure, with an unexpectedly high increase in values especially after 144 h of exposure, and more pronounced for the paints with higher metallic content. Here, the influence of metal type could be noticed, i.e., the conductivity of paints with Al content is more sensitive to thermal exposure compared to that of paints with Fe content, meaning that in this case, Al is the main factor that may catalyze some destruction processes at the binder level.

The resistance to the action of molds was comparatively analyzed taking into account the initial paint samples and aged samples (thermal aging—1776 h in dry heat at 100 °C and UV aged—432 h exposed to UV radiation of 100 W/m^2), because the stabilization and destructive effect of molds may be enhanced on aged paint samples. The UV aging effect is more destructive from the point of view of mold action compared to thermal exposure. In order to assure a higher stability of paints, along with the limitation of fungus effect, two strategies should be taken into account: addition of UV protection additives to the paint, and most relevant, addition of fungal protection additives within the plastic carcasses which are supposed to be submitted to paint covering for electromagnetic shielding features. The mold action significantly decreases the dielectric features of paints, but the weathering aging effect is much more enhanced if the samples are cumulatively submitted to thermal aging and UV-exposure, along with the mold action. The aging effect due to mold action is diminished for the paints with higher metallic particles content, in all cases, even if those paints are more aged when exposed to thermal or UV aging alone. This aspect confirms synergetic effects of aging under thermal–mold and/or UV–molds action. The Tg(delta) factor diminishing is quite high, reaching about 80% for M1 and M3 under UV-mold exposure, M3 being in fact the most sensitive sample of all. Because molds have a significant impact on the dielectric properties of paints, it is advisable to use a mold inhibitor. However, it should be compatible with the neutral pH of water-based paints. For instance, adding 0.2%–0.3% of Dryzone® ACS [34] is recommended, but further testing is necessary before demonstrating it in an operational environment.

The potential application of this study is related mainly in the development of new autonomous electric cars, which need special conditions of electromagnetic shielding, to avoid interference and protect the large quantity of sensors and IoT-related devices, but the electromagnetic shielding efficiency assured by layers of conductive paints is normally very sensitive to environmental factors, leading to the deterioration of the paint layers and so affecting the equipment performance and security.

Author Contributions: Conceptualization, A.R.C. and R.C.C.; methodology, R.C.C., M.A., M.V.L., N.O.N. and E.M.L.; validation, R.C.C. and M.A.; formal analysis, A.R.C., R.C.C. and M.A.; investigation, A.R.C., R.C.C., M.A., M.V.L., N.O.N. and E.M.L.; data curation, R.C.C., M.A. and A.R.C.; writing—original draft preparation A.R.C. and R.C.C.; writing—review and editing, R.C.C. and M.A.; visualization, R.C.C. and A.R.C.; supervision, M.V.L. and R.C.C. All authors have read and agreed to the published version of the manuscript.

Funding: This research received no external funding.

Institutional Review Board Statement: Not applicable.

Informed Consent Statement: Not applicable.

Data Availability Statement: The data presented in this study are available on request from the corresponding author.

Acknowledgments: The research presented in this paper represents a partial dissemination of the results achieved within the following grants: 1. Nanostructured paints and primers with electromagnetic shielding properties, with impact in the field of automotive components, 298/30.06.2020, SMIS 120155; 2. PNCDI III, Program 1/Project number PN23140201-42N/2023, beneficiary National Institute for Research and Development in Electrical Engineering ICPE—CA Bucharest.

Conflicts of Interest: The authors declare no conflicts of interest.

References

1. EMC Electrically Conductive Paints. Available online: https://www.solianiemc.com/en/cp/emc-electrically-conductive-paints/?gad_source=1&gclid=Cj0KCQjwjLGyBhCYARIsAPqTz1-DOF1Sw7J8wFzhbDIZLBd4b8Z5UxsiopHr2oeQ_mM4k1MuQkk-btgaAsFvEALw_wcB (accessed on 30 May 2024).
2. EMF and RFI Shielding with Conductive Paints. Available online: https://www.antala.uk/emf-and-rfi-shielding-with-conductive-paints/ (accessed on 30 May 2024).
3. Conductive Paints and Coatings. Available online: https://limitless-shielding.com/conductive-paints-and-coatings/ (accessed on 30 May 2024).
4. ECOS Paints. Available online: https://ecospaints.net/blog/what-to-know-about-electromagnetic-shielding-materials (accessed on 30 May 2024).
5. Conductive Translucent Paint. Available online: https://hollandshielding.com/en/conductive-translucent-paint?gad_source=1&gclid=CjwKCAjw9cCyBhBzEiwAJTUWNZC2A5l8HgsLs4KaJrIJbPz6e8rSoxmem-6Wv9nuq7kMi8Koz6ZhDhoCCHAQAvD_BwE (accessed on 30 May 2024).
6. Conductive Paints. Available online: https://mgchemicals.com/category/conductive-paint/ (accessed on 30 May 2024).
7. Electric Paint. Available online: https://www.bareconductive.com/collections/electric-paint (accessed on 30 May 2024).
8. Electrically Conductive Paints. Available online: https://www.euro-technologies.eu/en/product/electrically-conductive-paints/ (accessed on 30 May 2024).
9. Reflective Paint: A Low-Tech Solution for Sustainable Cooling in Buildings. Available online: https://www.neto-innovation.com/post/reflective-paint-a-low-tech-solution-for-sustainable-cooling-in-buildings (accessed on 30 May 2024).
10. Merino, G.; Celeste, M. Synthesis and characterization of Co_3O_4 nanoparticles for use as pigments in solar absorbing paints. *GSC Adv. Eng. Technol.* **2021**, *1*, 7–20. [CrossRef]
11. Gunde, M.K.; Orel, Z.C. Absorption and scattering of light by pigment particles in solar-absorbing paints. *Appl. Opt.* **2000**, *39*, 622–628. [CrossRef] [PubMed]
12. Coser, E. Development of paints with infrared radiation reflective properties. *Polímeros* **2015**, *25*, 305–310. [CrossRef]
13. Joglekar-Athavale, A. Solar absorptive coating: A thermally stable spinel pigment based coating with inorganic binder for waterborne paint. *Pigment. Resin Technol.* **2021**, *50*, 302–308. [CrossRef]
14. Kamjunk, N.; Spohn, U.; Morig, C.; Wagner, G. A Test Device for Microalgal Antifouling Using Fluctuating pH Values on Conductive Paints. *Water* **2020**, *12*, 1597. [CrossRef]
15. Miszczyk, A.; Darowicki, K. Effect of environmental temperature variations on protective properties of organic coatings. *Prog. Org. Coat.* **2003**, *46*, 49–54. [CrossRef]
16. Miszczyk, A.; Darowicki, K. Accelerated aging of organic coating systems by thermal treatment. *Corros Sci.* **2001**, *43*, 1337–1343. [CrossRef]
17. Fedrizzi, L.; Bergo, A.; Deflorian, F.; Valentinelli, L. Assessment of protective properties of organic coatings by thermal cycling. *Prog. Org. Coat.* **2003**, *48*, 271–280. [CrossRef]
18. Ciobanu, R.; Spohn, U.; Morig, C.; Wagner, G.; Neu, T.R. Composite Paints with High Content of Metallic Microparticles for Electromagnetic Shielding Purposes. *Coatings* **2024**, *14*, 874. [CrossRef]
19. Caramitu, A.R.; Mitrea, S.; Marinescu, V.; Ursan, G.A.; Aradoaie, M.; Lingvay, I. Dielectric Behavior and Morphostructural Characteristics of Some HDPE Composites /Metal Nanopowders. *Mater. Plast.* **2019**, *56*, 103–109. [CrossRef]
20. Caramitu, A.; Ion, I.; Bors, A.M.; Ciobanu, C.R.; Schreiner, C.; Aradoaei, M.; Caramitu, A.M.D. Physico-chemical Characterization of Paint Films with Electromagnetic Properties. *Mater. Plast.* **2022**, *59*, 9–23. [CrossRef]
21. Mancini, D.; Percot, A.; Bellot-Gurlet, L.; Colomban, P.; Carnazza, P. On-site contactless surface analysis of Modern paintings from Galleria Nazionale (Rome) by Reflectance FTIR and Raman spectroscopies. *Talanta* **2021**, *227*, 122159. [CrossRef] [PubMed]
22. Hayes, P.A.; Vahur, S.; Leito, I. ATR-FTIR spectroscopy and quantitative multivariate analysis of paints and coating materials. *Spectrochim. Acta Part A Mol. Biomol. Spectrosc.* **2014**, *133*, 207–213. [CrossRef] [PubMed]
23. Ortiz-Herrero, L.; Cardaba, I.; Setien, S.; Bartolomé, L.; Alonso, M.L.; Maguregui, M.I. OPLS multivariate regression of FTIR-ATR spectra of acrylic paints for age estimation in contemporary artworks. *Talanta* **2019**, *205*, 120114. [CrossRef] [PubMed]
24. Hamada, I.; Kumagai, T.; Shiotari, A.; Okuyama, H.; Hatta, S.; Aruga, T. Nature of hydrogen bonding in hydroxyl groups on a metal surface. *Phys. Rev. B* **2012**, *86*, 075432. [CrossRef]
25. *SR EN ISO 175/2011*; Plastics—Methods of Test for the Determination of the Effects of Immersion in Liquid Chemicals. ISO: Geneva, Switzerland. Available online: https://e-standard.eu/en/standard/186982 (accessed on 30 May 2024).
26. *ISO 4892-3:2016*; Plastics—Methods of Exposure to Laboratory Light Sources, Part 3: Fluorescent UV Lamps. ISO: Geneva, Switzerland. Available online: https://www.iso.org/standard/67793.html (accessed on 30 May 2024).
27. Aguilar-Rodríguez, P.; Mejía-González, A.; Zetina, S.; Colin-Molina, A.; Rodríguez-Molina, B.; Esturau-Escofet, N. Unexpected behavior of commercial artists' acrylic paints under UVA artificial aging. *Microchem. J.* **2021**, *160*, 105743. [CrossRef]
28. van der Weijde, D.H.; van Westing, E.P.M.; Ferrari, G.M.; de Wit, J.H.W. Lifetime Prediction of Organic Coatings with Impedance Spectroscopy. *Polym. Mater. Sci. Eng.* **1996**, *74*, 12–16.
29. *SR EN 60216-3:2007*; Electroinsulating Materials. Thermal Endurance Properties. Part 3: INSTRUCTIONS for the Calculation of Thermal Endurance Characteristics. ISO: Geneva, Switzerland. Available online: https://magazin.asro.ro/ro/standard/117649 (accessed on 30 May 2024).

30. *IEC 60068-2-10:2005*; Environmental Testing—Part 2-10: Tests—Test J and Guidance: Mould Growth. IEC: London, UK. Available online: https://standards.iteh.ai/catalog/standards/clc/d098bcec-f96d-46df-9495-300001cf8218/en-60068-2-10-2005 (accessed on 30 May 2024).
31. Caramitu, A.; Butoi, N.; Rus, T.; Luchian, A.M.; Mitrea, S. The Resistance to the Action of Molds of Some Painting Materials Aged by Thermal Cycling and Exposed to an Electrical Field of 50 Hz. *Mat. Plast.* **2017**, *54*, 331–337. [CrossRef]
32. Iscen, A.; Forero-Martinez, N.; Valsson, O.; Kremer, K. Acrylic Paints: An Atomistic View of Polymer Structure and Effects of Environmental Pollutants. *J. Phys. Chem. B* **2021**, *125*, 10854–10865. [CrossRef] [PubMed]
33. Cogulet, A.; Blanchet, P.; Landry, V. Evaluation of the Impacts of Four Weathering Methods on Two Acrylic Paints: Showcasing Distinctions and Particularities. *Coatings* **2019**, *9*, 121. [CrossRef]
34. Available online: https://safeguardstore.co.uk/dryzone-acs-anti-mould-paint-additive/ (accessed on 30 July 2024).

polymers

Article

Thermoplastic Electromagnetic Shielding Materials from the Integral Recycling of Waste from Electronic Equipment

Mihaela Aradoaei [1], Romeo C. Ciobanu [1,*], Cristina Schreiner [1], Andrei George Ursan [1], Elena Gabriela Hitruc [2] and Magdalena Aflori [2,*]

[1] Department of Electrical Measurements and Materials, Gheorghe Asachi Technical University, 700050 Iasi, Romania; mihaela.aradoaei@academic.tuiasi.ro (M.A.); cristina-mihaela.schreiner@academic.tuiasi.ro (C.S.); andrei_urs@yahoo.com (A.G.U.)

[2] Petru Poni Institute of Macromolecular Chemistry, 41A Aleea Gr. Ghica Voda, 700487 Iasi, Romania; gabihit@icmpp.ro

* Correspondence: rciobanu@yahoo.com (R.C.C.); maflori@icmpp.ro (M.A.)

Abstract: The European Green Deal's goals are anticipated to be fulfilled in large part thanks to the New Circular Economy Action Plan. It is believed that recycling materials will have a significant positive impact on the environment, particularly in terms of reducing greenhouse gas emissions and the impacts this will have on preventing climate change. Due to the complexity of the issue and its significant practical ramifications, the activity of Waste Electrical and Electronic Equipment (WEEE) collection networks is a subject of interest for researchers and managers, in accordance with the principles that recent laws have addressed in a large number of industrialized countries. The goal of this paper is to characterize and obtain composite materials using an injection process with a matrix of LDPE, PP, and HDPE, with up to a 10% addition of nonmetallic powders from PCBs and electronic parts from an integrated process of WEEE recycling. The composites present relevant thermal, electrical, and mechanical properties. Such composite materials, due to their relevant dielectric properties, may be further tested for applications in electromagnetic shielding at frequencies above 1 kHz, or for electromagnetic interference/electromagnetic compatibility (EMI/EMC and ESD) applications at lower frequencies due to their superior dielectric loss factor values, associated with relevant behaviors around exploitation temperatures, mainly for the electric, electronic, or automotive industries.

Keywords: integral recycling of WEEE; thermoplastic composites; electromagnetic interference; electromagnetic compatibility

check for updates

Citation: Aradoaei, M.; Ciobanu, R.C.; Schreiner, C.; Ursan, A.G.; Hitruc, E.G.; Aflori, M. Thermoplastic Electromagnetic Shielding Materials from the Integral Recycling of Waste from Electronic Equipment. *Polymers* **2023**, *15*, 3859. https://doi.org/10.3390/polym15193859

Academic Editor: Keon-Soo Jang

Received: 4 August 2023
Revised: 7 September 2023
Accepted: 20 September 2023
Published: 22 September 2023

1. Introduction

In several domains of application nowadays, plastic materials are employed more often in daily life. After use, these plastic materials are dumped outside. As the majority of plastics are nonbiodegradable by nature, these are known as plastic wastes and are bad for the environment. Therefore, in order to safeguard our environment, the effective treatment of these waste products is required. There are numerous methods for managing these plastic wastes, including recycling, land filling, and degradation (including thermo-, photo-, bio-, and chemo-degradation). Currently, a sizable amount of the plastic trash that is produced is either burnt or dumped in landfills, resulting in both resource loss and environmental pollutants, most notably CO_2 from burning. Global CO_2 emissions from the life cycle of plastics are estimated at 400 million tonnes per year (2012) [1,2]. If the current trends continue, by 2050, it may account for 20% of the world's oil consumption and 15% of the carbon emissions produced annually around the world. The plastics strategy is a milestone of the New Circular Economy since it addresses these issues. The core of this strategy is the packaging, reuse, and recycling of plastic garbage [3,4].

Although the materials used in electrical and electronic applications have significant value and a wide range of uses, they suffer from severe electromagnetic interference (EMI) [5–8]. Broadcasting, the medical area, research, the defense industry, communication, and other businesses can all benefit greatly from the use of these materials. With the use of efficient EMI shielding materials, the EMI can be controlled. Recent works described different methods for creating EMI shielding from industrial waste, agricultural waste, and other wastes. The procedure for gathering end-of-life products and moving them to designated treatment facilities is acknowledged as a crucial task because its effective execution ensures the reduction of both the consumption of virgin materials and the dissemination of hazardous substances in soil, water, and air [9–11]. The requirements must be met in terms of electrical equipment and device emissions as well as their resistance to disruptions. When electrical equipment and devices are connected or placed near to each other, they have an impact on one another. Electromagnetic compatibility (EMC) is the process of ensuring that electrical devices or equipment are both immune to and do not cause disturbances that would impact other devices or equipment [12–14]. Due to the wide range of hazardous materials (lead, chlorofluorocarbons, fluorescent dust, etc.) and the difficulties involved in the recovery process, where frequently specialized technologies and controlled-atmosphere storage and treatment are required, waste electrical and electronic equipment (WEEE) recycling is a subject of reticence for high-value applications [15–18].

Previous research on the purposes of EMI/EMC and antistatic shielding applications has solely involved selected virgin polymer matrices and tailored conductive or ferritic powders for manufacturing relevant composites for electric, electronic, or automotive use.

Such examples may employ virgin PE/carbon nanotube (CNT) composites as EMI shielding materials with three distinct CNT kinds and various network architectures [19], with segregated network-structured composites with an efficiency of 46 dB with only 5 wt% CNT loading.

In all, studies related to the use of recycled PE as a matrix for antistatic and EMI shielding composites are extremely limited, and studies on recycled PP as a matrix are missing due to the structure and quality of polymeric waste streams that need to be improved using a variety of techniques, including restabilization, rebuilding, compatibilization, and the inclusion of elastomers and specialized fillers [20–25]. Because thermo-mechanical degradation via multiple processing affects polyolefins (HDPE and PP) more than thermo-oxidative aging does, special attention should be paid to controlling the processing conditions during mechanical recycling [26–31]. On the other hand, if recycled polyolefins from packaging are used as the matrices for composites for electromagnetic shielding applications, expensive conductive or ferritic powders are added to achieve the imposed dielectric properties; a clear drawback, because the economy of using recycled matters becomes insignificant in the cost of the final product [2,32–37].

This article describes a fully innovative process of the integral recycling of waste from electronic equipment towards manufacturing thermoplastic electromagnetic shielding composites. The advantage lies in a more uniform source of recycled polyolefins (LDPE, HDPE, and PP), which do not need extra processing to increase their thermal, electrical, and mechanical properties. Another advantage lies, on the other side, in the manufacturing of cheap powders obtained from the non-metallic thermoset components of WEEE (electronic components) to substitute expensive conductive or ferritic powders, due to them having homologue dielectric features.

2. Materials and Methods

2.1. Integral Recycling of WEEE

Plastic wastes should be given fresh thought as valuable resources for product manufacturing, on par with virgin oil-based plastics and biologically derived polymers [38–40]. The end-of-life application sector, from which the plastic waste streams originated, dictates the technological techniques to be used for the successful recycling of their plastic wastes. According to their sources, the following categories have been suggested for classifying plastic waste streams: packaging, agriculture, municipal solid waste, construction and demolition, end-of-life vehicles, and waste electrical and electronic equipment (WEEE).

Under the concept of a circular economy, it is a must to develop technologies for the integral use of WEEE towards innovative applications due to the larger and larger quantities of WEEE, which, according to novel electronic technologies, cannot be recycled via classical ways, which mainly recover the metallic components and only partially recover the thermoplastic carcass components, practically ignoring the main parts of the thermoset components after the partial recovery of precious metals. Our paper suggests an integrated recycling of the thermoplastic and non-metallic components of WEEE, according to the scheme in Figure 1, after all classical recycling processes are accomplished.

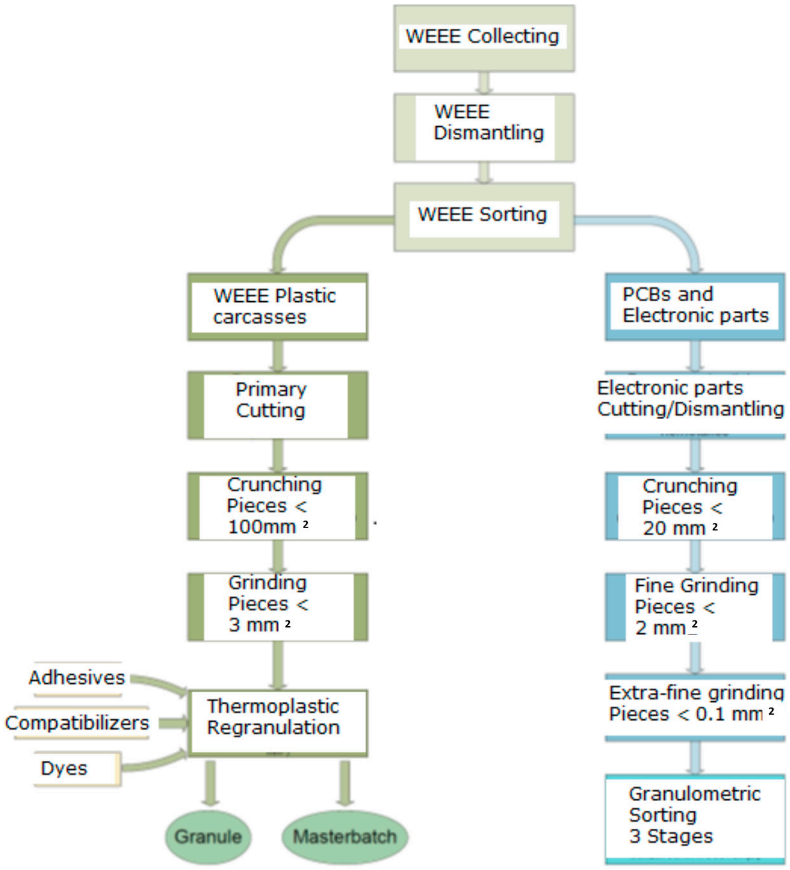

Figure 1. Technological process for the integral recycling of WEEE.

2.2. *Powder Obtaining from Thermoset Components of WEEE (Electronic Components)*

Such components as the rest of the printed circuit boards, integrated circuits, diodes, capacitors, resistors, etc., exclude metallic, glass, and ferritic items, which are separately selected in a preliminary process, due to them having separate recycling stages in ways that have been demonstrated to be profitable.

Grinding was carried out using a SPEX type mill, 8000 M series (SPEX Europe, Rickmansworth, UK). The grinding time was 4 h, and the rotation speed was 875 cycles/min. Grinding is done in metal or ceramic mini containers made of steel, tungsten carbide, alumina, zirconium, or silicon nitride. Dry grinding is the simplest method to use. For samples that tend to form lumps during mixing or grinding, a particle accelerator can be used. Water, alcohol, or other liquids can also be used. It is recommended to use a fluorocarbon fluid that does not chemically affect the sample and evaporates quickly after use. Water can be easily removed via heating in plastic boxes in an oven at a low temperature.

The powder aspect after the final metallic separation is shown in Figure 2.

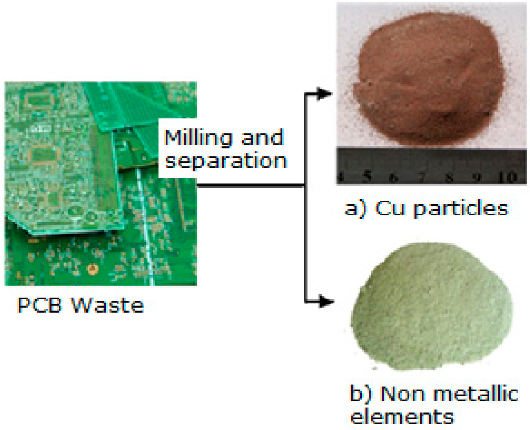

Figure 2. Non-metallic powder aspect after final metallic separation.

The freely poured density of the powder (ρ) was calculated according to the standards SR ISO 3923-1 [41] and SR ISO 3923-2 [42] (Table 1).

Table 1. The freely poured density of powder (ρ) as a function of powder weight.

Nr. Test	Hole Size (mm)	Powder Weight (mg)	$\rho_a = m/V_a$ (g/cm^3)	$\rho_{average}$ (g/cm^3)
1	5	3.0234	0.6694	0.6630
2		3.0321	0.6713	
3		2.9886	0.6617	
4		2.9346	0.6497	

The equipment used to perform X-ray diffraction analyses on powders was an X-ray diffractometer type D8 ADVANCE.

Via X-ray diffraction analysis, it was found that the powder consisted of a mixture of metal oxides (CaO, Fe_2O_3, CuO, SiO_2, SnO_2, PbO, BaO, Br, $Cr2O_3$, ZnO, MnO, NiO, ZrO_2, SrO, Ag) and metals (Pb, Sn, Au, Ag, Si, Ge) in significant concentrations, as given in Table 2 and Figure 3. The total concentration of the metal-derived compounds was approximately 88.32%. Of the rest, up to 100% is expected to be of a polymeric component (thermoset covers of integrated circuits and parts of printed circuit boards). In all, according to the components, the powder presented features related to nanoconductivity, an aspect that is very important when using such powders as additives within recycled polyolefins towards the manufacturing of thermoplastic electromagnetic shielding materials. This aspect will be demonstrated when analyzing the dielectric properties of the composites.

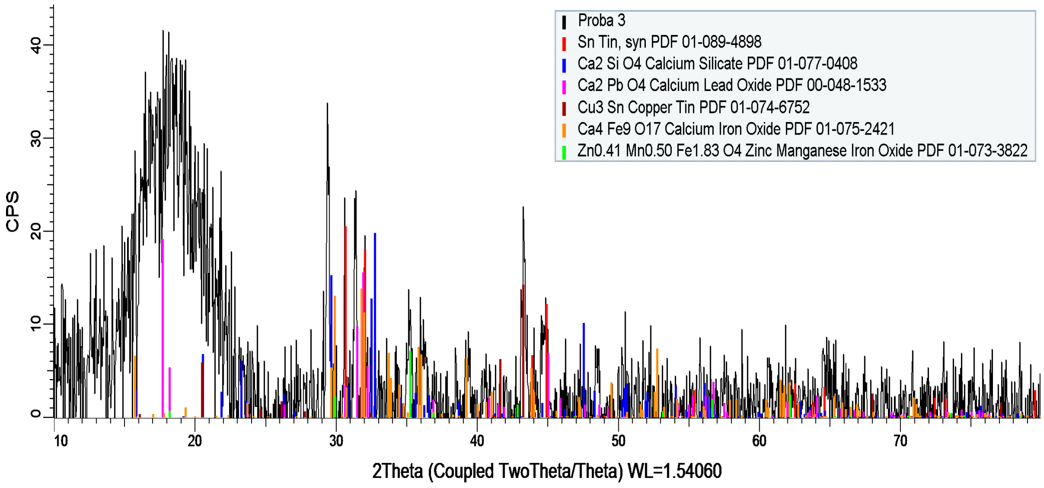

Figure 3. X-ray diffraction spectra of the powder.

Table 2. Powder components.

Formula	Z	Concentration (%)	The Most Intense Peak	The Net Intensity of the Signal	Statistical Error (%)	Lower Limit of Detection	The Thickness of the Analyzed Layer
CaO	20	25.16	Ca KA1-HR-Tr	25.2	0.625	282.3 PPM	42 µm
Fe_2O_3	26	15.72	Fe KA1-HR-Tr	15.72	0.409	126.0 PPM	101 µm
CuO	29	13.91	Cu KA1-HR-Tr	13.9	0.657	126.4 PPM	145 µm
SiO_2	14	12.69	Si KA1-HR-Tr	12.7	1.61	478.4 PPM	7.2 µm
SnO_2	50	7.93	Sn KA1-HR-Tr	7.93	0.865	699.6 PPM	1.80 mm
PbO	82	7.68	Pb LB1-HR-Tr	7.683	0.528	219.1 PPM	0.37 mm
BaO	56	3.39	Ba LA1-HR-Tr	3.39	2.73	574.9 PPM	44 µm
Br	35	3.10	Br KA1-HR-Tr	3.105	0.504	78.5 PPM	0.31 mm
Cr_2O_3	24	2.68	Cr KA1-HR-Tr	2.68	1.35	133.7 PPM	69 µm
ZnO	30	2.61	Zn KA1-HR-Tr	2.61	0.652	73.2 PPM	172 µm
MnO	25	1.88	Mn KA1-HR-Tr	1.88	1.27	133.0 PPM	85 µm
NiO	28	1.57	Ni KA1-HR-Tr	1.57	2.06	97.2 PPM	119 µm
ZrO_2	40	0.69	Zr KA1-HR-Tr	0.532	1.22	134.7 PPM	0.52 mm
SrO	38	0.61	Sr KA1-HR-Tr	0.605	1.24	70.7 PPM	0.42 mm
Ag	47	0.38	Ag KA1-HR-Tr	0.38	8.77	381.5 PPM	1.25 mm

Scanning electron microscopy (SEM) analysis was performed with the help of the FESEM-FIB workstation, Auriga model, produced by Carl Zeiss, Göttingen, Germany, through the secondary electron/ion detector (SESI) in the sample room for the topographic study of the surface. The determination of the chemical composition was carried out with the help of the EDS (energy-dispersive spectrum for characteristic X-ray) probe produced by Oxford Instruments (Oxford, UK), model Inca PET X3. The composition was cooled with liquid nitrogen, and integrated on the FESEM-FIB Auriga workstation. The analyses were carried out in accordance with the Auriga Smart SEM V05.04 Workstation Manual [43].

The powder dimension depends on the milling process of the WEEE; in our case, we anticipated a quasi-uniform dispersion with dimensions of about 25 µm on average (Figure 4).

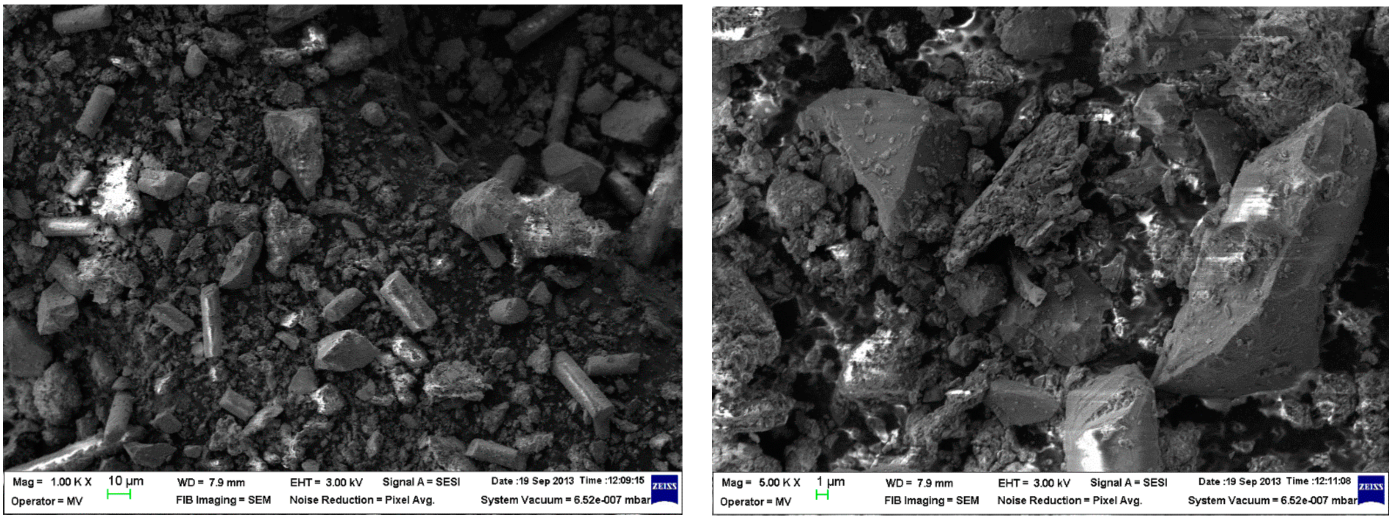

Figure 4. The powder SEM images at 1000× and 5000× magnitude.

According to Figure 5, a comparative sectorial analysis of the powder components was made via energy dispersive X-ray spectroscopy upon the 8 random areas of analysis, in order to have a complete and an average value of the components, which are metals and metallic oxides. The results are presented in the table of Figure 5, and are in line with the results from Table 2.

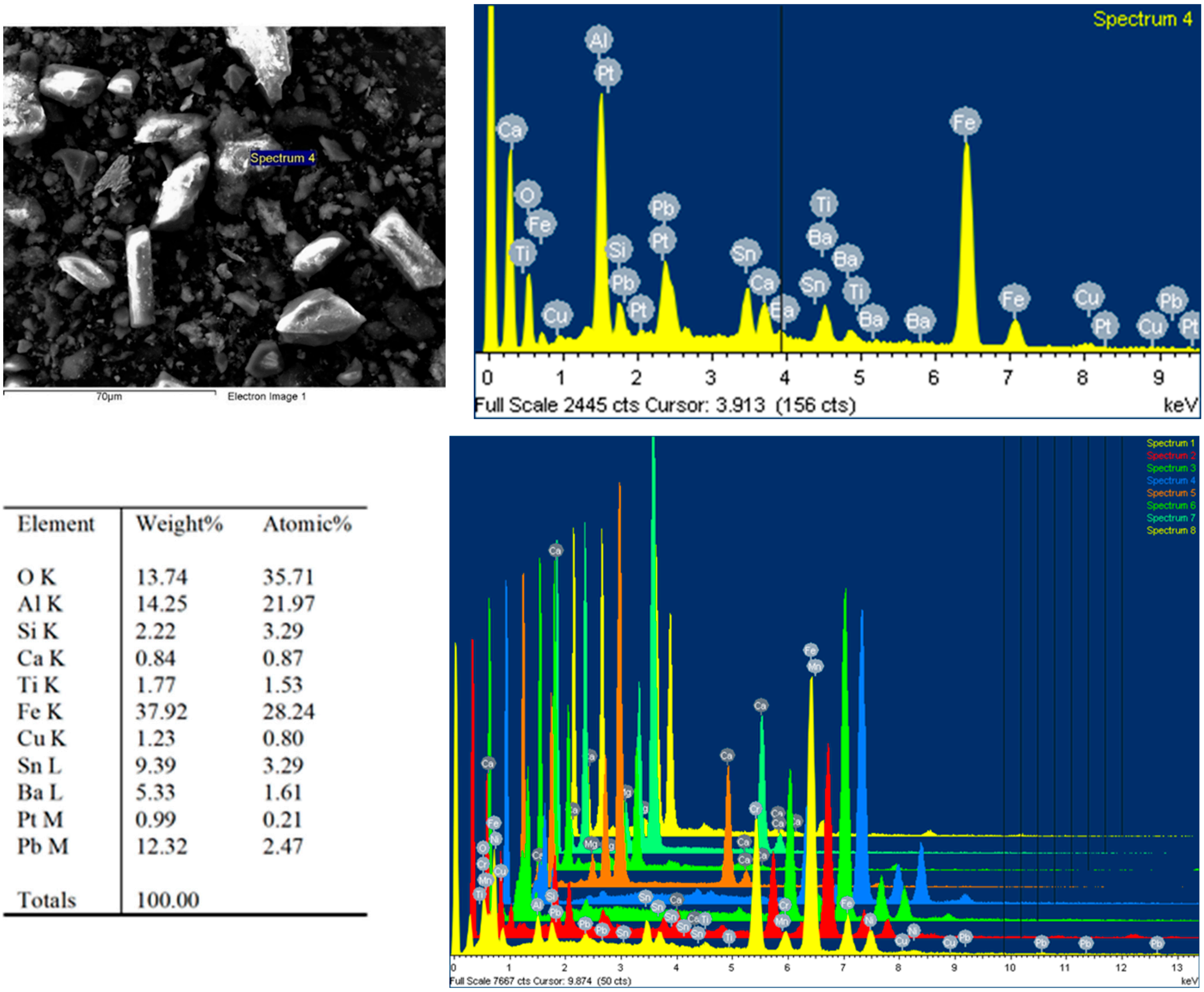

Element	Weight%	Atomic%
O K	13.74	35.71
Al K	14.25	21.97
Si K	2.22	3.29
Ca K	0.84	0.87
Ti K	1.77	1.53
Fe K	37.92	28.24
Cu K	1.23	0.80
Sn L	9.39	3.29
Ba L	5.33	1.61
Pt M	0.99	0.21
Pb M	12.32	2.47
Totals	100.00	

Figure 5. Example of comparative sectorial analysis of powder components.

2.3. Composites Obtained from Recycled Polyethylene and Powder from WEEE

The physical–chemical and mechanical properties of the LDPE/HDPE/PP matrices used are similar with the ones obtained from the same WEEE sources (WEEE carcasses) [44–48].

The injection procedure was used to create composite materials from the melt. Thus, a material based on macromolecular compounds was brought to a flow condition under pressure and inserted into a forming mold, where it was held under pressure and hardened via cooling. The samples were created using a Dr. Boy 35A laboratory micro-extruder from Koenigswinter, Germany. The interface and thermal diagrams of the injection machine are presented in Figure 6, where the sequential temperatures for the PE and PP can be noticed. These samples have the advantage of having reduced internal tensions in the end product due to their injection into an open mold that closes after the injection process is completed.

PP regranulat din deseuri electronice

	5	4	3	2	1
T °C	220	220	210	200	180
T °C	220	220	210	202	177
t ⎍⎍ %	18	17	5	0	4

Figure 6. The interface and thermal diagrams of the injection machine.

Three types of samples were created, beginning with ground and regranulated thermoplastic matrices that were derived from electronic waste. To increase their thermal, electrical, and mechanical qualities, the LDPE, PP, and HDPE materials recycled from electronic waste were reinforced with increasing percentages (3%, 7%, and 10%) of WEEE powder, as follows:

- LDPE + 3%-Regranulated LDPE from electronic waste/3% WEEE powder;
- LDPE + 7%-Regranulated LDPE from electronic waste/7% WEEE powder;
- LDPE + 10%-Regranulated LDPE from electronic waste/10% WEEE powder;
- HDPE + 3%-Grinding of HDPE from electronic waste/3% WEEE powder;
- HDPE + 7%-Grinding of HDPE from electronic waste/7% WEEE powder;
- HDPE + 10%-Grinding of HDPE from electronic waste/10% WEEE powder;
- PP + 3%-Regranulated PP from electronic waste/3% WEEE powder;
- PP + 7%-Regranulated PP from electronic waste/7% WEEE powder;
- PP + 10%-Regranulated PP from electronic waste/10% WEEE powder.

The hydrostatic density was calculated using the XS204 Analytical Balance (Mettler-Toledo AG, Greifensee, Switzerland), which has the following specifications: maximum capacity, 220 g; precision, 0.1 mg; linearity, 0.2 mg; internal calibration; density kit for solids and liquids; and an RS 232 interface. The temperature at work was 25.2 °C.

An X-ray diffractometer type D8 Advance was used to perform polycrystalline material analysis and resonant incident technique thin layer analysis, with a software acquisition and interpretation database for PDF-ICDD. The diffractometer's technical specifications are as follows: X-ray tube with Cu anode; Ni K filter; step of 0.04°; measurement time of 2 s/step; measuring range, $2\theta = 2–60°$.

An SEM equipped with a field emission source and a focused ion beam was used. Element chemical analyses were performed using the EDX type dispersive probe mounted on the microscope to provide information on the point composition on the surface of the analyzed material. As a result, in order to obtain the most accurate information on the composition, different areas of the material's surface were explored, with the software then allowing for the integration of the obtained compositional information and the formation of an image of the material's degree of homogeneity in particular.

The simultaneous thermal analyzer TG-DSC type STA 449 F3 Jupiter, NETZSCH, Selb Germany, allows for the determination of mass variations and thermal changes for many types of materials, including inhomogeneous materials. The technical specifications are as follows: a temperature range of −150 °C–1550 °C; heating speeds of 0.1–50 °C min; a cooling time of 1500–50 °C <30 min; a balance maximum capacity of 35 g; a balance resolution of 1 µg; a DSC resolution < 1 µW (depending on the sensor); a working atmosphere including inert, oxidizing, reducing, static, and dynamic states; and a vacuum system of a maximum of 10^{-2} mbar.

The thermal conductivity was measured with the LFA 447 Nanoflash device (Netzsch, Selb, Germany). The thermal diffusivity of a material is a thermophysical property that determines the speed of heat propagation via conduction during the variation of temperature with time. The higher a material's thermal diffusivity is, the faster the heat propagation is. A thermal diffusivity of between 25 °C and 95 °C was determined with an LFA 447 NanoFlash–Netzsch (Germany) device, according to the ASTM E-1461:2007 standard [49], using the "flash" method. A powerful xenon lamp was used as the radiation energy source, and the irradiation time on the front face of the sample was 0.18 ms. The samples were analyzed three times at each temperature. The increase in temperature on the other surface of the sample was measured with the help of an InSb type infrared (IR) detector.

3. Results and Discussion

3.1. Physical Property Testing and Hydrostatic Density Determination

According to the results in Table 3, adding increasing percentages of nanoconductive powder enhances the density of the composite material. The HDPE composite material milled with 10% WEEE powder has the highest density of all the studied samples, whereas the LDPE regranulated from electronic waste has the lowest density with 3% WEEE powder.

Table 3. Results of hydrostatic density determination.

Material	Density (g/cm^3)
LDPE	0.893
LDPE + 3%	0.902
LDPE + 7%	0.903
LDPE + 10%	0.952
HDPE	0.929
HDPE + 3%	0.935
HDPE + 7%	0.941
HDPE + 10%	1.02
PP	1.001
PP + 3%	1.003
PP + 7%	1.005
PP + 10%	1.006

3.2. Identifying Crystalline Phases

Figures 7–9 illustrate the spectra of the composite materials made from the basic polymers LDPE, HDPE, and PP. The powder enhances the density of the composite material. The HDPE composite material milled with 10% WEEE powder has the highest density of all the studied samples, whereas the LDPE regranulated from electronic trash has the lowest density with 3% WEEE powder. The analysis identifies chemicals that have a crystalline state and are present in at least 3% quantities in the material to be tested. As a result, this approach cannot identify chemicals that are amorphous or have very low concentrations.

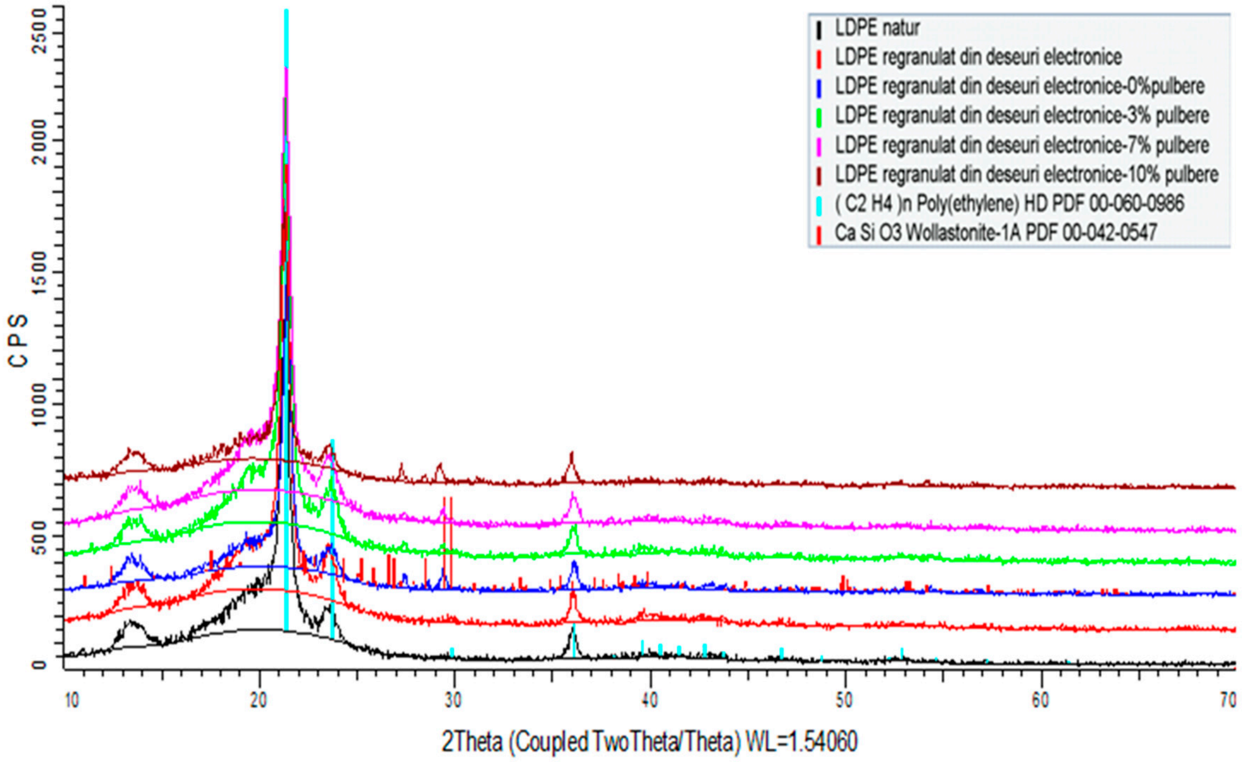

Figure 7. XRD spectra of composites including LDPE as the basis polymer.

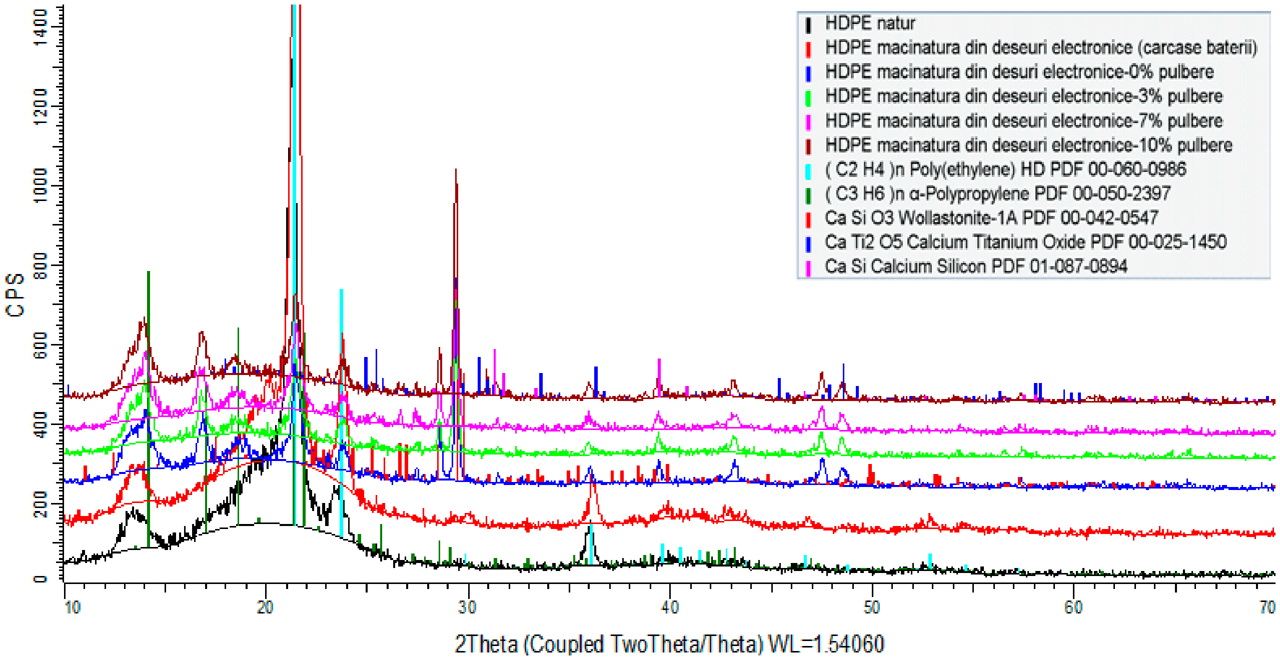

Figure 8. XRD spectra of composites including HDPE as the basis polymer.

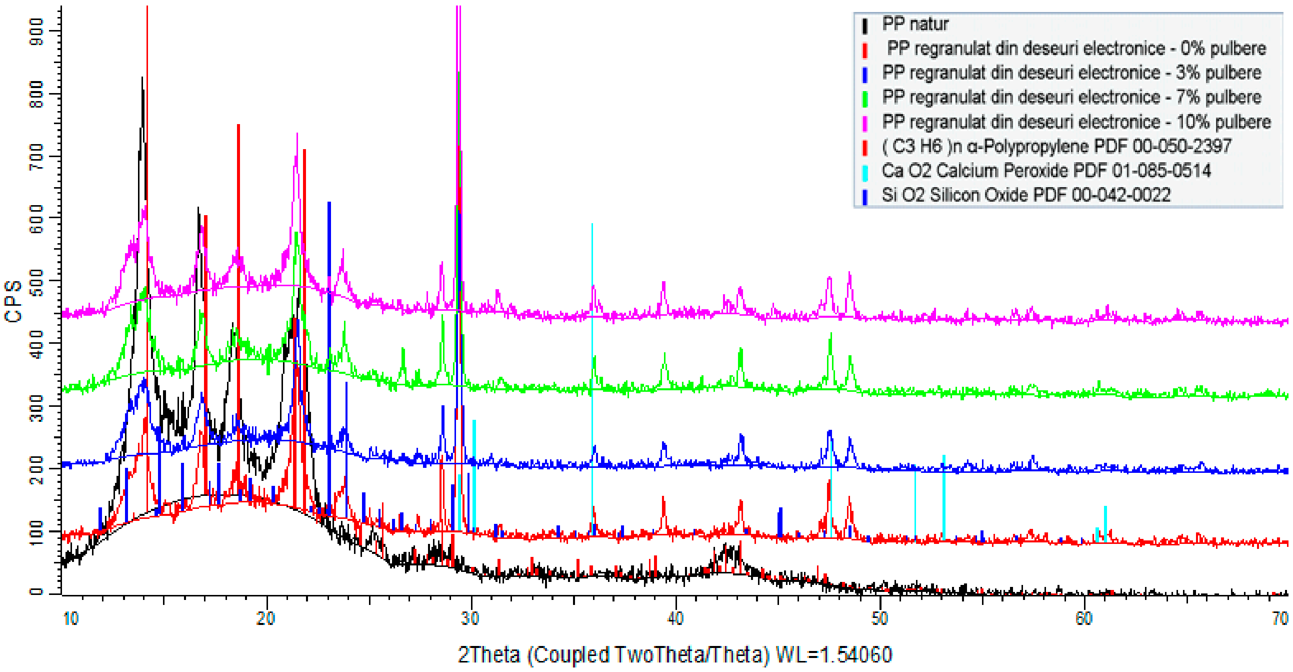

Figure 9. XRD spectra of composites including PP as the basis polymer.

The X-ray diffraction study of all composite material samples produced under the contract indicated the following:

a. High-density polyethylene (re-granulated HDPE from electronic trash) product samples:
  - The basic polymer composition is made up of a blend of high-density polyethylene and residual polypropylene (about 4%);
  - Adding conductive nanopowder resulted in the emergence of peaks specific to the compounds present (calcium oxides, titanium oxides, silicon oxides, and/or their mixtures).

b. Samples of regranulated low-density polyethylene products (regranulated LDPE from electronic waste):
  - The basic polymer composition is entirely composed of low-density polyethylene;
  - The addition of conductive nanopowder resulted in the emergence of distinct peaks.

c. Polypropylene-based product samples (regranulated from electronic waste):
  - The fundamental polymer composition consists completely of low-density polyethylene;
  - Peaks specific to the chemicals present (calcium oxides, silicon oxides) occurred with the addition of conductive nanoparticles.

3.3. *Mechanical Characteristics Determination*

3.3.1. Tensile Strength Determination

When the nanoconductive powder is introduced within the polymer matrix, the composite material stiffens, indicating an increase in mechanical resistance but also a decrease in elongation (Table 4). The best mechanical resistance is provided by PP from electronic waste with 10% WEEE powder, whereas HDPE and PP from electronic waste with 3% WEEE powder offer the best flow resistance.

Table 4. Tensile strength for the tested materials.

Material	Mechanical Resistance (MPa)	Flow Resistance (MPa)	Elongation A (%)	Young's Modulus (GPa)
LDPE	12.9	2.13	351.1	0.16
LDPE + 3%	13.2	2.06	349.5	0.14
LDPE + 7%	13.54	1.81	342.26	0.1
LDPE + 10%	14.03	0.66	339.87	0.07
HDPE	14.23	8.82	0.29	0.61
HDPE + 3%	14.61	8.68	0.26	0.59
HDPE + 7%	15.77	7.37	0.24	0.57
HDPE + 10%	15.93	6.34	0.17	0.56
PP	17.89	8.53	0.28	0.69
PP + 3%	18.03	8.42	0.21	0.65
PP + 7%	18.89	8.17	0.18	0.64
PP + 10%	19.66	8.08	0.17	0.57

3.3.2. Three-Point Bending Strength Measurement

The mechanical strength obtained via tensile testing for the LDPE samples (regranulated LDPE from electronic waste with the addition of 3%, 7%, and 10% WEEE powder) is nearly the same as the mechanical resistance obtained via three-point bending. The same phenomenon can be noticed when the values of the resistance to flow obtained in the tensile tests—specifically, the three-point bending measurement—are compared to the values of the longitudinal modulus of elasticity (Young's modulus) obtained in the tensile tests, specifically via three-point bending (Table 5). As a result, the mechanical properties stay fairly constant regardless of the percentage of WEEE powder used. However, when the percentage of added conductive powder increases, the mechanical resistance to bending increases across three points. This mechanical behavior is explained by the fact that when the nanoconductive powder is added to the polymer matrix, the composite material stiffens, indicating an increase in mechanical resistance. It is observed that PP from electronic waste with 10% WEEE powder has the highest mechanical resistance to three-point bending, whereas PP from electronic waste with 3% WEEE powder has the highest flow resistance.

Table 5. The three-point bending strength of all materials.

Material	Mechanical Resistance (MPa)	Flow Resistance (MPa)	Young's Modulus (GPa)
LDPE	16.34	2.32	0.17
LDPE + 3%	16.85	2.79	0.2
LDPE + 7%	17.48	3.1	0.29
LDPE + 10%	18.23	3.25	0.33
HDPE	38.02	22.76	1.00
HDPE + 3%	38.67	24.56	1.01
HDPE + 7%	38.82	20.17	1.41
HDPE + 10%	39.07	20.07	1.45
PP	35.09	26.83	1.23
PP + 3%	36.49	27	1.67
PP + 7%	38.07	24.07	1.36
PP + 10%	45.18	21.02	1.53

3.3.3. Shore Hardness Determination

The Shore hardness evolution graph shows that no changes exist for the samples of regranulated LDPE from electronic waste with 3%, 7%, and 10% WEEE powder; the Shore hardness value is the same regardless of the percentage of nanopowders (Table 6). There is no significant difference in the measured hardness of the composite materials with increasing percentages of powder. At the same time, the addition of increasing percentages of powder (3%, 7%, and 10%) did not result in a substantial increase in hardness.

Table 6. The results of the Shore hardness determination.

Material	Shore Hardness A (HS)
LDPE	97
LDPE + 3%	97
LDPE + 7%	97
LDPE + 10%	97
HDPE	97
HDPE + 3%	97
HDPE + 7%	98
HDPE + 10%	98
PP	95
PP + 3%	95
PP + 7%	95
PP + 10%	97

3.4. Chemical Property Testing

3.4.1. Swelling Degree Determination in Water and Solvent

The swelling capacity in water and solvent (toluene) of the examined compounds was determined using the SR EN ISO 175/2011 technique [37]. Thus, 1 g of the composite material was weighed and deposited in plastic ampoules. Two sets of samples were prepared: one to measure the degree of swelling in water and one for determining the degree of swelling in solvent (toluene). The ampoules containing the composite material were filled with double-distilled water and then with the solvent (toluene) and stored at room temperature for 24 h.

The following formula was used to calculate the degree of swelling:

$$Q = \frac{X_2 - X_1}{X_1} \times 100$$

where

Q—degree of swelling;
X_2—the inflated polymer mass;
X_1—dry polymer mass.

With a 95% confidence level, the degree of swelling was calculated as the average of five measurements done on five different samples, removing out-of-range values. According to the results of the experiments, the PP material regranulated from electronic waste with 10% WEEE powder has the highest degree of swelling. The material with the lowest degree of swelling in water at room temperature, namely the HDPE milled from electronic waste with 3% WEEE powder, was chosen among all the composite materials examined (Table 7), where $\Delta m = X_2 - X_1$ is the mass variation after immersion in water.

The degree of swelling in the solvent for all samples analyzed based on LDPE (regranulated LDPE from electronic waste with 3%, 7%, and 10% WEEE powder), HDPE (grinding of HDPE from electronic waste with 3%, 7%, and 10% WEEE powder), and PP (regranulated PP from e-waste with 3%, 7%, and 10% WEEE powder), is higher than the swelling limit in water of the same samples (Table 8). The material variant with the lowest degree of swelling in the solvent at room temperature, namely the regranulated PP from electronic waste/10% WEEE powder, can be chosen as the optimal option for use in conditions of exposure to organic solvents among all the composite materials studied.

Table 7. The results of the swelling tests in water at room temperature.

Material	X_1	X_2	Δm	Q
LDPE	1.2156	1.4453	0.0179	2.012
LDPE + 3%	1.4259	1.4563	0.0213	2.132
LDPE + 7%	1.4351	1.4919	0.0396	3.9579
LDPE + 10%	1.4512	1.5004	0.0339	3.3903
HDPE	1.3903	1.3981	0.0083	0.8103
HDPE + 3%	1.3927	1.4051	0.0089	0.8904
HDPE + 7%	1.3975	1.425	0.0197	1.9678
HDPE + 10%	1.4035	1.4237	0.0144	1.4393
PP	1.3698	1.3902	0.0187	2.0951
PP + 3%	1.3739	1.4064	0.0237	2.3655
PP + 7%	1.3711	1.3927	0.0158	1.5754
PP + 10%	1.3946	1.4979	0.0741	7.4071

Table 8. The results of the swelling tests in solvent (toluene) at room temperature.

	LDPE + 10%	HDPE + 10%	PP + 10%
C (organic)	93.80%	92.50%	90.30%
CaO	3.75%	5.41%	7.18%
TiO_2	0.63%	0.53%	0.49%
SiO_2	0.58%	0.51%	0.49%
Al_2O_3	0.47%	0.10%	0.10%
Cl	0.11%	0.16%	0.16%
Fe_2O_3	0.19%	0.19%	0.16%
MgO	0.10%	0.11%	0.14%
PbO	0.14%	0.10%	0.10%
P_2O_5	0.07%	0.09%	0.08%
Br	0.03%	0.09%	0.10%
CuO	0.10%	0.08%	0.07%
SnO_2	0.04%	0.05%	0.05%
ZnO	0.02%	0.02%	0.02%
SrO	0.0046%	0.01%	0.02%
ZrO_2	0.0026%	0.01%	0.01%
SO_3	0.00%	0.00%	0.06%
Cr_2O_3	0.00%	0.01%	0.00%
As_2O_3	0.0036%	0.00%	0.00%

3.4.2. X-ray Fluorescence Spectrometry (XRF) Elemental Chemical Analysis

The results obtained for the samples with the addition of 10% WEEE powder are shown among the samples with the addition of WEEE powder. Chemically, the samples with 3% and 7% additions of WEEE material did not provide any further information. In addition to the polymer matrix, the samples of products based on low-density polyethylene (LDPE range) contain mostly the elements Ca, Ti, Al, Si, Fe, P, Pb (in the form of oxides), Br, and Cl (Figure 10). Aside from the polymer matrix, the samples of products created in the form of grinding based on high-density polyethylene (HDPE range) contain mostly the elements Ca, Ti, Si, Fe, Mg, Pb, P, Cu, Sn (in the form of oxides), Br, and Cl. In addition to the polymer matrix, the samples of the regranulated products based on polypropylene (PP range) comprise mostly the elements Ca, Si, Ti, Fe, Mg, Pb, P, Cu, S, Sn (in the form of oxides), Br, and Cl.

It has also been observed that products based on LDPE regranulated from electronic waste with the addition of WEEE powder contain traces of As, an element that is not present in products based on HDPE or PP; products based on HDPE milled from electronic waste with the addition of WEEE powder as well as products based on regranulated PP from electronic waste with the addition of WEEE powder both contain Mg, and the percentage of Zn in the form of oxide is the same for all products based on LDPE, HDPE, and PP.

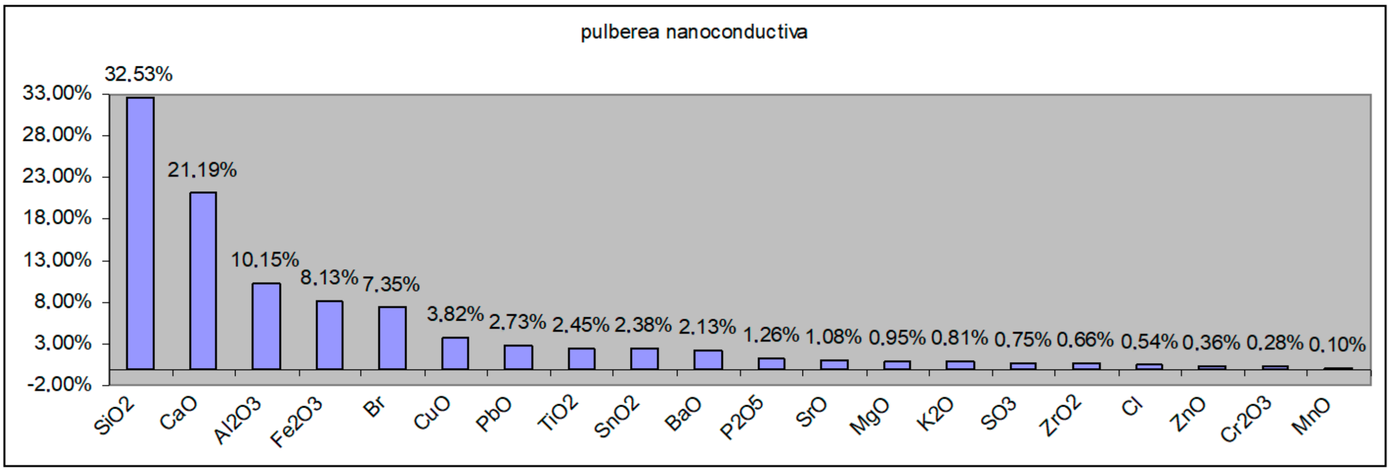

Figure 10. XRF results for WEEE powder component parts.

It is assumed that the existence of some traces of elements appearing incidentally in some samples is related to the previous processing of the polymer beads.

According to the graph below, the components of the conductive powder are present in considerable percentages in the composition.

To better highlight the elements contained in the examined samples, a graphic representation was created that excluded C (organic) and calcium oxide CaO (as an addition). All of the samples studied include a higher percentage of TiO_2; the presence of SiO_2 is also reported. MgO, Fe_2O_3, ZnO, Al_2O_3, PbO, and CuO are also present in trace amounts.

3.4.3. Chemical Element Analysis—SEM with the EDX Dispersive Probe

This type of examination was carried out using an SEM equipped with a field emission source and a focused ion beam. Element chemical analyses could be performed using the EDX type dispersive probe mounted on the microscope to provide information on the point composition on the surface of the analyzed material. As a result, in order to obtain the most accurate information on the composition, different areas of the material's surface were explored, with the software then allowing for the integration of the obtained compositional information and the formation of an image of the material's degree of homogeneity in particular.

It was discovered that the WEEE powder produced via WEEE processing has a significant organic component. Thus, a 10% WEEE powder addition in the composite mass represents a maximum contribution of 6% mineral components, with the rest being organic. The explanation is straightforward and stems from the fact that the powder is derived from the processing of printed circuits, which contain thermosetting elements with a significant content of organic components, as well as conductive and semi-conductive mineral and micro-metallic components.

It was found that the addition of progressive concentrations of WEEE powder from 3% to 7% and finally 10% determines a corresponding increase in the concentrations of inorganic elements/metal oxides identified in the analysis (Figures 11–13 and Table 9).

Finally, the presence of Br in the composition (approx. 0.05%) attests to the fact that brominated flame retardant compounds present in electronic equipment have been successfully stabilized and integrated, which is one of the EC's requirements for material recycling technologies—to stabilize hazardous materials, which cannot be recycled any other way. Additionally, the flame retardant features of WEEE are partially transferred to the composite materials, which is a clear benefit.

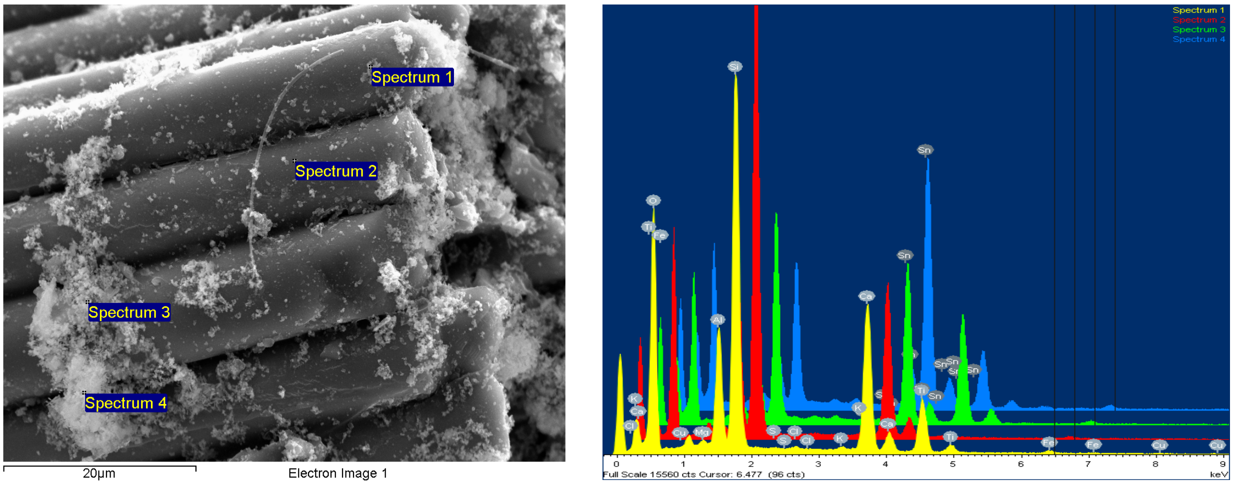

Figure 11. LDPE from e-waste with 10% NC powder composite sample—mag 5000× secondary electron (SE) image with spectra points on the sample, four areas analyzed.

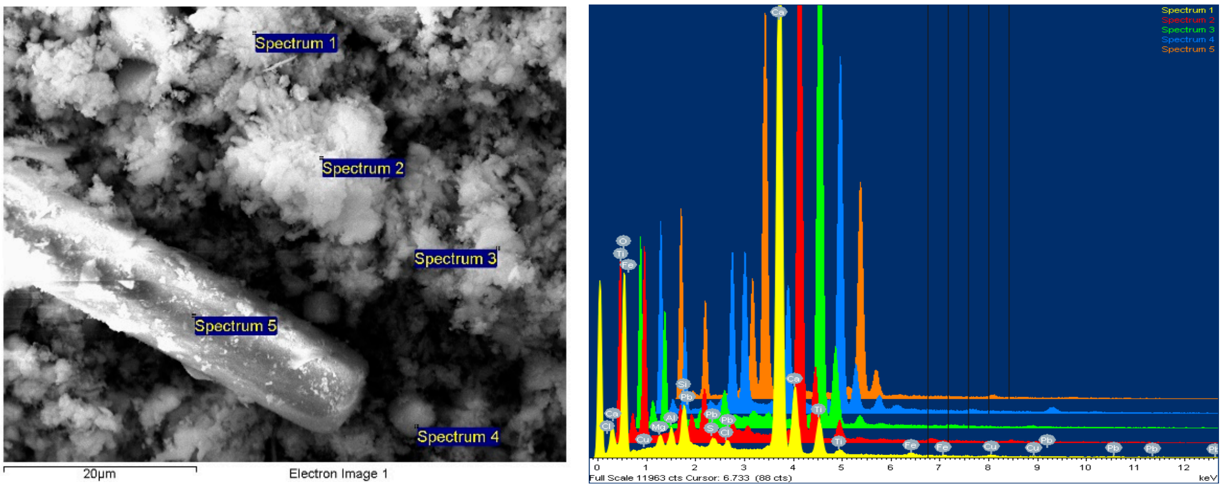

Figure 12. HDPE from e-waste with 10% NC powder composite sample—mag 5000× secondary electron (SE) image with spectra points on the sample, five areas analyzed.

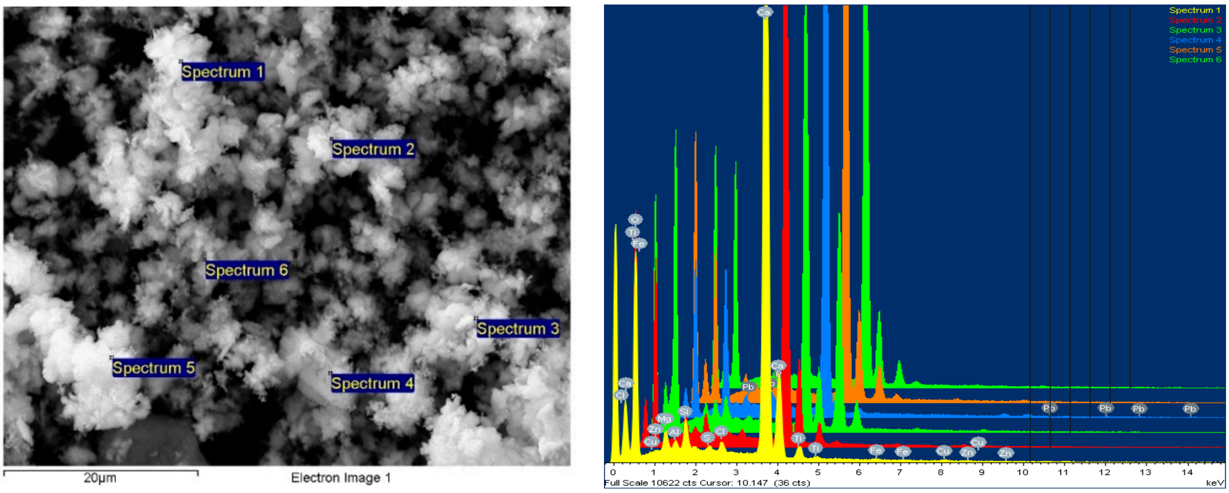

Figure 13. PP from electronic waste with 10% NC powder composite sample—mag 5000× secondary electron (SE) image with spectra points on the sample, six areas analyzed.

Table 9. EDAX results for all samples.

	O	Mg	Al	Si	S	Cl	K	Ca	Ti	Fe	Cu	Zn	Pb
LDPE + 3%	49.19	0.95	20.26	42.78	0.77	1.13	4.35	57.63	32.03	0.48	0.48	0.75	1.56
LDPE + 7%	46.29	13.07	0.83	23.68	0.36	0.55	62.9	6.83	1.53	0.61	4.38	1.93	46.29
LDPE + 10%	54.89	0.94	7.98	25.82	0.22	0.39	0.32	18.81	15.04	0.78	0.22	8.74	54.89
HDPE + 3%	58.76	1.34	8.17	27.04	0.19	1.09	50.65	2.56	0.5	0.47	0.82	58.76	1.34
HDPE + 7%	57.83	1.91	0.29	1.31	0.39	0.57	57.7	2.51	0.31	0.37	57.83	-	-
HDPE + 10%	53.26	1.76	9.16	26.05	0.27	9.33	48.73	3.87	0.7	2.11	1.17	53.26	1.76
PP + 3%	57.63	8.16	0.67	1.08	0.26	0.71	44.59	16.56	0.23	0.63	0.9	1.74	57.63
PP + 7%	57.83	1.91	0.29	1.66	0.39	0.57	56.7	10.56	2.13	0.37	57.83	-	-
PP + 10%	55.54	12.77	7.8	25.81	0.32	0.65	47.57	4.66	1.24	0.54	0.96	55.54	12.77

The studied images in Figures 11–13 and the compositions—obtained by scanning the composition on all micro-areas of interest—indicate a good homogeneity of the composite structure, attesting to the correct method of dispersing the additives and the thermoplastic processing. It is obvious that the LDPE matrix appears more filamented compared to that of HDPE and PP, which appear more dispersed with lumpy aspects.

However, the ability of such powders to disperse more uniformly, avoid reagglomeration/sedimentation, and have an increased affinity towards the polyolefin thermoplastic matrix makes them more appealing for use in customized composites for automotive applications. The presence of residual organic components from thermoset resins dispersed and linked among the inorganic components is beneficial, and ease the uniform dispersion within the matrix, with the phenomenon being similar to that of pre-composition—an eventual coating at the nano/micro scale of mineral components with organic particles, which is, in fact, a classical procedure to ease the uniform dispersion of additives within a thermoplastic matrix.

3.5. Thermal Property Analysis

The mathematical analysis of the distribution of the temperature variation as a function of time allows the determination of the thermal diffusivity "α". This is done via the analysis software of the device that allows for the manual or automatic control of the experimental process, as well as the evaluation of the results. The software contains several mathematical models for this application. The simplest model is the "adiabatic model". For this model, the thermal diffusivity is calculated according to the relationship below [2]:

$$\alpha = 0.1388 \times \frac{I^2}{t_{1/2}}$$

where

α = thermal diffusivity (mm^2/s);

I = sample height (mm);

$t_{1/2}$ = the time (s) when the temperature rises to half, measured on the other side of the sample.

The "flash" method is advantageous due to the simple geometry and small size requirements of the samples, the speed of the measurements, and the ease of use. For accurate measurements, it is recommended that the samples be cylindrical or parallelepiped, and have flat surfaces and parallel faces [2].

Specific heat (also called mass heat capacity) represents the amount of heat required per unit of mass (kg) of a homogeneous body to change its temperature by one degree, and is expressed according to the relationship below [2]:

$$C_P = \frac{Q}{m \times \Delta T}$$

where

C_P = specific heat (J/kg·K);
Q = heat (J);
m = sample mass (kg);
ΔT = temperature variation of the sample (K).

This technique involved a comparison between the temperature increase of the sample due to the pulse emitted by the xenon lamp (the voltage of the final detector minus the voltage of the baseline detector), and the temperature increase of the standard sample, tested at the same time and under the same conditions. In this way, the specific heat and the thermal diffusivity of the sample could be measured after a single analysis.

Thus, the specific heat of the sample was determined according to the following equation [2]:

$$C_P = \frac{(mC_P\Delta T)_{standard}}{(m\Delta T)_{sample}} = \frac{(mC_P\Delta V)_{standard}G_{standard}}{(m\Delta V)_{sample} \times G_{sample}}$$

where

V = voltage variation recorded by the detector (proportional to T) (V);
G = detector gain, which is a constant equal to 50,020.

Thermal Conductivity Measurement

Thermal conductivity is the physical quality that characterizes the ability of a material to transmit heat when it is subjected to a temperature difference.

Thermal conductivity is defined for a mass body that has a temperature gradient, and represents the heat flow that crosses a unit of transversal surface, in a unit of time, in the direction of the unit temperature gradient. The thermal conductivity of the samples was determined with the following equation [2]:

$$\lambda = \alpha \times C_P \times d$$

where

λ = thermal conductivity (W/m·K);
α = thermal diffusivity (m^2/s);
C_P= specific heat (J/kg·K);
d = density (kg/m^3).

From the values from Tables 10 and 11, we can draw the conclusion that by adding WEEE powders, the highest thermal conductivity value is obtained for materials with an addition of 10% WEEE powder. It can be observed that the highest thermal conductivity value is recorded for regranulated PP from electronic waste with 10% addition of WEEE powder.

From the analysis of the thermogravimetric data, presented in Table 12 it was observed for the composites made from recycled matrices with powder—compared to the matrices of origin—that the composite materials show a tendency to translate the thermal phenomena towards higher temperatures. This occurrence is confirmed by the temperature differences identified in the glass transition process, where the increase in the temperature at the beginning of the process can be observed (e.g., LDPE—initial T = 203.9 °C, compared to the composite based on LDPE with initial T = 230.4 °C), which is due to the addition of the conductive powder.

Table 10. The experimental results regarding glass transitions for all analyzed materials.

Material	Melting	Glass Transitions		
	Q (J/g)	Cp J/g·K	Initial Temperature (°C)	Final Temperature (°C)
LDPE	92.86	0.102	230.9	249.0
LDPE + 3%	93.82	0.121	230.4	248.9
LDPE + 7%	196.5	0.462	224.3	239.6
LDPE + 10%	90.43	-	-	-
HDPE	46.02	1.932	221	230
HDPE + 3%	46.86	1.951	225	234
HDPE + 7%	48.32	-	-	-
HDPE + 10%	59.61	1.111	229.1	238.7
PP	62.00	0.800	247.3	253.8
PP + 3%	62.45	0.718	246.9	254.9
PP + 7%	54.86	2.962	232	239.6
PP + 10%	62.57	0.407	249.8	259.3

Table 11. The results of the thermal conductivity determination.

Material	Diffusivity (mm^2/s)	Conductivity (W/(m·K))	Cp (J/g/K)
LDPE + 3%	0.197	0.179	2.551
LDPE + 7%	0.22	0.202	2.327
LDPE + 10%	0.226	0.208	2.275
HDPE + 3%	0.198	0.18	1.716
HDPE + 7%	0.2	0.182	2.155
HDPE + 10%	0.24	0.222	1.733
PP + 3%	0.223	0.205	1.597
PP + 7%	0.231	0.213	1.766
PP + 10%	0.273	0.255	2.018

Table 12. The results of the analysis of the thermogravimetric data.

Material Matrix + x% Powder	Air/Static Conditions										
	Process I Melting	Process II Oxidation			Process III Thermo-Oxidatuion			Process IV Decomposition			%Δm Total
	T_{min} DSC, °C	T_{max} DSC, °C	T_{DTG}, °C	%Δm	T_{max} DSC, °C	T_{DTG}, °C	%Δm	T_{max} DSC, °C	T_{DTG}, °C	%Δm	
LDPE	116 122	413	474	97	517	-	-	662	664	-	97
LDPE + 3%	118 123	415	474	97	516	-	-	665	665	-	98
LDPE + 7%	115 124	418	474	97	514 530	-	-	681	680	-	99
LDPE + 10%	116 126	406	474	87	521	-	-	672	672	-	89
HDPE	130 165	397	430	81	486	486	3.65	701	701	8.07	89
HDPE + 3%	131 166	399 429	432 457	81	489	489	3.69	702	702	8.08	89
HDPE + 7%	130 165	385 423	431	82	490	488	3.64	700	701	8	88

Table 12. *Cont.*

Material Matrix + x% Powder	Air/Static Conditions										
	Process I Melting	Process II Oxidation			Process III Thermo-Oxidatuion			Process IV Decomposition			%Δm Total
	T_{min} DSC, °C	T_{max} DSC, °C	T_{DTG}, °C	%Δm	T_{max} DSC, °C	T_{DTG}, °C	%Δm	T_{max} DSC, °C	T_{DTG}, °C	%Δm	
HDPE + 10%	130 165	379 422	427	75.24	473 488	492	3.71	696	700	5.32	84.43
PP	130 163	401 425	455	80.02	-	-	-	708	708	6.09	88.71
PP + 3%	130 165	402 426	456	79.52	-	-	-	709	708	6.12	88.93
PP + 7%	129 164	297 398 420	385 398 427	72.12	482	482	6.32	707	702	6.32	84.76
PP + 10%	129 163	438	457	-	487 514	-	-	708	708	6.57	84.41

These temperature values will constitute the starting basis for the technology scaling process by operating the screw extruder in a double adiabatic process in order to avoid scaling problems due to differences in heat transfer.

3.6. Dielectric Properties

A Novocontrol measuring device was used for the dielectric measurements [50], and includes the following:

- Novocontrol AlphaN, broadband dielectric analysis stand;
- Novocontrol BDS 1200, calibrated cells (max. freq. 8 GHz);
- QUATRO-Cryosystem: cooling and heating system with liquid nitrogen (−160 °C ÷ +400 °C);
- WinDETA/WinFIT—software package for measurement, calibration, and analysis;
- Rhode–Schwartz NVR Network Analyzer, frequency range 20 kHz ÷ 8 GHz, impedance 0.1 Ω ... 10 kΩ, tan(δ) accuracy > 3 × 10^{-2}.

Dielectric tests (Figures 14–16) were performed only for the composites with a 10% powder content due to their relevant behavior.

The analyzed dielectric properties were the relative permittivity (eps′), real conductivity (sigma′), and dielectric loss expressed as Tgδ (Tangent Delta).

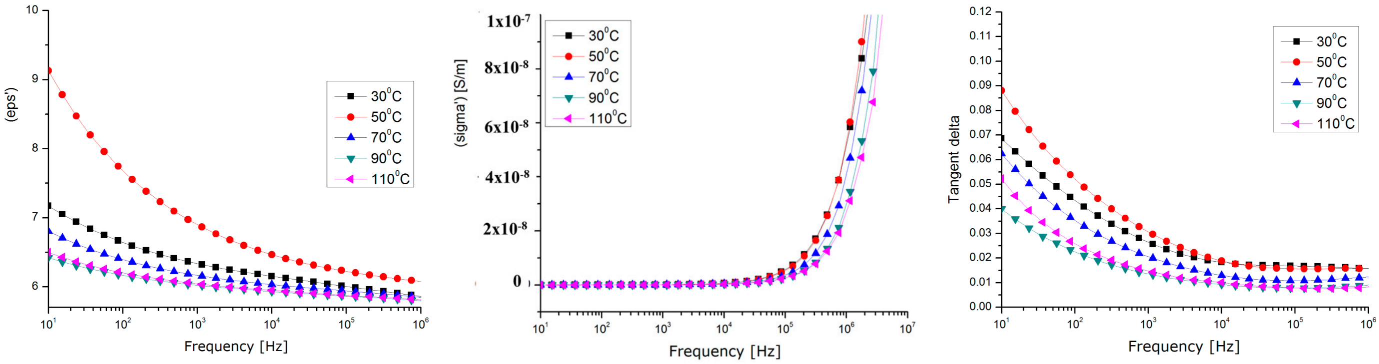

Figure 14. Dielectric measurements for HDPE composites with 10% powder content.

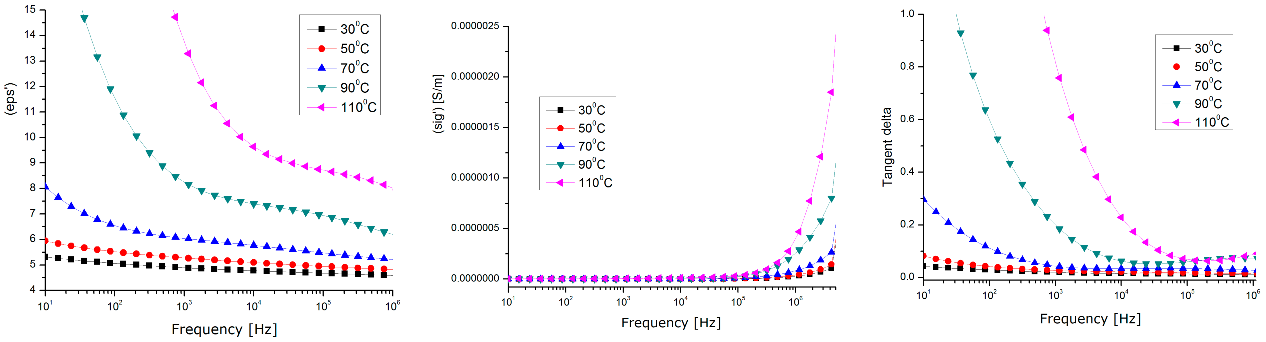

Figure 15. Dielectric tmeasurements for LDPE composites with 10% powder content.

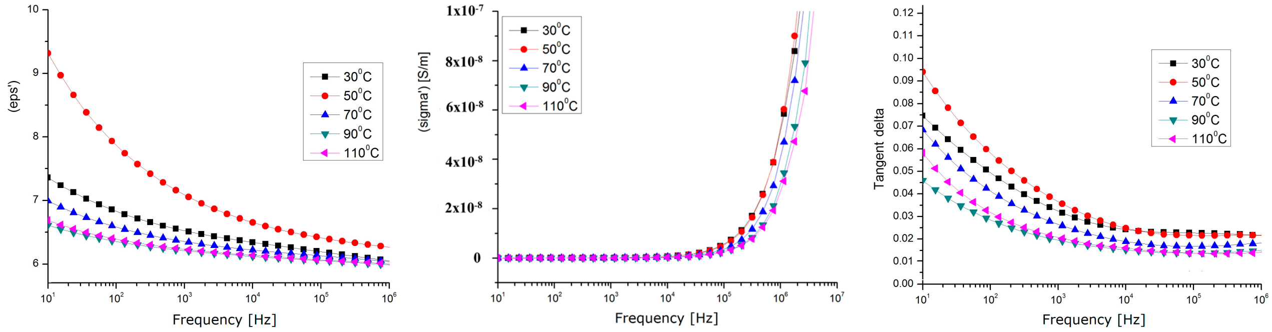

Figure 16. Dielectric measurements for PP composites with 10% powder content.

By correlating the dielectric characteristics obtained for the three samples of composites with their physico-chemical properties, it can be found that the values of the dielectric characteristics vs. temperature corresponding to the samples of HDPE and PP are relatively similar (Figures 14–16), but different values were achieved at higher temperatures for the sample of LDPE (the tg. Delta and the real permittivity were higher at over 70 °C). This may be explained by the fact that, in lower-density polyethene which has a lower viscosity at higher temperatures, the metallic components of the powder, i.e., Zn, Sn, and Pb, become more mobile and partially separate themselves from the oxide components, and so they act as higher-energy polarization centers, or higher-energy loss centers, due to a higher interfacial polarization effect at lower frequencies (with tg. Delta values of about one, even at the kHz frequency domain for LDPE).

In all cases, the maximum polarization effect is achieved at a temperature of approx. 50 °C, which may be explained by the optimal polarization at the interface between the polymer and the powder, when the thermal movement achieves its optimum level. In this context, considering the perspectives of the current research, the very high share of WEEE of electronic equipment produced after the 2000s (with a high degree of integration, in which there is a significantly large number of IC-type active components, and the passive ones are of a volume proportion below 30% compared to the active ones), and the future trends of electronic technology, the methods for the integral recycling of WEEE towards components with higher value in the context of a circular economy must become a stringent preoccupation of scientists.

The composite materials presented above, due to their relevant dielectric properties, may be further tested for applications in electromagnetic shielding at frequencies above 1 kHz, or for electromagnetic interference/electromagnetic compatibility (EMI/EMC and ESD) applications at lower frequencies, due to their superior dielectric loss factor values, which are associated with relevant behavior around exploitation temperatures, mainly for the electric, electronic, or automotive industries.

The obtained dielectric performance is in line and comparable with the results for similar composites from previous research, as presented in [2,31–37], but in our case, the main advantages are related, one side, to the integral recycling of WEEE towards an innovative product under the concept of a circular economy, and on the other side, to a clear economic benefit by substituting the very expensive powders that are actually used for applications in electromagnetic shielding with very cheap homologue powders obtained from the non-metallic thermoset components of WEEE (electronic components).

Hence, the presence of mineral additions is advantageous for improving mechanical, thermal, and electrical features, as well as, from the perspective of creating specific composite materials for automotive purposes, raising the fire resistance of the corresponding products.

4. Conclusions

Considering the concept of a circular economy and the perspectives of the current research, the very high share of waste electronic equipment produced after the 2000s (with a high degree of integration, in which there is a significantly large number of IC-type active components, and the passive ones are of a volume proportion below 30% compared to the active ones), and the future trends of electronic technology, the methods for the integral recycling of WEEE become an imperative purpose. Our paper suggests a method for the integrated recycling of thermoplastic and non-metallic components of WEEE, after all classical recycling processes are accomplished.

A relevant stage was dedicated to obtaining powder from the thermoset components of WEEE (electronic components), which was characterized by physical–chemical procedures and provided to include relevant components to be further used as additives in thermoplastic composites. The second stage referred to manufacturing and characterizing composites made of recycled LDPE, HDPE, and PP from WEEE, with up to a 10% addition of non-metallic powder. The composites proved a homogenous structure, with high chemical and thermal stability.

Finally, the dielectric properties were tested, and high values for the dielectric permittivity and loss factor (tgδ) were achieved. For all matrices, the maximum polarization effect was achieved at a temperature of approx. 50 °C, which may be explained by the optimal polarization at the interface between the polymer and the powder, when the thermal movement achieves its optimum level. The composite materials with up to a 10% addition of non-metallic powder, due to their relevant dielectric properties, may be further tested as good candidates for applications in electromagnetic shielding at frequencies above 1 kHz, or for electromagnetic interference/electromagnetic compatibility (EMI/EMC and ESD) applications at lower frequencies, due to their superior dielectric loss factor values, associated with the relevant behaviors around exploitation temperatures, mainly for the electric, electronic, or automotive industries.

The main advantages of this study are related, on one side, to the integral recycling of WEEE towards an innovative product under the concept of a circular economy, and on the other side, to a clear economic benefit by substituting the very expensive powders that are actually used for applications in electromagnetic shielding with very cheap homologue powders obtained from the non-metallic thermoset components of WEEE (electronic components). On the other hand, it was noticed that the brominated flame retardant compounds present in electronic equipment were successfully stabilized and integrated within composites, which is one of the EC's requirements for material recycling technologies—to stabilize hazardous materials, which cannot be recycled any other way.

Author Contributions: Conceptualization, R.C.C. and M.A. (Magdalena Aflori); methodology, R.C.C. and M.A. (Magdalena Aflori); software, A.G.U.; validation, C.S., M.A. (Mihaela Aradoaeiand) and E.G.H.; writing—original draft preparation, R.C.C. and M.A. (Magdalena Aflori); writing—review and editing, R.C.C. and M.A. (Magdalena Aflori); visualization R.C.C. and M.A. (Magdalena Aflori). All authors have read and agreed to the published version of the manuscript.

Funding: This research received no external funding.

Conflicts of Interest: The authors declare no conflict of interest.

References

1. EU Commission: A European Strategy for Plastics in a Circular Economy. Available online: https://ec.europa.eu/environment/circular-economy/pdf/plasticsstrategy-brochure (accessed on 1 August 2023).
2. Rahaman, M.; Al Ghufais, I.A.; Periyasami, G.; Aldalbahi, A. Recycling and Reusing Polyethylene Waste as Antistatic and Electromagnetic Interference Shielding Materials. *Int. J. Polym. Sci.* **2020**, *2020*, 6421470. [CrossRef]
3. Verma, S.; Mili, M.; Dhangar, M.; Jagatheesan, K.; Paul, S.; Bajpai, H.; Vedanti, N.; Mallik, J.; Khan, M.A.; Bhargaw, H.N.; et al. A review on efficient electromagnetic interference shielding materials by recycling waste—A trio of land to lab to land concept. *Environ. Sci. Pollut. Res.* **2021**, *28*, 64929–64950. [CrossRef] [PubMed]
4. Zhang, X.; Wang, X.; Lei, Z.; Wang, L.; Tian, M.; Zhu, S.; Xiao, H.; Tang, X.; Qu, L. A flexible MXene-decorated fabric with interwoven conductive networks for integrated joule heating, electromagnetic interference shielding and strain sensing performances. *ACS Appl. Mater. Interfaces* **2020**, *12*, 14459–14467. [CrossRef] [PubMed]
5. Safdar, F.; Ashraf, M.; Javid, A.; Iqbal, K. Polymeric textile-based electromagnetic interference shielding materials, their synthesis, mechanism and applications—A review. *J. Ind. Textiles* **2022**, *51*, 7293S–7358S. [CrossRef]
6. Calvert, G.; Ghadiri, M.; Tweedie, R. Aerodynamic dispersion of cohesive powders: A review of understanding and technology. *Adv. Powder Technol.* **2009**, *20*, 4–16. [CrossRef]
7. Zhang, J.; Shields, T.J.; Silcock, G.W.H. Effect of melting behaviour on flame spread of thermoplastics. *Fire Mater.* **1997**, *21*, 1–6. [CrossRef]
8. Jahed, H.; Shirazi, R. Loading and unloading behavior of a thermoplastic disc. *Int. J. Press. Vessels Pip.* **2001**, *78*, 637–645. [CrossRef]
9. Das, M.K.; Ghoshdastidar, P.S. Experimental validation of a quasi three-dimensional conjugate heat transfer model for the metering section of a single-screw plasticating extruder. *J. Mater. Process. Technol.* **2001**, *120*, 397–411. [CrossRef]
10. Qu, J.; Wong, C.P. Effective elastic modulus of underfill material for flip-chip applications. *IEEE Trans. Compon. Packag.* **2002**, *25*, 53–55.
11. Vo, H.T.; Shi, F.G. Towards model-based engineering of optoelectronic packaging materials: Dielectric constant modeling. *Microelectron. J.* **2002**, *33*, 409–415. [CrossRef]
12. Todd, M.G.; Shi, F.G. Validation of a Novel Dielectric Constant Simulation Model and the Determination of Its Physical Parameters. *Microelectron. J.* **2002**, *33*, 627–632. [CrossRef]
13. Todd, M.G.; Shi, F.G. Molecular basis of the interphase dielectric properties of microelectronic and optoelectronic packaging materials. *IEEE Trans. Compon. Packag.* **2003**, *26*, 667–672. [CrossRef]
14. Sriraam, R.C.; Brajendra, K.S. 13—From Waste to Resources: How to Integrate Recycling Into the Production Cycle of Plastics. In *Plastics Design Library, Plastics to Energy*; Al-Salem, S.M., Ed.; William Andrew Publishing: Norwich, NY, USA, 2019; pp. 345–364. [CrossRef]
15. Schwedes, J. Review on testers for measuring flow properties of bulk solids. *Granul. Matter* **2003**, *5*, 1–43. [CrossRef]
16. Li, K.; Qin, Y.; Zhu, D.; Zhang, S. Upgrading waste electrical and electronic equipment recycling through extended producer responsibility: A case study. *Circ. Econ.* **2023**, *2*, 100025. [CrossRef]
17. Eraslan, A.N.; Orcan, Y. On the rotating elastic–plastic solid disks of variable thickness having concave profiles. *Int. J. Mech. Sci.* **2002**, *44*, 1445–1466. [CrossRef]
18. Kaynak, I.; Sen, F.; Sayman, O. Thermo-elastic stress analysis of injection molding short glass fiber filled polymer composite disc with holes. *J. Reinf. Plast. Compos.* **2008**, *27*, 1117–1134. [CrossRef]
19. Jia, L.-C.; Yan, D.-X.; Cui, C.-H.; Jiang, X.; Ji, X.; Li, Z.-M. Electrically conductive and electromagnetic interference shielding of polyethylene composites with devisable carbon nanotube networks. *J. Mater. Chem.* **2015**, *3*, 9369–9378. [CrossRef]
20. Tagami, N.; Hyuga, M.; Ohki, Y.; Tanaka, T.; Imai, T.; Harada, M.; Ochi, M. Comparison of dielectric properties between epoxy composites with nanosized clay fillers modified by primary amine and tertiary amine. *IEEE Trans. Dielectr. Electr. Insul.* **2010**, *17*, 214–220. [CrossRef]
21. Todd, M.G.; Shi, F.G. Characterizing the interphase dielectric constant of polymer composite materials: Effect of chemical coupling agents. *J. Appl. Phys.* **2003**, *94*, 4551–4557. [CrossRef]
22. Yi, Y.B.; Sastry, A.M. Analytical approximation of the two-dimensional percolation threshold for fields of overlapping ellipses. *Phys. Rev. E* **2002**, *66*, 066130. [CrossRef]
23. Brosseau, C.; Queffelec, P.; Talbot, P. Microwave characterization of filled polymers. *J. Appl. Phys.* **2001**, *89*, 4532–4540. [CrossRef]
24. Farag, N.; Kliem, H. Interactions in Point-Dipole Systems: Effects of Size, Electrodes, and Lattice Defects. *Phys. Status Solidi B* **2002**, *233*, 180–187. [CrossRef]
25. Wagner, H.D. Paving the way to stronger materials. *Nat. Nanotechnol.* **2007**, *2*, 742–744. [CrossRef] [PubMed]
26. Sen, F. An investigation of thermal elasto-plastic stress analysis of laminated thermoplastic composites with a circular hole under uniform temperature loading. *Sci. Eng. Compos. Mater.* **2006**, *13*, 213–224. [CrossRef]
27. Sen, F. Estimation of elasto-plastic thermal and residual stresses in a thermoplastic composite disc under uniform temperature effect. *J. Reinf. Plast. Compos.* **2006**, *25*, 1485–1498. [CrossRef]
28. Ciobanu, R.C.; Aradoaei, M.; Caramitu, A.R.; Ion, I.; Schreiner, C.M.; Tsakiris, V.; Marinescu, V.; Hitruc, E.G.; Aflori, M. Special Packaging Materials from Recycled PET and Metallic Nano-Powders. *Polymers* **2023**, *15*, 3161. [CrossRef] [PubMed]

29. Kuehn, M.; Kliem, H. Simulation of heterogeneous nanodielectrics using the local field method. *IEEE Trans. Dielectr. Electr. Insul.* **2005**, *12*, 844–853. [CrossRef]
30. Kuhn, M.; Kliem, H. Local Fields in Dielectric Nanospheres from a Microscopic and Macroscopic Point of View. *IEEE Trans. Dielectr. Electr. Insul.* **2009**, *16*, 596–600. [CrossRef]
31. Kuehn, M.; Kliern, H. The method of local fields: A bridge between molecular modelling and dielectric theory. *J. Electrostat.* **2009**, *67*, 203–208. [CrossRef]
32. From Waste to Wealth: A Critical Review on Advanced Materials for EMI Shielding. Available online: https://onlinelibrary.wiley.com/doi/full/10.1002/app.52974 (accessed on 10 July 2023).
33. Structural Design Strategies of Polymer Matrix Composites for Electromagnetic Interference Shielding: A Review. Available online: https://link.springer.com/article/10.1007/s40820-021-00707-2 (accessed on 21 July 2023).
34. Progress in Polymers and Polymer Composites Used as Efficient Materials for EMI Shielding. Available online: https://pubs.rsc.org/en/content/articlelanding/2021/na/d0na00760a (accessed on 5 July 2023).
35. Thermoplastic Polymer Composites for EMI Shielding Applications. Available online: https://www.sciencedirect.com/science/article/abs/pii/B9780128175903000051 (accessed on 1 August 2023).
36. Polymer-Based EMI Shielding Composites with 3D Conductive Networks: A Mini-Review. Available online: https://onlinelibrary.wiley.com/doi/full/10.1002/sus2.21 (accessed on 21 July 2023).
37. Comprehensive Review on Polymer Composites as Electromagnetic Interference Shielding Materials. Available online: https://journals.sagepub.com/doi/full/10.1177/09673911221102127 (accessed on 21 July 2023).
38. Kuhn, M.; Kliem, H. Time variance of interacting dipole systems. *Phys. Status Solidi B* **2007**, *244*, 1418–1428. [CrossRef]
39. Karkkainen, K.; Sihvola, A.; Nikoskinen, K. Analysis of a three-dimensional dielectric mixture with finite difference method. *IEEE Trans. Geosci. Remote Sens.* **2001**, *39*, 1013–1018. [CrossRef]
40. Bektas, N.B.; Sayman, O. Elasto-plastic stress analysis in simply supported thermoplastic laminated plates under thermal loads. *Compos. Sci. Technol.* **2001**, *61*, 1695–1701. [CrossRef]
41. Metallic Powders—Determination of Apparent Density. Part 1: Funnel Method. Available online: https://cdn.standards.iteh.ai/samples/69219/73e768c2dd64481eb5d96ff1c0e0a6a2/ISO-3923-1-2018.pdf (accessed on 14 July 2023).
42. Metallic Powders—Determination of Apparent Density. Part 2: Scott Volumeter Method. Available online: https://cdn.standards.iteh.ai/samples/9559/99cc189d9e014797b3fc44916d52bf11/ISO-3923-2-1981.pdf (accessed on 12 July 2023).
43. AURIGA Series. Modular CrossBeam Workstation. Available online: http://www.rochester.edu/urnano/assets/pdf/sem_fib_zeiss_auriga_manual.pdf (accessed on 1 August 2023).
44. Comparison of Properties with Relevance for the Automotive Sector in Mechanically Recycled and Virgin Polypropylene. Available online: https://www.mdpi.com/2313-4321/6/4/76 (accessed on 21 July 2023).
45. Closed Loop Recycling of WEEE Plastics: A Case Study for Payment Terminals. Available online: https://www.sciencedirect.com/science/article/pii/S2212827120301852: (accessed on 14 July 2023).
46. Reprocessing of Polymer Blends from WEEE: A Methodology for Predicting Embrittlement. Available online: https://hal.science/hal-03520723/document (accessed on 2 July 2023).
47. Mechanical and Thermal Properties of Recycled WEEE Plastic Blends. Available online: https://publications.lib.chalmers.se/records/fulltext/229768/229768.pdf (accessed on 1 August 2023).
48. Electronic Waste Plastics Characterisation and Recycling by Melt-processing. Available online: https://publications.lib.chalmers.se/records/fulltext/175356/175356.pdf (accessed on 12 July 2023).
49. *ASTM E-1461:2007*; Standard Test Method for Thermal Diffusivity of Solids by the Flash Method. ASTM International: West Conshohocken, PA, USA, 2007.
50. Concept Turnkey Dielectric, Conductivity and Impedance Spectrometers with Temperature Control. Available online: https://www.novocontrol.de/php/turn_key_10_90.php (accessed on 25 July 2023).

polymers

Article

Three-Dimensional Printable Flexible Piezoelectric Composites with Energy Harvesting Features

Mihaela Aradoaei [1], Romeo C. Ciobanu [1,*], Cristina Schreiner [1], Marius Paulet [1], Alina R. Caramitu [2], Jana Pintea [2] and Mihaela Baibarac [3]

[1] Department of Electrical Measurements and Materials, Gheorghe Asachi Technical University, 700050 Iasi, Romania; mihaela.aradoaei@academic.tuiasi.ro (M.A.); cristina-mihaela.schreiner@academic.tuiasi.ro (C.S.); mpaulet@tuiasi.ro (M.P.)
[2] National Institute for Research and Development in Electrical Engineering ICPE—CA, 030138 Bucharest, Romania; alina.caramitu@icpe-ca.ro (A.R.C.); jana.pintea@icpe-ca.ro (J.P.)
[3] National Institute of Materials Physics, Atomistilor Street 405A, P.O. Box MG-7, 077125 Bucharest, Romania; barac@infim.ro
* Correspondence: r.c.ciobanu@tuiasi.ro or rciobanu@yahoo.com

Abstract: The purpose of this work was to obtain an elastic composite material from polymer powders (polyurethane and polypropylene) with the addition of $BaTiO_3$ until 35% with tailored dielectric and piezoelectric features. The filament extruded from the composite material was very elastic but had good features to be used for 3D printing applications. It was technically demonstrated that the 3D thermal deposition of composite filament with 35% $BaTiO_3$ was a convenient process for achieving tailored architectures to be used as devices with functionality as piezoelectric sensors. Finally, the functionality of such 3D printable flexible piezoelectric devices with energy harvesting features was demonstrated, which can be used in various biomedical devices (as wearable electronics or intelligent prosthesis), generating enough energy to make such devices completely autonomous only by exploiting body movements at variable low frequencies.

Keywords: flexible composites with piezoelectric features; 3D printable flexible piezoelectric devices; energy harvesting

check for updates

Citation: Aradoaei, M.; Ciobanu, R.C.; Schreiner, C.; Paulet, M.; Caramitu, A.R.; Pintea, J.; Baibarac, M. Three-Dimensional Printable Flexible Piezoelectric Composites with Energy Harvesting Features. *Polymers* **2023**, *15*, 2548. https://doi.org/10.3390/polym15112548

Academic Editors: Anton Ficai and Cristina-Elisabeta Pelin

Received: 1 May 2023
Revised: 25 May 2023
Accepted: 29 May 2023
Published: 31 May 2023

1. Introduction

The past 10 years have witnessed enormous interest in the efficient capture of environmental energy through the development of energy-harvesting devices that transform mechanical energy into electricity and greatly reduce our dependence on fossil fuels and CO_2 emissions. The application segments for piezoelectric energy harvesters based on ferroelectrics have dramatically expanded during the past 5 years. For several applications, ferroelectric micro- and nano-crystals with a defined one- (1D), two- (2D), and three-dimensional (3D) shape are of great scientific and technological interest because of their spontaneous polarization as well as their shape- and size-dependent properties. The subject of moldable piezoelectric sensors with energy harvesting features is very actual; research in this area extensively reports mainly thermo-rigid devices based on epoxy, PVDF, or other composite structures, mainly with PZT powders, such as [1–13].

Regarding the analysis of costs vs. benefits of adapted technology and the life cycle of such devices, we note that the basic literature largely supports piezoelectric energy as being applicable in special-purpose niches with high market impact, such as wireless sensor networks (IoT). The harvesting of piezoelectric energy must be interpreted through direct indicators: the power required for the real purpose and the surplus power, which is unused and stored over time. A decision model for analyzing costs vs. benefits would include aspects such as power consumption (both active and stored), physical size/energy density requirements, storage battery technology, and working circuit technology. For example, the CC2630 Zigbee TI controller uses 1.0 μA in passive mode, whereas the CC2538 uses between 1.3 and 600 μA. In "sleep mode", consumption is 0.1 vs. 0.4 μA.

The overall cost is also given by the relevant and precise characterization of the physical conditions that contribute to energy harvesting: the occurrence of dynamic force, vibration frequency, temperature range over time, etc. Depending on the complexity of the equipment, evaluations are made of potential improvements in energy efficiency, price, normalized price, and lifetime. As for the lifetime, the energy harvesting technologies are guaranteed for a minimum of 10 years, being made on the basis of robust materials, a sufficient element to make them very competitive on the renewable energy market, and for the technological design according to the forecasts of microelectronic applications.

From the point of view of technological feasibility, the advantages of piezoelectric generators are mentioned as being simple structures, easy to manufacture on a large scale (mass production), on the one hand, and easy to implement in electronic systems of the 'energy harvesting' type.

The new trend is defined by flexible energy-harvesting devices, which are yet more difficult to manufacture. Some achievements are presented as [14–28], but they are practically never combined with 3D printing technology, which is the interest of our research and the subject of the actual paper. In general, a wide range of composites made of ceramic powders and polymers can be processed by 3D printing technology; however, the receipt at the nanoscale is a key factor in successful part fabrication. The main unmet need is related to the difficulty of adapting any new variant of composite with individual thermo-mechanical characteristics on any 3D printing machine, and there is a must—achieved only by an extended R&D activity—the technological balance between the desired features of filament material, on the one side, and 3D printing capabilities, on the other side, in order to create the best characteristics of the obtained component. The values of material density, viscosity, and surface tension must be correlated. When the ratio is too small, viscous forces predominate, which implies high pressure for ejection; inversely, if this ratio is too large, a continuous column is ejected, which can lead to the formation of satellite drops behind the main drop. The rheology of thermoplastic nano-composite and its behavior at different processing temperatures are problems related to compound melting temperature, stability in the quasi-liquid phase, and final product isotropy. If mixed dissimilar materials are used for nano-composites, e.g., ceramic powder/CNT with a polymer matrix, even if the product is homogenous and stable after extruding—when the filament is generated—it may suffer important physical modifications during the subsequent stage of 3D printing technology. The flowability of powders in quasi-liquid phases is an essential parameter for 3D processing. Sufficient flowability allows the building of high 3D resolution [29–31].

The 3D architectural design of printable piezoelectric components involved a good knowledge of the adsorption of thermoplastic polymers on the surface of ceramic nanoparticles. In the stages prior to the realization of the 3D printable flexible piezoelectric composites with energy harvesting features, the following results were reported by the authors [32–34] as preliminary methods of preparing films containing thermoplastic polymers and their composites with $BaTiO_3$, along with some optical and structural properties.

Our study presents an example of good practice under the circumstances that it is obvious that by an extruding process pellets from thermoplastic composites may be manufactured, even if the inorganic powder content goes towards 80–90%, but it is also well known that the manufacture of rigorous filament in terms of diameter tolerance and reasonable length from thermoplastic composites with more than 10–15% inorganic powders is extremely difficult, mainly due to the fragility of the filament, which in many cases breaks itself under the reeling operation. That is why a tailored compounding of thermoplastic olefin with thermoplastic polyurethane was used. On the other hand, at higher powder contents, the filament homogeneity can suffer important changes under cooling operations due to dilatation, exfoliation, or delamination processes. Another major difficulty noticed by many practitioners refers to the thermal printer adaptation for such composites with a high content of inorganic powders, which makes the actual commercial printers useless for such applications, mainly when higher printing precision (micrometer scale) is compulsory.

The innovation presented by the present study includes a clear demonstration of the conditions imposed on such composites to become 3D printable, i.e., starting from the compounding and filamentation stage, through the 3D thermal deposition of composite filament with no clogging of the nozzle, no problems with multilayer deposition, and no 3D printing defects, to generating structures of rectangular network type with micro-meter precision, along with innovative tests to demonstrate their use as piezoelectric sensors within a dedicated signal processing circuit and the use of virtual instruments to assess their energy harvesting features.

2. Materials and Preparation Methods

2.1. Materials

In order to obtain the composite structures, the following raw materials were used: a thermoplastic olefin TPO (for the presented study, polypropylene TIPPLEN H 318), a thermoplastic polyurethane TPU (Estane 58,887 TPU), and $BaTiO_3$ powder of a maximum 2 micron dimension from Sigma Aldrich (Merck KGaA, Darmstadt, Germany). The present study completes and particularizes the previous research presented in [34] and refers only to TPO:TPU 2:1 type composites with $BaTiO_3$ powder content up to 35% in order to emphasize their piezoelectric features.

2.2. Processing Equipment

The polymers as powders (TPU and TPO—herein polypropylene) and the $BaTiO_3$ powder were homogenized by mixing for one hour in a cylindrical mixer with a 1.3 L capacity TURBULA T2F type with a rubber ring holding device, and the rotation speed was 40 rpm. In this way, we sought to obtain a uniform distribution of the components of the mixtures throughout the structure without using specific additives or adhesives for compatibility. Processing conditions involved a rotation speed (in counter-rotation) of the extruder of 95 rpm and a feed speed from the feed hopper of 450 rpm.

The injection of composite was performed on a Dr. Boy 35A injection machine (Dr. Boy GmbH & Co. KG, Neustadt-Fernthal Germany) with the following characteristics: a screw diameter of 28 mm, an L/D ratio of 18.6 mm, a calculated injection capacity of 58.5 cm^3, a maximum material pressure of 2200 bar, and a real injection capacity minimum of 500 mm. The interface of the injection machine for obtaining the composite materials and the temperature regime on the areas of the cylinders of the injection machine are briefly presented in Figure 1.

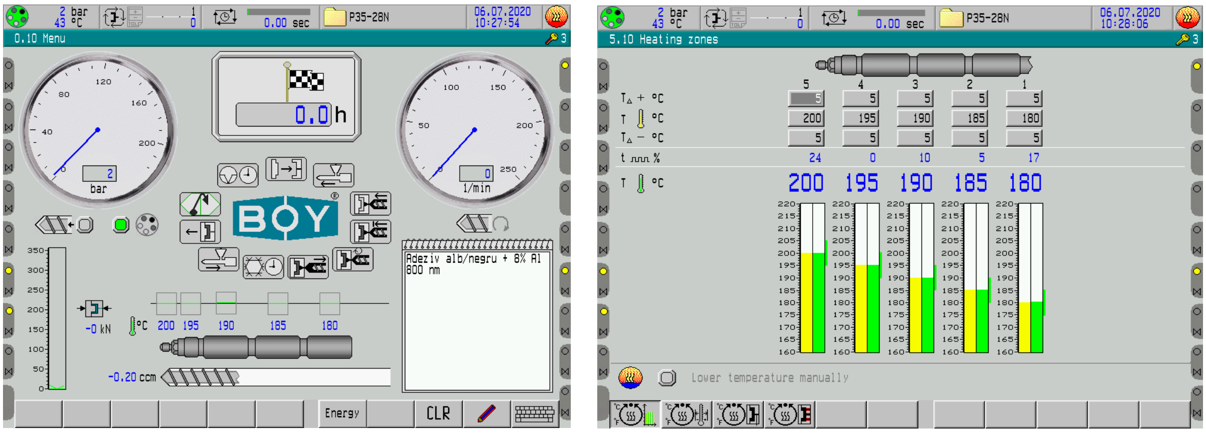

(**a**) (**b**)

Figure 1. (**a**) The interface of the injection machine, and (**b**) the temperature regime on the areas of the cylinder of the injection machine.

2.3. Characterization Equipment

The characterization of the composite materials was carried out with the use of the following equipment:

- The photoluminescence (PL) spectra of composites were recorded with a Fluorolog-3 spectrophotometer, FL3-2.2.1 model, from Horiba Jobin Yvon (Palaiseau, France), with some expertise related in [35].
- SEM optical scanning microscopy was performed with a field emission and focused ion beam scanning electron microscope (SEM) model Tescan Lyra III XMU (Brno—Kohoutovice, Czech Republic).
- The AFM analysis was performed with a WIKO NT 1100 type interferometric microscope in accordance with ISO 10109-7:2001 [36].
- Dielectric features were determined by using the Broadband Dielectric Spectrometer (Novocontrol GMBH), which encompasses an Alpha frequency response analyzer and Quattro temperature controller with tailored measurement cells. The manufactured samples were sandwiched between two copper electrodes of 20 mm diameter and placed inside the temperature-controlled cell [37].
- The piezoelectric features were measured using an Aixact TF Analyzer 2000-Electric Hysteresis Curve Lift System (static and dynamic hysteresis); the voltage that can be applied to the sample is +/− 100 V to +/− 10 kV). The device measures bulk samples (maximum diameter of 20 mm and a maximum thickness of 1.8 mm). The hysteresis curves were raised starting with a frequency of 0.1 Hz at an electric voltage 20% lower than the breakdown voltage of the samples. Simultaneously, the displacement of the sample can be measured with a laser interferometry system.
- TG/DSC thermal analysis, performed on a STA 449 F3 Jupiter TG-DSC simultaneous thermal analyzer, Netzsch (Selb, Germany), working in the temperature range up to 1550 °C, in an inert, oxidizing, reducing, static, or dynamic working atmosphere. The device is provided with a vacuum system with a maximum of 10^{-2} mbar.

3. Results and Discussion at the Composite Level

3.1. Photoluminescence Spectrum

The photoluminescence spectrum of thermoplastic composites exhibits a maximum at 462 nm when the excitation wavelength used to record the photoluminescence spectrum is 350 nm. Anisotropy (r) and bond angle (ϕ) of macromolecular compounds, adsorbed on the surface of inorganic particles, can be calculated using anisotropic photoluminescence with the following formulas:

$$r = (I_{vv} - GI_{vH})/(Ivv + 2GI_{vH})$$
$$r = 0.4[(3\cos^2\phi - 1)/2],$$

where I_{vH} corresponds to the photoluminescence intensity when the polarizer is positioned vertically for excitation and horizontally for emission in the spectrophotometer; $G = I_{HV}/I_{HH}$, where I_{HV} corresponds to the light intensity measured when the polarizer is positioned horizontally for excitation and the polarizer is positioned vertically for emission.

The photoluminescence spectra in polarized light of composites with $BaTiO_3$ nanoparticles having concentrations of 12 wt.%, 25 wt.%, and 35 wt.%, respectively, are presented in Figure 2. In Table 1, the values of the intensity of the photoluminescence spectra (PL) are presented, taking into account the way of mounting the polarizers for excitation and emission. According to Table 1, the gradual decrease in the intensity of the PL spectra of TPU:TPO, regardless of the way of mounting the polarizers, as the concentration of inorganic nanoparticles increases, indicates the role of $BaTiO_3$ as quenching agent of polymeric matrix's PL. This result is in agreement with our previous paper [34]. Considering the I_{VV}, I_{VH}, I_{HV}, and I_{VV} values experimentally obtained, which are presented in Table 1, the r and ϕ values in the case of: (i) TPU:TPO 2:1 are equal to 0.302 and 23.70; (ii) TPU:TPO 2:1 + 12% $BaTiO_3$ are equal to 0.0862 and 46.30; (iii) TPU:TPO 2:1 + 25% $BaTiO_3$ equal to

0.078 and 47.10; and (iv) TPU:TPO 2:1 + 35% $BaTiO_3$ equal to 0.029 and 51.80, respectively. In regard to the anisotropy, the composite with 12% $BaTiO_3$ presents the maximum value and is explained by a more homogenous dispersion of particles with different spatial orientations, which is a phenomenon expected for homogenous dispersions with low quantities of particles. In regard to the bond angle, the maximum value is reached by the composite with 35% $BaTiO_3$, which is explained by the composite architecture and will be further analyzed by SEM optical scanning microscopy. The value of r is less than 0.4, a fact that indicates that the excitation and emission transition dipoles are not aligned, which explains the complex dielectric polarization presented further in the paper. This aspect originates in the exchange reaction of the repeating units of the TPU-type polymer with $BaTiO_3$ [33] because it is expected for the dipole of TPU to make the main contribution to both interfacial and dipolar polarizations.

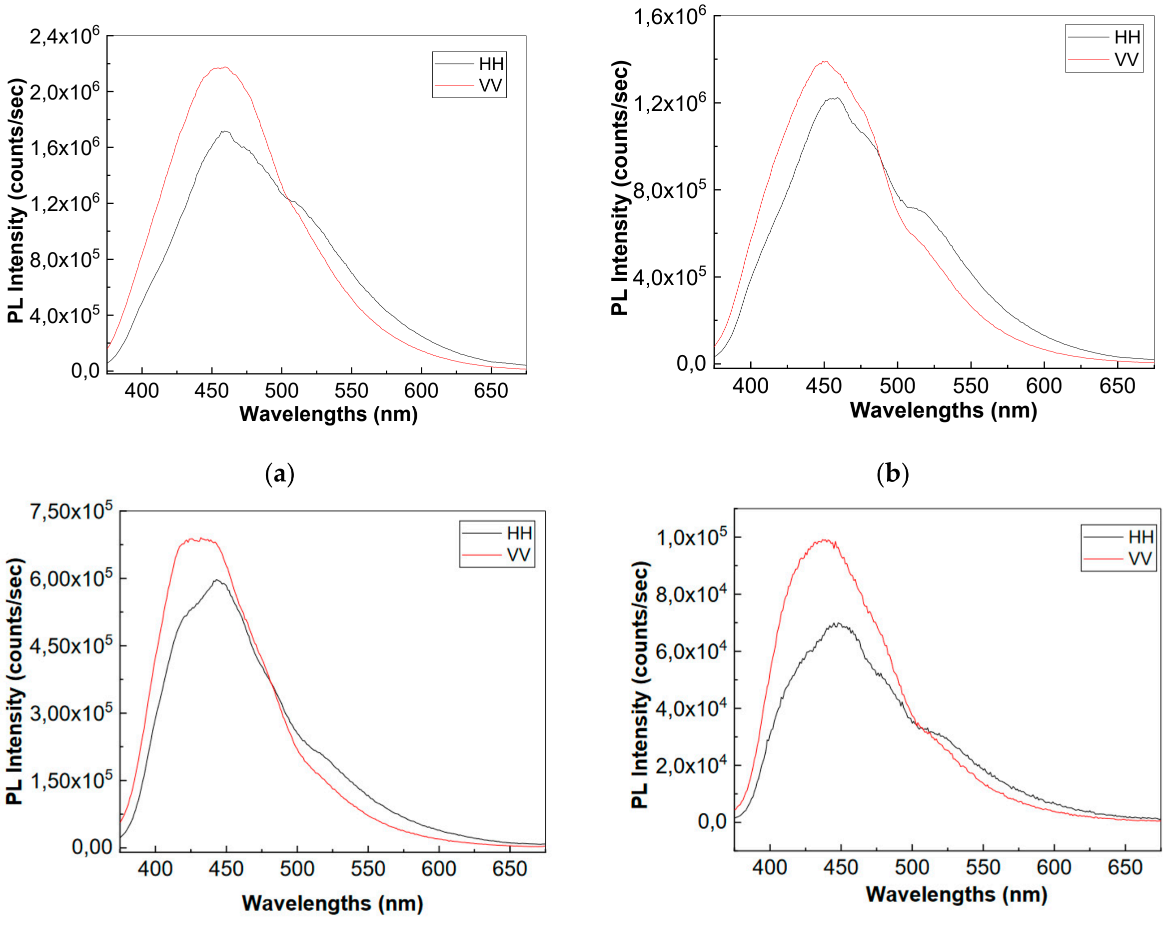

(**a**) (**b**)

(**c**) (**d**)

Figure 2. Photoluminescence spectra in polarized light of the following: (**a**) TPU:TPO 2:1; (**b**) TPU:TPO 2:1 + 12% $BaTiO_3$, (**c**) TPU:TPO 2:1 + 25% $BaTiO_3$, and (**d**) TPU:TPO 2:1 + 35% $BaTiO_3$.

Table 1. I_{HH}, I_{HV}, I_{VH}, and I_{VV} values of the PL spectra of the TPO:TPU 2:1 compound and its composites with $BaTiO_3$ nanoparticles.

Compound	I_{HH} (counts/s)	I_{HV} (counts/s)	I_{VH} (counts/s)	I_{VV} (counts/s)
TPO:TPU 2:1	1.72×10^6	1.8×10^6	1.78×10^6	2.17×10^6
TPO:TPU 2:1 + 12% $BaTiO_3$	1.22×10^5	1.17×10^5	1.13×10^5	1.39×10^5
TPO:TPU 2:1 + 25% $BaTiO_3$	5.96×10^5	6.08×10^5	5.38×10^5	6.87×10^5
TPO:TPU 2:1 + 35% $BaTiO_3$	6.99×10^4	8.22×10^4	7.73×10^4	9.91×10^4

3.2. SEM Structural Analyses

SEM structural analyses were performed to highlight the degree of homogeneity of the obtained materials. These analyses were performed on the field emission source and focused ion beam scanning electron microscope. The average dimension of BaTiO3 parti-cles was about 1 µm, (Figure 3 a,b).

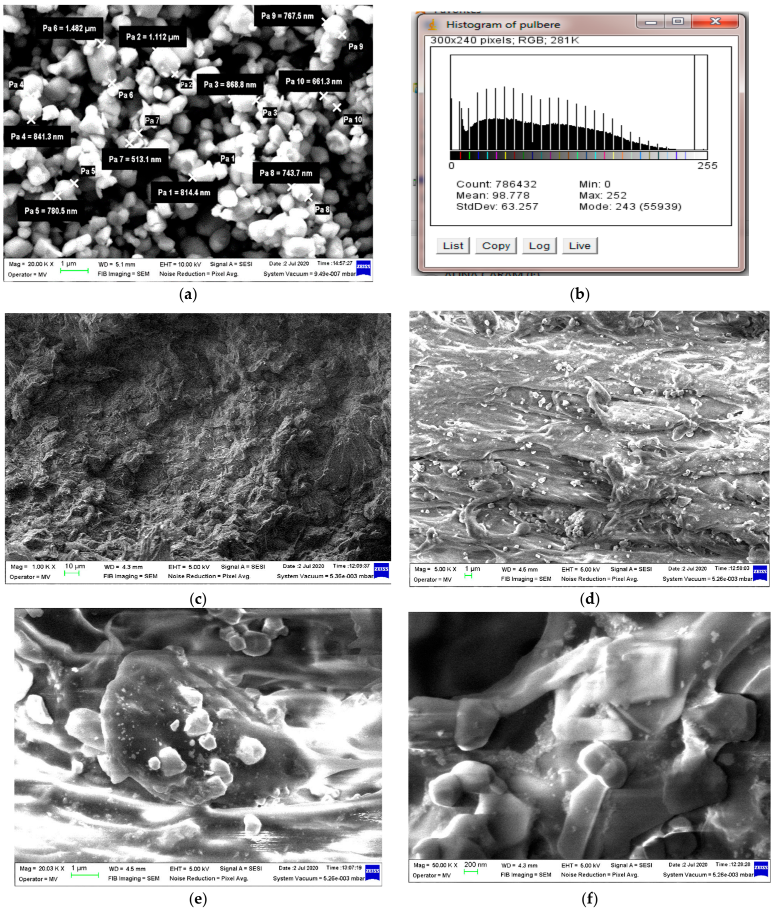

Count: 786432 Min: 0
Mean: 98.778 Max: 252
StdDev: 63.257 Mode: 243 (55939)

(**a**) (**b**) (**c**) (**d**) (**e**) (**f**)

Figure 3. Micrograph of $BaTiO_3$ with 50,000× magnification (**a**), and related $BaTiO_3$ particle histogram (**b**); Micrographs of composite with 35% $BaTiO_3$ with magnifications (**c**) 1000×, (**d**) 5000×, (**e**) 20,000× and (**f**) 50,000×.

It can be generally seen that the filler is well homogenized within the polymer structure with a uniform dispersion, Figure 3c–f. Though slight agglomerations of the filler particles may appear, which may induce a slight inhomogeneity; however, in small, negligible areas, this aspect can be remediated by a longer mixing time and homogenizing the $BaTiO_3$ powder at a higher powder content.

3.3. Atomic Force Microscopy (AFM) Analysis

Basically, the experimental models made of polymer composite materials are very difficult to withstand atomic force microscopy tests because, for the AFM microscopy tests, a surface with nanometric roughness (preferably approx. 50 nm) is required. The roughness was determined as the average value between three measurements performed on the same sample in its central area at a focal distance of 90 µm. Roughness was obtained in the range of 75–450 nm, which gives some minor errors under the circumstances presented as above. In Figure 4, an AFM microscopy image is presented for the composite with 35% $BaTiO_3$, which is considered more relevant due to the higher content of powder, and the resulted roughness was below 100 nm. The roughness of such composites may be relevant in the case of producing filaments for 3D printing purposes, and the obtained value is in line with the requirements for such applications.

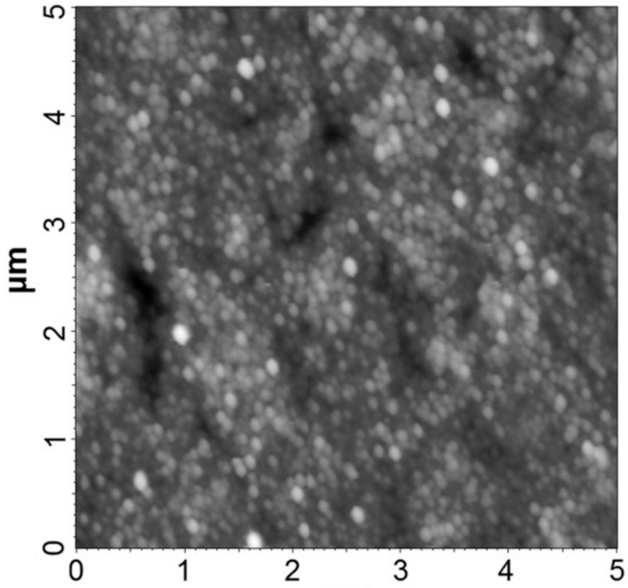

Figure 4. AFM microscopy image of the composite with 30% $BaTiO_3$.

A quasi-uniform distribution of the particles on the surface of the composite material can be observed as a whole, eventually depending on the size of the particle and its concentration. In the case of inorganic powders ($BaTiO_3$), the effect appears more blurred, but there is also a subjective cause given by the optical contract of such powders. These preliminary conclusions from the AFM analysis can be clearly correlated with those from the SEM analysis.

3.4. Dielectric Tests

The dielectric characteristics of the composite materials are presented in Figures 5 and 6, for the blended matrix the thermoplastic composite with 12% $BaTiO_3$, and the thermoplastic composite with 35% $BaTiO_3$.

It is obvious that the addition of $BaTiO_3$ dramatically increases the dielectric permittivity, from about 3.5 of the matrix towards about 13 for an addition of 12% $BaTiO_3$ and finally towards about 28 for an addition of 35% $BaTiO_3$ at 10 Hz frequency. With the increase in frequency, all permittivity values are decreasing, with the largest decrease being for the composite with the higher content of $BaTiO_3$.

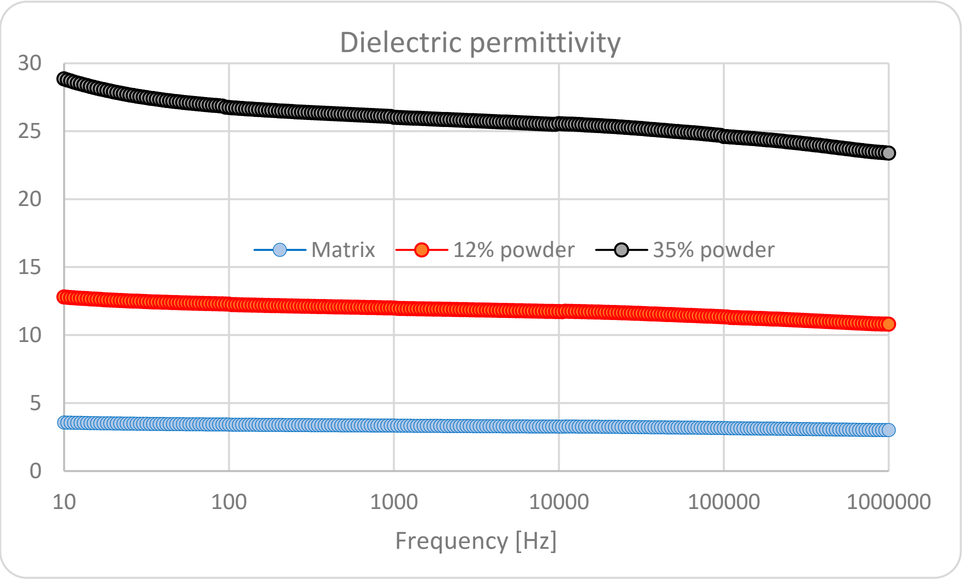

Figure 5. Relative permittivity.

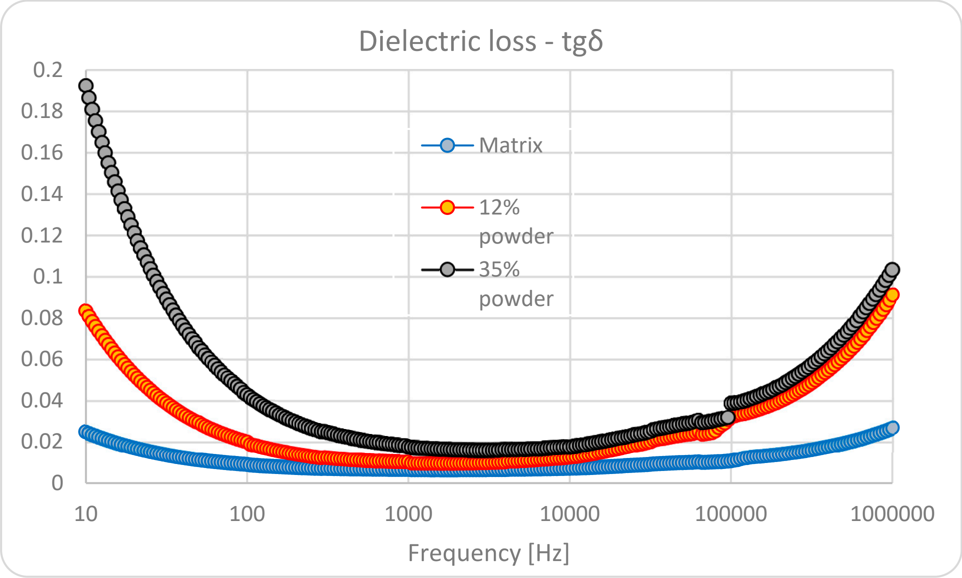

Figure 6. Dielectric loss (Tg Delta).

In regard to the dielectric loss, at lower frequencies, the effect of interfacial polarization is detrimental, with a very significant value for an addition of 35% $BaTiO_3$. Herewith, we speak about three types of complex interfaces: one related to blended matrix and the others related to polymers and $BaTiO_3$. That is why we can notice an increased value at low frequencies for blended matrixes as well. At medium frequencies in the kHz domain, the difference is not so relevant, but at higher frequencies, over 50 kHz, the dielectric polarization effect is obvious, with relevant higher values for the highest content of $BaTiO_3$.

On the other hand, when analyzing the dielectric loss characteristics of the samples with $BaTiO_3$, an interesting variation effect with frequency may be noticed in the vicinity of the 100 kHz frequency domain. Here we can speak about a saltation of the tgδ characteristic, correlated with the architecture of composites, which induces an additional ionic-dipolar conjugated polarization, e.g., a displacement due to the balance between the resonance and anti-resonance frequencies. Such phenomena explain the use of such composites with piezoelectric powders as resonators/filters for tailored applications in the radiofrequency electronic field. In our case, even if such phenomena occur, the low quantity of $BaTiO_3$

powder cannot make the respective composites relevant candidates for such electronic applications. But this phenomenon can be further exploited in relation to 3D printing in order to achieve a quasi-4D effect with frequency. Such an effect may become useful when collecting electrical signals from 3D printable flexible piezoelectric devices to be obtained from such composites for energy harvesting purposes, mainly when they are used for biomedical applications—communications at MHz frequencies.

As long as for reasonable piezoelectric effects the concordance of the highest value of three parameters is needed, i.e., the content of $BaTiO_3$, dielectric permittivity, and dielectric loss at lower frequencies, we may admit that the most relevant sample is the one with 35% $BaTiO_3$, which will be analyzed with priority as follows.

3.5. Piezoelectric Characteristics

The piezoelectric characteristics for the composite with 35% $BaTiO_3$ without preliminary activation under a tailored electric field are presented in Figure 7 at three different frequencies. The respective frequencies were chosen taking into account the potential use of such composites for 3D printable flexible piezoelectric devices with energy harvesting features for biomedical applications, i.e., in conjunction with wearable electronics or intelligent prosthesis.

The values in each table are specific for the hysteresis curve obtained at different frequencies and clearly indicate an alternating current ferroelectricity of the composite.

The values expressed as positive P_{max} and negative P_{max} show the symmetry of the curve at the maximum polarization level. The values expressed as negative Pr and positive Pr show a small difference due to the fact that the hysteresis curves do not fully close, but this aspect is characteristic of $BaTiO_3$. Vc values depend on applied voltage and can be further correlated with the size of the granules, but this is not relevant in our case. Depending on the voltage applied to the samples, different hysteresis curves are obtained, and the maximum polarization is correlated with the applied voltage values. By increasing the frequency value of the applied voltage, a flatter curve is obtained. The angle of inclination of the curve depends on the concentration of the inorganic powder; e.g., an angle of about 45° is observed at 10 Hz for the addition of 35% $BaTiO_3$.

The hysteresis losses, the most relevant parameters for piezoelectric analysis, are correlated with the volume of the hysteresis curve and expressed by W_{loss}. The ideal curve for analyzing the piezoelectric features of the composite is the one at 0.1 Hz, where the W_{loss} value reaches 2556.79 $\mu J/cm^2$.

The results are remarkable for a material without preliminary activation under a tailored electric field, and the relatively high polarization at low frequencies is in line with body reactions, which can be used as a source of energy harvesting via the piezoelectric effect. Further, the features of such composites with activation under a tailored electric field will be presented after the related piezoelectric devices are obtained by 3D printing technology from the filaments achieved with composites with $BaTiO_3$.

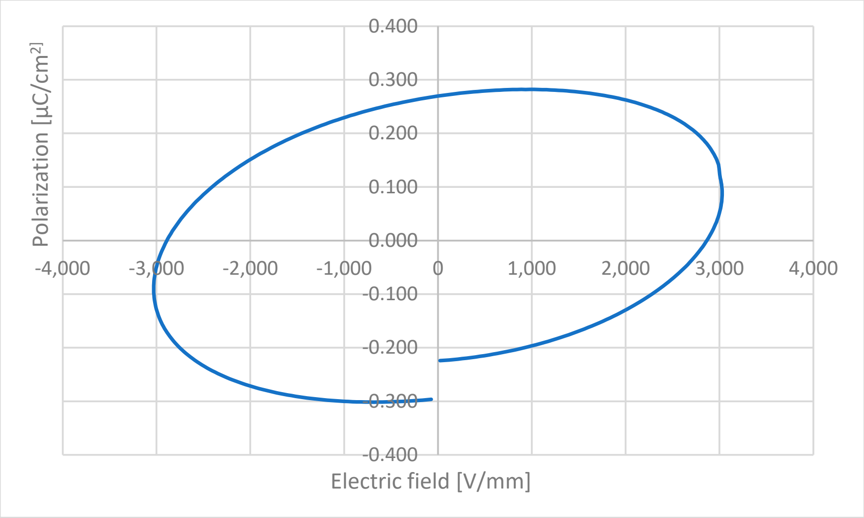

Composite with 35%$BaTiO_3$
Surface [mm^2]: 484
Thickness [mm]: 1
Intensity of current [μA]: 10
Electric field [V/mm]: 3000 V
Frequency [Hz]: 0.1
Vc$^+$ [V]: 2866.51
Vc$^-$ [V]: −2888.91
Pr$^+$ [μC/cm^2]: 0.26942
Pr$^-$ [μC/cm^2]: −0.296397
P_{max+} [μC/cm^2]: 0.0886311
P_{max-} [μC/cm^2]: −0.0886311
W_{loss} [μJ/cm^2]: 2556.79

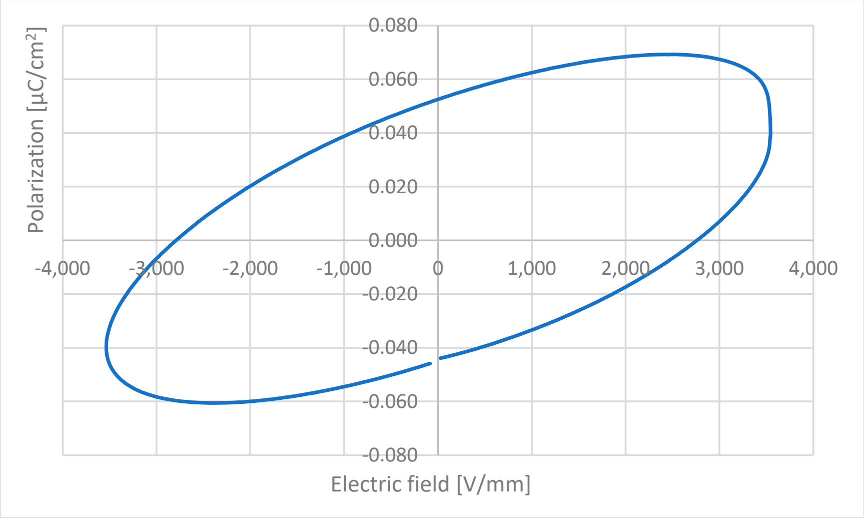

Composite with 35%$BaTiO_3$
Surface [mm^2]: 484
Thickness [mm]: 1
Intensity of current [μA]: 10
Electric field [V/mm]: 3500 V

Figure 7. *Cont.*

Frequency [Hz]: 1
Vc^+ [V]: 2760.88
Vc^- [V]: −2791.09
Pr^+ [μC/cm^2]: 0.0524941
Pr^- [μC/cm^2]: −0.0458722
P_{max+} [μC/cm^2]: 0.0394723
P_{max-} [μC/cm^2]: −0.0394723
W_{loss} [μJ/cm^2]: 557.933

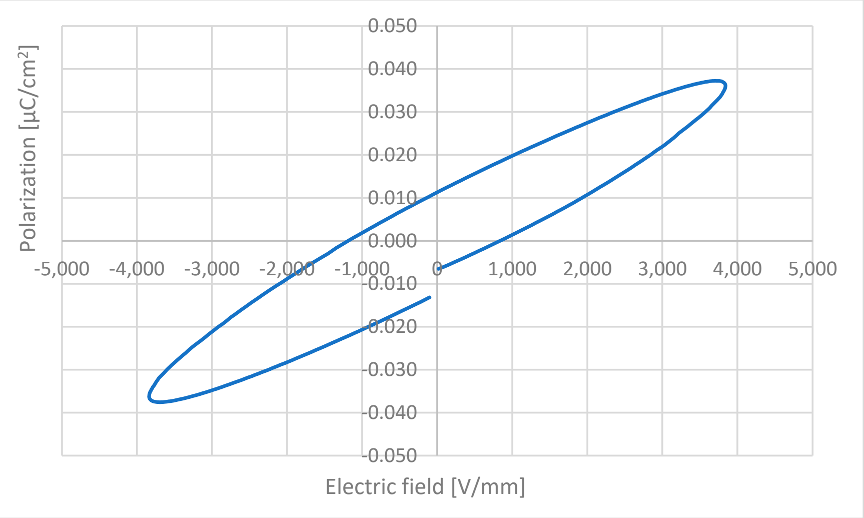

Composite with 35%$BaTiO_3$
Surface [mm^2]: 484
Thickness [mm]: 1
Intensity of current [μA]: 10
Electric field [V/mm]: 3800 V
Frequency [Hz]: 10
Vc^+ [V]: 838.496
Vc^- [V]: −1183.72
Pr^+ [μC/cm^2]: 0.011266
Pr^- [μC/cm^2]: −0.0131741
P_{max+} [μC/cm^2]: 0.0361097
P_{max-} [μC/cm^2]: −0.0361097
W_{loss} [μJ/cm^2]: 126.353

Figure 7. Polarization characteristics at 0.1, 1, and 10 Hz.

3.6. Thermal Stability

TG-DSC (Differential Scanning Calorimetry) independently measures the heat flow rates between a sample and a reference subjected to the same temperature program (isothermal or dynamic). The difference in heat flow between the sample and the reference, which are heated (or cooled) over a certain temperature range, is then determined, and this difference is plotted as a function of temperature. The direction of the thermal flow towards the DSC sensor is well defined and reproducible [38]. The results for the composite with 35% $BaTiO_3$ are presented in Figure 8.

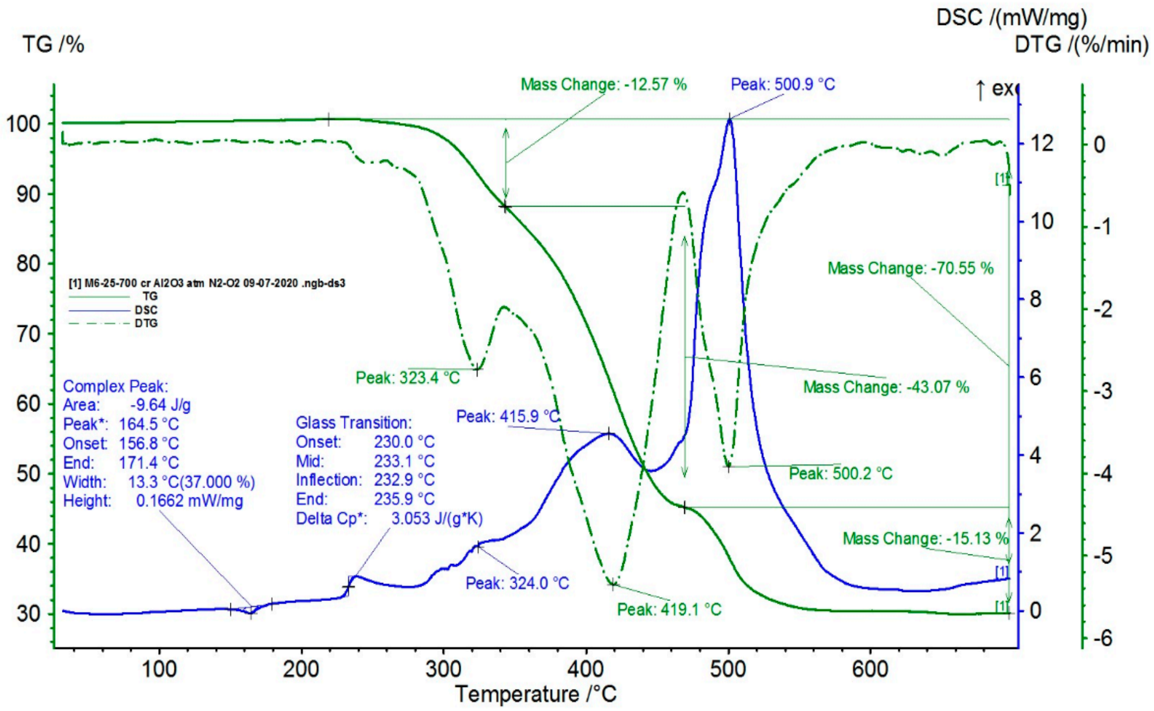

Figure 8. TG and DSC variation curves for the sample with 35% $BaTiO_3$.

For such composite material, in addition to glass transition processes and chemical oxidation processes, there is also a first-order phase transformation process (melting) due to the TPO (PP) melting process. The maximum melting temperature is around 170 °C.

4. Development of 3D Printed Flexible Piezoelectric Structures

The development of flexible and elastic piezoelectric energy capture devices based on customized composite elastomers and 3D printing technology involved modeling by fused deposition of composite materials in the form of filaments. The preliminary tests for making specific filaments for 3D printing with a diameter of 1.75 mm were carried out on a small laboratory extruder (Figure 9) from extruded pellets. It is obvious that by an extruding process pellets from thermoplastic composites may be manufactured, even if the inorganic powder content goes towards 80–90%, but it is also well known that the manufacture of rigorous filament in terms of dimeter tolerance and reasonable length from thermoplastic composites with more than 10–15% inorganic powders is extremely difficult, mainly due to the fragility of the filament, which in many cases breaks itself under the reeling operation. On the other hand, at higher powder contents, the filament homogeneity can suffer important changes under cooling operations due to dilatation, exfoliation, or delamination processes. The purpose of the experiment was to develop the optimal extrusion technology, i.e., to account for the optimal temperatures and the speed of pulling the filament to make filaments with rigorously constant dimensions at higher quantities of inorganic powders.

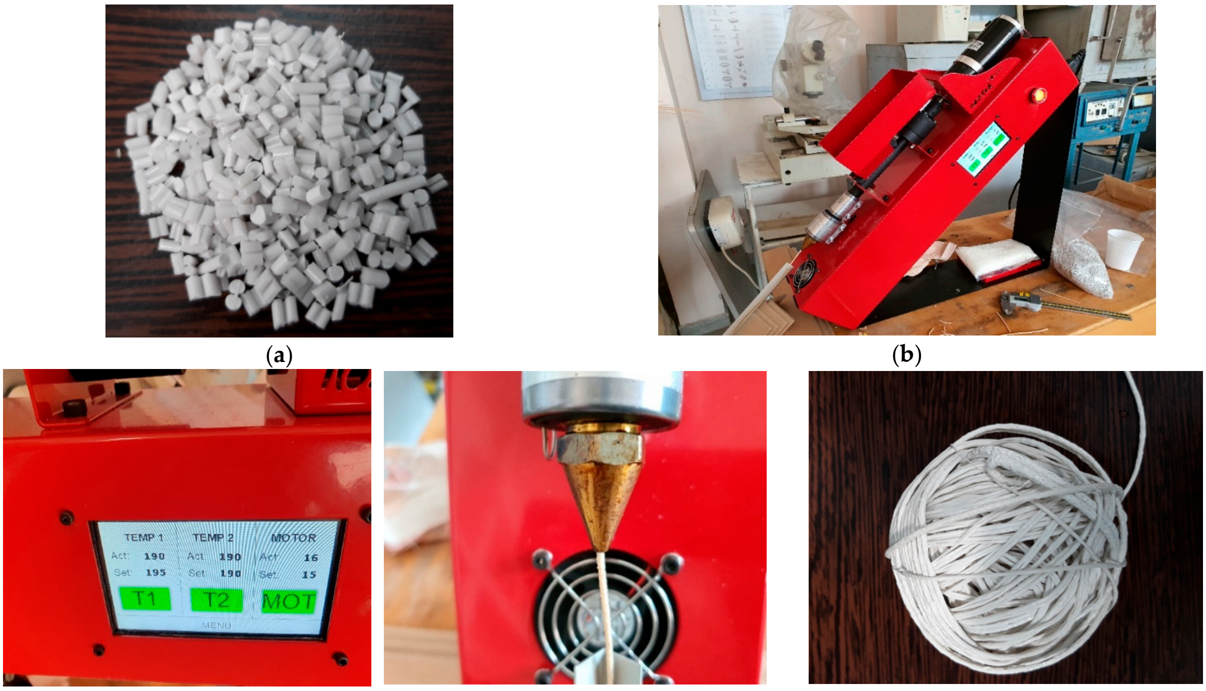

(**a**) (**b**)

(**c**) (**d**) (**e**)

Figure 9. Specific filaments for 3D printing with a diameter of 1.75 mm from the composite pellets with 35% $BaTiO_3$; (**a**) pellets; (**b**) laboratory extruder; (**c**) temperature control; (**d**) filament generation through the extruder head; (**e**) filament reel.

In this context, adequate thermal control of the extruder was important, with the used temperature being between 180 and 190 °C and more composite recipes being tested [34]. Finally, the filament from the composite material with 35% $BaTiO_3$ resulting from the extrusion operation was elastic, mainly due to the innovative addition of TPO, even close to the elasticity of rubber, but it provided good features to be used for 3D printing applications as well and presented a reasonable variation in a maximum diameter of 10%. The optimal temperatures were around 190 °C with a pulling speed of 15 cm/min. The filament was homogenous, with a smooth surface and no mechanical defects, and had reasonable winding features (Figure 9).

The preliminary 3D printing tests for the realization of structural models were performed using an adapted laboratory 3D thermal printer with a maximum working surface of 120 × 120 mm^2. Other parameters taken into account for printing the models were the viscosity and density of the topical filament. Preliminary testing of the 3D printing parameters is listed in Table 2. A comparison was made between the experimental filaments and the commercial ScotchBlue™ Original Painter's Tape-type PLA filaments and revealed similarities and compatibility by testing the successive depositions of the two filaments; hence, the base deposition support can be made with the commercial one (Figure 10).

Table 2. Setting the parameters of the laboratory 3D thermal printer.

Parameter	Grid
Layer height	0.2 mm
Angle of deposition	90
Deposit density	100%
Print speed	15 mm/s
Nozzle diameter	0.4 mm
Base temperature	60 °C
Extrusion temperature	190 °C
Turns	2
MULTIPLIER	1.2

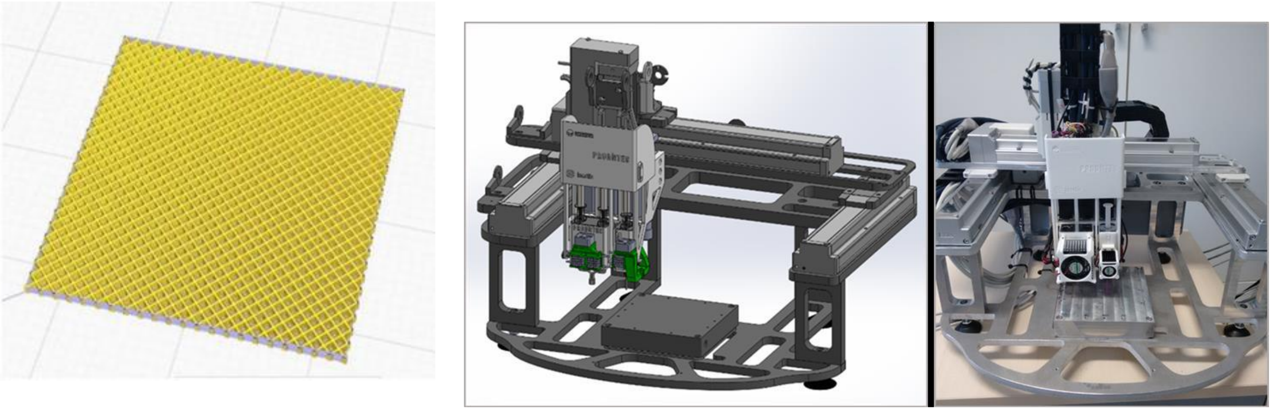
(**a**) (**b**) (**c**)

Figure 10. Three-dimensional printed experimental structural model and the dedicated printer; (**a**) rectangular parallelepiped mesh; (**b**,**c**) images of the tailored printer (face and side view).

Using the Solid Works CAD program or other specialized CAD software, 3D models can be designed, e.g., one of the rectangular parallelepiped network types, which are in fact a 25 × 25 × 1 mm mesh type. After the creation of the CAD model, it is transferred to the laboratory 3D thermal printer software. The experimental structural model is presented in Figure 10.

It was shown that the deposition of composite filament with 35% $BaTiO_3$ was a convenient process with no clogging of the nozzle, no problems with multilayer deposition, and no 3D printing defects. In the end, very good precision structures were obtained experimentally by adjusting the deposition parameters. Even precision mesh structures were made at an angle of 90 compared to the initially planned one of 45 and at deposition densities higher than 50% (Figure 11), to be further tested as basic devices for energy harvesting. As a final comment on this chapter, we can estimate that the mesh structures manufactured by thermal printing provide similar features as homologue structures described in the literature, e.g., in [39], but these are achieved by less productive and more complicated and expensive processes, i.e., stereolithography. Therefore, the advantages of the composite recipe and technology for 3D printing described in this paper are obvious.

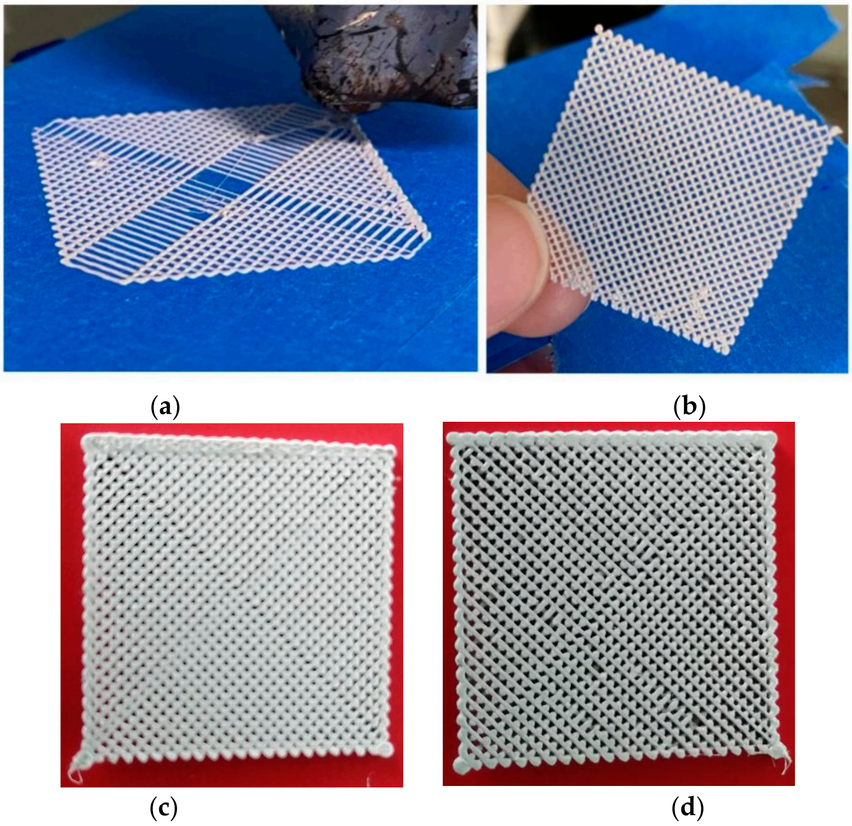
(**a**) (**b**) (**c**) (**d**)

Figure 11. Three-dimensional printed devices for energy harvesting as precision mesh structures; (**a**,**b**) tests with progressive deposition of filament with different angles; (**c**,**d**) final mesh structures with different densities.

5. Testing the Energy Harvesting Features of 3D Printed Devices

For the development and integration of the signal processing circuits and the demonstration of the functionality of the energy harvesting features of 3D printed devices, a special test stand was developed, as in Figure 12, to produce tailored vibrations to activate the devices—here with functionality as piezoelectric sensors. To realize sensorial features, the mesh structures are covered on both sides with self-adhesive copper strips in order to collect the electrical charges obtained by piezoelectric phenomena.

To generate the vibrations, specialized equipment (2) with two windings was used (composed of a fixed part and a mobile part, the mobile part being connected to the fixed one by means of an elastic mechanical suspension), supplied with a constant voltage of 24 V dc from the direct voltage source (5) and also with alternating voltage from the autotransformer (6). The vibration force is proportional to the currents absorbed by the two windings, according to Equation (1):

$$F_{din} = kI_{cc}I_{ca} \quad (1)$$

The vibration frequency was up to 50 Hz, and their amplitude was proportional to F_{din}. When the position of the cursor of the autotransformer is changed, the increase in the alternating voltage applied to the device (2) is achieved, and the mobile part (on which the sensor (1) is placed) will start to vibrate, and thus a signal will be generated at the two terminals of the self-adhesive copper strips of the sensor. Further, this signal is used to charge a capacitor with the role of an energy harvester, and if a resistor R is connected to the output of the sensor, the effective value U of the voltage of the oscillations generated by the sensor can be measured, with the power value to be determined with Equation (2):

$$P = U^2/R \quad (2)$$

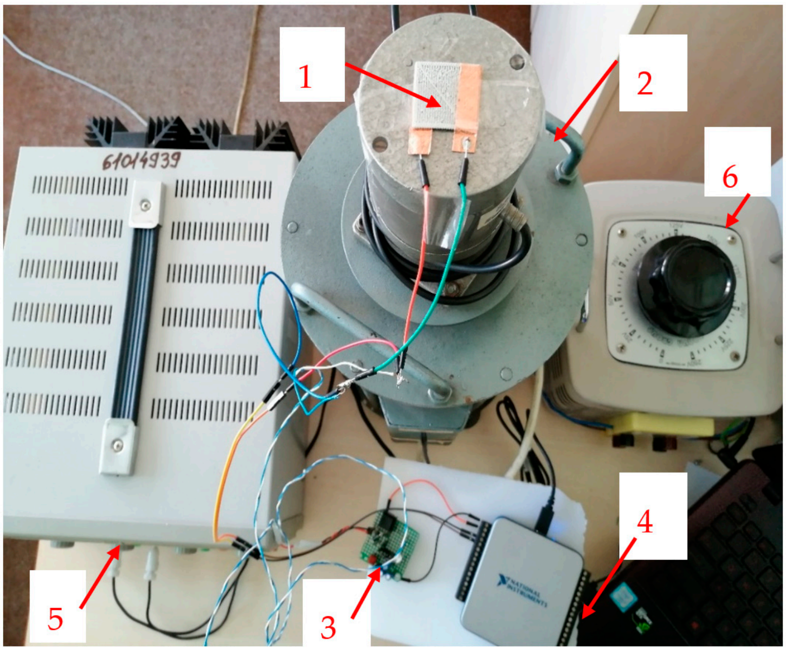

Figure 12. The test stand used for the production and acquisition of the signal includes the following: 1—device/sensor; 2—vibration creation equipment; 3—capacitor charging circuit; 4—NI USB acquisition board—6001; 5—direct current source (constant voltage 24 V); 6—autotransformer (alternating voltage supply)—for vibration increase/decrease regime.

In our case, a very common electronic processing module, as presented in Figure 13, was used to collect the energy of the oscillations generated by the sensor and identified in Figure 12 as 3—capacitor charging circuit.

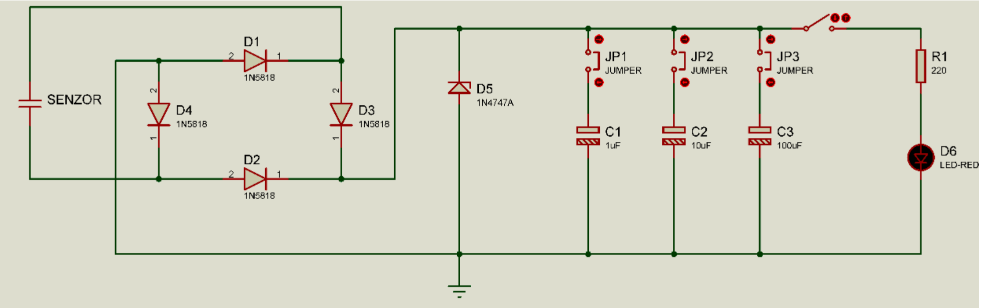

Figure 13. The circuit for acquiring and rectifying the voltage from the sensor.

The output from the sensor is applied to a rectifier bridge made with 4 Shottky diodes of type 1N5818 in order to achieve a continuous charge process only and avoid the reverse bias effect.

The time variation of the voltage $u(t)$ on the capacitor is given by Equation (3), where U is the voltage applied to the capacitor resulting from the rectification and R is the equivalent load resistance of the capacitor.

$$u(t) = U\left(1 - e^{-\frac{t}{RC_H}}\right) \tag{3}$$

The maximum energy E accumulated in the capacitor to which the voltage U is applied is given by Equation (4).

$$E = \frac{C_H U^2}{2} \tag{4}$$

The analog signals when increasing the voltage of the vibration device, i.e., the vibration amplitude level increases, are presented in Figure 14. The signal on the sensor is represented by red oscillations, and the signal on the charging capacitor by white oscillations. The scale is related to signal period, and so the interpretation of the results is difficult without analyzing the real charging phenomenon.

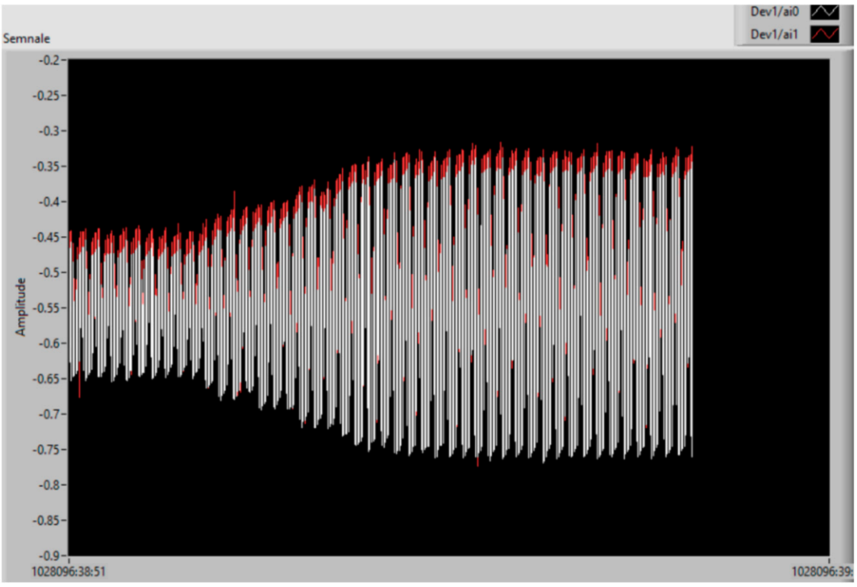

Figure 14. The analog signals by increasing the voltage/vibration level: sensor (red); charging capacitor (white).

That is why intelligent signal processing was embedded by using a virtual instrument (VI) developed under the LabVIEW graphical programming environment [40], briefly presented in Figure 15. After the signal has been acquired with the acquisition board, it is digitized and then transferred to the PC via the USB port. From the USB port, the acquired signal is then processed and displayed using the VI. Block 1 is the data acquisition board setup in subVI. The measured quantity will be set; in our case, it will be "AI Voltage", i.e., the analog voltage. Block 2 is a block used to open a signal acquisition "task". If this subVI is not used, it is possible for the application to start an unsynchronized signal acquisition by itself. If the "DAQmx Start Task VI" subVI and the "DAQmx Stop Task VI" subVI are not used when the "DAQmx Read VI" subVI or the "DAQmx Write VI" subVI are used multiple times (how it would be in a loop) and the acquisition starts and stops repeatedly, starting and stopping a purchase repeatedly reduces app performance. For a continuous acquisition of the signal, the acquisition block (3) is inserted into a "WHILE" loop (9) that will run until an event occurs that will interrupt the running of this loop, either an error or pressing the "STOP" button.

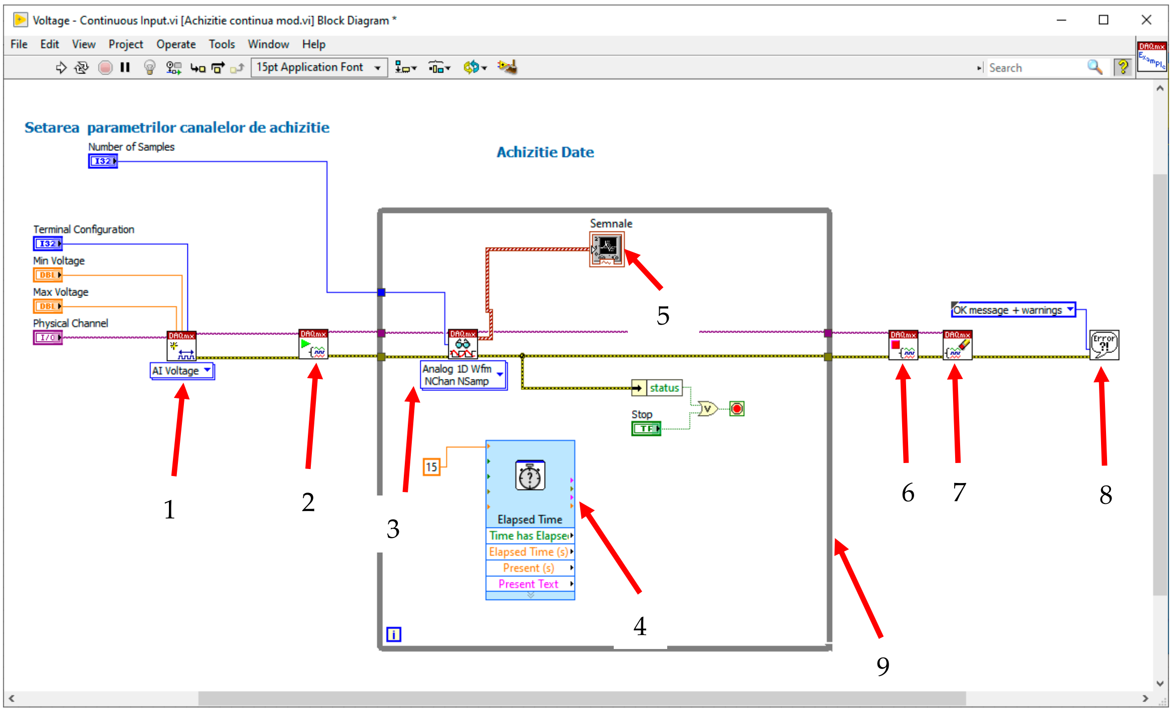

Figure 15. Block diagram of the instrument.

Block 3 is the actual signal acquisition block and has been configured for the acquisition of analog signals. Because we are acquiring signals on several channels, "Multiple Channels" will be selected. Block (4) is a timer used to synchronize the acquisition with the display. After acquiring the signals, these vectors in which the values are stored are displayed value by value on display 5, after which these values are interpolated. These values will be presented on the Y-axis vs. the X-axis, which will show the effective time.

SubVI (6) is used to close the "task" and is opened by block (2). Blocks (2) and (6) will always be used together. The SubVI (7) will clear all values stored in the 1D-type variables to prepare the VI for the next acquisition. The SubVI (8) will display an error message if errors occur. A sample count of 100 has been set, so we will store the values in a 1D vector variable.

The front panel of the signal acquisition instrument was designed to simulate different functional regimes of the energy harvester, i.e., the resistor value, the time, the range (limits) of the input voltage, and the number of signal samples to be processed vs. time.

Two signals are acquired, one directly from the sensor on channel A1 (the waveform is red) and the signal from the capacitors on channel A0 (the waveform is white), the latter being displayed separately for an analysis vs. charging time and charging regime.

The first experiments are performed with the sensor without a preliminary activation with an electric field.

The signals from the sensor output and the charging voltage of the capacitor are shown in Figure 16, where the increase in the amplitude of the signals and the energy of the capacitor according to the value of the applied alternating voltage are presented. The charging of the capacitor starts after the vibrations reach a minimum level, i.e., after a voltage of min. 145 V (case 2) is applied. That is why, in case 1, at 100 V, no charge is noticed. When the voltage exceeds 145 V (case 3), the amplitude of charge on the capacitor increases.

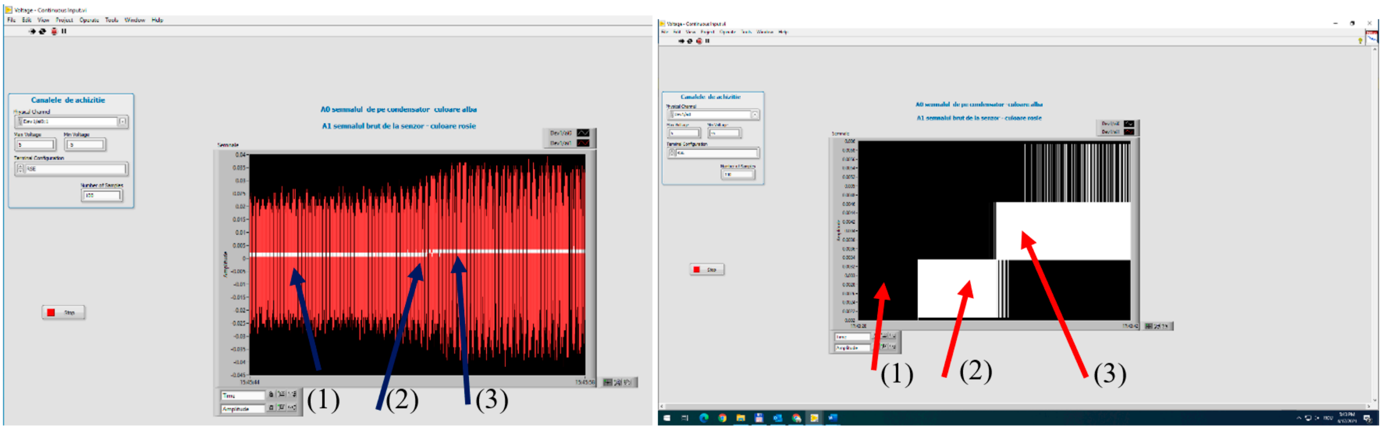

(**a**) (**b**)

Figure 16. Increasing vibration level at the test equipment (**a**) and the voltage/the energy level of the capacitor (**b**), for: (1) 100 V; (2) 145 V; (3) 210 V—voltages applied to the test equipment.

In Figure 17, this process is more explicitly explained, where in Figure 17b, 1–represents the individual charging voltage levels, and 2–represents the average charging characteristic of the capacitor. When associating the digital signal on the capacitor with the charging characteristic. Here, 1 represents the instant charging values from the sensor (green), and 2 represents the cumulative charging of the capacitor (red curve).

(**a**)

Figure 17. *Cont.*

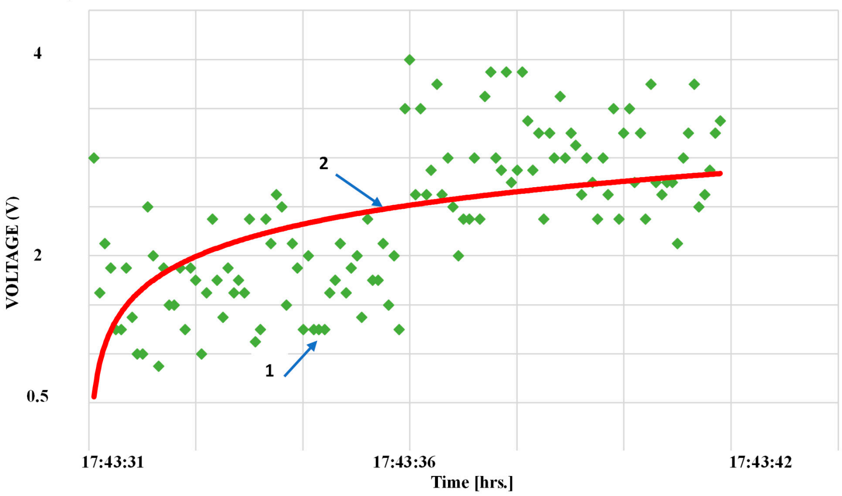

(**b**)

Figure 17. Digital signal on the capacitor (**a**) and charging characteristic (**b**), for the sensor without activation.

As seen in Figure 17, a minimum charging voltage is needed for the process to start, associated with the amplitude of the vibrations corresponding to 145 V, as explained above. The transient regime depends on the signal applied to the capacitor, and so the capacitor charges exponentially until it is theoretically close to full charge, then it will charge more and more slowly until it is fully charged. The charging characteristic shows the relatively long period of transient regime of capacitor charge, in this case 11 s for the sensor without electrical activation.

The following experiments are made with the sensor after the activation by the electric field. The sensor was activated by applying to its surfaces a continuous voltage of 31.6 V for 72 h to ensure saturation of the hysteresis effect.

Figure 16 shows the evolution of the signal on the capacitor when the vibrations increase.

Here also, the charging of the capacitor starts after the vibrations reach a minimum level, but much earlier compared to a non-activated sensor, i.e., after a voltage of min. 85 V is applied (Figure 18). In this case, even the transient regime is minimal, and the response to the increase in voltage in steps is immediate, as shown by the charging characteristic in Figure 19, where the voltage on the capacitor immediately increases to 5.5 V. In this specified case of excitation in 4 steps, the capacitor reaches a state close to full charge after about 13 s, e.g., 9 V.

At this point in the studies, the feature of 'energy harvesting' mode was demonstrated. By preliminary activating the sensor in the electric field, the value of the electric signal generated by the sensor increases, the efficiency of the sensor is higher, and the charging of the capacitor is faster.

An interesting aspect occurs when comparing the non-activated and activated sensors when the vibrations decrease.

In the case of a non-activated sensor, when the applied voltage goes below 140 V, the sensor becomes passive, and the capacitor is not charged any more. However, in the case of an activated sensor, the charging of the capacitor continues even if the voltage is decreased to 70 V, until saturation (Figure 20) (when the black area becomes compact). In such cases, we can also speak about a mechanical hysteresis in the behavior of electrically activated matrix sensors. The conclusion is also sustained by analyzing the charging characteristic when vibrations decrease (Figure 21), where the charging of the capacitor continues until saturation. Here we practically reached the saturation charge of the capacitor, e.g., 11 V, even under the conditions when the vibrations decreased up to the limit of 1 V on the sensor.

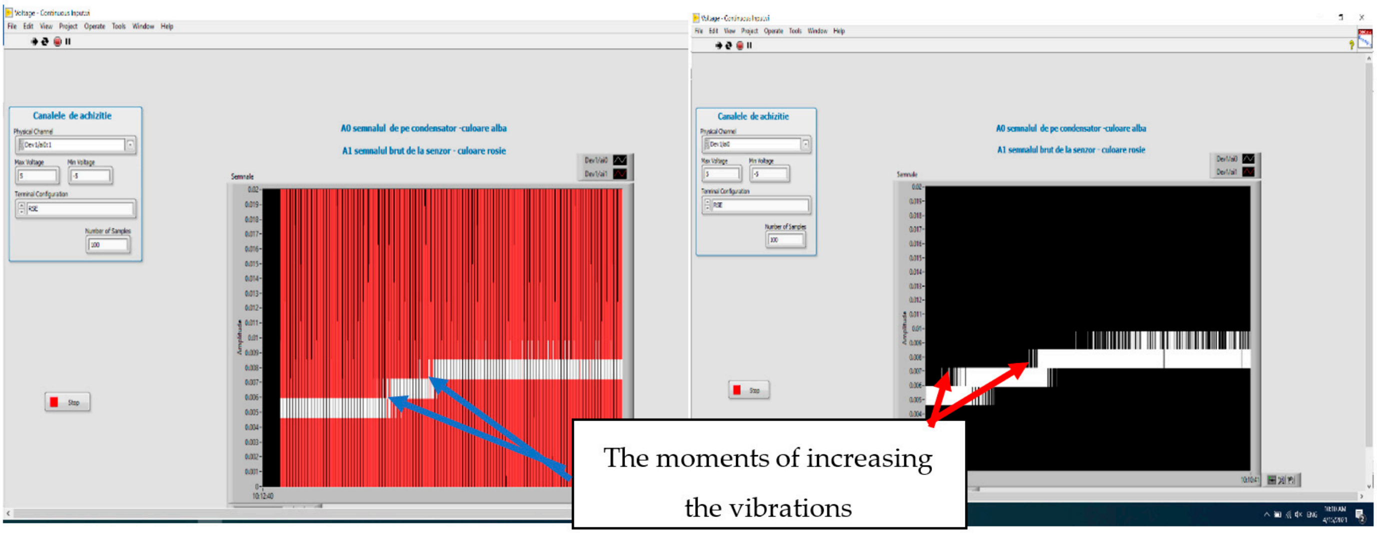

(**a**) (**b**)

Figure 18. Vibration variation of the test equipment (**a**) and its influence upon the voltage on the capacitor (**b**), when the vibration increases on the activated sensor.

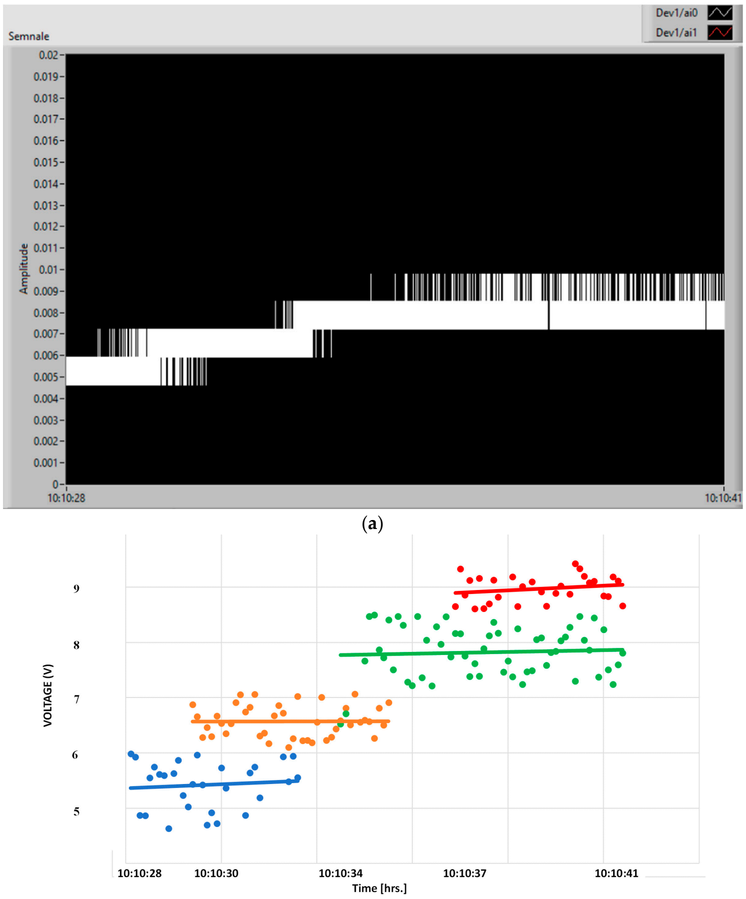

(**a**)

(**b**)

Figure 19. Digital signal on the capacitor (**a**) and charging characteristic (**b**) for the activated sensor.

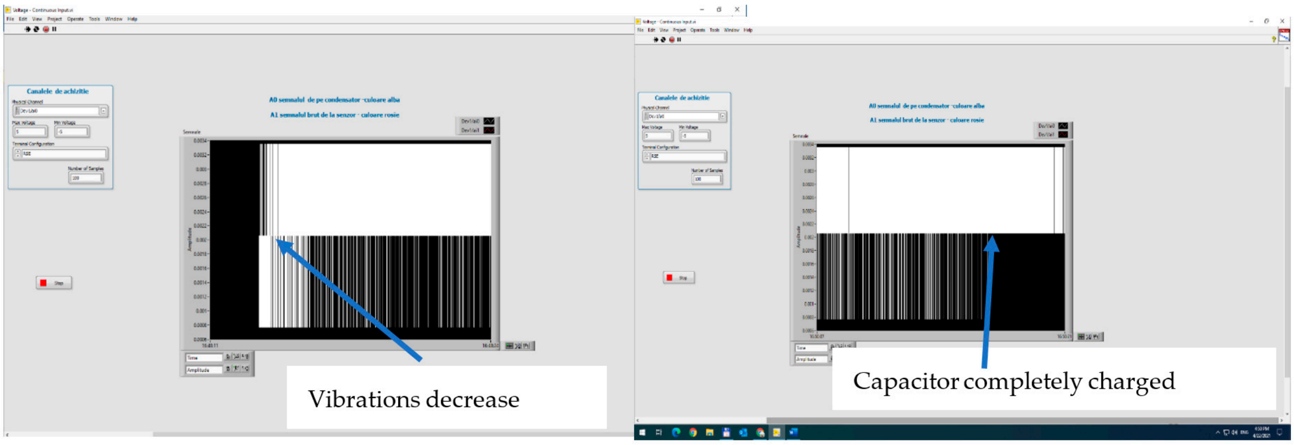

Physical Channel: Dev1/ai0
Max Voltage: 5
Min Voltage: -5
Terminal Configuration: RSE
Number of Samples: 100

(**a**) (**b**)

Figure 20. The charging of the capacitor when vibrations decrease: (**a**) capacitor on charge; (**b**) capacitor fully charged.

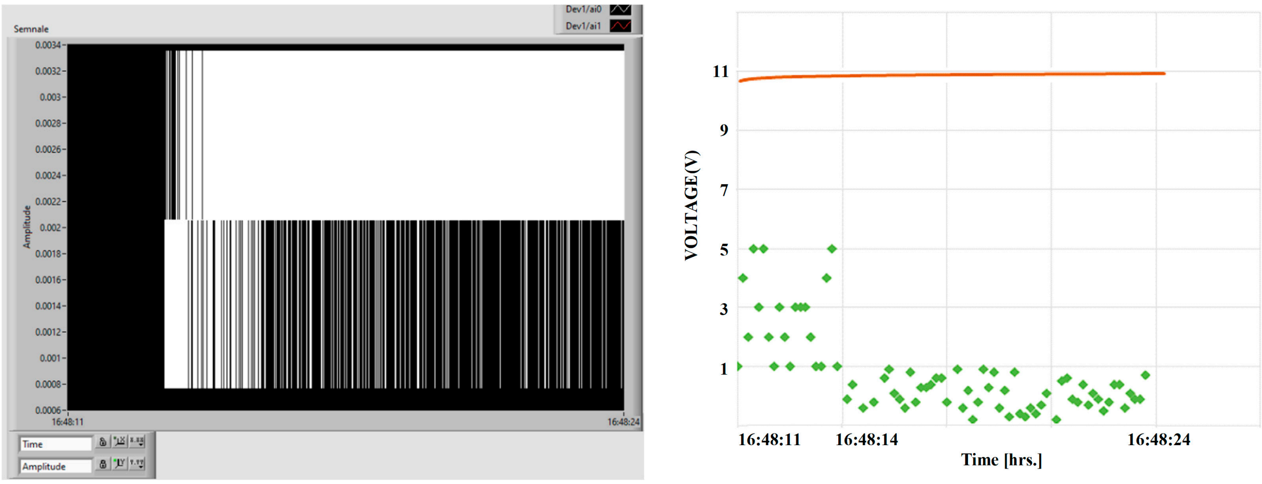

(**a**) (**b**)

Figure 21. Digital signal on capacitor (**a**) and charging characteristic (**b**), when vibrations decrease for the activated sensor.

6. Conclusions

The overall picture based on the actual literature shows that many researchers are carrying out research with the aim of testing piezoelectricity as the main source for energy harvesting, and the applications are very innovative, especially in the case of flexible piezoelectric systems.

Composite materials from polymer powders (TPU and TPO—herein polypropylene) with the addition of $BaTiO_3$ until 35% were manufactured and interdisciplinary tested, and it was proved that the filler is well homogenized within the polymer structure with a uniform dispersion. For such composite material, in addition to glass transition processes and chemical oxidation processes, there is also a first-order phase transformation process—melting, due to the TPO (PP) melting process.

The addition of $BaTiO_3$ dramatically increases the relative dielectric permittivity, from about 3 for pure polymers to about 10 for an addition of 12% $BaTiO_3$, and finally to about 30 for an addition of 35% $BaTiO_3$. In regard to the dielectric loss, at lower frequencies the effect of interfacial polarization is detrimental, with a very significant increase for an addition of 35% $BaTiO_3$. The piezoelectric characteristics of the composite with 35% $BaTiO_3$, without preliminary activation under a tailored electric field, are remarkable, especially at lower frequencies.

The filament extruded from the composite material with 35% $BaTiO_3$ was very elastic, close to the elasticity of rubber, but it provided good features to be used for 3D printing applications and presented a variation in a maximum diameter of 10%.

The importance and degree of novelty of our study consist in the demonstration of the operation in energy harvesting mode of the new concept of sensors made by 3D printing technology, made in the form of thermoplastic composites deposited in various forms; here, the testing was performed on a structure of rectangular network type, acting as a piezoelectric sensor in a dedicated signal processing circuit.

It was technically demonstrated that the 3D thermal deposition of composite filament with 35% $BaTiO_3$ was a convenient process with no clogging of the nozzle, no problems with multilayer deposition, and no 3D printing defects.

For the development and integration of the signal processing circuits and the demonstration of the functionality of the energy harvesting features of 3D printed devices, an innovative test stand was developed and is assisted by a virtual instrument to produce and analyze the tailored vibrations to activate devices with functionality as piezoelectric sensors. As brief conclusions upon the electronic tests performed with non-activated and electrically activated devices:

- The electrically activated device has superior performance in terms of the generated electrical signal; the device with 35% $BaTiO_3$ has an immediate and proportional response to periodic mechanical excitation.
- The device, with a higher concentration of $BaTiO_3$ and a quasi-4D effect with frequency, responds better at lower frequencies to the variation of mechanical oscillations and achieves a quasi-uniform charging of the capacitor of the energy harvesting circuit, even if the mechanical oscillations become reduced in intensity.
- The higher the concentration of $BaTiO_3$, the lower the minimum response threshold at low levels of mechanical oscillations, with an induced mechanical hysteresis effect when the mechanical oscillations decrease.

Such flexible piezoelectric systems can be used in various biomedical devices (as wearable electronics or intelligent prosthesis), generating enough energy to make such devices completely autonomous only by exploiting body movements at variable low frequencies.

Author Contributions: Conceptualization, R.C.C. and A.R.C.; methodology, M.A., R.C.C., C.S., A.R.C. and M.P.; software, M.P. and J.P.; validation, R.C.C., C.S., A.R.C., M.P., J.P. and M.B.; formal analysis, M.A., R.C.C. and M.B.; investigation, M.A., R.C.C., C.S., A.R.C., J.P. and M.B.; data curation, R.C.C.; writing—original draft preparation, M.A. and R.C.C.; writing—review and editing, M.A. and R.C.C.; supervision, R.C.C. All authors have read and agreed to the published version of the manuscript.

Funding: This work was supported by a publication grant from Technical Univ. Iasi, and it was based on the joint experimental research of participating organizations, partially financed by a grant (4DPrintEN) under COFUND-ERANET MANUNET III, including the contribution of the Spanish company IZERTIS, which technically modified and updated a specialized 3D printer for the project purpose.

Institutional Review Board Statement: Not applicable.

Data Availability Statement: The data presented in this study are available on request from the corresponding author.

Conflicts of Interest: The authors declare no conflict of interest.

References

1. Kozioł, M.; Szperlich, P.; Toro, B.; Olesik, P.; Jesionek, M. Assessment of the Piezoelectric Response of an Epoxy Resin/SbSINanowires Composite Filling FDM Printed Grid. *Materials* **2020**, *13*, 5281. [CrossRef] [PubMed]
2. Lee, J.; Choi, W.; Yoo, Y.K.; Hwang, K.S.; Lee, S.-M.; Kang, S.; Lee, J. A micro-fabricated force sensor using an all thin film piezoelectric active sensor. *Sensors* **2014**, *14*, 22199–22207. [CrossRef] [PubMed]
3. Tadaki, D.; Ma, T.; Yamamiya, S.; Matsumoto, S.; Imai, Y.; Hirano-Iwata, A.; Niwano, M. Piezoelectric PVDF-based sensors with high pressure sensitivity induced by chemical modification of electrode surfaces. *Sens. Actuators A Phys.* **2020**, *316*, 112424. [CrossRef]
4. Wan, C.; Bowe, C.R. Multiscale-structuring of polyvinylidene fluoride for energy harvesting: The impact of molecular-, micro- and macro-structure. *J. Mater. Chem. A Mater. Energy Sustain.* **2017**, *5*, 3091–3128. [CrossRef]
5. Jia, H.; Li, H.; Lin, B.; Hu, Y.; Peng, L.; Xu, D.; Cheng, X. Fine scale 2-2 connectivity PZT/epoxy piezoelectric fiber composite for high frequency ultrasonic application. *Sens. Actuators A Phys.* **2021**, *324*, 112672. [CrossRef]
6. Meshkinzar, A.; Al-Jumaily, A. Cylindrical Piezoelectric PZT Transducers for Sensing and Actuation. *Sensors* **2023**, *23*, 3042. [CrossRef]
7. Jian, G.; Jiao, Y.; Feng, L.; Meng, Q.; Yang, N.; Zhu, S.; Lü, M.; Wong, C.P. High energy density of $BaTiO_3$-TiO_2 nanosheet/polymer composites via ping-pong-like electron area scattering and interface engineering. *NPG Asia Mater.* **2022**, *14*, 4. [CrossRef]
8. Su, J.; Zhang, J. Recent development on modification of synthesized barium titanate ($BaTiO_3$) and polymer/$BaTiO_3$ dielectric composites. *J. Mater.Sci. Mater. Electron.* **2019**, *30*, 1957–1975. [CrossRef]
9. Jian, G.; Jiao, Y.; Meng, Q.; Wei, Z.; Zhang, J.; Yan, C.; Moon, K.S.; Wong, C.P. Enhanced dielectric constant and energy density in a BaTiO3/polymer-matrix composite sponge. *Commun. Mater.* **2020**, *1*, 91. [CrossRef]
10. Pratap, A. Dielectric behavior of nano barium titanate filled polymeric composites. *Int. J. Mod.Phys. Conf. Ser.* **2013**, *22*, 1–10. [CrossRef]
11. Charif, A.R.C.; Diorio, N.; Fodor-Csorba, K.; Jákli, A.; Puskas, J. A piezoelectric thermoplastic elastomer containing a bent-core liquid crystal. *RSC Adv.* **2013**, *3*, 7446–17452. [CrossRef]
12. Qiu, L.; Coskun, M.B.; Tang, Y.; Liu, J.Z.; Alan, T.; Ding, J.; Truong, V.; Li, D. Ultrafast Dynamic Piezoresistive Response of Graphene-Based Cellular Elastomers. *Adv. Mater.* **2016**, *28*, 194–200. [CrossRef] [PubMed]
13. Xie, S.H.; Zhu, B.K.; Wei, X.Z.; Xu, Z.K.; Xu, Y.Y. Polyimide/$BaTiO_3$ composites with controllable dielectric properties. *Compos. Part A Appl. Sci. Manuf.* **2005**, *36*, 1152–1157. [CrossRef]
14. Stojchevska, E.; Popeski-Dimovski, R.; Kokolanski, Ž.; Gualandi, C.; Bužarovska, A. Effect of Particle Functionalization on Structural and Dielectric Properties of Flexible TPU/$BaTiO_3$/MWCNTs Composite Films. *Macromol. Chem. Phys.* **2023**, *224*, 2200401. [CrossRef]
15. Wondu, E.; Lule, Z.C.; Kim, J. Fabrication of thermoplastic polyurethane composites with a high dielectric constant and thermal conductivity using a hybrid filler of CNT-$BaTiO_3$. *Mater. Today Chem.* **2023**, *27*, 101287. [CrossRef]
16. Luo, Z.; Zhang, L.; Liang, Y.; Wen, S.; Liu, L. Improved the dielectric properties of thermoplastic polyurethane elastomer filled with MXene nanosheets and $BaTiO_3$ nanofibers. *Polym.Test.* **2022**, *111*, 107592. [CrossRef]
17. Gupta, R.; Badel, B.; Gupta, P.; Bucknall, D.G.; Flynn, D.; Pancholi, K. Flexible low-density polyethylene–$BaTiO_3$ nanoparticle composites for monitoring leakage current in high-tension equipment. *ACS Appl. Nano Mater.* **2021**, *4*, 2413–2422. [CrossRef]
18. Ma, Z.; Xie, Y.; Mao, J.; Yang, X.; Li, T.; Luo, Y. Thermoplastic Dielectric Elastomer of Triblock Copolymer with High Electromechanical Performance. *Macromol. Rapid Commun.* **2017**, *3*, 1700268. [CrossRef]
19. Ko, Y.S.; Nüesch, F.A.; Opris, D.M. Charge generation by ultra-stretchable elastomeric electrets. *J. Mater. Chem. C* **2017**, *5*, 1826–1835. [CrossRef]
20. Yaqoob, U.; Uddin, A.S.M.I.; Chung, G. A novel tri-layer flexible piezoelectric nanogenerator based on surface- modified graphene and PVDF-$BaTiO_3$ nanocomposites. *Appl. Surf. Sci.* **2017**, *405*, 420–426. [CrossRef]
21. Dagdeviren, C.; Joe, P.; Tuzman, O.L.; Park, K.I.; Lee, K.J.; Shi, Y.; Huang, Y.; Rogers, J.A. Recent progress in flexible and stretchable piezoelectric devices for mechanical energy harvesting, sensing and actuation. *Extrem. Mech. Lett.* **2016**, *9*, 269–281. [CrossRef]
22. Göksenin, H.; Sümer, Ç.B. A Flexible Piezoelectric Energy Harvesting System for Broadband and Low-frequency Vibrations. *Procedia Eng.* **2015**, *120*, 345–348.
23. Park, S.; Lee, H.; Yeon, S.; Park, J.; Lee, N. Flexible and Stretchable Piezoelectric Sensor with Thickness-Tunable Configuration of Electrospun Nanofiber Mat and Elastomeric Substrates. *ACS Appl. Mater. Interfaces* **2016**, *8*, 24773–24781. [CrossRef] [PubMed]
24. Wei, Y.; Chen, S.; Dong, X.; Lin, Y.; Liu, L. Flexible piezoresistive sensors based on "dynamic bridging effect" of silver nanowires toward grapheme. *Carbon* **2017**, *113*, 395–403. [CrossRef]
25. Niu, D.; Jiang, W.; Ye, G.; Wang, K.; Yin, L.; Shi, Y.; Chen, B.; Luo, F.; Liu, H. Graphene-elastomer nanocomposites based flexible piezoresistive sensors for strain and pressure detection. *Mater. Res. Bull.* **2018**, *102*, 92–99. [CrossRef]
26. Yan, Y.; Potts, M.; Jiang, Z.; Sencadas, V. Synthesis of highly-stretchable graphene—Poly(glycerol sebacate) elastomeric nanocomposites piezoresistive sensors for human motion detection applications. *Compos. Sci. Technol.* **2018**, *162*, 14–22. [CrossRef]
27. Shen, Y.; Wang, S.; Zhi, Y.; Han, B. Properties of novel 0–3 PZT/silicone resin flexible piezoelectric composites for ultrasonic guided wave sensor applications. *Front. Mater. Sec. Smart Mater.* **2022**, *9*, 958775.
28. Arul, K.T.; Rao, M.R. Ferroelectric properties of flexible PZT composite films. *J. Phys. Chem. Solids* **2020**, *146*, 109371. [CrossRef]

29. Khoo, Z.X.; Teoh, J.M.; Liu, Y.; Chua, C.K.; Yang, S.; An, J. 3D printing of smart materials: A review on recent progresses in 4D printing. *Virtual Phys. Prototyp.* **2015**, *10*, 103–122. [CrossRef]
30. Lee, J.; Kim, H.; Choi, J.; Lee, I.H. A review on 3D printed smart devices for 4D printing. *Int. J. Precis. Eng. Manuf. -Green Technol.* **2017**, *4*, 373–383. [CrossRef]
31. Li, X.; Shang, J.; Wang, Z. Intelligent materials: A review of applications in 4D printing. *Assem. Autom.* **2017**, *37*, 170–185. [CrossRef]
32. Baibarac, M.; Nila, A.; Smaranda, I.; Stroe, M.; Singescu, L.; Cristea, M.; Cercel, R.C.; Lorinczi, A.; Ganea, P.; Mercioniu, I.; et al. Optical, structural and Dielectric properties of composites based on thermoplastic polymers of the polyolefin and polyurethane type and $BaTiO_3$ nanoparticles. *Materials* **2021**, *14*, 753. [CrossRef] [PubMed]
33. Smaranda, I.; Nila, A.; Ganea, P.; Daescu, M.; Zgura, I.; Ciobanu, R.C.; Trandabat, A.; Baibarac, M. The influence of the ceramic nanoparticles on the thermoplastic polymers matrix: Their structural, optical and conductive properties. *Polymers* **2021**, *13*, 2773. [CrossRef] [PubMed]
34. Ciobanu, R.; Schreiner, C.; Aradoaei, M.; Hitruc, G.E.; Rusu, B.G.; Aflori, M. Characteristics of composite materials of the type: TPU/PP/$BaTiO_3$ Powder for 3D printing applications. *Polymers* **2023**, *15*, 73. [CrossRef] [PubMed]
35. Baibarac, M.; Arzumanyan, G.; Daescu, M.; Udrescu, A. Anisotropic photoluminescence of poly(3-hexyl thiophene) and their composites with single-walled carbon nanotubes highly separated in metallic and semiconducting tubes. *Molecules* **2021**, *26*, 294. [CrossRef]
36. *ISO 10109-7:2001*; Optics and Optical Instruments. Environmental Requirements—Part 7: Test Requirements for Optical Measuring Instruments. International Organization for Standardization: Geneva, Switzerland, 2001.
37. Available online: https://www.novocontrol.de/php/turn_key_10_90.php (accessed on 20 April 2023).
38. Operating Instructions-Simultaneous TG-DTA/DSC Apparatus (STA 449F3) Jupiter), Selb, October 2008, NE-TZSCH Gerätebau GmbH. Available online: https://www.cif.iastate.edu/sites/default/files/uploads/Other_Inst/TGA/STA449%20F1%20Operating%20Instructions.pdf (accessed on 20 April 2023).
39. Tao, R.; Granier, F.; Therriault, D. Multi-material freeform 3D printing of flexible piezoelectric composite sensors using a supporting fluid. *Addit. Manuf.* **2022**, *60*, 103243.
40. Available online: https://www.ni.com/ro-ro/shop/labview.html (accessed on 20 April 2023).

materials

MDPI

Article

Influences of Dispersions' Shapes and Processing in Magnetic Field on Thermal Conductibility of PDMS–Fe_3O_4 Composites

V. Stancu [1], A. Galatanu [1], M. Enculescu [1,*], M. Onea [1,2], B. Popescu [1], P. Palade [1], M. Aradoaie [3], R. Ciobanu [3,4] and L. Pintilie [1]

[1] National Institute of Materials Physics, Atomistilor 405A, 077125 Magurele, Romania; stancu@infim.ro (V.S.); gala@infim.ro (A.G.); melania.onea@infim.ro (M.O.); bogdan.popescu@infim.ro (B.P.); palade@infim.ro (P.P.); pintilie@infim.ro (L.P.)
[2] Faculty of Physics, University of Bucharest, Atomistilor 405, 077125 Magurele, Romania
[3] Department of Electrical Measurements and Materials, Faculty of Electrical Engineering, Technical University Gh. Asachi Iasi, Boulevard Profesor Dimitrie Mangeron 67, 70050 Iasi, Romania; mihaela.aradoaei@academic.tuiasi.ro (M.A.); rciobanu@yahoo.com (R.C.)
[4] All Green SRL, 8 G. Cosbuc Street, 700470 Iasi, Romania
* Correspondence: mdatcu@infim.ro

Abstract: Composites of magnetite (Fe_3O_4) nanoparticles dispersed in a polydimethylsiloxane (PDMS) matrix were prepared by a molding process. Two types of samples were obtained by free polymerization with randomly dispersed particles and by polymerization in an applied magnetic field. The magnetite nanoparticles were obtained from magnetic micrograins of acicular goethite (α-FeOOH) and spherical hematite (α-Fe_2O_3), as demonstrated by XRD measurements. The evaluation of morphological and compositional properties of the PDMS:Fe_3O_4 composites, performed by SEM and EDX, showed that the magnetic particles were uniformly distributed in the polymer matrix. Addition of magnetic dispersions promotes an increase of thermal conductivity compared with pristine PDMS, while further orienting the powders in a magnetic field during the polymerization process induces a decrease of the thermal conductivity compared with the un-oriented samples. The shape of the magnetic dispersions is an important factor, acicular dispersions providing a higher value for thermal conductivity compared with classic commercial powders with almost spherical shapes.

Keywords: PDMS; magnetite; magnetic field polymerizations; thermal conductivity properties

Citation: Stancu, V.; Galatanu, A.; Enculescu, M.; Onea, M.; Popescu, B.; Palade, P.; Aradoaie, M.; Ciobanu, R.; Pintilie, L. Influences of Dispersions' Shapes and Processing in Magnetic Field on Thermal Conductibility of PDMS–Fe_3O_4 Composites. *Materials* **2021**, *14*, 3696. https://doi.org/10.3390/ma14133696

Academic Editors: Dario Pasini and Jānis Andersons

Received: 28 May 2021
Accepted: 28 June 2021
Published: 1 July 2021

1. Introduction

Composites of magnetic nanoparticles randomly dispersed in a polymer matrix are promising materials widely applied in many engineering areas for magnetic separation, catalysis, MRI contrast agents, or electromagnetic shielding [1–5]. Polydimethylsiloxane (PDMS) is a suitable polymer for embedded composite materials that combine the properties of the matrix and the nanoparticles [6–8].

In the early stage of electromagnetic actuator evolution, the actuator was designed by incorporating a bulky permanent magnet placed on the top of the deforming membrane [9]. At the beginning, thin silicon membrane was used as actuator membrane [10,11]. However, silicon is a fragile material with low flexibility and low fracture [11], and for this reason, a lot of research has been done to solve the MEMS problems such as membrane rupture [12]. One way to solve the problem is to use polymer as membrane. In this context, polydimethylsiloxane (PDMS) was demonstrated to be a suitable polymer for composite materials, and has been attracting a large interest in the field of electromechanical actuators, force sensors, piezoelectric generators, and other stretchable electronics [13,14] due to its high flexibility. The final properties of these composites depend upon various parameters, such as size of particles, method of preparation of composite, and dispersion of particles into the polymer matrix [15–17]. Spin interactions between magnetic nanoparticles can also influence the final properties of the composites [18–20].

Another research direction in the composite materials' field is the study of anisotropic properties, which can be relevant for material design of particle-reinforced polymer composites for advanced field-assisted additive manufacturing strategies. Anisotropic properties are required for new applications such as flexible electronics [21] or bionic devices [22,23]. Control over particle organization is exercised by enhancing the field strength, which improves particle alignment [24]. Gold and iron oxide nanoparticles were frequently used in biomedical applications [25,26] for magnetic drug targeting, which is a delivery scheme in which the medications and suitable magnetically active components are transported by stable pharmaceutical carriers [27,28].

In the past decade, the combination of the magnetic particles with polymer matrix has been studied as it leads to formation of ferromagnetic polymer composite [29]. Another recent application of polymer–nanoparticles (including magnetic nanoparticles) composite is in thermal pads, designed for a rapid transfer of the heat from electronic devices (e.g., automotive microcontrollers) to the surrounding atmosphere [30,31]. Different strategies were tested to enhance the thermal conductivity of polymer–magnetic nanoparticles composites, such as core-shell structures or other additives in the composite [32–39]. However, the effect of a magnetic field, used to align the magnetic nanoparticles during the polymerization process, on the thermal properties of the composite was less studied [40].

In this work, we examine the thermal conductibility of the composites with two types of magnetite randomly dispersed particles in a PDMS matrix and the influence of applying a magnetic field to modify the particle arrangement on the thermal properties of the composite materials.

2. Materials and Methods

The magnetite particles with the acicular structure were obtained starting from the goethite (α-FeOOH). The goethite nanoparticles with 50–100 nm in diameter and a few microns in length were obtained from 5M $Fe(NO_3)_3$ and 1M KOH aqueous solutions, mixed at 70 °C for 48 h. Acicular hematite particles (α-Fe_2O_3) were obtained by treating goethite at 400 °C in air for 2 h. When acicular α-Fe_2O_3 particles are treat in a reducing gas flow (5% H_2/Ar) with very high purity 99.999% for 2 h at 300 °C, acicular magnetite (Fe_3O_4) is obtained.

A second experimental route to obtain magnetite (Fe_3O_4) was to treat the commercial hematite powders with the granular morphology (α-Fe_2O_3, Merck, 99.99% purity) in a reducing gas flow (5% H_2/Ar) for 2 h at 330 °C. Thus, we obtained magnetite grains with dimensions scaling from 100 to 400 nm in size.

The PDMS base (Sylgard 184, Dow Corning, Midland, MI, USA) and the curing agent with a mass ratio of 10:1 were mixed. Subsequently, the magnetite powders in mass ratio polymer:magnetite of 10:3 were immediately added into the uncured PDMS matrix. After being uniformly mixed, the uncured composite was put into a mold for free polymerization (Figure 1). The oriented sample was obtained by placing the mold into a magnetic field of about 400 mT, as illustrated in Figure 1. Both types of samples were placed in an oven, at 100 °C for 60 min. Thus, we obtained discs of about 10 mm diameter and about 1 mm thickness (Figure 2).

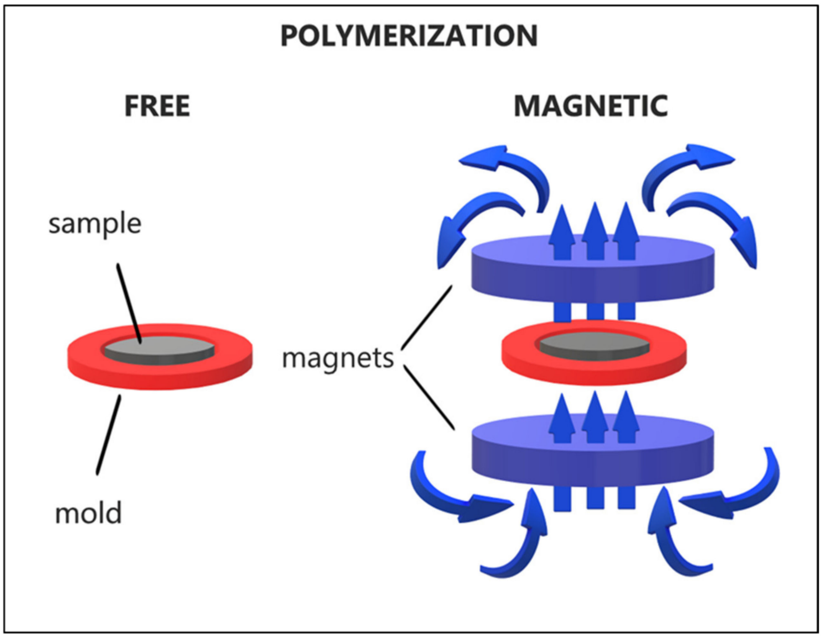

Figure 1. Schematic illustration of the fabrication process.

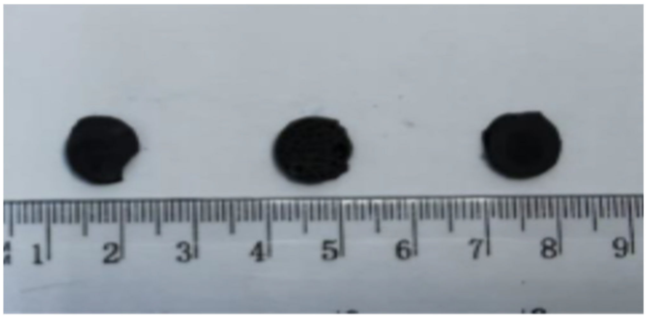

Figure 2. Discs of PDMS:Fe_3O_4 composites obtained by free polymerization (left and right) and magnetic polymerizations (middle).

The morphology and elemental compositions of the samples were studied with a Carl Zeiss EVO 50XVP scanning electron microscope (SEM) equipped with Bruker Quantax 200 energy dispersive X-ray spectrometer (EDS) with energy resolution of 129 eV and Peltier cooling, and a field emission scanning electron microscope (FESEM; Gemini 500, Carl Zeiss, AG Germany, Oberkochen, Germany). The crystal structure was analyzed by X-ray diffraction (XRD) using a Bruker D8 Advance equipment (BRUKER-AXS GmbH, Karlsruhe, Germany). Hysteresis loops for acicular magnetite obtained from goethite and for magnetite obtained from commercial hematite were investigated at 300 K using a SQUID magnetometer (MPMS Quantum Design). Thermal conductivity characterizations were performed with Laser Flash Analyzer “Microflash” LFA457 model, Netzsch-Gerätebau GmbH, Germany. All samples were investigated at 25 °C in air, in a transversal configuration, i.e., the heat flow was in the same direction as the magnetic field orientation during the sample processing.

For a good accuracy, the thermal properties results presented were obtained from averaging of 5 measurements for each sample. With the LFA equipment, the thermal diffusivity was directly measured, while the specific heat was obtained by a differential method using a reference material, in this case, a NBS standard alumina sample. The sample and the reference material were exposed to the same amount of laser radiation. To avoid the effects of different reflectance and emissivity of the materials, both materials were covered on both sides with graphite layers having a thickness of a few tens of nanometers and the heating step was analyzed with the same method. Knowing the specific heat of the reference material and having a direct proportionality between the infrared signal step read and the temperature change, the specific heat was obtained as

$$C_p^{sample} = \frac{C_p^{ref} \times m^{ref} \times \Delta T^{ref}}{m^{sample} \times \Delta T^{sample}}$$

Thermal conductivity, κ, was calculated according to formula $\kappa = \alpha \times C_p \times \rho$, where α is thermal diffusivity, C_p is the specific heat, and ρ is the density of the material. The density was determined by Archimedes method in ethanol at room temperature.

3. Results and Discussion

The morphologies of the goethite, hematite and magnetite, were evaluated, as presented in Figure 3a–c. It can be observed that the starting materials as well as the magnetite obtained using the first route of fabrication have acicular morphologies. On the other hand, the magnetite obtained by the second route of fabrication has a similar granular morphology as the commercial hematite that was used, as observed in Figure 3d,e.

The confirmation of obtaining acicular magnetite was achieved by XRD measurements, presented in Figure 4a. The second experimental route of magnetite fabrication was confirmed also by the XRD measurements, as shown in Figure 4b.

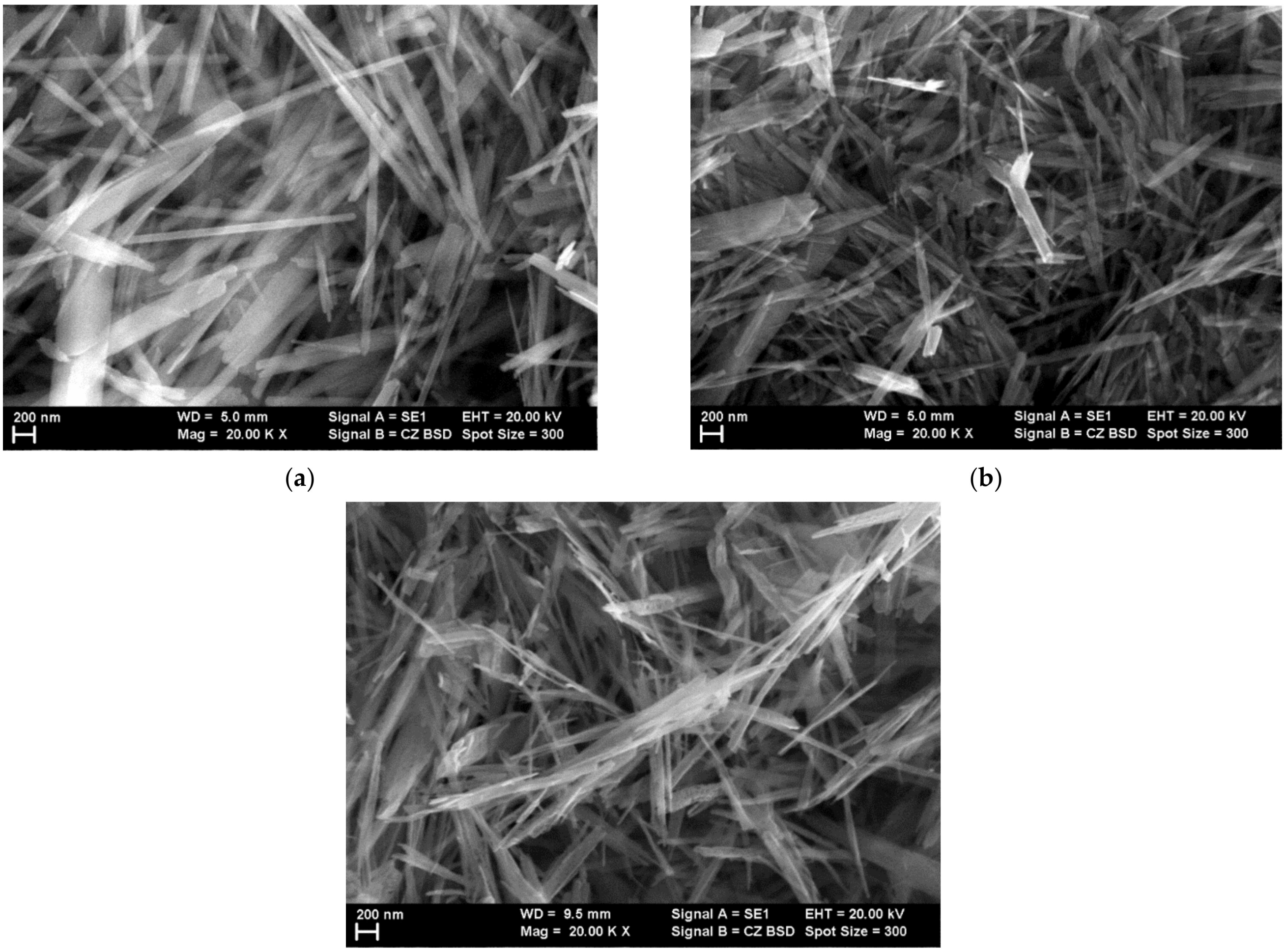

(**a**) (**b**)

(**c**)

Figure 3. *Cont.*

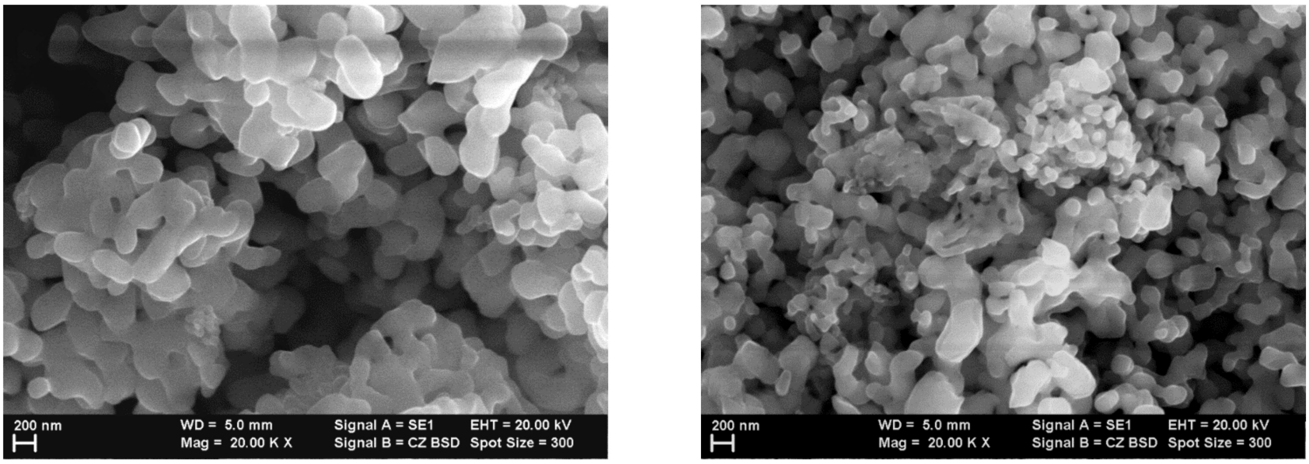

(**d**) (**e**)

Figure 3. SEM images of (**a**) acicular goethite, (**b**) acicular hematite, (**c**) acicular magnetite, (**d**) commercial hematite, and (**e**) magnetite grains.

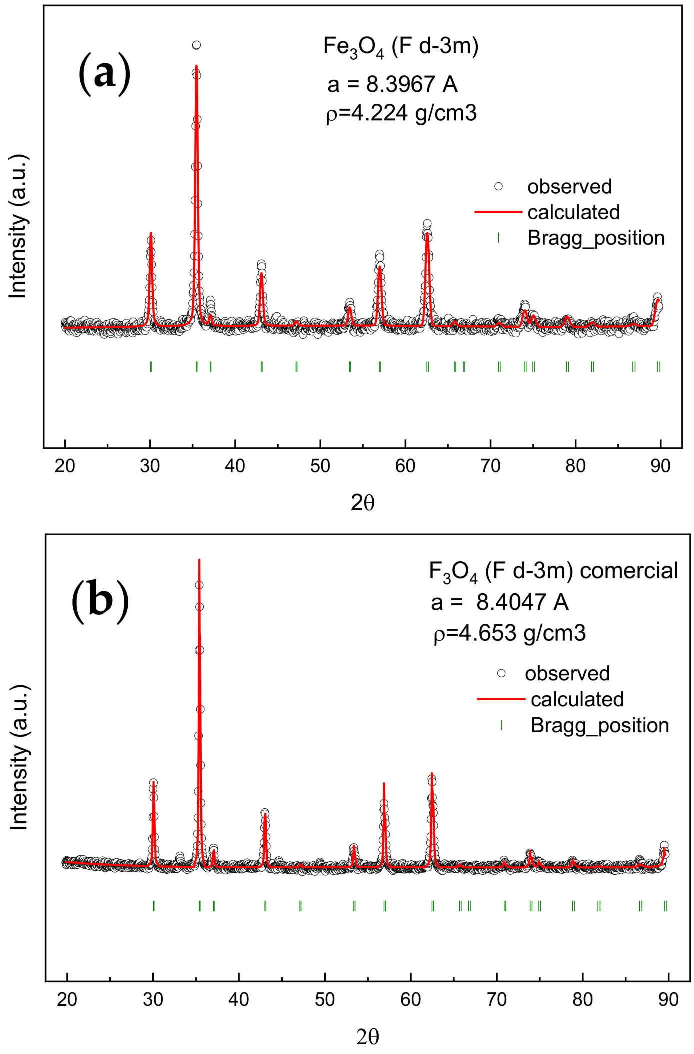

Figure 4. XRD patterns for (**a**) acicular magnetite and (**b**) magnetite obtained from commercial α-Fe_2O_3.

The morphology of PDMS:Fe_3O_4 composites fabricated using magnetite powders was evidenced by SEM images, as shown in Figure 5. The samples obtained by free polymerization display a good packaging structure, with a homogeneous distribution of the magnetite grains in the PDMS matrix and very small pores (Figure 5a,c). For the samples produced using the magnetic polymerization, the magnetic powder presents an alignment on the direction of the field lines (Figure 5b,d).

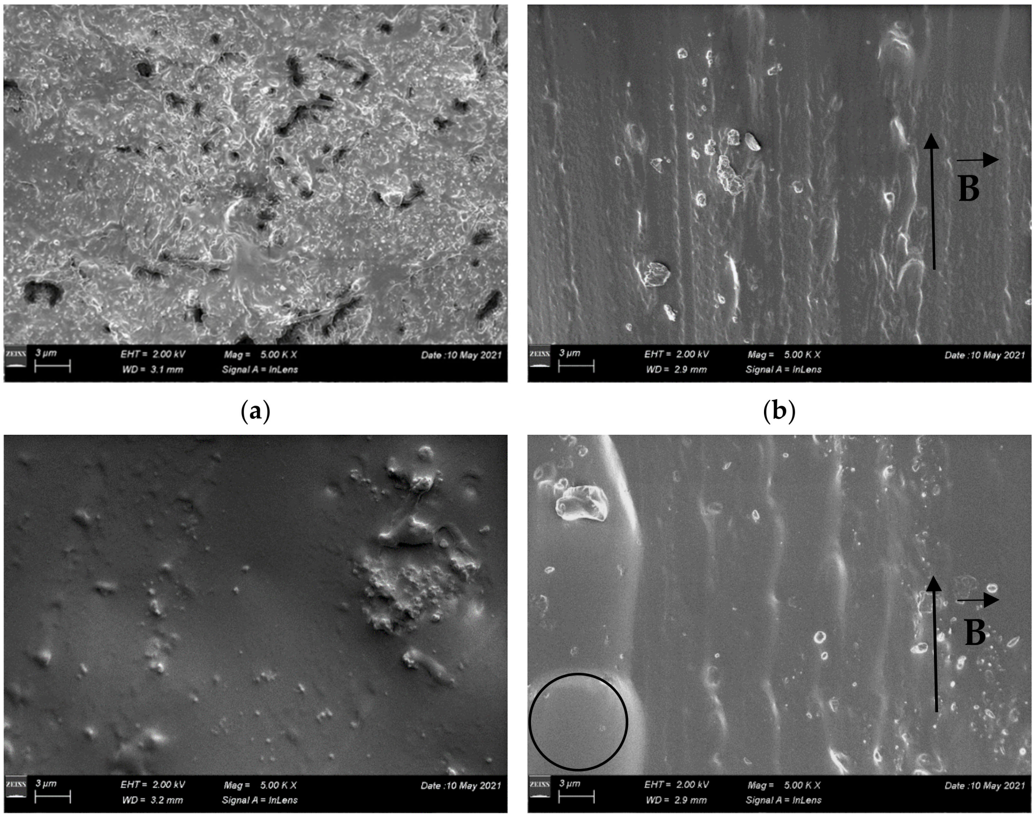

(**a**) (**b**)

(**c**) (**d**)

Figure 5. SEM micrographs of acicular PDMS: magnetite composites prepared by (**a**) free polymerization and (**b**) magnetic field polymerization and of spherical PDMS: magnetite composites prepared by (**c**) free polymerization and (**d**) magnetic field polymerization.

In spite of similar composition, the samples exhibit different densities. Moreover, for the sample prepared using the commercial powder of magnetite polymerized in magnetic field, the density is lower than the value obtained for the pristine PDMS. This can be related to the presence of a considerable amount of closed porosity, as indicated in Figure 5d by the circle.

The XRD measurements are in a good agreement with compositional EDS analyses (Figure 6). The characteristic bands of the elements from the polymer base composition (C, O, and Si) appear in all spectra and additionally, when magnetite is dispersed in polymer, the very intense Fe bands are evidenced.

In order to assess the magnetic properties of the magnetite powders used to fabricate the PDMS:Fe_3O_4 composites, powders were evaluated. Hysteresis loops at 300 K for acicular magnetite obtained from goethite provide the following values: magnetization at saturation (M_s) of 83.8 emu/g, coercive field of 265 Oe, and remanence M_r/M_5 = 29%, where M_r is remanent magnetization (Figure 7a). Hysteresis loops at 300 K for magnetite obtained from commercial hematite provide magnetization at saturation (M_s) of 83.95 emu/g, coercive field of 210 Oe, and remanence M_r/M_5 = 17% (Figure 7b).

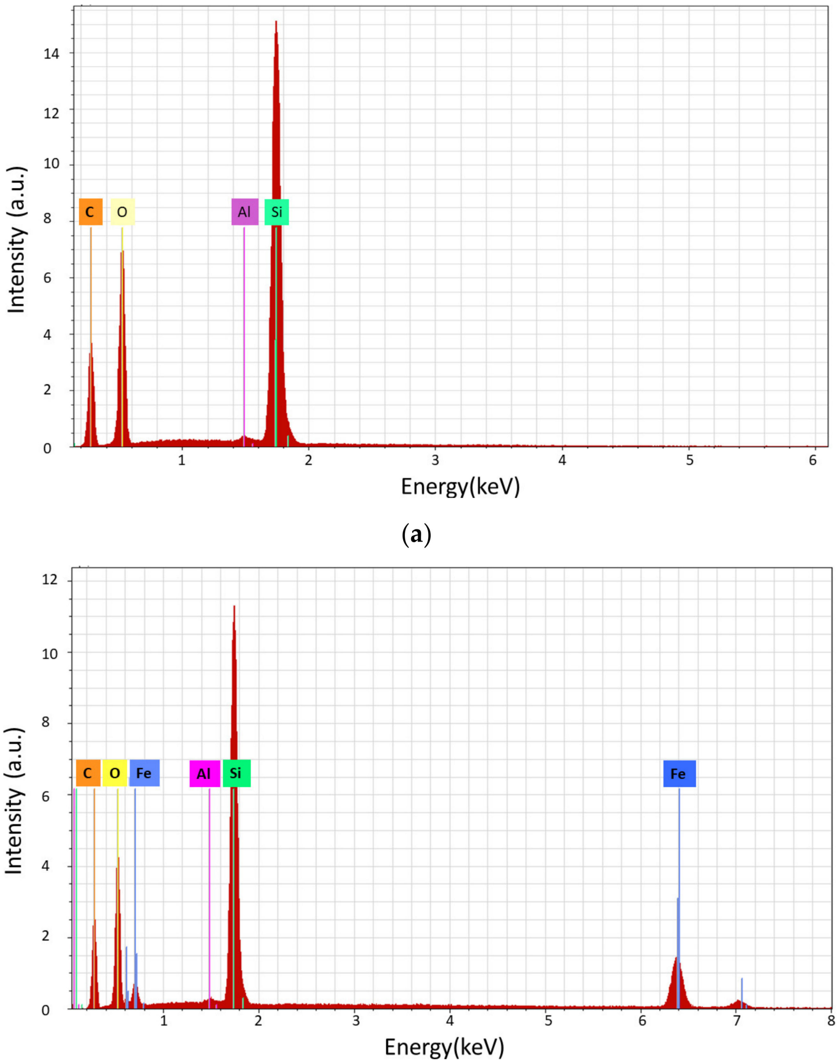

(**a**)

(**b**)

Figure 6. EDX spectra of (**a**) PDMS matrix and (**b**) PDMS: magnetite composites.

These values of magnetization at saturation (M_s) clearly indicate the presence of magnetite. Both hematite and goethite have much smaller M_s values, below 5 emu/g.

The high values of M_s obtained both for acicular magnetite obtained from goethite and for magnetite obtained from commercial hematite show well-formed magnetite grains with ferrimagnetic (not superparamagnetic) behavior, taking into consideration the significant values of remanence and coercive field. Additionally, both remanence and coercive field are significantly higher for acicular magnetite obtained from goethite than for magnetite obtained from commercial hematite, proving the shape anisotropy due to the acicular shape of the magnetite obtained from goethite.

The thermal diffusivity for the investigated materials is plotted in Figure 8. The diffusivity is a direct measure of the thermal inertia of the material. A higher value indicates a faster spread of the heat in the material. Not surprisingly, the higher value is obtained for the sample produced without an applied magnetic field. Since the powder is magnetic (its Curie temperature being at around 580 °C) the dispersed particles tend to spontaneously agglomerate inside the polymer into clusters, which can eventually create magnetite bridges to transport the heat. The thermal diffusivity of magnetite can be deduced from thermal conductivity values measured in [41] and specific heat data from [42] to be between 0.6 and 0.8 mm^2/s, that is an order of magnitude higher than the value of PDMS. Thus, contiguity of random patterns of magnetite can provide shortcuts for the heat flux across the sample. Applying a magnetic field creates a more regular pattern for the dispersed powders, which are distributed along the magnetic flux lines, in this case, in the direction parallel to the heat flow. Thus, a decrease of thermal diffusivity is observed for the sample with oriented powders at about half of the value obtained for the sample with unaligned dispersions. It has to be mentioned that using acicular dispersions instead of the commercial powder results in a small increase in thermal diffusivity of that sample compared to the sample with spherical dispersions. A possible explanation might be connected to a better alignment of the shaped magnetite, which could also be concluded for the higher density of this sample (Figure 9), exhibiting a strongly reduced porosity.

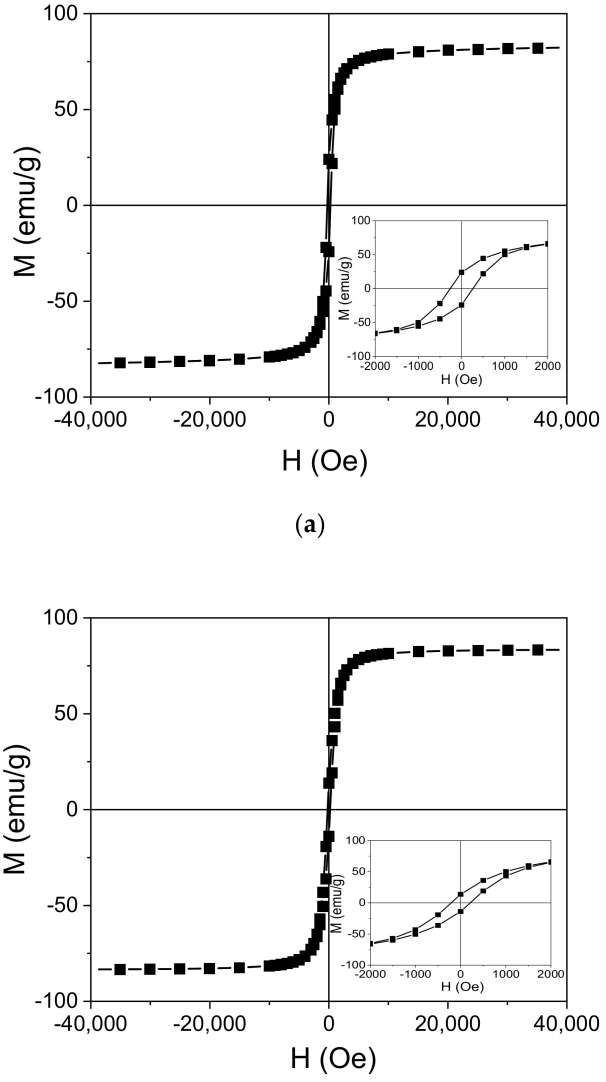

(**a**)

(**b**)

Figure 7. Hysteresis loops measured at 300 K for acicular magnetite obtained from goethite (**a**) and magnetite obtained from commercial hematite (**b**). The insets show the central part of the figures with higher magnification.

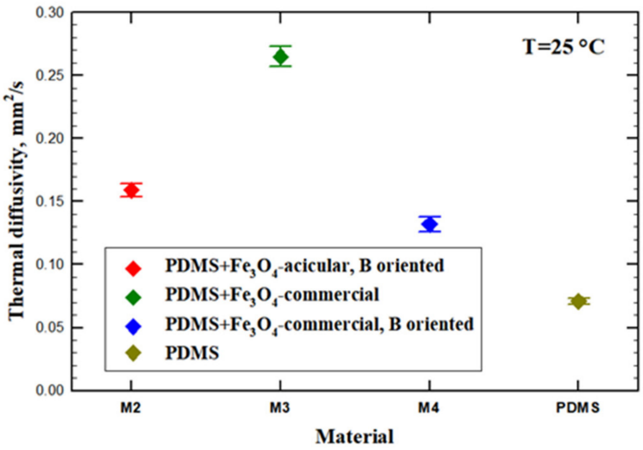

Figure 8. Thermal diffusivity of PDMS: magnetite composites. The points represent the mean values of five measurements, while the horizontal lines are the corresponding error bars.

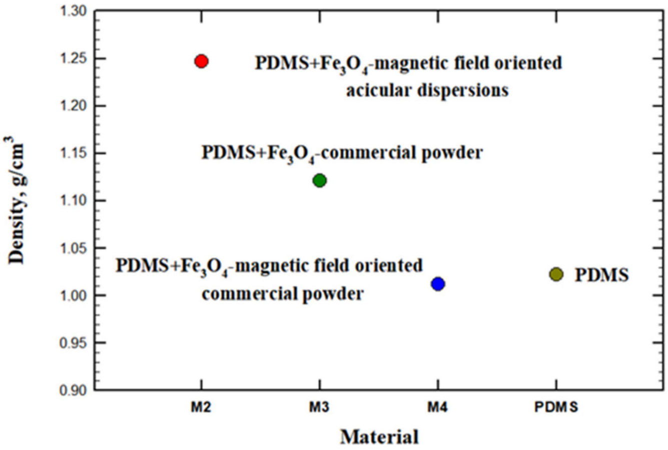

Figure 9. Density of PDMS: magnetite composites determined by Archimedes method.

The specific heat values of the investigated samples are depicted in Figure 10a. From a theoretical point of view, the specific heat of a composite material follows the direct mixture rule, i.e., is the pondered sum of the constituents' specific heat. The PDMS specific heat value was measured by the LFA differential method on a sample without dispersions, while for magnetite we used the values reported in the literature. The deviations observed from the direct mixing rule and among samples can be related to the presence of porosity. Assuming a 0.65 J/g/K specific heat value at room temperature in the case of magnetite [42] and about 1.87 J/g/K specific heat value for PDMS, the expected composite specific heat should be around 1.59 J/g/K. As it can be seen from Figure 10a, the measured values are close to the theoretical value.

Using the measured values for thermal diffusivity, specific heat, and density, the thermal conductivity was calculated, the results being plotted in Figure 10b. The thermal conductivity values reproduce the trend observed in thermal diffusivity; however, here, the higher density of the sample with acicular dispersions oriented in magnetic field results in an enhancement of the thermal conductivity value, while for the corresponding sample with spherical aligned dispersions, the porosity plays an opposite role reducing the thermal conductivity.

In the sample with unaligned spherical dispersions, self-agglomeration and clustering of the magnetic particles is the most likely explanation for the strongest enhancement of thermal conductivity values observed in this study. In fact, a similar effect was observed also in nanofluids containing even smaller nanometrical particles of Fe_3O_4 particles [43].

The presence of magnetic dispersions in the polymer affects the thermal conductivity of the material, increasing its value up to a factor reaching 2.5 times. The unoriented magnetic dispersions give the highest enhancement of the thermal conductivity, but at the cost of a lower density. Thus, the spontaneous agglomeration of magnetic dispersions produces clusters that contribute to an increase of thermal conductivity but also form the solidifying PDMS matrix with many pores. On the other hand, applying a magnetic field to orient the magnetic dispersions has different effects on thermal conductivity, depending also on the shape of dispersions. Acicular dispersions can be better aligned and help produce a denser matrix, while spherical dispersions produce more voids in the PDMS matrix, resulting in a lower density. As a consequence, the composite with spherical dispersions aligned in the field has also a lower thermal conductivity due to the lower density.

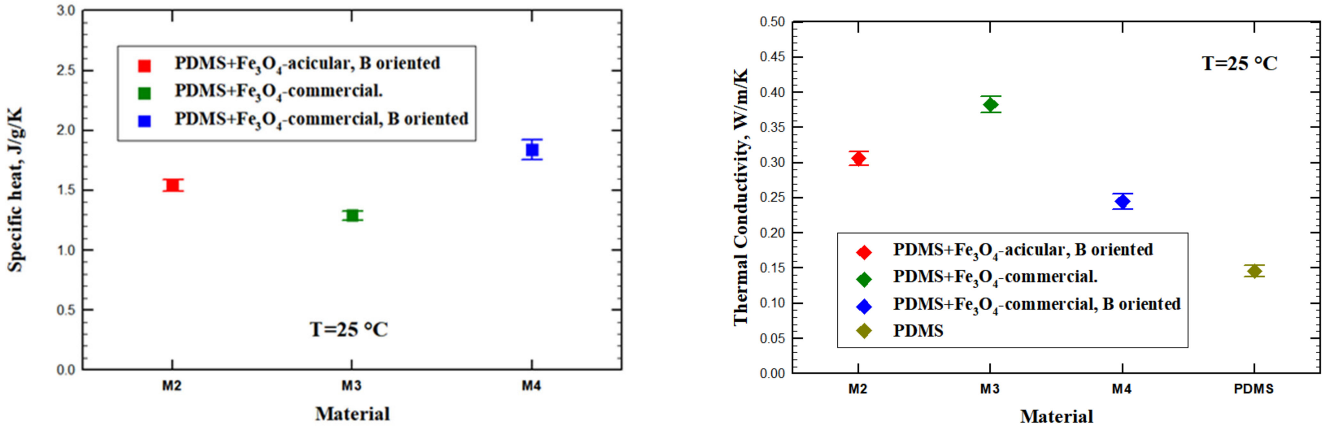

(**a**) (**b**)

Figure 10. (**a**) Specific heat and (**b**) thermal conductivity of PDMS:magnetite composites. Each point represents the mean value of five measurements, while the horizontal lines are the corresponding error bars.

4. Conclusions

We demonstrated how thermal conductivity of composite materials can be influenced by the orientation of the magnetite added into the polymer matrix. Using the experimental route presented in this study, it is possible to achieve nano-structured anisotropic conductive films with good application in microelectronics. Un-oriented magnetite dispersions in the PDMS matrix are able to increase the thermal conductivity with a factor of 2.5 compared to the pristine PDMS film, but also produce a substantial porosity. Orientation of the included dispersions using a magnetic field during the sample polymerization results in slightly lower thermal conductivity values (still about 2 times higher than the value of the bare PDMS in the case of acicular dispersions). For oriented dispersions, in the case of acicular-shaped magnetite, the thermal conductivity is higher than in the case of spherical magnetite and also the acicular dispersions promote a strongly reduced porosity, almost annihilated, resulting in a more compact and homogenous sample.

Author Contributions: Conceptualization, V.S. and M.E.; methodology, V.S., A.G., M.E., M.O., P.P. and B.P.; investigation, V.S., A.G., M.E., M.O., B.P. and P.P.; data curation, P.P., M.A.; writing—original draft preparation, V.S., M.E. and A.G., P.P.; writing—review and editing, M.E.; supervision, R.C. and L.P.; project administration, L.P.; funding acquisition, L.P. All authors have read and agreed to the published version of the manuscript.

Funding: This work was supported by a grant of the Romanian National Authority for Scientific Research and Innovation, UEFISCDI, through POC-G project MAT2IT (contract 54/2016) and the Core Program 2019–2022 (contract 21N/2019).

Institutional Review Board Statement: Not applicable.

Informed Consent Statement: Not applicable.

Data Availability Statement: Data is contained within the article.

Acknowledgments: This work was supported by the Romanian National Authority for Scientific Research and Innovation, UEFISCDI, through POC-G project MAT2IT (contract 54/2016), and the Core Program 2019–2022 (contract 21N/2019).

Conflicts of Interest: The authors declare no conflict of interest.

References

1. Katz, E. Synthesis, Properties and Applications of Magnetic Nanoparticles and Nanowires—A Brief Introduction. *Magnetochemistry* **2019**, *5*, 61. [CrossRef]
2. Lage, T.; Rodrigues, R.O.; Catarino, S.; Gallo, J.; Bañobre-López, M.; Minas, G. Graphene-Based Magnetic Nanoparticles for Theranostics: An Overview for Their Potential in Clinical Application. *Nanomaterials* **2021**, *11*, 1073. [CrossRef] [PubMed]
3. Suvith, V.S.; Devu, V.S.; Philip, D. Facile synthesis of SnO2/NiO nano-composites: Structural, magnetic and catalytic properties. *Ceram. Int.* **2020**, *46*, 786–794. [CrossRef]
4. Köwitsch, I.; Mehring, M. Coatings of magnetic composites of iron oxide and carbon nitride for photocatalytic water Purification. *RSC Adv.* **2021**, *11*, 14053–14062. [CrossRef]
5. Kumar, D.; Moharana, A.; Kumar, A. Current trends in spinel based modified polymer composite materials for electromagnetic shielding. *Mater. Today Chem.* **2020**, *17*, 100346:1–100346:21. [CrossRef]
6. Denver, H.; Heiman, T.; Martin, E.; Gupta, A.; Borca-Tasciuc, D.A. Fabrication of polydimethylsiloxane composites with nickel nanoparticle and nanowire fillers and study of their mechanical and magnetic properties. *J. Appl. Phys.* **2009**, *106*, 64909:1–64909:5. [CrossRef]
7. Antonel, P.S.; Jorge, G.; Perez, O.E.; Butera, A.; Leyva, A.G.; Negri, R.M. Magnetic and elastic properties of $CoFe_2O_4$—polydimethylsiloxane magnetically oriented elastomer nanocomposites. *Macromol. Rapid Commun* **2011**, *110*, 43920:1–43920:8.
8. Sotebier, C.; Michel, A. Jerome Fresnais Polydimethylsiloxane (PDMS) Coating onto Magnetic nanoparticle induced by attractive electrostatic interaction. *Appl. Sci.* **2012**, *2*, 485–495. [CrossRef]
9. Said, M.M.; Yunas, J.; Pawinanto, R.E.; Majlis, B.Y.; Bais, B. PDMS based electromagnetic actuator membrane with embedded magnetic particles in polymer composite. *Sens. Actuators A Phys.* **2016**, *245*, 85–96. [CrossRef]
10. Nguyen, N.T.; Truong, T.Q. A fully polymeric micropump with piezoelectricactuator. *Sens. Actuators B Chem.* **2004**, *97*, 139–145. [CrossRef]
11. De Bhailıs, D.; Murray, C.; Duffy, M.; Alderman, J.; Kelly, G. Modelling andanalysis of a magnetic microactuator. *Sens. Actuators* **2000**, *81*, 285–289. [CrossRef]
12. Pawinanto, R.E.; Yunas, J.; Majlis, B.Y.; Bais, B.; Said, M.M. Fabricationand testing of electromagnetic MEMS microactuator utilizing PCB basedplanar microcoil. *ARPN J. Eng. Appl. Sci.* **2015**, *10*, 8399–8403.
13. Jang, H.; Yoon, H.; Ko, Y.; Choi, J.; Lee, S.S.; Jeon, I.; Kim, J.H.; Kim, H. Enhanced performance in capacitive force sensors using carbon nanotube/polydimethylsiloxane nanocomposites with high dielectric properties. *Nanoscale* **2016**, *8*, 5667–5675. [CrossRef] [PubMed]
14. Dickey, M.D. Stretchable and Soft Electronics using Liquid Metals. *Adv. Mater.* **2017**, *29*, 1606425. [CrossRef] [PubMed]
15. Chiang, C.K.; Popielarz, R. Polymer Composites with High Dielectric Constant. *Ferroelectrics* **2002**, *275*, 1. [CrossRef]
16. Kontos, G.A.; Soulintzis, A.L.; Karahaliou, P.K.; Psarras, G.C.; Georga, S.N.; Krontiras, C.A.; Pisanias, M.N. Electrical relaxation dynamics in TiO_2—polymer matrix composites. *Polym. Lett.* **2007**, *1*, 781. [CrossRef]
17. Psarras, G.C.; Gatos, K.G.; Karahaliou, P.K.; Georga, S.N.; Krontiras, C.A.; Karger-Kocsis, J. Relaxation Phenomena in Rubber/Layered Silicate Nanocomposites. *Polym. Lett.* **2007**, *1*, 837. [CrossRef]
18. Sadovnikov, A.V.; Odintsov, S.A.; Beginin, E.N.; Grachev, A.A.; Gubanov, V.A.; Sheshukova, S.E.; Sharaevskii, Y.P.; Nikitov, S.A. Nonlinear Spin Wave Effects in the System of Lateral Magnonic Structures. *JETP Lett.* **2018**, *107*, 25–29. [CrossRef]
19. Sadovnikov, A.V.; Grachev, A.A.; Gubanov, V.A.; Odintsov, S.A.; Martyshkin, A.A.; Sheshukova, S.E.; Sharaevskii, Y.P.; Nikitov, S.A. Spin-wave intermodal coupling in the interconnection of magnonic units. *Appl. Phys. Lett.* **2018**, *112*, 142402:1–142402:5. [CrossRef]
20. Sadovnikov, A.V.; Bublikov, K.V.; Beginin, E.N.; Nikitov, S.A. The Electrodynamic Characteristics of a Finite_Width Metal/Dielectric/Ferroelectric/Dielectric/Metal Layer Structure. *J. Commun. Technol. Electron.* **2014**, *59*, 914–919. [CrossRef]
21. Siegel, A.C.; Phillips, S.T.; Dickey, M.D.; Lu, N.; Suo, Z.; Whitesides, G.M. Foldable printed circuit boards on paper substrates. *Adv. Funct. Mater.* **2010**, *20*, 28–35. [CrossRef]
22. Kong, Y.L.; Gupta, M.K.; Johnson, B.N.; McAlpinem, M.C. 3D printed bionic nanodevices. *Nano Today* **2016**, *11*, 330–350. [CrossRef]
23. Compton, B.G.; Lewis, J.A. 3D-printing of lightweight cellular composites. *Adv. Mater.* **2014**, *26*, 5930–5935. [CrossRef] [PubMed]
24. Collino, R.R.; Ray, T.R.; Fleming, R.C.; Sasaki, C.H.; Haj-Hariri d, H.; Begleyab, M.R. Acoustic field controlled patterning and assembly of anisotropic particles. *Extreme Mech. Lett.* **2015**, *5*, 37–46. [CrossRef]

25. Levy, R.; Shaheen, U.; Cesbron, Y.; See, V. Gold nanoparticles delivery in mammalian live cells: A critical review. *Nano Rev.* **2010**, *1*, 4889. [CrossRef]
26. Lin, M.M.; Kim, H.H.; Kim, H.; Muhammed, M.; Kim, D.K. Iron oxide-based nanomagnets in nanomedicine: Fabrication and applications. *Nano Rev.* **2010**, *1*, 4883.
27. Yang, Y.-M.; Tsai, H.-H.; Hsu, T.-H.; Su, Y.-C. Magnetic shaping of ferrite-PDMS composite and its application in magnetic carrier targeting. *Transducers* **2009**, 21–25.
28. Driscoll, C.F.; Morris, R.M.; Senyei, A.E.; Widder, K.J.; Heller, G.S. Magnetic Targeting of Microspheres in Blood Flow. *Microvasc. Res.* **1984**, *27*, 353–369. [CrossRef]
29. Carlson, J.D.; Jolly, M.R. MR fluid, foam and elastomer devices. *Mechatronics* **2000**, *10*, 555. [CrossRef]
30. Górecki, K.; Ptak, P.; Torzewicz, T.; Janicki, M. Influence of a Thermal Pad on Selected Parameters of Power LEDs. *Energies* **2020**, *13*, 3732. [CrossRef]
31. Sim, L.C.; Ramanan, S.R.; Ismail, H.; Seetharamu, K.N.; Goh, T.J. Thermal characterization of Al2O3 and ZnO reinforced silicone rubber as thermal pads for heat dissipation purposes. *Thermochim. Acta* **2005**, *430*, 155–165. [CrossRef]
32. Geng, J.; Men, Y.; Liu, C.; Ge, X.; Yuan, C. Preparation of rGO@Fe_3O_4 nanocomposite and its application to enhance the thermal conductivity of epoxy resin. *RSC Adv.* **2021**, *11*, 16592–16599. [CrossRef]
33. Wu, Z.; Chen, J.; Li, Q.; Xia, D.-H.; Deng, Y.; Zhang, Y.; Qin, Z. Preparation and Thermal Conductivity of Epoxy Resin/Graphene-Fe_3O_4 Composites. *Materials* **2021**, *14*, 2013. [CrossRef]
34. Shayganpour, A.; Clausi, M.; Bayer, I.S. Flexible hematite (α-Fe_2O_3)-graphene nanoplatelet (GnP) hybrids with high thermal conductivity. *Appl. Phys. Lett.* **2020**, *118*, 091903:1–091903:6.
35. Kuncser, V.; Chipara, D.; Martirosyan, K.S.; Schinteie, G.A.; Ibrahim, E.; Chipara, M. Magnetic properties and thermal stability of polyvinylidene fluoride—Fe_2O_3 nanocomposites. *J. Mater. Res.* **2020**, *35*, 132–140. [CrossRef]
36. Do, J.Y.; Son, N.; Shin, J.; Chava, R.K.; Joo, S.; Kang, M. n-Eicosane-Fe_3O_4@SiO_2@Cu microcapsule phase change material and its improved thermal conductivity and heat transfer performance. *Mater. Des.* **2021**, *198*, 109357:11–109357:15. [CrossRef]
37. Flaifel, M.H. An Approach Towards Optimization Appraisal of Thermal Conductivity of Magnetic Thermoplastic Elastomeric Nanocomposites Using Response Surface Methodology. *Polymers* **2020**, *12*, 2030. [CrossRef] [PubMed]
38. Li, X.; Li, Y.; Alam, M.M.; Chen, P.; Xia, R.; Wu, B.; Qian, J. Enhanced thermal conductivity of nanocomposites with MOF-derived encapsulated magnetic oriented carbon nanotube-grafted graphene polyhedral. *RSC Adv.* **2020**, *10*, 3357–3365. [CrossRef]
39. Ozaytekin, I.; Oflaz, K. Synthesis and characterization of high-temperature resistant and thermally conductive magnetic PBI/Fe_3O_4 nanofibers. *HIGH Perform. Polym.* **2020**, *32*, 1031–1042. [CrossRef]
40. Jin, Z.; Liang, F.; Lu, W.; Dai, J.; Meng, S.; Lin, Z. Effect of Particle Sizes of Nickel Powder on Thermal Conductivity of Epoxy Resin-Based Composites under Magnetic Alignment. *Polymers* **2019**, *11*, 1990. [CrossRef]
41. Moolgard, K.; Smeltzer, W.W. Thermal conductivity of Magnetite and Hematite. *J. Appl. Phys.* **1971**, *42*, 3644–3647. [CrossRef]
42. Westrum, E.F.; Gronvold, F. Magnetite (Fe_3O_4) heat capacity and thermodynamic properties from 5 to 350 K, low-temperature transition. *J. Chem. Thermodyn.* **1969**, *1*, 543–557. [CrossRef]
43. Zhu, H.; Zhang, C.; Liu, S.; Tang, Y.; Yin, Y. Effects of nanoparticle clustering and alignment on thermal conductivities of Fe_3O_4 aqueous nanofluids. *Appl. Phys. Lett.* **2006**, *89*, 023123.

polymers

MDPI

Article

Feasibility of Producing Core-Shell Filaments through Fused Filament Fabrication

Alexandru Sover [1,*], Vasile Ermolai [1,*], Ashok M. Raichur [2], Romeo Ciobanu [3], Mihaela Aradoaei [3] and Nicolae Lucanu [3]

[1] Department of Technology, Technical Faculty, Ansbach University of Applied Sciences, 91522 Ansbach, Germany
[2] Department of Materials Engineering, Indian Institute of Science, Bengaluru 560012, India; amr@iisc.ac.in
[3] Department of Electrical Measurements and Electrotechnical Materials, Gheorghe Asachi Technical University, 700050 Iasi, Romania; rciobanu@ee.tuiasi.ro (R.C.); mihaela.aradoaei@academic.tuiasi.ro (M.A.); nicolae.lucanu@academic.tuiasi.ro (N.L.)
* Correspondence: a.sover@hs-ansbach.de (A.S.); vasile.ermolai@hs-ansbach.de (V.E.)

Abstract: Fused filament fabrication is a technology of additive manufacturing that uses molten thermoplastics for building parts. Due to the convenient shape of the raw material, a simple filament, the market offers a great variety of materials from simple to blends of compatible materials. However, finding a material with the desired properties can be difficult. Making it in-house or using a material manufacturer can be costly and time-consuming, especially when the optimum blend ratios are unknown or new design perspectives are tested. This paper presents an accessible method of producing core-shell filaments using material extrusion 3D printing. The printed filaments are characterised by a polycarbonate (PC) core and acryl butadiene styrene (ABS) shell with three material ratios. Their performance was investigated through printed samples. Additionally, the material mixing degree was studied by varying the extrusion temperature, nozzle feeding geometry, and layer thickness. The influence of all four factors was evaluated using a graphical representation of the main effects. The results showed that a core-shell filament can be processed using a 3D printer with a dual extrusion configuration and that the mechanical properties of the samples can be improved by varying the PC–ABS ratio. This research provides an accessible method for developing new hybrid filaments with a predesigned structure using a 3D printer.

Keywords: fused filament fabrication; multi-material; core-shell filament; 3D printed filament

check for updates

Citation: Sover, A.; Ermolai, V.; Raichur, A.M.; Ciobanu, R.; Aradoaei, M.; Lucanu, N. Feasibility of Producing Core-Shell Filaments through Fused Filament Fabrication. *Polymers* **2021**, *13*, 4253. https://doi.org/10.3390/polym13234253

Academic Editors: Guillermo Ahumada and Dapeng Wang

Received: 3 November 2021
Accepted: 1 December 2021
Published: 4 December 2021

1. Introduction

Additive manufacturing (AM) represents a versatile set of technologies that can be used conveniently in product development. All parts are manufactured layer by layer directly from the digital 3D data [1,2]. AM comprises a wide range of technologies, materials, and according to ISO 17296-2: 2015, they can be categorised in the following seven groups vat photopolymerisation (VP), material jetting (MJ), binder jetting (BJ), powder bed fusion (PBF), material extrusion (ME), direct energy deposition (DED), and sheet lamination (SL) [3]. Each of these categories contains more than one manufacturing technology. Due to this fact, there is a wide range of available materials such as plastic, metals, and ceramics in liquid, powder, or solid-state [2,4]. The AM process can produce prototypes, tools, and fully functional parts. Besides engineering applications, AM technologies are interdisciplinary and are used in many fields such as medicine, architecture, archaeology [5,6], and many others.

Fused filament fabrication (FFF) or fused deposition modelling (FDM) is a ME technique that uses molten thermoplastic materials to produce parts. As an advantage, FFF disposes of a wide variety of materials from conventional to high-performance polymers with various equipment designs and performances [7].

A drawback of FFF is that the part's performance is highly influenced by print orientation. For this reason, printed parts are characterised by high anisotropy, and depending on the load direction or the part's growth direction (z-direction), the behaviour under stress can vary significantly [8]. This downside has led to the need to develop new specimens that better describe the properties of additively manufactured parts. Watschke et al. (2018) developed such samples to characterise the layer bond quality for ME [9].

The appearance of multi-material extrusion systems introduced new opportunities in 3D printing, boosting the quality of the parts (e.g., by using soluble support structure) or the part's performance under stress (e.g., by producing multi-material components) [10] and has led to new research in the layer bond formation of parts made of similar and dissimilar materials [11]. Besides these, introducing composite materials (e.g., particle reinforced, short carbon, glass, or aramid fibre reinforced) improved the mechanical properties, giving more stability to the components [8,10,12].

The development of co-extrusion equipment allowed parts' reinforcement with continuous fibres of glass, aramid, or carbon. This way, the mechanical properties of the component produced via FFF registered a significant performance improvement [7,12,13], but implies the acquisition of new hardware.

Besides co-extrusion printing, the use of core-shell filaments was explored, which can be used on conventional FFF 3D printers.

Peng et al. (2018) studied the impact resistance of 3D printed samples made of a bisphenol-A PC core and an ionomer of partially zinc-neutralised polyethene-co- methacrylic acid shell filament produced via conventional extrusion. They concluded that a simple core-shell filament enhances the impact performance by generating new pathways to energy dissipation [14].

The research was continued and in 2019 by studying the tensile properties and impact resistance of filaments with a PC-ABS blend core, with low-density polyethene (LDPE) and high-density polyethene (HDPE) shell produced via screw extrusion. The results show a change in the mechanical properties from brittle, for the PC-ABS material, to a ductile behaviour for the core-shell materials for the tensile test. As for the impact test, samples made from the same filament led to a significant improvement [15].

Ai et al. (2021) extended the work from [15] by studying the dimensional accuracy of core-shell filaments of bisphenol-A PC, copolymer PC (cPC), or PC-ABS core and HDPE shell produced in the same way. Through a higher solidification point, the core acts as a reinforcement, and the shell, due to the lower solidification temperature, offers increased mobility between printed cores, improving the mechanical properties [16].

Hart et al. (2020) studied a different approach of producing core-shell filaments with a PC core and ABS shell via thermal drawing of a FFF 3D printed preform. The study covered the impact performance of core-shell filaments with different core designs, from a star shape to a simple circle. The study shows that thermal drawing is a potential solution for manufacturing a high-performance filament for FFF [17].

This paper aimed to study the feasibility of producing a FFF core-shell filament for research purposes using a dual-extrusion 3D printer. The study covered the design of the filaments and printing process with a PC core and ABS shell with different material ratios. In addition, through a Taguchi L9 experimental matrix, the influence of other printing process parameters was studied. These were nozzle input geometry, extrusion temperature, and layer height. Overall, the most significant factor over sample strength is the ratio of the materials. The tensile test result showed that the sample's behaviour could transition from ductile to brittle depending on PC–ABS ratios. Multi-material 3D printing can be an accessible solution for developing new filaments with a specific structure for research purposes.

2. Materials and Methods

ABS and PC polymers were considered for printing the filament due to their good compatibility and available PC–ABS blend filament on the market as a point of comparison.

Since PC material is tougher than ABS, using it as a core can behave similarly to continuous fibres to reinforce the ABS shell [16]. The resulting filaments were printed as samples with flat orientation and evaluated for the tensile test.

2.1. Materials

For 3D printing, the core-shell filaments were chosen: a white colour ABS (i.e., Ultrafuse ABS from BFAS) and a black colour PC (i.e., PolyMax PC from PolyMaker). In addition, a third material was used as a benchmark, a white colour PC-ABS (i.e., PolyMaker PC-ABS). According to the manufacturers' recommendations, all filaments were dried and kept in a dry storage box throughout the study. The same printing conditions were applied for the printed filaments.

2.2. Experimental Setup

As a design of experiments method, a Taguchi L9 matrix was used with four factors and three levels of variation (3^4). For the tensile tests, the 1BA ISO 527 specimen was considered. This setup resulted from the limited filament produced on the printer's build plate area.

The considered variables were PC–ABS ratios, material extrusion temperature, nozzle input orifices, and layer thickness, and their levels of variation are presented in Table 1. The other process parameters involved in the sample printing process were kept at constant values and are presented in Table 2.

Table 1. Process variable of the Taguchi L9 matrix.

Variable/Level	Level 1	Level 2	Level 3
(1) PC–ABS ratios (%)	25–75	50–50	75–25
(2) Extrusion temperature (°C)	250	255	260
(3) Nozzle input orifices	Simple	Double	Triple
(4) Layer thickness (mm)	0.1	0.15	0.2

Table 2. Constant process parameters and their levels.

Parameter	Value	Parameter	Value
(1) Nozzle diameter (mm)	0.4	(10) Retraction distance (mm)	8
(2) Bed temperature (°C)	100	(11) Retraction speed (mm/s)	30
(3) Deposition speed (mm/s)	30	(12) [2] No. top layers	5–7–10
(4) First layer speed (mm/s)	15	(13) [2] No. bottom layers	5–6–10
(5) Line width (mm)	0.43	(14) Infill (%)	0
(6) Raster width (mm)	0.4	(15) Brim	Yes
(7) No. of walls	6	(16) Brim width (mm)	3
(8) [1] Material flow (%)	105	(17) Closed environment	Yes
(9) Fan speed (%)	0	(18) Bed temperature for print removal (°C)	30

[1] (8) The material flow was changed to compensate for the 3D printed core-shell filament diameter inconsistency, [2] (12) No. of top and (13) No. bottom layers are influenced by the layer thickness presented in Table 1.

The variable PC–ABS ratio describes the volume of material of each printed coaxial filament, where the PC is the core and the ABS is the shell. The extrusion temperature range was set between 250 and 260 °C. The lower limit represents the mean melting value of the ABS, and the upper limit the middle melting point of the PC. This range was considered to avoid ABS burning. Nozzle input orifice is a parameter that is related to tool design. For this setup, three types of nozzles were considered: one with a regular geometry with a simple, direct feeding channel, and two with an intermediary wall having two, respectively, three input orifices (Figure 1a). These orifices are drilled holes that start independently and converge at the nozzle's output channel. This design increases the contact surface area between the material and nozzle, providing even heating (heating the filament from outside-in and inside-out). Due to the increased heating area, material flow and homogeneity were improved [18]. In order to appreciate the influence of nozzle input geometry over the homogeneity, for each run included in the experiment matrix, a sample of extruded material was taken and used for visual inspection (Figure 1b). The last considered parameter is layer thickness. As the nozzles exercise a certain pressure over the material during the deposition, the layer height could influence the material flow [19].

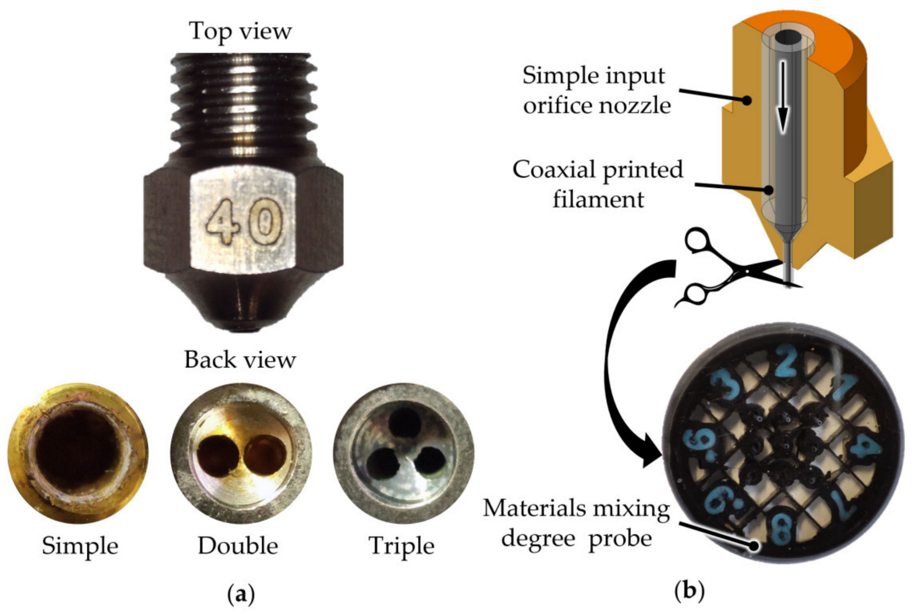

Figure 1. Considered nozzles in the experimental runs. (**a**) Nozzles' input geometry. (**b**) The method used to take samples of the extruded material.

2.3. Design and Parametrisation

The available print area in dual extrusion mode defines the maximum filament length and must be considered in the CAD design (for Ultimaker 3 printer (Utrecht, the Netherlands), the build area is 193 × 193 mm). After defining the limits, the design process is typical, replicable in any CAD software. First, the directory curve is defined as a spiral characterised by revolutions, start and end radius. Then, the generative profiles must be defined and constrained to respect the materials' ratios. Two sketches are needed, one for the filament's core, represented by a circle and one for the shell, defined as a ring, with the smaller circle identical to the core diameter. Then, using a CAD sweep function, each body of the core-shell filament is generated. By knowing the outer shell diameter (i.e., 2.85 mm), the core diameter can be calculated by equalising the areas of the cross-sections. The resulting core diameters for each material ratio are shown in Figure 2. In the case of 75PC-25ABS, the material ratios need to be adjusted due to printing limitations. At PC content of 75%, the wall thickness of the ABS shell was 0.19 mm, below the minimum extrusion width of a 0.25 mm nozzle (i.e., 0.2 mm). Therefore, a core ratio of 73.9% was adopted to obtain the 0.2 mm shell thickness. The 75PC-25ABS designation remained unchanged because the PC material volume was reduced by 1.46% from the nominal ratio.

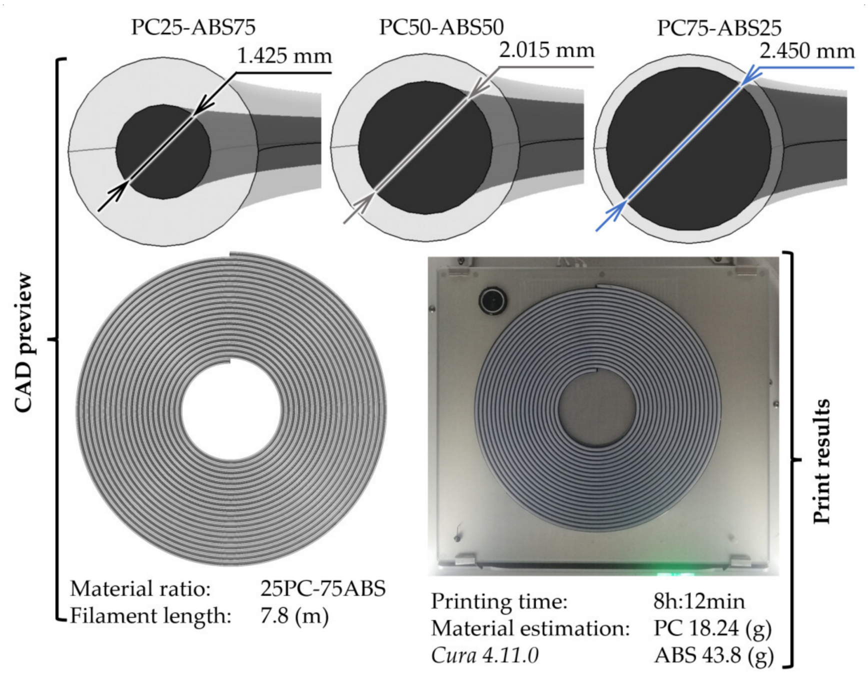

Figure 2. From CAD design to 3D printed core-shell filaments.

All three filaments were produced with similar parameters settings, with a 0.4 mm nozzle, 0.15 mm layer height, a line width of 0.35 mm, and 35 mm/s printing speed. However, to print the 75PC-25ABS filament's shell, a smaller nozzle was necessary (i.e., 0.25 mm) and a line width of 0.2 mm. As shown in Figure 3, the resulting core-shell interface does not have a circular profile because the slicing tool alternates (zig-zagging) the core and shell lines to increase horizontal and vertical adhesion between walls, improving the materials' bond.

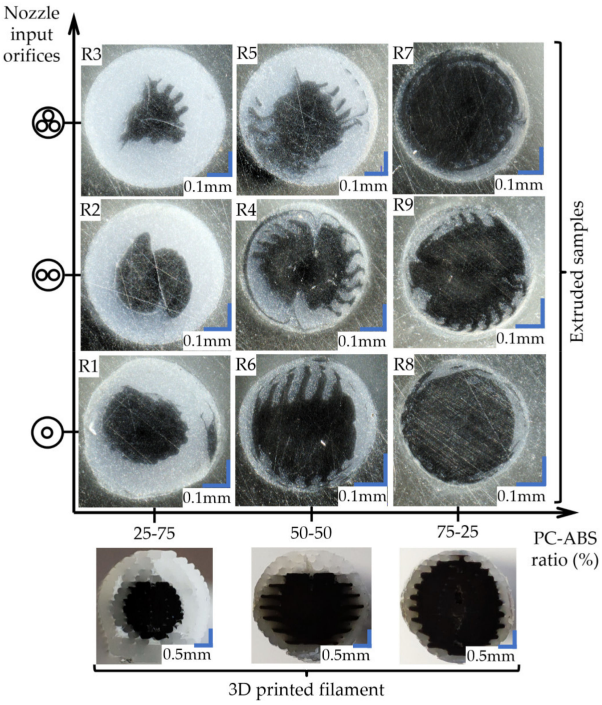

Figure 3. Cross-sectional images of the extruded coaxial filament (300× magnification) and the 3D printed filament cross-section view.

2.4. Evaluation Methods

An Instron 4411 (Darmstadt, Germany) universal uniaxial testing machine was used with a load cell of 5 kN to evaluate the tensile strength of the samples made of core-shell filament. For each trial covered by the experimental setup, five replicates were tested. The same pattern was used for PC–ABS's benchmark specimens. Additionally, as a second benchmark, samples made o materials used in printing the core-shell filament were tested. The Minitab 20.4 tool was used as a statistic tool for the data preparation. All reference specimens were produced with the same setup described in Table 2 at 0.15 mm layer height.

To analyse the influence of nozzle feeding geometry and extrusion temperature over the material mixing homogeneity, samples of extruded filament (as presented in Figure 2) were visually evaluated using a Keyence vhx-7000 (Neu-Isenburg, Germany) microscope.

3. Results

The results include the study of extruded material homogeneity and the specimens' tensile strength resulting from the experimental plan with their response discussion. As a result, the main factors of influence were analysed using graphical representation and variance of the responses of the mechanical test. In the end, the fidelity of the linear regression model was validated through empirical trials.

3.1. Mixing Degree Performance

The extruded wires were evaluated under a microscope (Figure 3) to appreciate the influence of the extrusion temperature and nozzle input geometry over the PC distribution in the ABS mass.

In the case of samples extruded through the nozzle with simple geometry, it can be observed how the extruded section preserves the structure of the input filament regarding the core-shell concentricity and cross-section aspect. The "zig-zag" pattern was kept between layers even after forcing the material through the nozzle (Figure 3). Furthermore, even with a temperature increase, the proportions of the filament's cross-section were kept with no noticeable mixing between materials. This aspect suggests that the structure of the 3D printed filament can be maintained during the entire printing process.

Samples extruded through the nozzle with two input orifices showed deformation of the filament's initial cross-section, giving the PC core more spread in the ABS. In the case of the R2 sample made of 25PC-75ABS and extruded at 255 °C (Figure 3), the two halves of the initial "circular" core glide, resulting in a double snail cam profile. Even so, the core-shell aspect of the materials was preserved for all three extrusion temperatures. Regarding mixing homogeneity, no significant fuse between materials was observed.

The filaments extruded via the nozzle with three input orifices displayed the highest deformation of the PC core from the initial shape. For the 25PC-75ABS material extruded at 260 °C, the core deformed in a triangular shape (Figure 3). The 50PC-50ABS material also presented a high core deformation with an irregular shape, with a higher spread in the ABS mass (Figure 3). Overall, the core-shell form of the materials was maintained for all samples in the group.

3.2. Tensile Strength

All samples were tested in the same laboratory conditions with 58% humidity and 23 °C room temperature and at a speed of 5 mm/s. In addition, five replicates were tested for each configuration of the experimental setup, including the benchmark materials.

The first group of specimens made of the 25PC-75ABS filament presented similar failure behaviour (Figure 4), characterised by average stress of 44.8 MPa and an average strain of 5.5% before the peak. After reaching the maximum stress, crazing occurred on the gauge length. All samples from this group showed a high elongation with an average of 56.0% before the final break at 35.0 MPa.

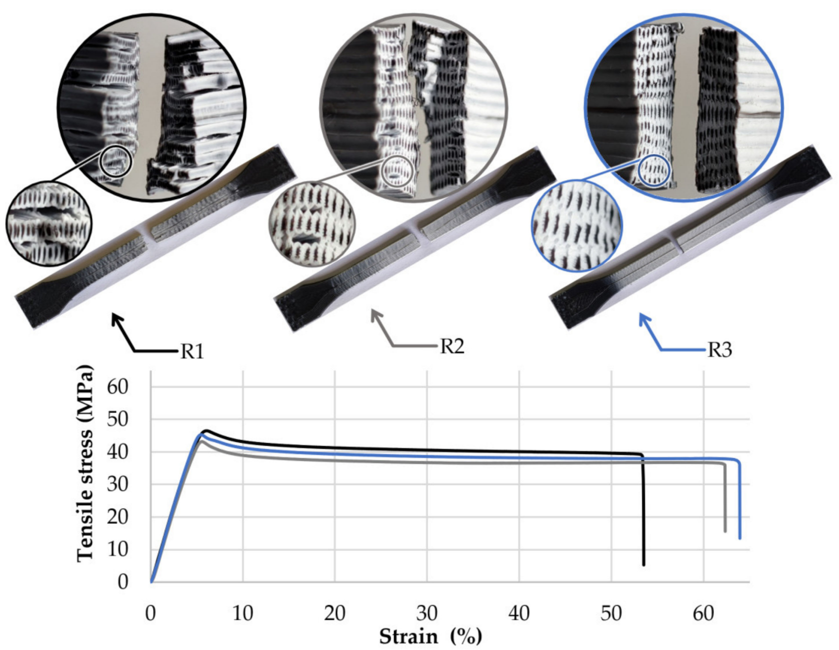

Figure 4. Tensile stress-strain curves, breaking behaviour, and layer structure of the 50PC-50ABS 3D printed filament specimens.

The second group of samples made of 50PC-50ABS filament showed similar breaking behaviour in each set. Their failure modes are presented in Figure 5. Due to the higher content of PC in the filament, the average maximum stress was 49.1 MPa and 7.4% strain before the peak. On average, samples presented a maximum elongation of 23.1% and a yield strength of 38.0 MPa. As soon as the specimens exceeded the maximum stress limit, microfractures of the ABS material whitened the probes' skin across the gauge length.

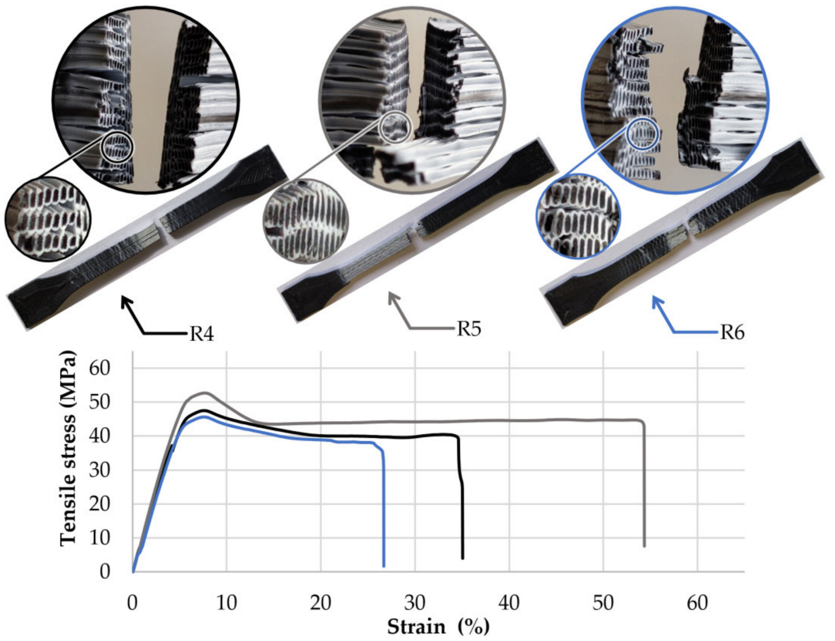

Figure 5. Tensile stress-strain curves, breaking behaviour, and layer structure of the 50PC-50ABS 3D printed filament specimens.

The third group of specimens made of 75PC-25ABS filament (Figure 6) is characterised by high tensile strength of 54.6 MPa with an average elongation of 7.4%. The failure behaviour was akin in each set of samples. In the case of the R8 group with a 0.2 mm layer thickness, sample yield was outside the gauge length and in the same region of the transition radius. Possible explanations are that improper layers fuse due to low extrusion temperature (i.e., 255 °C) correlated with higher layer thickness than other specimens, or residual tension in the area where the samples' walls merge with the solid layers. The same results were obtained after testing the second set of R8 probes with three replicates. Because of the higher PC content in the filament, all specimens in this group presented a brittle breaking behaviour characterised by higher strength and rapid failure. Again, crazing occurred but in a smaller degree due to the low ratio of ABS.

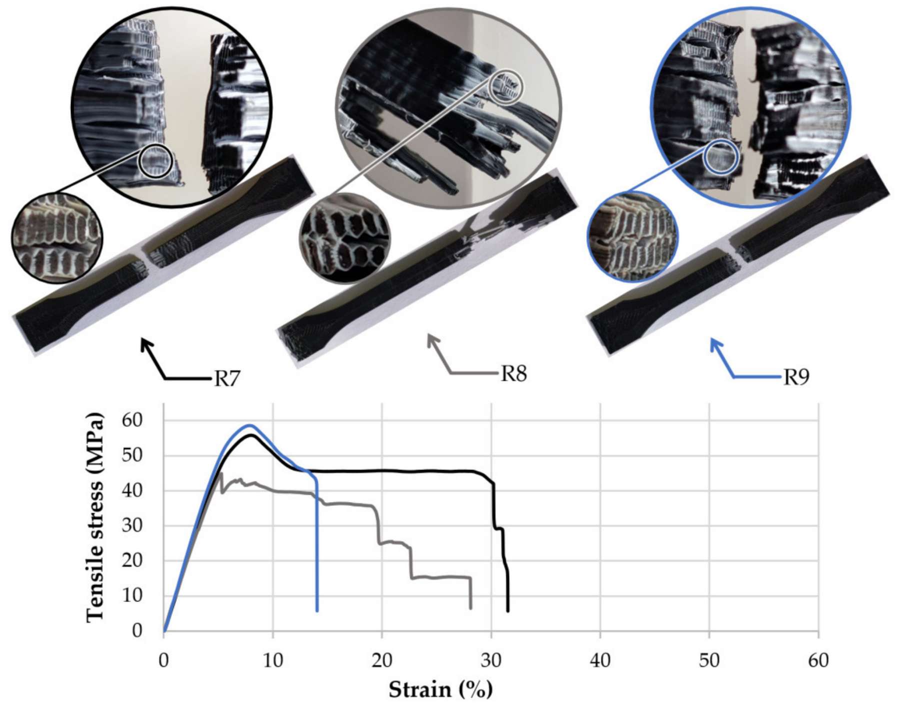

Figure 6. Tensile stress-strain curves, breaking behaviour, and layer structure of the 75PC-25ABS 3D printed filament specimens.

By analysing the fracture zone of the samples, it can be observed that the core-shell profile of the 3D printed filaments was maintained even after the material was pressed by the nozzle and reshaped in the form of lines (see detail views, Figures 4–6).

After the mechanical tests, the raw data were used to calculate the average stress and strain at peak for each group of samples, including the benchmark probes and the materials used to produce the 3D printed filaments. The results are relevant, presenting minor standard deviations. Overall, stress averages display a standard deviation included in the range (0.59, 2.32) and the strain whiting the interval (0.06, 1,18). The average results were analysed graphically using clustered column charts (Figure 7).

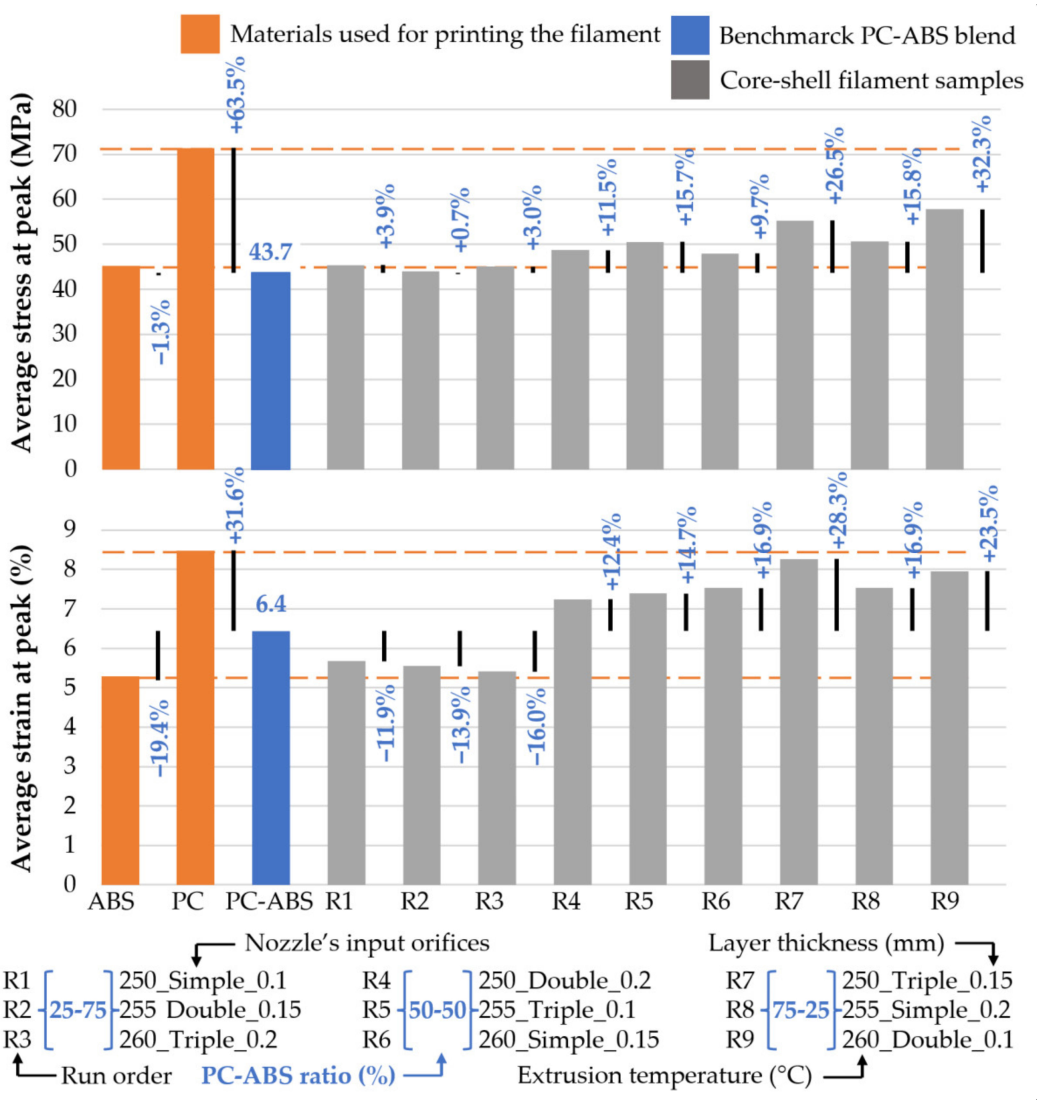

Figure 7. Average tensile stress and strain at the peak of the experimental run specimens referred to the PC-ABS benchmark blend.

In terms of tensile strength, load capacity was augmented by increased PC content in the 3D printed filament. If in the 25PC-75ABS group, the capacity to take loads increased by 3.9% (R1 set made with a 0.1 mm layer height) compared with the benchmark PC-ABS material (43.7 MPa at peak). For the specimens made of 50PC-50ABS filament, the maximum load increased by up to 15.7% (R5 group, printed with 0.1 mm layer thickness). The highest tensile strength was obtained by samples made of 75PC-25ABS, obtaining an improvement of 32.3% for R9 samples with a 0.1 mm layer height. Thus, it can be observed that besides PC-ABS ratios, the layer thickness plays a significant role load capacity undertaken of the samples.

Regarding the strain, compared to the PC–ABS blend benchmark (6.4% elongation at peak), the samples made of the 25PC-75PC showed a decrease in the maximum elongation before the peak. The best results were obtained by the R1 set of samples (printed with 0.1 mm layer thickness), having a decrease of 11.9%. On the other hand, the specimens made of 50PC-50ABS material displayed an increase in elongation at peak. The best result was obtained for the R6 group (with 0.15 mm layer height) with 16.0% improvement. The last group of samples, printed with the 75PC-25ABS material, showed an increase of 28.3% for the R7 set of specimens with a 0.15 mm layer thickness.

Overall, besides the comparison with the PC–ABS blend reference material, it can be observed that most of the results of the experimental run lay between the stress and strain values of the materials used for 3D printing the core-shell filaments (Figure 7).

3.3. Variables Effects

The responses obtained from the experiments were analysed using a graphical representation of the main effects and an analysis of the variance of average tensile properties. Interaction effects between controlled variables were ignored as they were minimal. The response analysis helped identify the variables that had the most significant influence over the tensile strength of the specimens.

Overall, for both responses, stress and strain, the main effect plots showed that the PC–ABS ratio had the most significant influence over the tensile properties of the specimens (Figure 8).

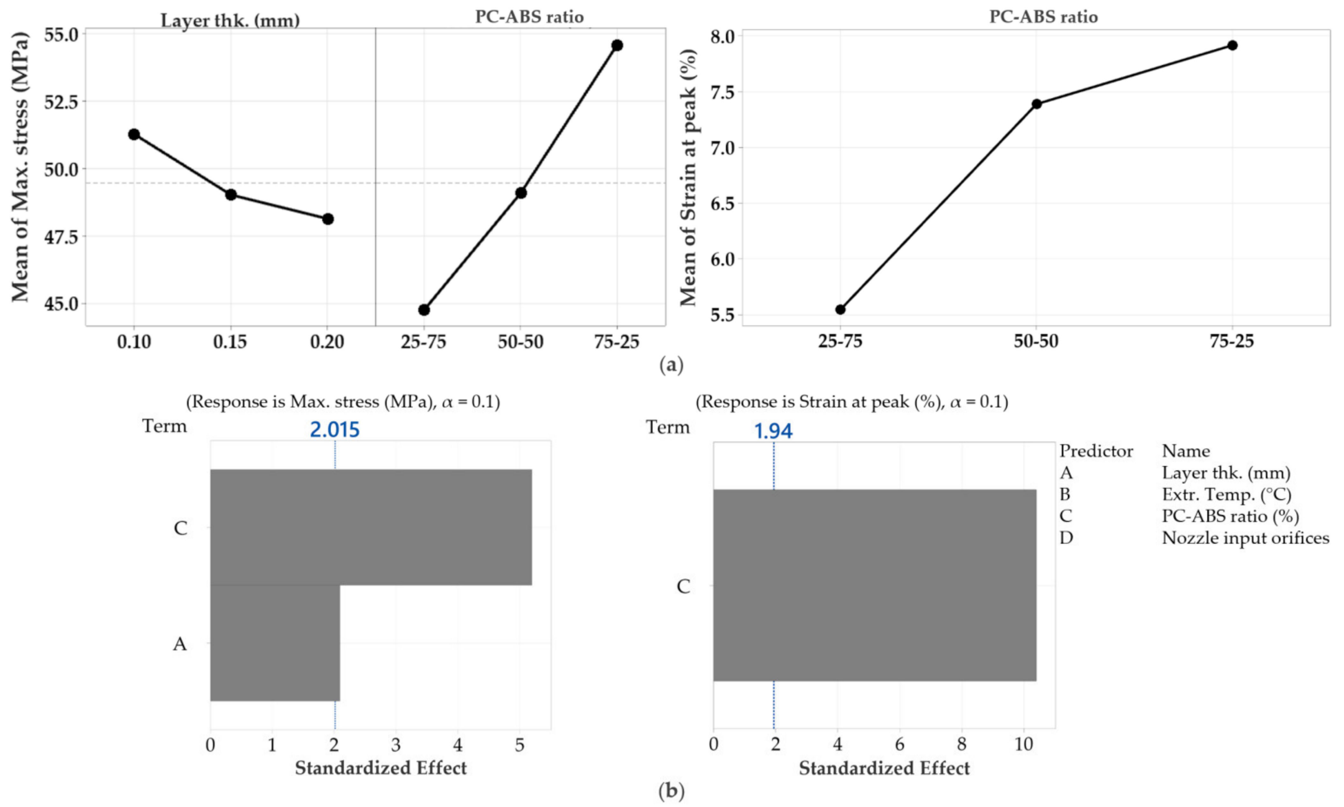

Figure 8. (**a**) Main effects plots of the variables. (**b**) Pareto chart of the standardised effects.

The regression analysis was performed with a confidence level of 90% for both responses with the forward selection method to exclude the insignificant factors. For maximum stress, the regression equation is expressed as a function of materials ratios and layer thickness (Equation (1)) and strain as a function of materials ratios (Equation (2)),

$$\text{Stress (MPa)} = 54.17 - 31.3 \times \text{Lt} - 4.711 \times (25\text{-}75) - 0.388 \times (50\text{-}50) + 5.099 \times (75\text{-}25) \quad (1)$$

$$\text{Strain (\%)} = 6.9491 - 1.404 \times (25\text{-}75) + 0.438 \times (50\text{-}50) + 0.966 \times (75\text{-}25) \quad (2)$$

where Lt is the Layer thickness in mm, and (25–75), (50–50), and (75–25) are the PC–ABS ratios.

3.4. Model Validation

In order to validate the regression models, three supplementary trials were conducted, which included all materials ratios, printed at a 0.2 mm layer thickness at 260 °C, and with a regular nozzle. All resulting values fit the confidence and prediction intervals with a confidence level of 95%. The prediction data and results are available in Table 3.

Table 3. Prediction and results for stress and strain.

Setting		**Prediction**			
Variable	**Value**	**Fit (MPa)**	**SE [1] Fit**	**95% CI [1] (MPa)**	**95% PI [1] (MPa)**
PC–ABS ratio (%)	25–75	43.2	1.29	(37.4, 46.5)	(37.4, 49.0)
	50–50	47.5		(41.7, 53.3)	(41.7, 53,3)
	75–25	53.0		(49.7, 58.8)	(47.2, 58.8)
Result	25–75	Average (MPa)	41.7	Standard deviation	1.6
	50–50		50.0		1.0
	75–25		54.2		1.5
Setting		**Prediction**			
Variable	**Value**	**Fit (%)**	**SE [1] Fit**	**95% CI [1] (%)**	**95% PI [1] (%)**
PC-ABS ratio (%)	25–75	5.5	1.38	(5.2, 5,9)	(4.9, 6.2)
	50–50	7.4		(7.0, 7,7)	(6.7, 8,1)
	75–25	7.9		(7.6, 8.6)	(7.2, 8.6)
Result	25–75	Average (%)	5.4	Standard deviation	0.1
	50–50		7.5		0.1
	75–25		7.9		0.2

[1] with SE—Standard Error; CI—Confidence Interval; PI—Prediction Interval.

4. Discussion

For the experimental setup, it was considered that the nozzles' geometry and extrusion temperature could significantly influence the material flow behaviour and homogeneity. As a result, regardless of the PC–ABS ratios, nozzle input geometry, extrusion temperature, or layer height, the fracture zones showed the same pattern, characterised by a PC core and an ABS envelope similar to the initial core-shell structure of the 3D printed filaments (Figures 4–6). These facts, correlated with the microscope analysis, showed that the filaments' core-shell profile is maintained during the 3D printing process.

Except for R2 and R3 printing setups, which registered a lower tensile strength, the average strength and strain fit into the limits of materials used for printing the core-shell filament (Figure 7). Therefore, we assumed extrusion inconsistency or improper layer fusing affected R2 and R3 samples' strength.

Peng et al. (2019) studied the impact and tensile properties of core-shell filaments of a PC–ABS core and an LDPE and HDPE shell produced through a normal extrusion process [15]. The results showed that the samples' behaviour transitioned from brittle in the PC-ABS blend to ductile with the core-shell filament. Furthermore, similar properties were obtained for the 25PC-75ABS and 50PC-50ABS samples.

Ai et al. (2021) continued the previous work [12] by studying the dimensional accuracy of core-shell filaments of PC, cPC, or PC-ABS core and HDPE shell produced via conventional extrusion. The study highlights that the extrusion temperature does not significantly influence the tensile properties of the core-shell filaments [17]. This statement confirms the result of the regression equations (Equations (1) and (2)).

Producing filaments via 3D printing could be a potential solution in designing and testing new material blends at affordable prices but is not free of limitations and risks.

The first limitation is related to the maximum quantity of filament that can be produced in a printing process. It is dependent on printer build area (i.e., for Ultimaker 3, the maximum printable filament length was ≈8 m), and depending on the material ratios and feature size (e.g., shell thickness), smaller nozzles can be necessary (i.e., 75PC-25ABS was printed with a 0.25 mm nozzle), resulting in a higher printing time (i.e., ≈15 h).

Although the resulting average diameter was satisfactory (2.85 ± 0.1 mm), filament diameter could be affected during the brim removal. Another possible issue is print gaps that could appear in the filament structure (Figure 9a). As a precaution, an extrusion flow of ≈105% should be adopted to avoid the under-extrusion during printing.

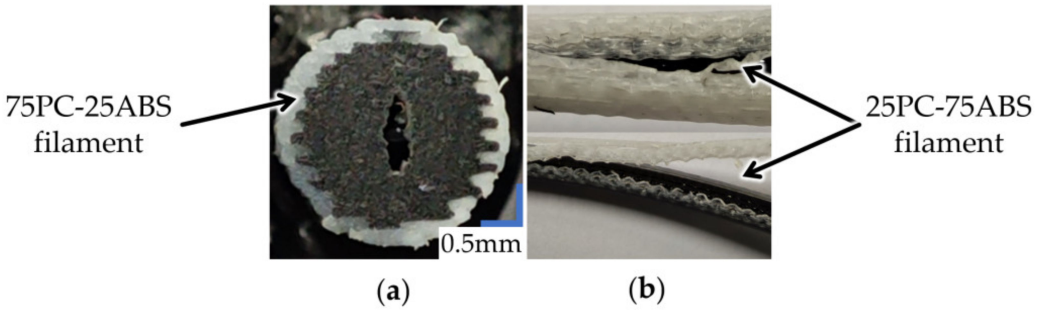

Figure 9. Possible defects of 3D printed filaments. (**a**) Gaps inside the 3D printed filament. (**b**) Shell detach during the printing.

During the printing process, shell detaching from the core (Figure 9b) can lead to filaments sticking in the printer Bowden tube. This defect may occur if the feeding mechanism presses the filament too hard.

Further research must be undertaken to characterise the performance of these materials for impact and bending strength, along with increasing the extrusion temperature to the upper limit of the used PC material (i.e., 270 °C).

5. Conclusions

This work studied a different approach to producing core-shell filaments for research purposes. Printable core-shell filaments with varying ratios of PC and ABS were made using a multi-material 3D printer. Specimens for tensile strength tests were produced with the resulting filaments. Other parameters such as nozzle input geometry, extrusion temperature, and layer thickness were considered to study the mixing degree of the core-shell filaments' materials. Interestingly, regardless of these, the aspect of the core-shell filament was maintained throughout the entire printing process. Pure ABS samples were characterised by high ductility and low tensile stress, and PC specimens by brittleness and high load capacity. Thus, by combining them in the shape of a core-shell filament, it was possible to print samples with results between the limits of the materials. Higher content of ABS increases the specimens' ductility but lowers the strength, and a higher content of PC makes the samples more brittle but increases the load resistance. Therefore, the FFF 3D printing process could be a convenient solution to explore and design new materials with a specific structure made of similar or dissimilar materials for research purposes.

Author Contributions: A.S. supervised and designed the research planning, experiments and results, and technical proofreading of the manuscript; V.E. conceived, designed, performed experiments, analysed the results, and wrote the manuscript; A.M.R., R.C., M.A. and N.L. analysed the experiments, technical proof of results, and review of the manuscript. All authors have read and agreed to the published version of the manuscript.

Funding: This work was supported by a publication grant of the TUIASI, project number GI/P5/2021.

Institutional Review Board Statement: Not applicable.

Informed Consent Statement: Not applicable.

Data Availability Statement: The data presented in this study are available on request from the corresponding author.

Conflicts of Interest: The authors declare no conflict of interest.

References

1. Gibson, I.; Rosen, D.; Stucker, B.; Khorasani, M. Introduction and Basic Principles. In *Additive Manufacturing Technologies*, 3rd ed.; Springer: Cham, Switzerland, 2021; pp. 1–22.
2. Niaki, M.K.; Nonino, F. What Is Additive Manufacturing? Additive Systems, Processes and Materials. In *The Management of Additive Manufacturing*, 1st ed.; Springer: Cham, Switzerland, 2021; pp. 1–35.
3. International Organization for Standardization. *ISO 17296-2 Additive Manufacturing—General Principles—Part 2: Overview of Process Categories and Feedstock*; International Organization for Standardisation: Geneva, Switzerland, 2015.
4. Abdulhameed, O.; Al-Ahmari, A.; Ameen, W.; Mian, S.H. Additive Manufacturing: Challenges, trends, and applications. *Adv. Mech. Eng.* **2019**, *11*, 3–9. [CrossRef]
5. Ngo, T.D.; Kashani, A.; Imbalzano, G.; Nguyen, K.T.Q.; Hui, D. Additive manufacturing (3D printing): A review of materials, methods, applications and challenges. *Compos. Part B Eng.* **2018**, *143*, 181–189. [CrossRef]
6. Kumar, R.; Kumar, M.; Chohan, J.S. Material-specific properties and applications of additive manufacturing techniques: A comprehensive review. *Bull. Mater. Sci.* **2021**, *44*, 181. [CrossRef]
7. Rahim, T.N.A.T.; Abdullah, A.M.; MdAkil, H. Recent Developments in Fused Deposition Modeling-Based 3D Printing of Polymers and Their Composites. *Polym. Rev.* **2019**, *59*, 2–18. [CrossRef]
8. Gao, X.; Qi, S.; Kuang, X.; Su, Y.; Li, J.; Wang, D. Fused filament fabrication of polymer materials: A review of interlayer bond. *Addit. Manuf.* **2021**, *37*, 101658. [CrossRef]
9. Watschke, H.; Waalkes, L.; Schumacher, C.; Vietor, T. Development of novel test specimens for characterisation of multi-material parts manufactured by material extrusion. *Appl. Sci.* **2018**, *8*, 1220. [CrossRef]
10. Singh, S.; Singh, G.; Prakash, C.; Ramakrishna, S. Current status and future directions of fused filament fabrication. *J. Manuf. Processes* **2020**, *55*, 291–300. [CrossRef]
11. Lopes, L.R.; Silva, A.F.; Carneiro, O.S. Multi-material 3D printing: The relevance of materials affinity on the boundary interface performance. *Addit. Manuf.* **2018**, *23*, 45–52. [CrossRef]
12. Dey, A.; Roan Eagle, I.N.; Yodo, N. A Review on Filament Materials for Fused Filament Fabrication. *J. Manuf. Mater. Process.* **2021**, *5*, 69. [CrossRef]
13. Dikshit, V.; Goh, G.D.; Nagalingam, A.P.; Goh, G.L.; Yeong, W.Y. Recent progress in 3D printing of fiber-reinforced composite and nanocomposites. In *Micro and Nano Technologies, Fiber-Reinforced Nanocomposites: Fundamentals and Applications*; Elsevier: Amsterdam, The Netherlands, 2020; pp. 371–394.
14. Peng, F.; Zhao, Z.; Xia, X.; Cakmak, M.; Vogt, B.D. Enhanced Impact Resistance of Three-Dimensional-Printed Parts with Structured Filaments. *ACS Appl. Mater. Interfaces* **2018**, *10*, 16087–16094. [CrossRef] [PubMed]
15. Peng, F.; Jiang, H.; Woods, A.; Joo, P.; Amis, E.J.; Zacharia, N.S.; Vogt, B.D. 3D Printing with Core−Shell Filaments Containing High or Low Density Polyethylene Shells. *ACS Appl. Polym. Mater.* **2019**, *1*, 275–285. [CrossRef]
16. Ai, J.-R.; Peng, F.; Joo, P.; Vogt, B.D. Enhanced Dimensional Accuracy of Material Extrusion 3D-Printed Plastics through Filament Architecture. *ACS Appl. Polym. Mater.* **2021**, *3*, 2518–2528. [CrossRef]
17. Hart, K.R.; Bunn, R.M.; Wetzel, E.D. Tough, Additively Manufactured Structures Fabricated with Dual-Thermoplastic Filaments. *Adv. Eng. Mater.* **2020**, *22*, 1901184. [CrossRef]
18. Beck, C.B. 3D Printer. WO Patent 2017183992A1, 19 April 2016.
19. Rashid, A.A.; Koç, M. Fused Filament Fabrication Process: A Review of Numerical Simulation Techniques. *Polymers* **2021**, *13*, 3534. [CrossRef] [PubMed]